Immunocompetent 3D pancreatic ductal adenocarcinoma (PDAC) BioChip model for preclinical drug testing

Inaugural-Dissertation

Zur Erlangung des Doktorgrades
der Mathematischen-Naturwissenschaftlichen Fakultät
der Heinrich-Heine-Universität Düsseldorf

vorgelegt von

Alina Deipenbrock

aus Münster

Düsseldorf, Juni 2026

aus dem Institut für Pharmazeutische Biologie und Biotechnologie der Heinrich-Heine-Universität Düsseldorf

durchgeführt an dem Institut für Pharmazeutische Biologie und Biotechnologie der Heinrich-Heine-Universität Düsseldorf

Gedruckt mit der Genehmigung der

Mathematischen-Naturwissenschaftlichen Fakultät der

Heinrich-Heine-Universität Düsseldorf

Berichterstatter:

1. Frau Prof. Dr. Nicole Teusch
2. Herr PD Dr. Rüdiger Sorg

Tag der mündlichen Prüfung: 28.10.2026

Summary

Pancreatic ductal adenocarcinoma (PDAC) is one of the deadliest malignant tumors worldwide and is characterized by a dense, desmoplastic, and immunosuppressive tumor microenvironment (TME), as well as marked resistance to conventional and immunotherapeutic approaches. Traditional preclinical models often fail to replicate the complex spatial architecture and dynamic cellular interactions between tumor cells, cancer-associated fibroblasts (CAF), and immune cells. To address this gap, this doctoral thesis demonstrates the development, validation, and application of a translational 3D biochip platform for preclinical drug testing.

The research followed a stepwise translational strategy. First, the pharmacological potential of a novel histone deacetylase (HDAC) inhibitor was evaluated using three-dimensional (3D) PANC-1-based spheroids. This study showed that dual HDAC-2/6 inhibition induces apoptosis and effectively reverses the epithelial-mesenchymal transition (EMT) by upregulating E-cadherin, which significantly reduced tumor cell invasion. These results provided a molecular basis for subsequent integration into more complex systems.

Building on these results, a vascularized biochip platform was developed. This system incorporated human umbilical vein endothelial cells (HUVEC) to simulate a dynamic vascular barrier, enabling continuous perfusion of therapeutics and immune cells. In a proof-of-concept study, the HDAC inhibitor vorinostat demonstrated that the biochip model, consisting of HUVEC and co-culture spheroids generated with PANC-1 tumor cells and pancreatic stellate cells (PSC), could accurately detect dose-dependent drug responses under flow conditions. Furthermore, the platform enabled the recruitment and infiltration of monocytes into the co-culture spheroids, where they differentiated into an immunosuppressive M2 macrophage phenotype. Furthermore, the presence of M2 macrophages reduced the sensitivity of the co-culture spheroids to the chemotherapeutic agent paclitaxel, thereby mimicking a characteristic feature of the PDAC TME.

The final part of the thesis focused on mechanisms of T-cell dysfunction in PDAC. By using both cell line-based and patient-derived spheroids (PDS), the model successfully replicated the clinical checkpoint signature of tumor-infiltrating lymphocytes, which is characterized by high expression of programmed cell death protein 1 (PD-1), cytotoxic

T-lymphocyte-associated protein 4 (CTLA-4), and lymphocyte-activation gene 3 (LAG-3). The results identified stromal C-X-C chemokine ligand (CXCL)12-C-X-C chemokine receptor (CXCR)4 signaling as the primary mediator of T-cell exclusion. Furthermore, pharmacological CXCR4 antagonism enhanced infiltration, while treatment with the anti-PD-1 antibody pembrolizumab partially restored T-cell effector function. The high concordance between PDS and patient-specific clinical data underscores the platform's translational capabilities.

In summary, this work establishes a versatile, animal-free 3D platform that captures key mechanisms of immune evasion and treatment resistance in PDAC. By providing a scalable tool for analyzing TME-driven immunosuppression and evaluating personalized immunotherapeutic strategies, this work makes a significant contribution to the advancement of precision oncology research and the implementation of the 3Rs principles (Replace, Reduce, Refine).

Zusammenfassung

Das duktale Adenokarzinom des Pankreas (PDAC) zählt weltweit zu den tödlichsten bösartigen Tumoren und zeichnet sich durch ein dichtes, desmoplastisches und immunsuppressives Tumormikromilieu (TME) sowie durch eine ausgeprägte Resistenz gegenüber konventionellen und immuntherapeutischen Ansätzen aus. Herkömmliche präklinische Modelle versagen häufig dabei, die komplexe räumliche Architektur und die dynamische zelluläre Interaktion zwischen Tumorzellen, krebsassoziierten Fibroblasten (CAF) und Immunzellen nachzubilden. Um diese Lücke zu schließen, demonstriert diese Doktorarbeit die Entwicklung, Validierung und Anwendung einer translationalen 3D-Biochip-Plattform für die präklinische Wirkstoffprüfung.

Die Forschung folgte einer schrittweisen translationalen Strategie. Zunächst wurde das pharmakologische Potenzial eines neuartigen Histon-Deacetylase (HDAC)-Inhibitors unter Verwendung dreidimensionaler (3D) PANC-1-basierter Sphäroide evaluiert. Diese Studie zeigte, dass eine duale HDAC-2/6-Hemmung Apoptose induziert und die epitheliale-mesenchymale Transition (EMT) durch Hochregulierung von E-Cadherin wirksam umkehrt, was die Invasion von Tumorzellen signifikant reduziert. Diese Ergebnisse lieferten eine molekulare Grundlage für die anschließende Integration in komplexere Systeme.

Aufbauend auf diesen Ergebnissen wurde eine vaskularisierte Biochip-Plattform entwickelt. Dieses System integrierte Endothelzellen der menschlichen Nabelschnurvene (HUVEC), um eine dynamische Gefäßbarriere zu simulieren, die eine kontinuierliche Perfusion von Therapeutika und Immunzellen ermöglichte. In einer Proof-of-Concept-Studie zeigte der HDAC-Inhibitor Vorinostat, dass das Biochip-Modell, bestehend aus HUVEC und Co-Kultur-Sphäroiden, die mit PANC-1-Tumorzellen und Pankreas-Sternzellen (PSC) generiert wurden, unter Strömungsbedingungen dosisabhängige Arzneimittelreaktionen genau nachweisen kann. Darüber hinaus ermöglichte die Plattform die Rekrutierung und Infiltration von Monozyten in die Co-Kultur-Sphäroide, wo sie sich zu einem immunsuppressiven M2-Makrophagen-Phänotyp differenzierten. Zudem verringerte die Anwesenheit von M2-Makrophagen die Empfindlichkeit der Co-Kultur-Sphäroide gegenüber dem Chemotherapeutikum Paclitaxel und ahmte damit ein charakteristisches Merkmal der PDAC-TME nach.

Der letzte Teil der Dissertation konzentrierte sich auf Mechanismen der T-Zell-Dysfunktion bei PDAC. Durch die Verwendung sowohl von Zelllinien-basierten als auch von patientenabgeleiteten Sphäroiden (PDS) replizierte das Modell erfolgreich die klinische Checkpoint-Signatur von tumorinfiltrierenden Lymphozyten, die durch eine hohe Expression von Programmed cell death protein 1 (PD-1), Cytotoxic T-lymphocyte-associated protein 4 (CTLA-4) und Lymphocyte-activation gene 3 (LAG-3) gekennzeichnet ist. Die Ergebnisse identifizierten die stromale C-X-C-Chemokin-Ligand (CXCL)12 - C-X-C-Chemokin-Rezeptor (CXCR)4-Signalübertragung als primären Mediator der T-Zell-Ausschließung. Darüber hinaus zeigten sie, dass ein pharmakologischer CXCR4-Antagonismus die Infiltration verstärkte, während die Behandlung mit dem Anti-PD-1-Antikörper Pembrolizumab die Effektor-Funktion der T-Zellen teilweise wiederherstellte. Die hohe Übereinstimmung zwischen PDS und patientenspezifischen klinischen Daten unterstreicht die translationalen Fähigkeiten der Plattform.

Zusammenfassend lässt sich sagen, dass mit dieser Arbeit eine vielseitige, tierversuchsfreie 3D-Plattform etabliert wurde, die Schlüsselmechanismen der Immunumgehung und Therapieresistenz bei PDAC erfasst. Durch die Bereitstellung eines skalierbaren Werkzeugs zur Analyse der TME-gesteuerten Immunsuppression und zur Bewertung personalisierter immuntherapeutischer Strategien leistet diese Arbeit einen wesentlichen Beitrag zum Fortschritt der präzisionsonkologischen Forschung und zur Umsetzung der 3R-Prinzipien (Ersetzen, Reduzieren, Verfeinern).

Table of Contents

Summary I
Zusammenfassung III
Table of Contents V
List of Tables VII
List of Figures VIII
1.1 PDAC models for preclinical drug testing 1
1.1.1 3D *in vitro* models 1
1.1.2 On-chip models 2
1.1.3 *In vivo* models 3
List of Abbreviations V
2 Introduction 9
2.1 Pancreatic ductal adenocarcinoma 9
2.2 Treatment of PDAC 12
2.3 Tumor microenvironment of PDAC 16
2.3.1 Cancer associated fibroblasts 17
2.3.2 Tumor associated macrophages 18
2.3.3 T-cells 19
2.4 Aims and Objectives 21
3 Publications and manuskripts 23
3.1 Novel Histone Deacetylase (HDAC) Inhibitor Induces Apoptosis and Suppresses Invasion via E-Cadherin Upregulation in Pancreatic Ductal Adenocarcinoma (PDAC) 23
3.1.1 Supplementary Information 58
3.2 Modelling of the multicellular tumor microenvironment of pancreatic ductal adenocarcinoma (PDAC) on a fit-for-purpose biochip for preclinical drug discovery 60
3.2.1 Supplementary Information 94
3.2.2 Additional unpublished data 100
3.3 Targeting stroma-mediated T-cell exclusion and functional exhaustion in pancreatic ductal adenocarcinoma (PDAC) through CXCR4 and PD-1 blockade 101
3.3.1 Supplementary Information 139
4 Unpublished data 145
4.1 Implementation of T-cells into the biochip model 145
4.1.1 Infiltration of T-cells into PDAC spheroids under perfusion on the biochip 145
4.1.2 Checkpoint expression of infiltrated T-cells after perfusion on the biochip 146

4.2 Material and Methods 148
4.2.1 Material 148
4.2.2 Methods 153
5 Discussion 157
5.1 Interactions between the tumor and the TME as drivers of PDAC progression and therapy resistance 157
5.2 Epigenetic remodeling in PDAC 158
5.3 The desmoplastic stroma as a barrier to chemotherapy 159
5.4 Overcoming the T-cell exclusion and dysfunction 161
5.4.1 Targeting stomal-mediated T-cell exclusion through CXCR4 antagonism 163
5.4.2 Targeting T-cell dysfunction through PD-1 blockade 164
5.5 Translational relevance of the immunocompetent PDAC model 165
5.6 Limitations and future perspectives 167
5.7 Conclusion 171
5 References XX
6 Appendix XXXIII
Publications and participation at scientific conferences XXXVIII
Danksagung XL
Eidesstattliche Erklärung XLII

List of Tables

Table 2.1-1 HDAC2, HDAC4 and HDAC6 inhibition assay of MPK544 30

Table 2.1-2 Cytotoxic efficacy of HDAC inhibitors represented by the respective IC50 values [µM] in 2D PANC-1 and pancreatic stellate cells (PSC) cultures as well as in 3D co-culture spheroids after 72 h incubation. The arithmetic means and their respective standard deviations of three independent experiments are depicted. 30

Table 2.2-1 Absorption data of vorinostat in the biochip 74

Table 3.2-1 Suppliers and their locations 148

Table 3.2-2 Chemicals 148

Table 3.2-3 Buffer 149

Table 3.2-4 Basic cell culture medium, supplements, and reagents 149

Table 3.2-5 Commercially available cell culture medium and supplements 149

Table 3.2-6 Cell culture medium composition 150

Table 3.2-7 Cytokines and growth factors 150

Table 3.2-8 Treating compounds 151

Table 3.2-9 Commercially available kits 151

Table 3.2-10 Primary antibodies 151

Table 3.2-11 Secondary antibodies 152

Table 3.2-12 Consumables 152

Table 3.2-13 Devices 153

List of Figures

Figure 1.1-1 Pathogenesis of pancreatic cancer. Healthy ductal epithelium first develops into low-grade, then high-grade dysplastic pancreatic intraepithelial neoplasia (PanIN), and finally into invasive adenocarcinoma, associated with genetic mutational changes. Healthy ductal epithelium may harbor KRAS-activating mutations. Low-grade PanIN exhibits the earliest somatic alterations associated with activation of the KRAS oncogene and early inactivation of the tumor suppressor gene cyclin-dependent kinase inhibitor 2A (CDKN2A). High-grade PanIN display accumulated inactivation of the cell cycle-regulating tumor suppressor genes TP53 and/or SMAD4. Invasive adenocarcinomas present more structural and copy number variants, including complex processes such as chromothripsis. Created with BioRender. 12

Figure 1.3-1 Composition of the tumor microenvironment (TME) in PDAC. Schematic illustration of the different cellular and non-cellular components of the TME in PDAC. Cancer associated fibroblasts (CAF) represent the most prevalent cell type within the TME [105]. In addition, the TME also harbors a variety of immune cells, including myeloid-derived suppressor cells (MDSC), tumor-associated macrophages (TAM (pro-inflammatory M1; anti-inflammatory M2)), cytotoxic T-cells (CTL), T-helper cells (Th cells), regulatory T-cells (Treg), and natural killer cells (NK cells). Moreover, the TME contains neuronal cells such as Schwann cells and sensory neurons. The acellular compartment, generally referred to as the extracellular matrix (ECM), consists primarily of collagens, fibronectins, and hyaluronic acid. Due to resulting elevated interstitial pressure within the PDAC microenvironment, vessels frequently collapse, resulting in a dysfunctional, leaky vasculature. Generated with BioRender. 17

Figure 1.4-1 Preclinical models for PDAC. Preclinical models can be divided into *in vitro* and *in vivo* models. *In vitro* models, including multicellular tumor spheroids (MCTS), patient derived organoids (PDO), and on-chip models. *In vivo* models can be differentiated into genetically engineered mouse models (GEMM), patient-derived xenografts (PDX) and orthotopic mouse models. Generated with BioRender..... 4

Figure 2.1-1 Structure and isozyme profile of KSK64 [28]. 27

Figure 2.1-2 Upregulation of E-cadherin in PANC-1 cells after 24 h. PANC-1 cells were treated with MPK544, SAHA, and tubastatin A for 24 h. mRNA levels of E-cadherin in PANC-1 cells were analyzed by qRT-PCR (A) and at protein level by Western blot (B,C) (control ●; 1 µM MPK544 ▪; 4 µM MPK544; 7 µM MPK544). Representative Western blots are shown (B). Error bars indicate standard errors of mean (of at least three independent experiments, with; ** = $p \leq 0.01$; and **** = $p \leq 0.0001$). 32

Figure 2.1-3 Upregulation of E-cadherin expression in PANC-1 cells. PANC-1 cells were treated with MPK544, SAHA, and tubastatin A or with 20 ng/mL TGF-β, for 72 h. mRNA levels of E-cadherin in PANC-1 cells were analyzed by qRT-PCR (A) and at protein level by Western blot (B,C). Representative Western blots are shown (B). Control ●; 20 ng/mL TGF-β ▪; 20 ng/mL TGF-β with 4 µM MPK544; 20 ng/mL TGF-β with 4 µM SAHA; 20 ng/mL TGF-β with 10 µM tubastatin *). Error bars indicate standard errors of mean (of at least three independent experiments, with * = p ≤ 0.05; ** = p ≤ 0.01; and **** = p ≤ 0.0001)... 34

Figure 2.1-4 Expression of E-cadherin in 3D co-culture spheroids after treatment with MPK544 and SAHA. Co-culture spheroids were treated with 2 µM MPK544 or SAHA for 72 h, respectively. Expression of E-cadherin was quantified via flow cytometry. (A) Exemplary overlay histograms for E-cadherin expression after different treatments. (B) Quantification of MFI fold change in E-cadherin expression in co-culture spheroids after treatment with 2 µM MPK544 or SAHA for 72 (control ●; 2 µM MPK544 ▪; 2 µM SAHA). E-cadherin expression was measured in at least 3000 cells. Error bars indicate standard errors of mean (n = 3 independent experiments with * = p ≤ 0.05. 35

Figure 2.1-5 The invasion of PANC-1 cells into a 3D matrix. (A) PANC-1 cells were mixed in a ratio of 1:1 with matrigel and seeded into a 24-well plate. After 24 h, a second layer of matrigel was applied, and the cells were incubated for 72 h at 37 °C. The invasion of the PANC-1 cells into the second matrigel layer was studied by phase contrast microscopy (control in red; 20 ng/mL TGF-β in purple; 2 µM MPK544 in pink). The invasion assay ran for 72 h, and the area of invaded cells into the surrounding matrigel was visualized (control in red; 20 ng/mL TGF-β in purple; 2 µM MPK544 in pink) and calculated. (B) The quantification of the area of invaded cells upon treatment with 2 µM MPK544 in PANC-1 cells (control ●; 20 ng/mL TGF- β ▪; 2 µM MPK544). Error bars indicate the standard errors of the mean (n = 3 independent experiments with **** = p ≤ 0.0001). 36

Figure 2.1-6 Induction of apoptosis in PANC-1 cells. Cells were treated with 1 µM MKP544, 1 µM SAHA, 10 µM tubastatin A, or 0.1 µM paclitaxel for 48 h. For detection of apoptosis, cells were stained with Annexin V and PI and analyzed by flow cytometry. (A) Percentage of apoptotic cells treated with MPK544, SAHA, tubastatin A, or paclitaxel are shown in exemplary dot plots. (B) Quantification of apoptotic cells after 48 h of treatment. Apoptosis of at least 10,000 cells was analyzed via flow cytometry. Error bars indicate standard errors of mean (n = 3 independent experiments with ** = p ≤ 0.01)..... 38

Figure 2.1-7 Cell cycle analysis of PANC-1 cells. Cells were treated with 1 µM MPK544, 1 µM SAHA, 10 µM tubastatin A, or 0.1 µM paclitaxel for 48 h. Cell cycle analysis was performed according to Nicoletti method. (A) Percentage of cells in different cell cycles after treatment with MPK544, SAHA, tubastatin A, or paclitaxel for 48 h is shown in exemplary histograms. (B) Quantification of cell cycle phases. Cell cycles of at least 10,000 cells were analyzed via flow cytometry. Error bars indicate standard errors of mean (n = 3 independent experiments with ** = p ≤ 0.01; and **** = p ≤ 0.0001). 39

Figure 2.1-8 MPK544 demonstrates a synergistic interaction with the chemotherapeutic drug gemcitabine and no synergistic interaction with 5-fluorouracil (5-FU). A representative Bliss synergy plot of MPK544 with gemcitabine (A) and 5-FU (B) in PANC-1 cells (n = 3) is depicted. The Bliss synergy was analyzed and visualized with the Combenefit software (version 2.021) [44]. 41

Figure 2.2-1 Design of the biochip. (A) Exploded view of the chip (B) translucent view of the chip. The upper panel shows the TOP view with underlying channels in dotted lines. Coloured circles indicate the location of ports for TOP (TOP), middle (MID) and bottom (BOT) channels. The lower panel shows a cross section of a chamber at the indicated position. The position of the bonding foil (BF), the membrane pore size of 8 µm (M) and microcavity membrane pore size of 2 µm (MCM) are indicated. Red numbers depict the channel height at the bottlenecks (red arrows) in millimeters. (C) Perfusion setup for the PDAC model. The tubing connects ports of the TOP and the BOT channel to create two independent perfusion circles. The MID channel is sealed. Arrows indicate the media flow direction in the TOP (magenta) and the BOT (blue) channel during perfusion. (D) Schematic illustration of the PDAC model. Arrows depict the flow direction in the TOP (magenta) and the BOT (blue) channel. 73

Figure 2.2-2 Cultivation of spheroids on the biochip. (A) Co-culture spheroids and PANC-1 spheroids loaded into the microcavities of the biochip. Images are taken via bright field microscopy after loading of the spheroids. Scale is 1000 µm. (B) If staining of 3D PANC-1 and co-culture spheroids after 72 h cultivation on the biochip shown as maximum intensity projection (MIP) of a Z-stack. DAPI-staining of nuclei (blue); staining of the proliferation marker Ki67 (green); staining of fibroblast marker α-SMA (purple); merging of all three channels. Scale bar is 500 µm. (C) Investigation of cell viability of 3D spheroids after 72 h cultivation on biochip either under flow or static conditions in comparison to the cultivation in a 96-well plate. Error bars indicate the standard errors of the mean of at least three independent experiments, with **** = $p \leq 0.0001$. 77

Figure 2.2-3 Cultivation of HUVEC on the biochip. HUVEC were cultivated for 72 h under static (upper row) or flow (bottom row) conditions. The endothelial markers VE-cadherin (green), von Willebrand factor (vWF) (red) and the nuclear dye DAPI (blue) were stained. Shown as MIP of a Z-stack. Scale bar is 200 µm. 78

Figure 2.2-4 Rescue strategy for HUVEC layer in the presence of pdac spheroids. The vasculature remains stable under static (A) and flow (B) with an addition of 2.5% matrigel both in the presence of co-culture spheroids (upper row) as well as in the presence of PANC-1 spheroids (bottom row). Stained the endothelial markers VE-cadherin (green), von Willebrand factor (vWF) (red) and the nuclear dye DAPI (blue) were stained. Shown as MIP of a Z-stack. Scale bar is 200 µm. 79

Figure 2.2-5 Dynamic administration of the HDAC inhibitor SAHA in the PDAC biochip model. (A) Investigation of the influence of increasing SAHA concentrations on the vasculature integrity. VE-cadherin (green), von Willebrand factor (red) as marker of the endothelial cells, DAPI for staining the cell nuclei (blue). Shown as MIP of a Z-stack. Scale 200 µm. (B) Investigation of the viability of the 3D PDAC spheroids in the biochip in the presence of SAHA after 72 h administration (with **** = $p \leq 0.0001$). (C) Permeability assay of HUVEC layer after treatment with SAHA for 72 h. FITC dextran assay was performed to measure the barrier integrity of the HUVEC layer after 72 h treatment with 1.5, 2.5, or 3.5 µm SAHA. FITC dextran solution was added into the top channel. After 1 h the leakage into the mid channel was determined via fluorescence measurement. 81

Figure 2.2-6 Polarization of monocytes after perfusion in the biochip. (A) If staining of co-culture spheroids after perfusion with primary monocytes over the endothelial layer. Co-culture spheroids were seeded into the biochip and primary monocytes were perfused over the endothelial layer in the TOP channel. After 72 h of perfusion the co-culture spheroids were stained for the tumor cell marker pan-cytokeratin (purple), the fibroblast marker α-SMA (blue), the immune cell marker CD45 (green), and the M2 marker CD163 (red); merging of all four channels. Shown as MIP of a Z-stack. Scale bar is 500 µm. (B) Marker characterization of polarized macrophages. Polarization after infiltration into co-culture spheroids was analyzed by flow cytometry 72 h after perfusion with monocytes in the biochip. Macrophages identified as $CD11b^+$ and $CD45^+$ were analyzed for surface expression of CD163, CD206, CD86, and HLA-DR. Infiltrated cells were compared to unstimulated monocytes as controls. Error bars indicate the standard errors of the mean of three independent experiments, with ** = $p \leq 0.01$; *** = $p \leq 0.005$. 83

Figure 2.2-7 Spatial distribution of infiltrated monocytes. (A) 3D-rendered confocal Z-stack image of a monocyte-infiltrated spheroid, consisting of 300 slices each 1 µm per step, visualized using image software Fiji with the 3D viewer plugin. For enhanced clarity, the spheroid was spatially cut in half, allowing better visualization of the fibrotic shell, the core of PANC-1 cells and the spatial distribution of infiltrating macrophages. Created in biorender. (B) Fluorescent 3D image of the halved spheroid. Scale bars in 100 µm steps are provided, and the spatial orientation of the halved section is indicated. If staining for the tumor cell marker pan-cytokeratin (purple), the fibroblast marker α-SMA (blue), the and the M2 marker CD163 (green) merged in one image. White arrows indicate $CD163^+$ signals. 85

Figure 2.2-8 Effect of macrophages on chemosensitivity. PBMC-derived monocytes were differentiated towards M2 macrophages for 7 days. M2 macrophages were added to co-culture spheroids 24 h after seeding the spheroids. Co-culture spheroids with or without (wo) M2 macrophages were treated on day four of the spheroid culture for 72 h. Cell viability was determined using the Cell Titer Glo Assay. Viability was normalized against the corresponding DMSO control. Error bars indicate the standard errors of the mean of three independent experiments, with * = p ≤ 0.05; ** = p ≤ 0.01; ***= p ≤ 0.005; **** = p ≤ 0.0001. 100

Figure 2.3-1 Intratumoral T-cell distribution and frequency in PDAC patients. Shown are two representative immunofluorescence staining of two tumor slices from PDAC patients with individual channels (A) alongside a merge of all fluorescence channels (B). Stained are the tumor cell marker pan-cytokeratin (magenta), the fibroblast marker alpha-smooth-muscle-actin (αSMA, cyan), and the T-cell markers CD8 (green) and CD4 (red). Scalebar: 200 µm. (C) Quantification of $CD4^+$ and $CD8^+$ percentages in tumor infiltrating lymphocytes (TIL). Percentages of $CD4^+$ and $CD8^+$ were quantified in tumor slices from 10 PDAC patients conducting image-based analysis. (D) Frequency plot of CD4 and CD8 percentages in PBMC and TIL. Frequency of $CD4^+$ and $CD8^+$ T-cells isolated from the blood of patients or the tumor tissue was analyzed via flow cytometry. PBMC from age-matched healthy donors served as a control group. Error bars indicate the standard errors of the mean of five independent patients, with ** = p≤0.01, **** = p ≤ 0.0001. 114

Figure 2.3-2 Checkpoint expression in T-cells isolated from the blood or the tumor tissue of PDAC patients. Checkpoint expression in $CD4^+$ (A) and $CD8^+$ (B) T-cells isolated from the blood or the tumor tissue of PDAC patients was analyzed by flow cytometry. T-cells identified as $CD3^+$ and $CD45^+$ were analyzed for surface expression of CTLA-4, PD-1, LAG-3 and CD69. T-cells isolated from the tumor tissue were compared to T-cells isolated from the blood. Error bars indicate the standard errors of the mean of four independent patients, with ** = p≤0.01; *** = p ≤ 0.005; **** = p ≤ 0.0001. 115

Figure 2.3-3 Checkpoint expression in T-cells after co-cultivation with PANC-1 spheroids. Checkpoint expression in $CD4^+$ (A) and $CD8^+$ (B) T-cells after co-cultivation with PANC-1 spheroids was analyzed by flow cytometry. PANC-1 spheroids were generated prior to infiltration with $CD3^+$ T-cell, isolated from PBMC from healthy donors. T-cells infiltration was performed for 72 h with either co-culture spheroids or PANC-1 monospheroids. T-cells identified as $CD3^+$ and $CD45^+$ were analyzed for surface expression of CTLA-4, PD-1, LAG-3 and CD69. Naïve T-cells isolated from the blood of healthy donors served as control. (C) Frequence of $CD25^+$ $FoxP3^+$ $CD4^+$ T-cells. Frequence of $CD25^+$ $FoxP3^+$ in $CD4^+$ T-cells was analyzed after 72 h of infiltration. Naïve T-cells isolated from the blood of healthy donors served as control. Error bars indicate the standard errors of the mean of at least three independent experiments from three different donors, with * = p≤0.05; ** = p≤0.01; **** = p ≤ 0.0001. 117

Figure 2.3-4 T-cell infiltration into PANC-1 spheroids. Shown are representative immunofluorescence images of PANC-1 spheroids with $CD3^+$ T-cells. PANC-1 monospheroids or co-culture spheroids containing PSC were infiltrated with $CD3^+$ T-cells isolated from PBMC from healthy donors for 72 h. Spheroids were stained for pan-cytokeratin (tumor cells, purple), CD4 (green), CD8 (red), and either nuclei or α-SMA (fibroblast) (blue). Representative single optical sections from a z-stack (A) and maximum intensity projections (MIP) of the complete z-stack (B) for the single channels alongside a merge of all fluorescence channels are shown. Scale bar, 500 µm; magnification, 10x. 118

Figure 2.3-5 Composition of patient-derived spheroids (PDS). (A) Spheroids composed of patient-derived tumor cells and patient-derived CAF were generated for four days. Spheroids were stained with the fibroblast marker α-SMA (red), the tumor cell marker cytokeratin 7 (green), and the nuclei (blue). Shown are representative single optical sections from a z-stack for the single channels alongside a merge of all fluorescence channels. Scale bar, 500 µm; magnification, 10×. (B) 3D-rendered confocal Z-stack image of a patient derived spheroid, consisting of 300 slices each 0.5 µm per step, visualized using Image Software Fiji with the 3D Viewer plugin. For enhanced clarity, the spheroid was spatially cut in half, allowing better visualization of the fibrotic shell, the nuclei and the tumor cells. The spatial orientation of the section is indicated. Scale bar are 100 µm steps. Magnification 20x. 120

Figure 2.3-6 T-cell infiltration into patient-derived spheroids (PDS). (A) Representative immunofluorescence images of PDS following infiltration with autologous $CD3^+$ T-cells. Spheroids composed of patient-derived tumor cells and patient-derived CAF were infiltrated with autologous $CD3^+$ T-cells isolated from PBMC from the same PDAC patient for 72 h. Spheroids were stained for pan-cytokeratin (tumor cells, purple), CD4 (green), CD8 (red), and α-SMA (fibroblast) (blue). Representative maximum intensity projections (MIP) from a whole z-Stack and single optical sections from a z-stack for the single channels alongside a merge of all fluorescence channels are shown. Scale bar, 500 µm; magnification, 10×. (B, C) Checkpoint expression in T-cells after 72 h infiltration in PDS. Checkpoint expression in $CD4^+$ (B) and $CD8^+$ (C) T-cells after infiltration in PDS were analyzed by flow cytometry. T-cells identified as $CD3^+$ and $CD45^+$ were analyzed for surface expression of CTLA-4, PD-1, LAG-3 and CD69. (D) Frequence of $CD25^+$ $FoxP3^+$ $CD4^+$ T-cells. Frequence of $CD25^+$ $FoxP3^+$ in $CD4^+$ T-cells was analyzed after 72 h of infiltration. Autologous naïve T-cells isolated from the blood of the same patient served as a control. Error bars indicate the standard errors of the mean of at least four independent experiments with * = $p \leq 0.05$; ** = $p \leq 0.01$; ** = $p \leq 0.001$; **** = $p \leq 0.0001$. 122

Figure 2.3-7 . T-cell infiltration in co-culture spheroids and PDS after AMD3100 treatment. (A) Schematic illustration of the mechanistic interaction of AMD3100 on T-cell infiltration. Created with BioRender. Representative IF staining of co-culture spheroids (B) and PDS (C) after infiltration with $CD3^+$ T-cells and treatment with AMD3100 for 24 h. Co-culture spheroids were infiltrated with $CD3^+$ T-cells isolated from healthy donors PBMC for 24 h. PDS were infiltrated with autologous T-cells derived from patients´ PBMC. Treatment with 4 µM AMD3100 was added directly after T-cell addition and performed for 24 h. Spheroids were stained for the T-cell marker CD45 (purple), the nuclei (blue), and the fibroblast marker α-SMA (green). Representative images of on layer of a z-stack (B, C) are displayed. Scale bar is 500 µm and the magnification 10x. (D, E) Quantification of the T-cell infiltration after treatment with AMD3100. The spheroids were divided into a shell region and a tumor cell core region based on the α-SMA signal. T-cells were associated with the core or shell region. Displayed are the percentage of T-cells in the tumor core region with or without 4 µM AMD 3100 treatment in co-culture spheroids (D) and PDS (E). Data represent the standard error of the mean of at least three independent experiments. Statistical significance is indicated as *p ≤ 0.05, **p ≤ 0.01. 125

Figure 2.3-8 IFN-γ, Granzyme B and perforin expression following treatment with pembrolizumab. PDAC spheroids were infiltrated with $CD3^+$ T-cells isolated from PBMC from healthy donors or, in the case of patient-derived spheroids (PDS), with autologous patient-derived PBMC. Pembrolizumab (1 µg/mL or 10 µg/mL) was added at the time of T-cell infiltration and maintained for 72 h. IFN-γ (A), Granzyme B (B) and perforin (C) mRNA expression was quantified by RT–qPCR. Data represent the mean ± SEM of three independent experiments. Statistical significance is indicated as *p ≤ 0.05, **p ≤ 0.01, ***p ≤ 0.001, and ****p ≤ 0.0001. 126

Figure 3.1-1 T-cell infiltration in PANC-1 spheroids on chip. Shown are representative immunofluorescence images of PANC-1 spheroids infiltrated with $CD3^+$ T-cells. PANC-1 monospheroids or co-culture spheroids containing PSC were perfused with $CD3^+$ T-cells isolated from PBMC from healthy donors for 72 h. Spheroids were stained for pan-cytokeratin (tumor cells, purple), CD4 (red), CD8 (green), and either nuclei or α-SMA (fibroblast) (blue). Representative single optical sections from a z-stack (A) and maximum intensity projections (MIP) of the complete z-stack (B) for the single channels alongside a merge of all fluorescence channels are shown. Scale bar, 500 µm; magnification, 10x..... 146

Figure 3.1-2 Checkpoint expression in T-cells after infiltration on the biochip. Checkpoint expression in $CD4^+$ (A) and $CD8^+$ (B) T-cells after perfusion on the biochip was analyzed by flow cytometry. PANC-1 spheroids were generated prior to loading on the biochip and perfusion with $CD3^+$ T-cell, isolated from PBMC from healthy donors. T-cells perfusion was performed for 72 h on either co-culture spheroids or PANC-1 monospheroids. T-cells identified as $CD3^+$ and $CD45^+$ were analyzed for surface expression of CTLA-4, PD-1, LAG-3 and CD69. Naïve T-cells isolated from the blood of healthy donors served as control. Naïve T-cells isolated from the blood of healthy donors served as control. Error bars indicate the standard errors of the mean of at least three independent experiments from three different donors, with * = p≤0.05; ** = p≤0.01; *** = p≤0.001; **** = p ≤ 0.0001. 147

1.1 PDAC models for preclinical drug testing

Improving the poor survival rates associated with PDAC requires the exploration of novel therapeutic strategies. A major challenge in PDAC research is the lack of preclinical models that accurately reflect the complex interactions between tumor cells, stromal components, and immune cells, which critically influence therapeutic response to chemotherapeutic agents and restrict the efficacy of other therapeutic approaches (e.g., CAR-T cells) [106, 159]. As a result, the predictive power of current drug testing platforms remains limited, contributing to the high failure rate in the translation of preclinical findings into clinical applications. Over the past decades, a wide range of preclinical models has been established for drug discovery and therapeutic testing in PDAC. These include simple two-dimensional (2D) cell line models, 3D *in vitro* models such as multicellular tumor spheroids (MCTS) and patient-derived organoids (PDO), as well as tumor-on-chip models and *in vivo* models [160-163]. However, each of these approaches possesses distinct advantages and limitations, and their suitability depends largely on the specific research question being addressed.

1.1.1 3D *in vitro* models

In vitro modulation of the multifaceted cellular interactions within the TME in PDAC represents a technical and scientific challenge, as conventional 2D tumor cell cultures are unable to adequately replicate cell-cell and cell-matrix signaling interactions, physicochemical matrix stiffness, gradients of nutrients and oxygen, and spatial organization [164]. This limitation considerably impairs the predictability of therapeutic efficacy in 2D tumor cell monolayers in general and in PDAC specifically.

To develop more physiologically relevant *in vitro* models, MCTS and PDO represent the latest advancements in preclinical tumor modeling aimed to better reflect the TME in PDAC [165]. MCTS were initially introduced by Kunz-Schughart et al. in 2001, who established co-culture spheroids consisting of breast cancer cells and fibroblasts [166]. Since then, a wide range of MCTS models has been developed across different tumor entities, including pancreatic cancer, typically combining malignant cells with one or more stromal components [161, 167-171]. Most of these early PDAC spheroid systems relied on pancreatic cancer cell lines in combination with CAF and a limited set of extracellular matrix components, such as collagen or Matrigel [161, 167, 170]. More advanced models incorporate additional stromal cell populations, including endothelial cells [169] and TAM [172]. Notably, the integration of monocytes into PDAC spheroids

has demonstrated that these systems can support their differentiation into macrophages and promote polarization toward an M2-like phenotype [172-174].

PDO have emerged as an important step towards personalized therapeutic approaches as they can be established directly from primary PDAC tumor tissue [163, 175]. However, most PDO systems are largely restricted to tumor epithelial cells and therefore do not capture the contribution of CAF which are key mediators of immune suppression and exclusion in PDAC [111, 175]. In contrast to conventional cell line-based systems, fully patient-derived models preserve the genetic, stromal, and immunologic complexity of the native TME. The incorporation of autologous tumor cells together with CAF and matched immune cells allows the study of tumor-immune interactions within an HLA-matched setting, thereby more closely reflecting physiologically relevant mechanisms such as T-cell exhaustion, checkpoint induction, and stromal-mediated immune exclusion [176, 177]. Consequently, patient-derived platforms improved translational relevance and may provide greater predictive power for evaluating immunotherapeutic strategies compared to reductionist cell line models. Despite these advantages, both spheroid- and organoid-based models remain limited by the absence of a functional vasculature, which restricts the ability to model dynamic processes such as immune cell trafficking and systemic drug delivery [178].

1.1.2 On-chip models

Recent advances in microfluidics have enabled the development of “tumor-on-a-chip” platforms that support the 3D co-culture of different cell types under defined flow conditions that simulate blood flow in a living organism [179]. These systems further allow for dynamic administration of therapeutic agents, providing a significant advantage over conventional static culture approaches. In contrast to fixed dosing, microfluidic-based delivery permits controlled and time-resolved modulation of drug concentrations, thereby more closely approximating physiological pharmacokinetics [180-182].

In the context of PDAC, a variety of tumor-on-chip models have been established over the past decade to investigate tumor-stroma interactions and treatment responses within a more physiologically relevant setting [160, 183-188]. Early or simplified systems typically combined PDAC tumor cells with CAF to study stromal crosstalk but lacked incorporation of immune and endothelial compartments [183, 187]. Other

platforms have been optimized for high-throughput drug screening; however, these often still miss key cellular components such as macrophages or a functional vasculature [181, 185]. Notably, these studies demonstrated that dynamic drug delivery can significantly alter the cytotoxic effect on PDAC spheroids, underscoring the importance of temporal drug exposure and distribution for treatment efficacy [181].

More advanced microfluidic models have incorporated patient-derived tumor material, further enhancing their clinical relevance [160, 186, 188]. Nevertheless, even these systems frequently lack critical features of the TME, such as an endothelial barrier [186] or integrated immune cell populations [160, 188]. The most sophisticated PDAC-on-chip model to date utilizes a compartmentalized design compromising PDO, PSC and an endothelial structure perfused with peripheral blood mononuclear cells (PBMC) [184]. However, this setup does not fully recapitulate continuous flow conditions, limiting its ability to model dynamic immune cell trafficking and drug delivery.

To this end, advanced 3D culture models have been developed that integrate key cellular components, including tumor cells, CAF, and immune cells, enabling the investigation of immunosuppressive mechanisms and therapeutic responses in a more physiologically relevant context [169, 171, 189]. However, a need remains for *in vitro* systems that more faithfully capture the complexity of the PDAC TME.

1.1.3 *In vivo* models

Despite advancements in 3D *in vitro* systems, the full recapitulation of the complexity of a living human organism is still lacking. Especially, evaluation of biodistribution and systemic toxicity is still very limited in 3D *in vitro* models. Therefore, *in vivo* models are still essential for drug development. *In vivo* models of PDAC include genetically engineered mouse models (GEMM), chemically induced systems, and implantation-based approaches such as xenografts and patient-derived xenografts [177, 190, 191]. GEMM harbor the key PDAC oncogene mutations and thereby closely mimic tumor initiation and progression within an intact immune system [190, 192]. However, species-specific differences in tumor genetics, stromal architecture, and immune composition, particularly within the myeloid and T-cell compartments, limit their ability to fully model human PDAC [191]. Xenograft-based models are based on the implantation of human tumor cells into mice [190, 193]. Depending on the source of the tumor cells, these xenograft models can be patient-derived, if patient-derived tumor

cells are injected [190, 194]. This preserves the genetic heterogeneity present in the patient. These models enable research into human tumor biology but do not exhibit functional immunity, as only immunodeficient mice are used [194]. To overcome this limitation, so called humanized mouse models have been developed [162]. These mice bear a mutation in the IL-2 receptor, resulting in profound immunodeficiency allowing the engraftment with hematopoietic stem cells and PBMC [195]. Still, this model does not recapitulate a fully functional human immune system and fails to reproduce key mechanisms of immune evasion, such as T-cell exclusion, which are considered critical contributors for the limited efficacy of ICI in PDAC [162].

Despite continuous improvements, no single model fully captures the complex interplay between tumor cells, stroma, and immune components that characterize human PDAC.

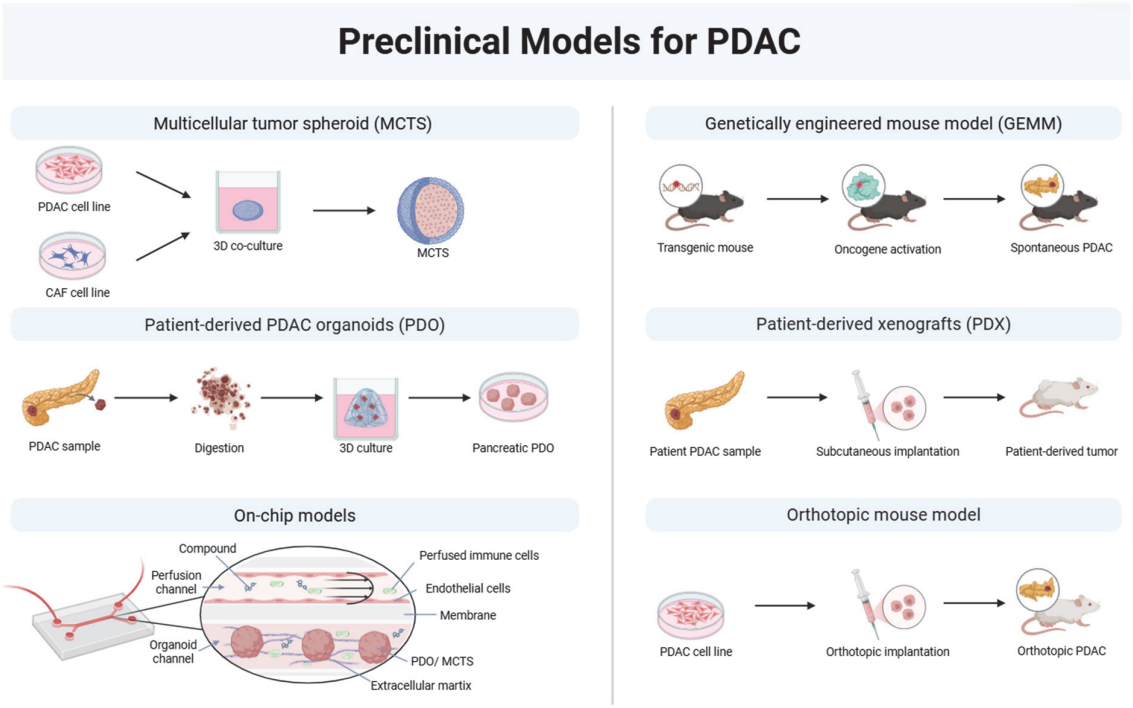


Figure 1.1-1 Preclinical models for PDAC. Preclinical models can be divided into *in vitro* and *in vivo* models. *In vitro* models, including multicellular tumor spheroids (MCTS), patient derived organoids (PDO), and on-chip models. *In vivo* models can be differentiated into genetically engineered mouse models (GEMM), patient-derived xenografts (PDX) and orthotopic mouse models. Generated with BioRender.

List of Abbreviations

°C	Degrees Celsius
µm	Micrometer
µM	Micromolar
2D	Two-dimensional
3D	Three-dimensional
5-FU	5-fluorouracil
AF	Alexa Flour
AMD	Acinar-to-ductal-metaplasia
APC	Allophycocyanin
apCAF	Antigen-presenting CAF
ATCC	American Type Culture Collection
CAF	Cancer-associated fibroblasts
CAR	Chimeric antigen receptor
CD	Cluster of differentiation
CDKN2A	Cyclin-dependent kinase inhibitor 2A
CO_2	Carbon dioxide
CTL	Cytotoxic T-cells
CTLA-4	Cytotoxic T-lymphocyte-associated protein 4
CXCL	C-X-C chemokine ligand
CXCR	C-X-C chemokine receptor
DAPI	4′,6-Diamidin-2-phenylindol
DMEM	Dulbecco's Modified Eagle Medium
DMEM F12	Dulbecco's Modified Eagle Medium/F-12
dMMR	Deficient mismatch repair
DMSO	Dimethylsulfoxide
DPBS	Dulbecco’s phosphate buffered saline
ECBM	Endothelial Cell Basal Medium-2
ECM	Extracellular matrix
EDTA	Ethylenediaminetetraacetic acid
EGFR	Epidermal growth factor receptor
EGM-2	Endothelial growth medium

EMT	Epithelial–mesenchymal transition
FAK	Focal adhesion kinase
FasL	Fas ligand
FBS	Fetal bovine serum
FDA	Food and Drug Administration
FFPE	Formalin-fixed, paraffin-embedded
FITC	Fluorescein isothiocyanate
FOLFIRINOX	5-fluorouracil, leucovorin, irinotecan, and oxaliplatin
FoxP3	Forkhead Box Protein P3
GAPDH	Glyceraldehyde 3-phosphate dehydrogenase
GEMM	Genetically engineered mouse models
GNAS	G protein subunit alpha S
h	Hours
HDAC	Histone deacetylases
HDACi	HDAC inhibitors
HER2	Human epidermal growth factor receptor-2
HLA-DR	Human Leukocyte Antigen – DR isotype
HUVEC	Human umbilical vein endothelial cells
IC_{50}	Inhibitory concentration 50
iCAF	Inflammatory CAF
IDO1	Indoleamine 2,3-dioxygenase 1
IF	Immunofluorescence
IFN-γ	Interferon-γ
IL	Interleukin
IPMN	Intraductal papillary mucinous neoplasms
ITPN	Intraductal tubulopapillary neoplasms
KRAS	Kirsten rat sarcoma virus oncogene homolog
LAG-3	Lymphocyte-activation gene 3
MACS	Magnetic-activated cell sorting
MAP	Mitogen-activated protein
MCN	Mucinous cystic neoplasms
M-CSF	Macrophage colony-stimulating factor
MCTS	Multicellular tumor spheroids
MDSC	Myeloid-derived suppressor cells

MFI	Mean fluorescence intensity
MHC II	Major histocompatibility complex class II
min	Minutes
MIP	Maximum intensity projections
mL	Milliliter
MMP	Matrix metalloproteinases
mRNA	Messenger ribonucleic acid
MSI-H	Microsatellite instability-high
myCAF	Myofibroblastic CAF
NALIRIFOX	Liposomal irinotecan, 5-FU, oxaliplatin, and leucovorin
ng	Nanogram
NK cells	Natural killer cells
nm	Nanometer
NRG1	Neuregulin-1
NTRK	Neurotrophic tyrosine receptor kinase
PanIN	Pancreatic intraepithelial neoplasia
PARP	Poly(ADP-ribose) polymerase 1
PBMC	Peripheral Blood Mononuclear Cells
PD-1	Programmed cell death protein 1
PDAC	Pancreatic ductal adenocarcinoma
PD-L1	Programmed cell death protein ligand 1
PDO	Patient-derived organoids
PDS	Patient-derived spheroids
PDX	Patient-derived xenografts
PE	Phycoerythrin
Pen-strep	Penicillin–streptomycin
PerCP-Cy5.5	Peridinin-Chlorophyll-Protein-Complex-Cyanin
PFA	Paraformaldehyde
PI3K	Phosphatidylinositol 3-kinase
PSC	Pancreatic stellate cells
RET	Rearranged-during-transfection
rpm	Rounds per minute
RPMI	Roswell Park Memorial Institute
RT-qPCR	Real-time quantitative polymerase-chain reaction

SAHA	Suberoylanilide hydroxamic acid
SMAD4	SMAD family member 4
TAM	Tumor-associated macrophages
TGF-β	Transforming growth factor β
Th cells	T-helper cells
TIGIT	T Cell Immunoreceptor with Ig and ITIM domains
TIL	Tumor-infiltrating lymphocytes
TME	Tumor microenvironment
TNF-α	Tumor necrosis factor alpha
TP53	Tumor protein p53
Treg	Regulatory T-cells
ULA	Ultra-low attachment
VEGF	Vascular endothelial growth factor
vWF	von Willebrand factor
α-SMA	α-smooth muscle actin

2 Introduction

2.1 Pancreatic ductal adenocarcinoma

Pancreatic ductal adenocarcinoma (PDAC) accounts for approximately 90% of all pancreatic malignancies and thus represents the most common form of pancreatic cancer [1]. It is one of the leading causes for cancer-related mortality in individuals over the age of 50, currently ranking third overall [2]. Mortality rates are continuing to rise by approximately 1% per year and projections suggest that PDAC, may become the second leading cause of cancer-related death by 2030 [1, 2]. This poor clinical outcome is reflected by a 5-year survival rate of approximately 13% and a median overall survival of about 8-12 months following diagnosis [3, 4]. A major challenge in PDAC is the late stage at diagnosis. In approximately 80% of the cases, PDAC is not detected until it has already reached an advanced stage and metastasized, largely due to the absence of specific symptoms in the early stages. Consequently, about 50% of the patients present with distant metastases at the time of diagnosis, most commonly in the liver, but also in the lungs, bones and peritoneum [5].

Age is the most important non-genetic demographic risk factor for PDAC, with 80% of cases occurring in people aged 60 to 80 [6]. Established modifiable risk factors for PDAC comprise tobacco use, heavy alcohol consumption, obesity, type 2 diabetes mellitus, environmental exposures such as pesticides, and chronic pancreatitis [3]. In addition, an estimated 5-10% of cases arise in the context of inherited predisposition [7]. Smoking is one of the most significant risk factors, increasing the likelihood of developing pancreatic cancer by approximately 2-fold and accounting for 11-32% of the cases [8]. Heavy alcohol consumption contributes indirectly by promoting chronic pancreatitis, a well-established risk factor for PDAC [9]. Obesity has been associated with a 1.19 to 1.72-fold increased risk [10, 11], while type 2 diabetes mellitus confers an approximately 2.4-fold elevated risk and is often linked to obesity and chronic inflammation [12, 13]. Furthermore, emerging evidence points toward a possible link between pesticide exposure and an increased risk of pancreatic cancer [14, 15]. Chronic pancreatitis represents one of the strongest risk factors for pancreatic cancer, increasing the risk by 9-fold and frequently appearing accompanied by other risk factors such as alcohol consumption and smoking [16]. Inherited predisposition is related to either hereditary cancer syndromes [17], hereditary pancreatitis and cystic fibrosis [18], or to familial pancreatic cancer [3, 19]. Collectively, these systemic and

environmental risk factors contribute to a state of chronic inflammation and cellular stress, which trigger the initial molecular events of pancreatic tumorigenesis. Understanding these early events is essential, as they not only drive tumor initiation but also shape the biological features that ultimately contribute to therapeutic resistance.

The pancreas is composed of both an exocrine and an endocrine compartment. The exocrine pancreas consists primarily of acinar and ductal cells. Acinar cells produce digestive enzymes such as lipase, protease, trypsin, and amylase, which are transported to the duodenum via a network of ducts [20]. The duct cells neutralize the acidic stomach contents by producing and secreting bicarbonate ions [20]. This cellular composition provides the basis for the remarkable plasticity of the pancreas, which plays a central role in the development of precursor lesions.

PDAC is traditionally thought to arise from the ductal epithelium; however, increasing evidence suggests that it can also originate from acinar cells undergoing acinar-to-ductal-metaplasia (AMD) [21]. The disease develops from defined precursor lesions including pancreatic intraepithelial neoplasia (PanIN), intraductal papillary mucinous neoplasms (IPMN), intraductal tubulopapillary neoplasms (ITPN) and mucinous cystic neoplasms (MCN), driven by the progressive accumulation of genetic mutations [22, 23]. While PanIN are microscopic lesions arising from smaller ducts, IPMN and MCN are macroscopic cystic precursors that follow distinct histological patterns but can progress to invasive PDAC through similar genetic alterations, such as Kirsten rat sarcoma virus oncogene homolog (KRAS) and G protein subunit alpha S (GNAS) [22]. In contrast, ITPN are also macroscopic precursors that harbor PI3KCA mutations, but typically lack KRAS or GNAS mutations [24].

PanIN are the most common form of precursor lesions and arise following somatic activation of oncogenic KRAS, often in the context of ADM [20]. PanIN are classified in three different stages according to the level of cytological architecture and the heterogeneity of the nucleus with increasing accumulation of mutations from PanIN-1 to PanIN-3 (Figure 2.1-1) [21]. Activating mutations in KRAS occur in over 92% of PDAC patients and are considered the first step in the development of PDAC tumors; they most commonly occur at the G12 codon [25]. These mutations result in constitutive activation of multiple downstream signaling pathways of RAS including mitogen-activated protein (MAP) kinase (RAF-MEK-ERK) and phosphatidylinositol 3-

kinase (PI3K)/AKT/mTOR, thereby promoting cellular proliferation and survival [25]. However, KRAS mutations alone are not enough to drive malignant PDAC progression [25].

Progression from low-grade PanIN to high-grade PanIN and ultimately invasive PDAC requires the simultaneous deactivation of key tumor suppressor genes including tumor protein p53 (TP53), SMAD family member 4 (SMAD4), and cyclin-dependent kinase inhibitor 2A (CDKN2A) [23, 26]. Loss of CDKN2A gene, observed in 90% of PDAC tumors and already detectable in PanIN-2 lesions, leads to dysregulation of cell cycle control [26, 27]. TP53 mutations occur in approximately 75% of PDAC tumors; increased invasiveness, as well as the loss of apoptosis and cell cycle arrest, are attributable to gain-of-function missense mutations [28, 29]. Alterations in SMAD4 are present in around 50% of PDAC tumors and lead to changes in the transforming growth factor β (TGF-β) signaling pathway, which in turn leads to increased invasiveness and tumor progression [23, 30]. Notably, TP53 and SMAD4 mutations are linked to late stages of PanIN differentiation and PDAC initiation [30].

In addition to the commonly occurring driver mutations in tumor suppressor genes, genomic instability, epigenetic alterations, and clonal evolution are key drivers of the transition from PanIN-3 to invasive PDAC [26, 31]. Furthermore, besides cell-intrinsic mechanisms, the surrounding tissue microenvironment and the associated immune cell milieu contribute substantially to both the initiation and progression of pancreatic precursor lesions [31, 32]. Despite significant progress in understanding the molecular causes of the development and progression of PDAC, these findings have had only a limited impact on the development of effective therapies, highlighting the significant gap between biological knowledge and clinical benefit.

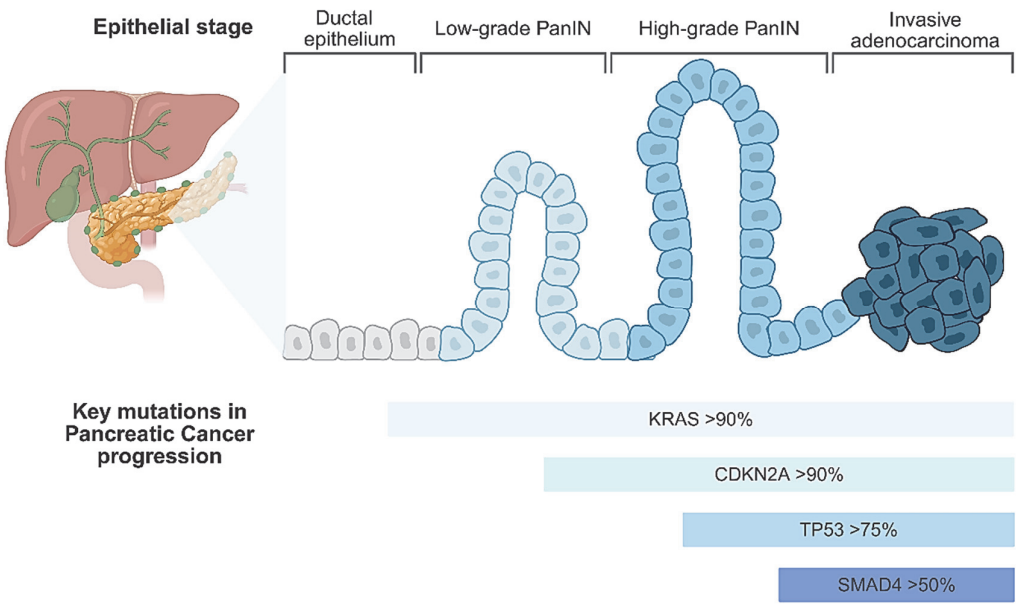


Figure 2.1-1 Pathogenesis of pancreatic cancer. Healthy ductal epithelium first develops into low-grade, then high-grade dysplastic pancreatic intraepithelial neoplasia (PanIN), and finally into invasive adenocarcinoma, associated with genetic mutational changes. Healthy ductal epithelium may harbor KRAS-activating mutations. Low-grade PanIN exhibits the earliest somatic alterations associated with activation of the KRAS oncogene and early inactivation of the tumor suppressor gene cyclin-dependent kinase inhibitor 2A (CDKN2A). High-grade PanIN display accumulated inactivation of the cell cycle-regulating tumor suppressor genes TP53 and/or SMAD4. Invasive adenocarcinomas present more structural and copy number variants, including complex processes such as chromothripsis. Created with BioRender. [23, 26]

2.2 Treatment of PDAC

The poor prognosis of PDAC is not only attributed to late diagnosis and early metastasis but also reflects the limited efficacy of current therapeutic strategies. To date the only potential curative treatment is surgical resection in combination with chemotherapeutics [6, 33]. However, due to strict resection criteria, only 15–20% of PDAC patients are eligible for resection at the time of diagnosis [6]. PDAC is classified as resectable, borderline resectable, locally advanced, or metastatic depending on the involvement of major vessels and the presence of metastases [34].

Surgical management depends on the tumor's localization. Pancreaticoduodenectomy (Whipple procedure) remains the standard approach for tumors in the pancreatic head, in which the pancreatic head, duodenum, gallbladder, and common bile duct are resected together [6]. For tumors in the body or tail of the pancreas, a distal pancreatectomy is performed, while a total pancreatectomy is reserved for extensive disease requiring complete removal of the gland [6]. For resectable PDAC the standard of care consists of surgery followed by adjuvant therapy with modified FOLFIRINOX

(5-fluorouracil (5-FU), leucovorin, irinotecan, and oxaliplatin), or gemcitabine in combination with capecitabine, or gemcitabine alone, depending on the patient´s fitness level [35]. These regiments combine cytotoxic agents targeting different aspects of tumor cell proliferation and survival [35]. Borderline resectable PDAC is neoadjuvant treated with modified FOLFIRINOX for patients with good performance status, or with gemcitabine in combination with nanoparticle albumin-bound (nab)-paclitaxel, to improve resectability, followed by surgery and adjuvant treatment [35, 36]. For locally advanced tumors the systemic therapy is performed, with the aim of disease control, and in selected cases, secondary resection [35, 36]. Radiotherapeutic approaches, including stereotactic body radiation therapy, may be considered in specific clinical settings [37, 38].

In the metastatic setting, first line treatment is performed with modified FOLFIRINOX, the recently established NALIRIFOX (liposomal irinotecan, 5-FU, oxaliplatin, and leucovorin), or gemcitabine with nab-paclitaxel as an alternative [35, 39]. The choice of treatment depends on the patient's performance status and underlying conditions. Second line treatment is based on prior treatment exposure, with liposomal irinotecan plus 5-FU following gemcitabine-based treatment and gemcitabine with nab-paclitaxel following FOLFIRINOX treatment [35]. Despite these therapeutic advances, overall survival rates remain limited, underscoring the urgent need for more effective treatment strategies. In addition, supportive and palliative care, including pain management and nutritional support, plays a crucial role in maintaining quality of life [6].

Recently advances in molecular profiling have enabled the identification of therapeutically exploitable genetic alterations in a subgroup of PDAC patients. Comprehensive molecular testing is increasingly recommended, particularly in the metastatic setting, to guide the use of targeted therapies. KRAS mutations occur in over 90% of PDAC patients but were long considered untreatable with drugs [36]. The development of sotorasib, a KRAS G12C inhibitor, has challenged this assumption [36]. In PDAC, KRAS G12C mutations occur in 1% of patients [26]. Initial clinical trials with sotorasib and adagrasib, another KRAS G12C inhibitor, resulted in moderate improvements in survival rates and disease progression [40, 41]. These promising results promoted further investigation and the clinical evaluation of other KRAS G12C inhibitors, including JDQ443 [42], D-1553 [43], BI-1823911 [44], LY3537982 [45], JAB-21822 [46], and GDC-6036 [47]. Beyond KRAS G12C inhibitors, KRAS inhibitors that target the most common (40%) KRAS mutation G12D, like MRTX-1133, or multiple

KRAS G12X mutations (RMC-6236) showed promising preclinical data and are currently under clinical investigation [48-51]. To date, the only Food and Drug Administration (FDA) approved treatment targeting downstream of KRAS, is the combination of the RAF inhibitor dabrafenib with the MEK inhibitor trametinib for the rare subset (approximately 3%) of BRAF V600E mutated PDAC patients [52].

In addition, several targeted therapies have received FDA approval for molecularly defined subgroups of PDAC [36]. These include zenocutuzumab for neuregulin-1 (NRG1)-fusion-positive tumors [53], the kinase inhibitor selpercatinib for tumors with rearranged-during-transfection (RET) fusions [54], and the antibody-drug conjugate trastuzumab deruxtecan for human epidermal growth factor receptor-2 (HER2)-positive (IHC 3^+) cancers [55]. In addition, multi-tyrosine kinase inhibitors such as entrectinib, larotrectinib, and repotrectinib target neurotrophic tyrosine receptor kinase (NTRK) fusion proteins [56-58]. Furthermore, the Poly(ADP-ribose) polymerase 1 (PARP) inhibitor olaparib is approved for patients with pancreatic cancer who have germline mutations in the breast cancer susceptibility genes BRCA1 and BRCA2 [59].

Advances in immunotherapy have largely centered on the reactivation of tumor-infiltrating T-cells through the blockade of immune checkpoint molecules using monoclonal antibodies [60, 61]. The first immune checkpoint inhibitor to receive FDA approval was the cytotoxic T-lymphocyte-associated protein 4 (CTLA-4) antibody Ipilimumab in 2011 for the treatment of metastatic melanoma [62]. Since then, multiple agents targeting CTLA-4, programmed cell death protein 1 (PD-1), or programmed cell death protein ligand 1 (PD-L1), such as pembrolizumab, nivolumab, durvalumab, atezolizumab, and avelumab, have been approved for a wide range of malignancies, including non-small cell lung cancer, urothelial carcinoma, Hodgkin lymphoma, and hepatocellular carcinoma [63-68].

In PDAC, several immune checkpoint inhibitors (ICI) have been evaluated or are currently under clinical investigation, including PD-1 inhibitors such as nivolumab and pembrolizumab, the PD-L1 inhibitor durvalumab, and the CTLA-4 inhibitor ipilimumab [69-72]. However, when administered as monotherapy, these agents have not demonstrated significant improvements in overall survival or progression-free survival compared to standard chemotherapy, while being associated with considerable toxicity, including severe (grade 3) adverse events in a substantial proportion of patients [73-76]. To address these limitations, recent clinical studies have increasingly

focused on combination strategies. These include the integration of immune checkpoint inhibitors with established chemotherapy regimens such as FOLFIRINOX or gemcitabine plus nab-paclitaxel [77-79], as well as combinations with targeted agents like PARP inhibitors [80, 81]. Furthermore, approaches modulating the tumor microenvironment have been explored, including the use of CXCR4 antagonists (e.g., motixafortide), indoleamine 2,3-dioxygenase 1 (IDO1) inhibitors [82, 83], and focal adhesion kinase (FAK) inhibitors [84]. Despite these efforts, no broadly effective immunotherapeutic strategy has yet been established for the majority of PDAC patients, particularly those with microsatellite-stable tumors. An exception is the small subset of patients with microsatellite instability-high (MSI-H) or deficient mismatch repair (dMMR), in whom pembrolizumab has shown clinically meaningful activity and has received FDA approval [73, 85, 86].

In addition to ICI, immunotherapies using adoptive cells and cancer vaccines are currently being investigated in the context of PDAC. Therapy with chimeric antigen receptor (CAR)-T cells has been clinically tested, using CAR-T cells that target various tumor antigens, including Claudin18.2 [87], the epidermal growth factor receptor (EGFR) [88], HER2 [89], and mesothelin [90]. Although the safety profile was generally good and side effects were tolerable, the efficacy of CAR-T cells was very low, with no significant improvement in disease progression and a generally low response rate [91]. This limited efficacy has been mainly attributed to low infiltration and short persistence of CAR-T cells in PDAC [91]. To overcome this limitation, CAR-natural killer (NK) cells and CAR-macrophages are currently under clinical investigation for PDAC, after showing promising results in preclinical studies [92-94].

Regardless of genetic mutations, epigenetic modulation is another factor that contributes to tumor development and disease progression. Epigenetic regulation not only affects tumor cell-intrinsic pathways but also modulates interactions with the tumor microenvironment. In particular, it has been found that histone deacetylases (HDAC) are dysregulated in PDAC and are associated with poor survival rates [95, 96]. The first FDA-approved HDAC inhibitor, vorinostat (suberoylanilide hydroxamic acid, SAHA), is currently used to treat cutaneous T-cell lymphoma [97]. Consequently, several HDAC inhibitors (HDACi) have been clinically investigated as potential treatment strategies for PDAC, including vorinostat, panobinostat, and entinostat, a selective class I inhibitor [98, 99]. However, clinical trials, particularly Phase II trials, have shown that these agents exhibit only limited efficacy when administered as

monotherapy [100, 101]. Furthermore, the clinical use of pan-HDACi, which target multiple HDAC isoforms simutanously, is limited by their unfavorable toxicity profiles [101]. Consequently, dose-limiting toxicities resulting from non-selective inhibition of multiple HDAC isozymes remain a major challenge in the therapeutic use of pan-HDACi [98]. Latest trends aim to enhance the efficacy of HDACi by using them in combination with existing chemotherapies, radiation therapies, targeted therapies, and immunotherapies [101-104].

Despite advances in chemotherapy, targeted therapy, and immunotherapy, PDAC remains largely resistant to treatment. This limited efficacy is caused by both tumor-intrinsic mechanism and the unique tumor microenvironment, which is characterized by a dense desmoplastic stroma and a highly immunosuppressive environment; together, these factors impair drug delivery and antitumor immunity. Understanding the tumor microenvironment in PDAC is therefore crucial for the development of novel therapeutic approaches.

2.3 Tumor microenvironment of PDAC

The tumor microenvironment (TME) of PDAC represents a key determinant of tumor progression, immune evasion, and therapeutic resistance [105]. It consists of a complex network of cellular and non-cellular components. Among these, cancer-associated fibroblasts (CAF) represent the most prevalent cell type within the TME [106]. In addition to CAF, the TME also harbors a variety of immune cells, including myeloid-derived suppressor cells (MDSC), tumor-associated macrophages (TAM), cytotoxic T-cells (CTL), T helper cells (Th cells), regulatory T-cells (Treg), and NK cells [106, 107]. Furthermore, the TME contains neuronal cells such as Schwann cells and sensory neurons, whose role in tumor growth and recurrence after resection is increasingly recognized [108]. The acellular compartment, collectively referred to as the extracellular matrix (ECM), consists primarily of collagens, fibronectins, and hyaluronic acid [106]. The dynamic interplay between stromal, immune and tumor cells, within the TME results in the formation of a dense, desmoplastic, and highly immunosuppressive TME, that critically shapes the biology of PDAC and its response to therapy [61, 106].

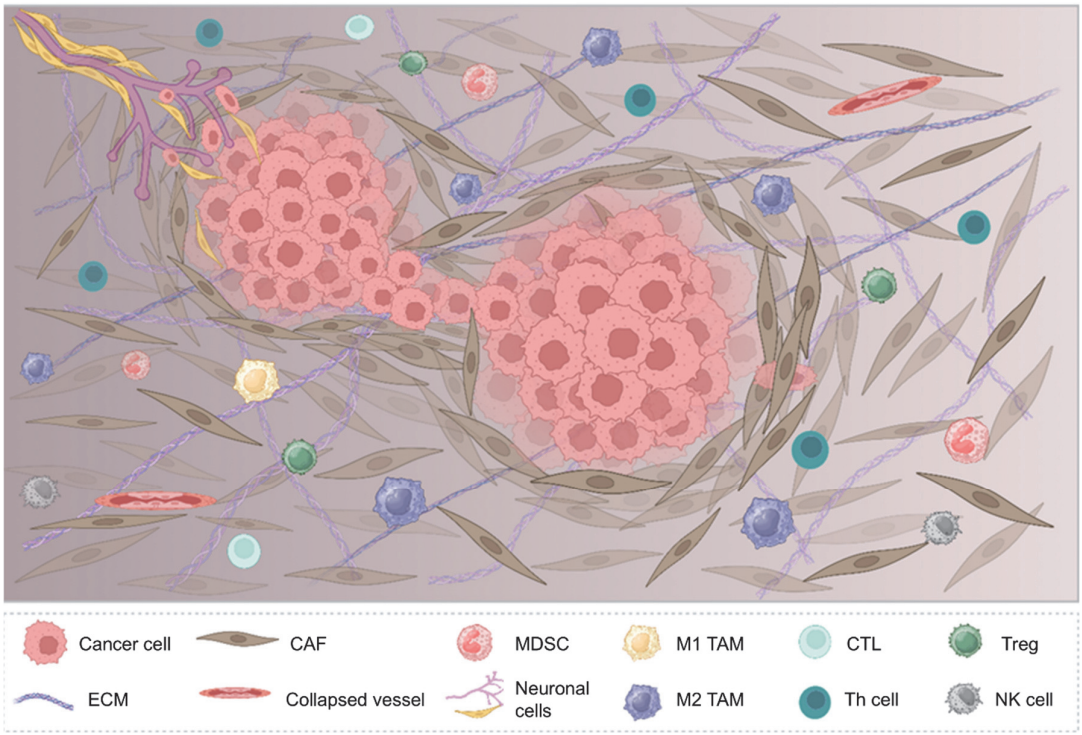


Figure 2.3-1 Composition of the tumor microenvironment (TME) in PDAC. Schematic illustration of the different cellular and non-cellular components of the TME in PDAC. Cancer associated fibroblasts (CAF) represent the most prevalent cell type within the TME [105]. In addition, the TME also harbors a variety of immune cells, including myeloid-derived suppressor cells (MDSC), tumor-associated macrophages (TAM (pro-inflammatory M1; anti-inflammatory M2)), cytotoxic T-cells (CTL), T-helper cells (Th cells), regulatory T-cells (Treg), and natural killer cells (NK cells). Moreover, the TME contains neuronal cells such as Schwann cells and sensory neurons. The acellular compartment, generally referred to as the extracellular matrix (ECM), consists primarily of collagens, fibronectins, and hyaluronic acid. Due to resulting elevated interstitial pressure within the PDAC microenvironment, vessels frequently collapse, resulting in a dysfunctional, leaky vasculature. Generated with BioRender.

2.3.1 Cancer associated fibroblasts

During pancreatic tumorigenesis fibroblasts undergo activation and differentiate into CAF (α-smooth muscle actin (α-SMA) positive), which can account for up to 85% of the TME [109, 110]. CAF originate from multiple cellular sources, including pancreatic stellate cells (PSC), quiescent resident fibroblasts, epithelial cells, endothelial cells, adipocytes, among others. They are classified as myofibroblastic CAF (myCAF), inflammatory CAF (iCAF) and antigen-presenting CAF (apCAF) [111]. myCAF display a contractile and matrix-producing phenotype; iCAF are characterized by their immunomodulatory phenotype; and apCAF can present antigens and express the major histocompatibility complex class II (MHC II) [106, 111]. Recent studies suggest that CAF populations exhibit substantial functional heterogeneity and may exert both tumor-promoting and tumor-restraining effects depending on the context [106, 110].

A major contributor to the CAF population in PDAC are PSC, which are critically involved in stoma remodeling. PSC exhibit a myofibroblast-like phenotype and are considered the main producers of ECM components, thereby contributing to the formation of a dense and stiff stromal architecture [112]. This desmoplastic stroma acts as a physical barrier surrounding tumor lesions and plays a critical role in disease progression, as it impairs drug delivery by increasing interstitial pressure and reducing vascular perfusion [110, 111, 113]. In addition to their structural function, activated PSC release a variety of soluble factors such as TGF-β, interleukin-6 (IL-6), macrophage colony-stimulating factor (M-CSF), interleukin-10 (IL-10), CXCL12, and vascular endothelial growth factor (VEGF) [60, 114, 115]. These mediators are involved in several tumor-promoting processes, including immunosuppression, epithelial–mesenchymal transition (EMT), and angiogenesis [60, 114, 115]. For example, M-CSF has been shown to drive the differentiation of monocytes into immunosuppressive M2 macrophages [116]. Furthermore, PSC-derived CXCL12 has been implicated in the exclusion of T-cells from the tumor core [117]. In addition, the secretion of pro-angiogenic factors such as VEGF stimulates the formation of structurally abnormal and highly branched blood vessels. Owing to elevated interstitial pressure within the PDAC microenvironment, these vessels frequently collapse, leading to a dysfunctional, leaky vasculature [118]. As a result, PDAC is characterized by a hypovascular and hypoxic tumor phenotype [118]. This impaired vascularization further limits the effective delivery of chemotherapeutic agents to the tumor tissue [119]. Taken together, the complex interplay between CAF and tumor cells contributes to the establishment of a highly desmoplastic and immunosuppressive microenvironment while simultaneously impairing drug delivery [120].

2.3.2 Tumor associated macrophages

In addition to CAF, the TME of PDAC comprises a diverse range of immune cell populations and is particularly enriched with TAM. Macrophages have traditionally been categorized into two functionally distinct phenotypes: the pro-inflammatory, immunogenic M1 subtype and the anti-inflammatory, immunosuppressive M2 subtype [121]. However, emerging evidence highlights the considerable plasticity and dynamic nature of TAM polarization [121]. In PDAC, TAM predominantly exhibit an M2-like phenotype, commonly characterized by CD163 expression [122, 123], and their abundance has been associated with poor clinical outcomes, including reduced overall survival [124, 125]. Functionally, TAM play a central role in tumor progression by

promoting immunosuppression and therapeutic resistance. They contribute to acinar-to-ductal metaplasia through the secretion of tumor necrosis factor alpha (TNF-α) and the activation of matrix metalloproteinases (MMP) [126-129]. In addition, TAM-derived soluble factors activate key oncogenic signaling pathways in tumor cells, including PI3K/AKT and JAK/STAT, thereby further enhancing chemoresistance [130-132]. Preclinical studies have demonstrated that depletion of macrophages or inhibition of their recruitment, for example via the CCL2 signaling axis, can restore sensitivity to standard chemotherapeutic regimens such as gemcitabine or FOLFIRINOX, underscoring their therapeutic relevance [133-135]. Consistent with their immunosuppressive phenotype, M2-like TAMs secrete anti-inflammatory cytokines and chemokines, including IL-10, IL-6, IL-1 receptor antagonist, CXCL7, and CCL2. These mediators contribute to the exhaustion of cytotoxic $CD8^+$ T cells [127, 136] and promote the polarization of $CD4^+$ T cells toward Th2, Th17, and Treg subpopulations, all of which are associated with tumor-promoting functions [105, 137]. Furthermore, TAM directly suppress anti-tumor immunity by expressing immune checkpoint ligands such as PD-L1 and Dectin-1 [138, 139]. They also induce the expression of these inhibitory molecules on tumor cells, thereby facilitating immune evasion [140]. Overall, TAM contribute directly and indirectly to treatment resistance in PDAC by mediating chemoresistance and immunosuppression.

2.3.3 T-cells

T-cells are divided into CTL ($CD8^+$) and Th cells ($CD4^+$). Th cells are further subdivided into different functional phenotypes including immunosuppressive Treg. Treg ($FoxP3^+$, $CD4^+$, $CD25^+$) contribute substantially to the immunosuppressive tumor microenvironment in PDAC. They secrete anti-inflammatory cytokines, including IL-10 and TGF-β, and express CTLA-4, thereby suppressing effector T-cell function and promoting polarization of TAM toward an M2-like phenotype [141]. Increased Treg infiltration has been shown to inversely correlate with $CD8^+$ T-cell density and is associated with unfavorable clinical outcomes in PDAC [142]. In addition, Treg induce a tolerogenic phenotype in dendritic cells, characterized by reduced expression of co-stimulatory molecules such as CD86 and CD40, decreased MHC class II expression, and impaired interferon-γ (IFN-γ) signaling, ultimately resulting in diminished activation of $CD8^+$ T-cells [143]. Consequently, increased Treg levels are viewed as a biomarker for a poor prognosis in PDAC [141, 142].

In addition to Treg cells, $CD4^+$ Th cells mostly polarize toward a Th2 phenotype, thereby enhancing immunosuppression through the release of anti-inflammatory cytokines such as IL-4 and IL-13, which polarize immune-suppressive M2 macrophages and support tumor cell metabolisms through enhanced JAK-STAT signaling-mediated glycolysis [144, 145]. In additional studies, $CD4^+$ Th17 cells have likewise been detected in the TME of PDAC patients, where they are linked to a worse prognosis because they promote the development of PanIN and enhance the stem cell-like properties of tumor cells [143, 146, 147]. Th17-derived interleukin-17 (IL-17) promotes fibrosis, angiogenesis, and myeloid cell recruitment, thereby supporting tumor growth and survival through activation of the gp130–JAK2–STAT3 signaling axis [147-149].

In contrast, cytotoxic $CD8^+$ T-cells represent the main effector population responsible for anti-tumor immunity, mediating tumor cell killing via granzyme B, perforin, IFN-γ, TNF-α, and Fas ligand (FasL)-induced apoptosis [141]. However, in PDAC, effector T-cells are largely excluded from the tumor core and instead accumulate in stromal, tumor-adjacent regions [141]. This spatial exclusion is primarily driven by CAF-derived CXCL12, which interacts with CXCR4 on T-cells and promotes their accumulation within the surrounding stroma [117, 150]. Furthermore, studies in patients with PDAC consistently demonstrate shifts in the ratio of $CD4^+$ to $CD8^+$ T-cells, which are detectable both locally in the TME and systemically in the blood [141, 151]. While the TME is primarily characterized by an accumulation of immunosuppressive $CD4^+$ subtypes such as Th2 and Treg cells, accompanied by a deficiency of cytotoxic $CD8^+$ effector cells, a more nuanced picture emerges in peripheral blood [141]. Here, the elevated $CD4^+/CD8^+$ ratio correlates less with a loss of $CD8^+$ cells and results primarily from the expansion of regulatory and memory $CD4^+$ populations [151]. These findings suggest a systemic immune shift, although the exact correlation between peripheral changes and the actual intratumoral T-cell landscape has not yet been conclusively clarified.

Moreover, T-cells within the PDAC TME frequently exhibit an exhausted phenotype, characterized by reduced proliferative capacity, impaired effector function, and increased expression of immune checkpoint receptors, including PD-1, lymphocyte-activation gene 3 (LAG-3), and CTLA-4 [141, 152-155]. Engagement of PD-1 with its ligands PD-L1 and PD-L2 on tumor and immune cells inhibits T-cell activation and

promotes apoptosis [73]. CTLA-4 competes with CD28 for binding to B7 molecules on antigen-presenting cells, thereby preventing co-stimulatory signaling required for full T-cell activation [156, 157]. LAG-3 further impairs T-cell receptor signaling through interaction with MHC class II molecules [158]. In summary, these mechanisms result in the suppression of both $CD4^+$ and $CD8^+$ T-cell effector functions and represent key drivers of resistance to immunotherapy in PDAC [157, 158].

Collectively, the TME of PDAC is a highly dynamic and complex system that influences tumor progression, immune evasion, and therapeutic resistance. In particular, the dense desmoplastic stroma, the presence of immunosuppressive cell populations like TAM and Treg, and the exclusion and dysfunction of T-cells collectively contribute to the limited efficacy of current treatment strategies. This complexity presents a major challenge for the development of predictive preclinical models.

2.4 Aims and Objectives

PDAC remains one of the most lethal cancers worldwide. Despite advancements in understanding the molecular and biological mechanisms underlying tumorigenesis and progression, the translation into clinical improvement remains poor. Besides tumor-intrinsic factors, a main contributor to therapy resistance is the unique and complex TME of PDAC. Current preclinical models fail to recapitulate the multifaceted mechanisms and cellular interactions underlying therapy resistance. Therefore, there is a critical need for advanced, human-relevant preclinical models that integrate tumor, stroma, and immune components to more accurately reflect PDAC biology and improve the predictive assessment of therapeutic strategies.

The main aim of this dissertation was to develop and apply advanced human-based 3D and microfluidic models of PDAC to better represent the cross talk between tumor cells and the TME, thereby improving the preclinical evaluation of therapeutic strategies.

Specifically, this work had the following objectives:

I. to establish physiologically relevant human-based 3D PDAC models incorporating tumor cells, stromal components, and immune cells to reproduce key features of the TME,
II. to investigate the role of the TME in shaping tumor progression, immune modulation, and therapeutic responses,

III. to characterize the functional state of tumor-infiltrating T-cells and macrophages within the PDAC microenvironment, and to assess mechanisms of immune modulation and dysfunction

IV. to evaluate the efficacy of therapeutic approaches, including epigenetic and immunomodulatory strategies, within advanced 3D models, and

V. to enhance the translational relevance of preclinical models through the integration of patient-derived systems, enabling patient-specific assessment of therapeutic responses.

3 Publications and manuskripts

3.1 Novel Histone Deacetylase (HDAC) Inhibitor Induces Apoptosis and Suppresses Invasion via E-Cadherin Upregulation in Pancreatic Ductal Adenocarcinoma (PDAC)

Katja Schiedlauske [1,†], Alina Deipenbrock [1,†], Marc Pflieger [2,†], Alexandra Hamacher [2], Jan Hänsel [1], Matthias U. Kassack [2], Thomas Kurz [2,*] and Nicole E. Teusch [1,*]

[1] Institute of Pharmaceutical Biology and Biotechnology, Heinrich-Heine-University Düsseldorf, Universitätsstr. 1, 40225 Düsseldorf, Germany

[2] Institute of Pharmaceutical and Medicinal Chemistry, Heinrich-Heine-University Düsseldorf, Universitätsstr. 1, 40225 Düsseldorf, Germany

*Correspondence: thomas.kurz@hhu.de (T.K.); nicole.teusch@hhu.de (N.E.T.)

† These authors contributed equally to this work

Published in: *Pharmaceuticals*

DOI: 10.3390/ph17060752

Keywords: pancreatic cancer; PDAC; histone deacetylase inhibitor; HDAC 2; HDAC 6; E-cadherin; apoptosis; invasion; EMT

Own contributions to the manuscript: 40%

- Conceptualization of the experiments (25%) together with Nicole Teusch and Katja Schiedlauske
- Methodology (100%), Investigation (100%), Validation (100%), Data curation (100%), Formal analysis (100%), and Visualization (100%) of the following experiments:
    - Analysis of protein expression of E-cadherin by western blot and flow cytometry in 2D and 3D (100%)
    - Measurement of apoptosis induction via flow cytometry (100%)
    - Cell cycle analysis by flow cytometry (100%)
- Writing and drafting the manuscript (60%) together with Nicole Teusch, Katja Schiedlauske, and Mark Pflieger

Abstract

Pancreatic ductal adenocarcinoma (PDAC) is the most lethal form of pancreatic cancer characterized by therapy resistance and early metastasis, resulting in a low survival rate. Histone deacetylase (HDAC) inhibitors showed potential for the treatment of hematological malignancies. In PDAC, overexpression of HDAC 2 is associated with epithelial-mesenchymal transition (EMT), principally accompanied by a downregulation of the epithelial marker E-cadherin and increased metastatic capacity. The effector cytokine transforming growth factor-β (TGF β) is known to be a major inducer of EMT in PDAC, leading to high metastatic and invasive potential. In addition, overexpression of HDAC 6 in PDAC is associated with reduced apoptosis. Here, we have demonstrated that a novel HDAC 2/ 6 inhibitor not only significantly increased E-cadherin expression in PANC-1 cells (5.5 fold) and in 3D PDAC co-culture spheroids (2.5-fold), but was also able to reverse the TGF-β-induced downregulation of E-cadherin expression. Moreover, our study indicates that the HDAC inhibitor mediated re-differentiation resulting in a significant inhibition of tumor cell invasion by approximately 60 % compared to control. We have shown that the HDAC inhibitor induces both apoptosis (2-fold) and cell cycle arrest. In conclusion, the HDAC 2/ 6 inhibitor acts by suppressing invasion via upregulating E-cadherin mediated by HDAC 2 blockade and by inducing a cell cycle arrest leading to apoptosis via HDAC 6 inhibition. These results suggest that HDAC 2/ 6 inhibitor HDAC inhibitors might represent a novel therapeutic strategy for the treatment of PDAC tumorigenesis and metastasis.

Introduction

Pancreatic ductal adenocarcinoma (PDAC) is the most common subtype of pancreatic cancer representing one of the most lethal cancers with a 5-year survival rate of less than 11% [1,2]. PDAC displays a large cellular heterogeneity including a highly fibrotic and immunosuppressive tumor microenvironment (TME) [3]. The PDAC tumor microenvironment, which is characterized by the presence of a heterogenous stroma including pancreatic stellate cells (PSCs), tumor endothelial cells, and a variety of immune cells, is mainly responsible for disease progression [3].

During tumorigenesis, pancreatic stellate cells acquire a myofibroblast-like phenotype referred to as cancer-associated fibroblasts (CAFs), which constitute up to 90% of the TME. CAFs excessively secrete extracellular matrix (ECM) proteins, such as collagens, fibronectins, and hyaluronic acid, culminating in the typical desmoplastic environment. Furthermore, the expression of pro-angiogenic factors such as VEGF and PDGF results in the initiation of angiogenesis [4]. Consequently, the creation of atypical multibranched vessels which collapse under the high interstitial pressure of the desmoplastic environment leads to a hypovascular, hypoxic phenotype [5]. Immune cells, including macrophages, T-cells, mast cells, and neutrophil granulocytes, infiltrate the desmoplastic stroma and play opposing roles in tumor progression [6]. Inflammatory immune cells, particularly cytotoxic $CD8^+$ T-cells, foster tumor cell elimination, whereas tumor-associated macrophages and regulatory T-cells (Treg) suppress the activation and proliferation of cytotoxic $CD8^+$ T-cells and of natural killer (NK) cells, thereby contributing to an immunosuppressive tumor microenvironment [7]. Hypoxia promotes the suppression of immune cells by inhibiting the proliferation of anti-tumor immune cells such as cytotoxic T-cells or NK cells and increasing the polarization of T-cells to Treg cells as well as the polarization of macrophages to an immunosuppressive M2 phenotype [8].

Histone deacetylases (HDACs) are enzymes that deacetylate lysine on histones as well as on many other cellular proteins. Histone deacetylation in general results in the blockage of DNA transcription and the subsequent downregulation of distinct target genes. For example, the HDAC-related suppression of genes encoding pro-apoptotic proteins like Nur77 or BH3-only protein NOXA leads to an increased cell proliferation [9]. In addition to gene transcription regulation via histone modification, HDACs control many cellular processes including cell cycle progression and cell survival by deacetylating a variety of proteins [10]. As one example, p53 was the first target protein discovered whose deacetylation leads to cell cycle progression and resistance to apoptosis. [11].

To date, the 18 known human histone deacetylases can be divided into four distinct groups. Class I HDACs, which include HDAC 1, 2, 3, and 8, are exclusively located within the nucleus except for HDAC8, while class IIa HDACs (comprising HDAC 4, 5, 7, 9) display nuclear and cytoplasmic localization. HDACs 6 and 10 encompass class IIb HDACs, which are exclusively found in the cytoplasm. In contrast, class IV (currently only consisting of HDAC 11) is predominantly located in the nucleus and subdivided

from class I based on the large C-terminus. HDACs require Zn^{2+} for their function. Finally, sirtuins belong to class III HDACs, which require NAD^{+} [12,13].

Aberrant HDACs appear in many different cancer types including PDAC. Recent studies indicate that HDAC class I, HDAC 6, and HDAC 7 tend to be overexpressed in PDAC tissue. Moreover, a high expression of HDAC 1, 7, and 8 is linked to a negative prognosis [14,15]. Different functions of HDACs in PDAC have been reported. For example, class I HDACs promote the epithelial–mesenchymal transition (EMT), leading to a high metastatic capacity, a hallmark in PDAC. Data in mice and in PDAC patients showed a clear correlation between the expression levels of HDAC1 and HDAC2 and the prevalence for metastasis [16]. Furthermore, class IIa HDACs promote angiogenesis by increasing the transcription of hypoxia-inducible factor 1α (HIF-1α) under hypoxic conditions. Moreover, the overexpression of HDAC6 in PDAC results in the upregulation of c-myc which is directly linked to cell proliferation [17]. However, despite the important role of HDAC in cancer progression, further studies are needed to fully understand the involvement of distinct HDACs in PDAC tumorigenesis.

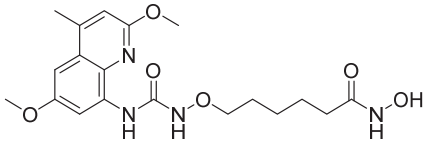
Pancreatic tumor cells undergo the process of the EMT early in their tumorigenic development, transforming from their original epithelial and immobile state to a mesenchymal, fibroblastoid, and mobilized phenotype, an essential step for tumor invasion, dissemination, and metastasis [18]. One key activator of the EMT is the effector cytokine TGF-β which leads to the increased invasion of tumor cells through the downregulation of the epithelial marker E-cadherin [19]. The downregulation of E-cadherin in PDAC is thought to be associated with the increased activity of HDAC 1 and HDAC 2 [20]. Subsequently, low levels of the E-cadherin protein correlate with an invasive and metastatic phenotype [18]. Specifically, a high expression of HDAC 2 is associated with high metastatic capacity resulting from the downregulation of E-cadherin. Moreover, a high expression of HDAC 6 is linked to resistance against apoptosis [14,16].

The latest European Society of Medical Oncology (ESMO) guidelines recommend primary resection followed by adjuvant chemotherapy with either FOLFIRINOX (leucovorin, 5-FU, irinotecan, and oxaliplatin) or, if not eligible for this treatment, gemcitabine/capecitabine for resectable pancreatic cancer as first-line treatment. In metastatic disease, the standard options for first-line chemotherapy are either FOLFIRINOX or gemcitabine/nab (nanoalbumin)-linked paclitaxel [21,22]. However,

due to the limited efficacy of the available non-specific cytotoxic drugs and the advanced stage of the disease at the time of diagnosis, with more than 80% of patients already diagnosed with an unresectable or metastatic stage, there is a high unmet medical need for new PDAC treatment strategies [23,24].

HDAC inhibition has lately gained significant attention in cancer drug discovery and development. For instance, the inaugural FDA-approved HDAC inhibitor vorinostat, also known as suberoylanilide hydroxamic acid (SAHA) [19,25], is employed in cutaneous T-cell lymphoma treatment [26]. Although HDAC inhibitors such as vorinostat and panbinostat and class I-specific HDAC entinostat have been investigated for PDAC treatment, they have failed in the latest phase 2 trials due to missing efficacies as monotherapies [20,27]. Additionally, unfavorable side effect profiles of pan-inhibitors arise from HDAC isoenzymes possessing toxic effects on non-tumor cells, mainly through the inhibition of HDAC 1, 2, and 3 leading to the dose limitation of pan-HDAC inhibitors [9].

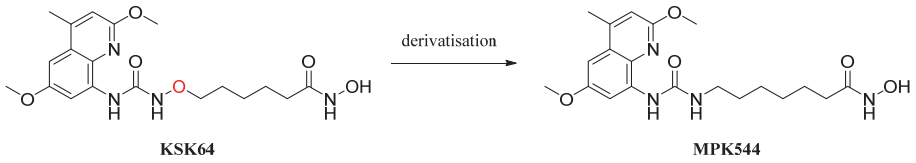
In contrast to the first generation pan-HDACi-like panobiostat, **KSK64** (1i) exhibits a refined HDAC isozyme profile with a preference towards class I HDACs (especially HDAC 1, 2) and HDAC6 [28]. This HDAC class I/HDAC6 isozyme profile is presumably the result of the large substituted quinoline Cap group in connection with the novel alkoxyurea moiety (Figure 3.1-1).



KSK64
IC_{50}(HDAC1) = 43.2 nM
IC_{50}(HDAC4) > 10.0 µM
IC_{50}(HDAC6) = 2.80 nM
IC_{50}(HDAC8) = 1.54 µM
SF (Cal27R) = 11.2

Figure 3.1-1 Structure and isozyme profile of KSK64 [28].

However, the N-O bond of the alkoyxurea structure in **KSK64** (1i) could represent a metabolic weak point. Therefore, we decided to synthesize and investigate its carba analogue **MPK544**. (Scheme 3.1.1). This involved the development of a synthetic strategy for the **MPK544** exhibiting a urea connecting unit (CU) and its anticancer property evaluation towards PANC-1 cells.



Scheme 3.1.1. Derivatisation of ***KSK64***.

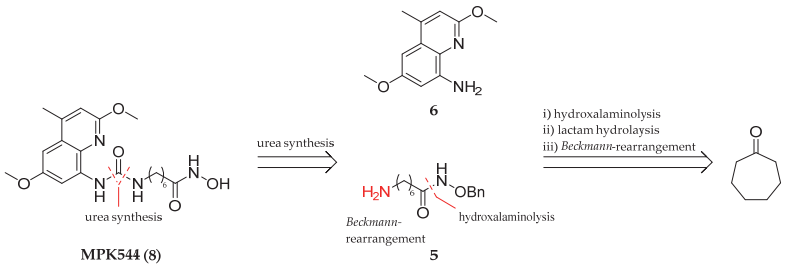
We here describe the new HDAC inhibitor **MPK544** which was designed based on a pharmacophore model of HDAC class I and IIb inhibitors. The inhibitor contains a substituted quinoline cap group, a urea connecting unit, an alkyl linker and a hydroxamic acid ZBG. HDAC class I and IIb inhibitors not only target histone proteins within their nuclear complexes by inhibiting HDAC 1-3, but also modulate various cytosolic cancer targets through inhibition of HDAC 6.

In summary, we demonstrate that our novel HDAC inhibitor **MPK544** exhibits slightly higher cytotoxicity in PANC-1 cells compared to the HDAC 1,2,3 and 6 inhibitor vorinostat and comparable efficacy in 3D PDAC spheroid models [29]. Notably, **MPK544** shows a significant reduction in invading a matrigel matrix through the upregulation of the epithelial marker E-cadherin in both, PANC-1 cells alone as well as in 3D co-culture spheroids. Overall, our findings provide evidence that HDAC 2/6 inhibitors warrant further investigation as a possible novel therapeutic strategies for PDAC treatment.

Results

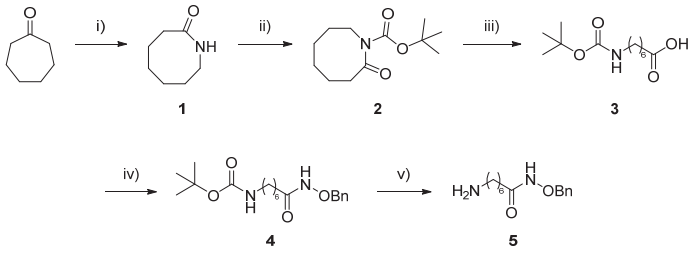
In this study, we have synthesized a novel carba analogue of **KSK64** featuring a urea component as CU, which resulted in the discovery of **MPK544**. The synthetic approach was guided by a detailed retrosynthetic analysis, breaking down the target molecule into readily commercially available synthetic precursors (Scheme 3.1.2). The urea derivative was disconnected into the amino-quinoline **7** and the 7-aminoheptanoic alkoxyamide derivative **8**. Our focus was on the efficient synthesis of the latter, which is a key building block for the target molecule. Our retrosynthetic strategy identified a critical path involving the synthesis of 7-amino-*N*-(benzyloxy)heptanamide **5**. This compound can be further derived from cycloheptanone by a Beckmann rearrangement. Our approach provides a reliable route to the alkoxyamide precursor, which is essential for the synthesis of the targeted urea derivative.

The successful implementation of this synthetic pathway, along with a detailed retrosynthetic analysis, underscores the viability of the synthetic method for producing novel **KSK64** derivatives with potent anti-cancer activity.



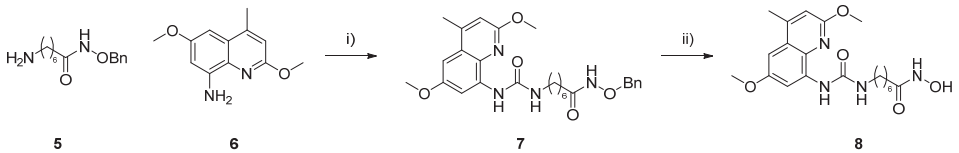
Scheme 3.1.2 Retrosynthetic analysis of MPK544.

Starting from cycloheptanone, a ring expansion was realised by a Beckmann rearrangement (Scheme 3.1.3**Fehler! Verweisquelle konnte nicht gefunden werden.**), followed by an *N*-Boc protection of the resulting lactam **2**. The *N*-Boc protected lactam **2** was, subsequently, hydrolysed under basis conditions to obtain the *N*-Boc protected amino acid **3**. Via a HATU mediated acylation, **3** was coupled to the *O*-benzyl hydroxylamine to obtain **4**. The synthesis of the linker was completed by the Boc deprotection of **4**, yielding **5**.



Scheme 3.1.3 Synthesis of 7-amino-N-(benzyloxy)heptanamide 5. i) 1.50 eq hydroxylamine-O-sulfonic acid, HCO_2H; ii) 1.00 eq nBuLi, 1.00 eq Boc_2O, THF; iii) 10.0 eq LiOH, THF/H_2O iv)

Afterwards, **5** and the 8-aminoquinoline derivative **6** were used for the synthesis of the urea **7,** in the presence of triphosgene (Scheme 3.1.4.) Finally, the *O*-benzyl protected hydroxamic acid precursor **7** was deprotected by catalytic hydrogenation to obtain the hydroxamic acid **MPK544 (8)**.



Scheme 3.1.4. Synthesis of the **MPK544** (**8**). i) 0.330 eq triphosgene, 1.00 eq DIPEA, DCM; ii) H_2, Pd/C, MeOH

A cytotoxicity screen of a library of 30 novel HDAC inhibitors against the PDAC cell line PANC-1 revealed **MPK544** as the most potent candidate. The cytotoxic efficacy of **MPK544** was evaluated after 72h in both, primary pancreatic stellate cells (PSC) and in PANC-1 cells, as well as in 3D co-culture spheroids composed of PANC-1 cells and PSC. In PANC-1 (IC_{50} 2.95 µM) and in PSC cells (IC_{50} 0.68 µM) **MPK544** was more cytotoxic than SAHA (Table 3.1-1). In the co-culture spheroids (IC_{50} 0.90 µM) the IC_{50} values of **MPK544** and SAHA were comparable (Table 3.1-2). In contrast, the specific HDAC 6 inhibitor tubastatin A did not display any cytotoxicity in these models (Table 3.1-2) Noteworthy, **MPK544** was even more cytotoxic in the reported models than the current PDAC standard therapeutic gemcitabine [30]. With respect to enzyme selectivity, **MPK544** showed inhibitory activity against HDAC class I and HDAC 6 (Table 3.1-1). In comparison, SAHA is described to inhibit HDAC 1, 2, 3, and 6 [29].

Table 3.1-1 HDAC2, HDAC4 and HDAC6 inhibition assay of MPK544

HDAC 2	**HDAC 4**	***HDAC 6***
	IC_{50} in µM	
0.058 ± 0,02	> 100	0,097 ± 0,062

Table 3.1-2 Cytotoxic efficacy of HDAC inhibitors represented by the respective IC50 values [µM] in 2D PANC-1 and pancreatic stellate cells (PSC) cultures as well as in 3D co-culture spheroids after 72 h incubation. The arithmetic means and their respective standard deviations of three independent experiments are depicted.

HDAC inhibitors	**PANC-1**	**PSC**	**Co-culture spheroid**
		IC_{50} in µM	
MPK544	2.95 ± 0.45	0.68 ± 0.48	0.90 ± 0.15
KSK64	7.04 ±0.58	14.87 ±4.55	3.30 ±0.58
SAHA	3.65 ± 0.43	3.50 ± 0.99	0.85 ± 0.25
tubastatin A	>100	>100	>100

The process of the epithelial–mesenchymal transition (EMT) is a critical step for tumor invasion and metastasis [18]. The characteristic suppression of the epithelial marker protein E-cadherin, controlled through HDAC 2 and HDAC 1 activity, is accompanied with a highly metastatic and invasive phenotype in PDAC [31,32]. The analysis of E-cadherin expression in PANC-1 cells via qPCR (Figure 3.1-2 A) and Western blot (Figure 3.1-2B,C) after treatment with **MPK544**, SAHA, or tubastatin A revealed that **MPK544** increased E-cadherin mRNA levels by 3-fold at a concentration of 1 µM and by 5-fold at 4 µM after 24 h (Figure 3.1-2A). After 72 h, compared to SAHA (2-fold), 1 µM **MPK544** induced a 3-fold induction of E-cadherin mRNA levels, whereas treatment with 10 µM tubastatin A did not significantly change E-cadherin mRNA levels in PANC-1 cells (Supplementary Figure 3.1-1A). Furthermore, in terms of protein levels, a 5-fold increase in E-cadherin protein expression was observed in the presence of 4 µM **MPK544** after 24 h of incubation (Figure 3.1-2B,C). After 72 h treatment with 1 µM **MPK544** (2.2-fold) or SAHA (4-fold) and 4 µM **MPK544** (2.4-fold) or SAHA (6.9-fold), it resulted in a significant protein upregulation of E-cadherin, respectively (Supplementary Figure 3.1-1B,C). Again, tubastatin A did not influence E-cadherin protein expression up to a concentration of 10 µM.

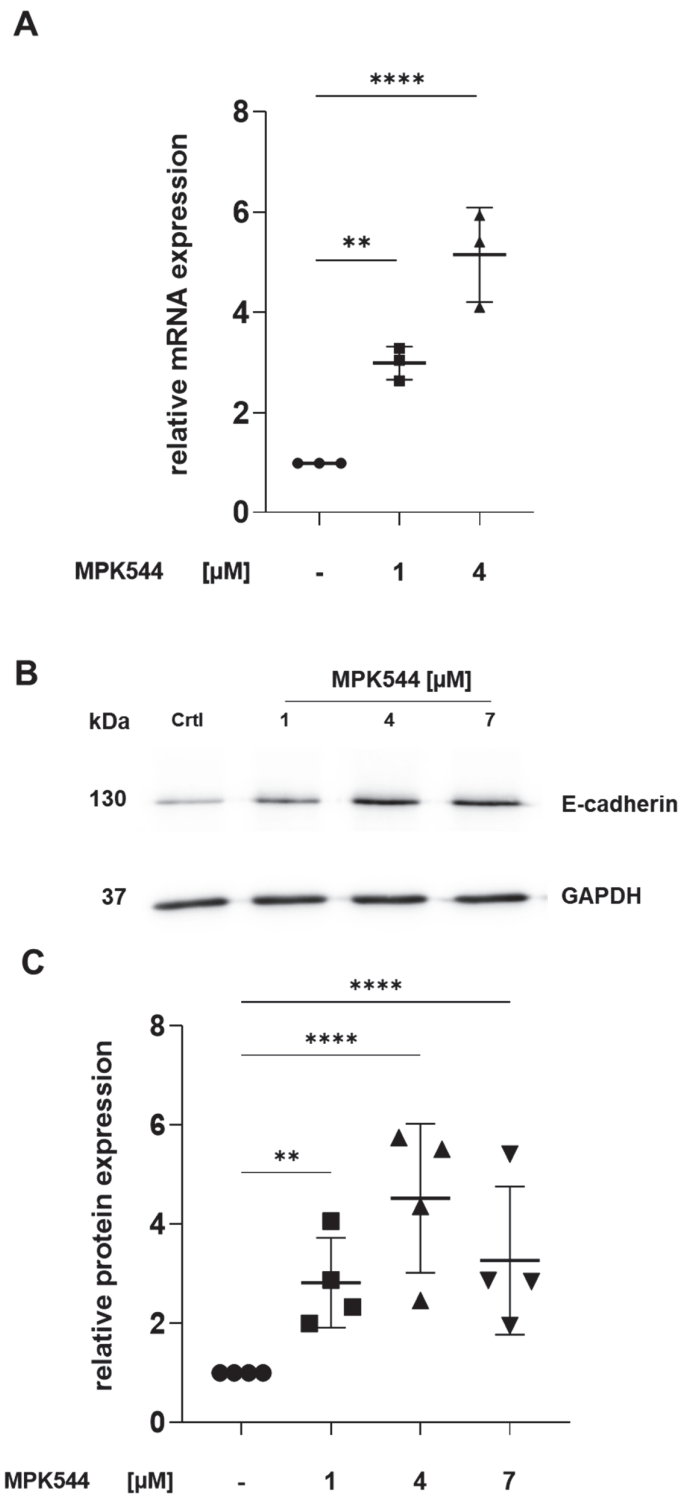


Figure 3.1-2 Upregulation of E-cadherin in PANC-1 cells after 24 h. PANC-1 cells were treated with MPK544, SAHA, and tubastatin A for 24 h. mRNA levels of E-cadherin in PANC-1 cells were analyzed by qRT-PCR (A) and at protein level by Western blot (B,C) (control ●; 1 µM MPK544 ▪; 4 µM MPK544;

7 µM MPK544). Representative Western blots are shown (B). Error bars indicate standard errors of mean (of at least three independent experiments, with; ** = $p \leq 0.01$; and **** = $p \leq 0.0001$).

The effector cytokine TGF-β has been identified as a key inducer of the EMT [33]. The TGF-β-induced EMT results in enhanced migratory and invasive properties of PDAC tumor cells, leading to a lower survival rate in patients [34,35,36]. Thus, PANC-1 cells were incubated with TGF-β in combination with **MPK544**, SAHA, or tubastatin A for 72 h, respectively. As expected, TGF-β significantly lowered both E-cadherin mRNA levels as well as E-cadherin protein expression compared to control (Figure 3.1-3). Co-treatment with 4 µM **MPK544** resulted in a significant increase in E-cadherin mRNA levels of 7.3-fold (Figure 3.1-3 A) and of 8.6-fold in the protein level (Figure 3.1-3 B,C). Co-treatment with 4 µM SAHA resulted in an 8.3-fold upregulation of E-cadherin mRNA levels (Figure 3A), as well as a 10.6-fold increase in the protein level (Figure 3.1-3 B,C). In line with our previous results, treatment with tubastatin A was not able to reverse the TGF-ß-induced downregulation of E-cadherin (Figure 3.1-3 A–C).

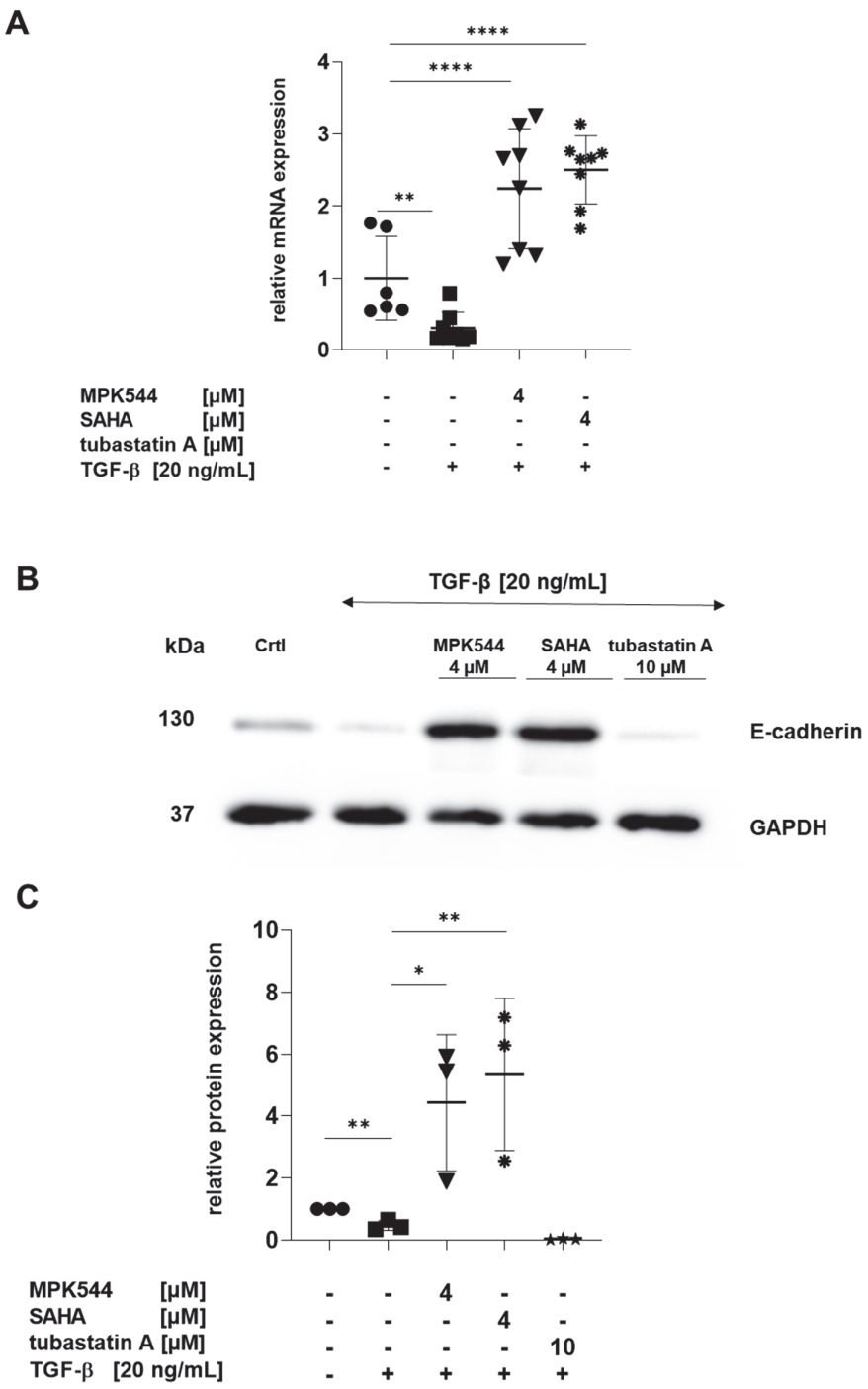


Figure 3.1-3 Upregulation of E-cadherin expression in PANC-1 cells. PANC-1 cells were treated with MPK544, SAHA, and tubastatin A or with 20 ng/mL TGF-β, for 72 h. mRNA levels of E-cadherin in PANC-1 cells were analyzed by qRT-PCR (A) and at protein level by Western blot (B,C). Representative Western blots are shown (B). Control ●; 20 ng/mL TGF-β ▪; 20 ng/mL TGF-β with 4 µM MPK544; 20 ng/mL TGF-β with 4 µM SAHA; 20 ng/mL TGF-β with 10 µM tubastatin *). Error bars indicate standard errors of mean (of at least three independent experiments, with * = $p \leq 0.05$; ** = $p \leq 0.01$; and **** = $p \leq 0.0001$).

To additionally analyze E-cadherin protein expression in 3D co-culture spheroids, the spheroids were digested after 72 h of treatment with 2 µM SAHA or **MPK544**. E-cadherin expression was subsequently quantified via flow cytometry. **MPK544** treatment significantly upregulated E-cadherin expression in co-culture spheroids (Figure 3.1-4 A,B). In co-culture spheroids, **MPK544** treatment increased E-cadherin expression approximately by 20-fold with 2 µM after 72 h. SAHA treatment increased E-cadherin expression in spheroids, with an 11-fold increase with the 2 µM treatment (Figure 3.1-4 A,B). Additionally, we also confirmed E-cadherin upregulation by the immunofluorescence staining of whole spheroids after treatment with **MPK544** and SAHA compared to the DMSO control (Supplementary Figure 3.1-2).

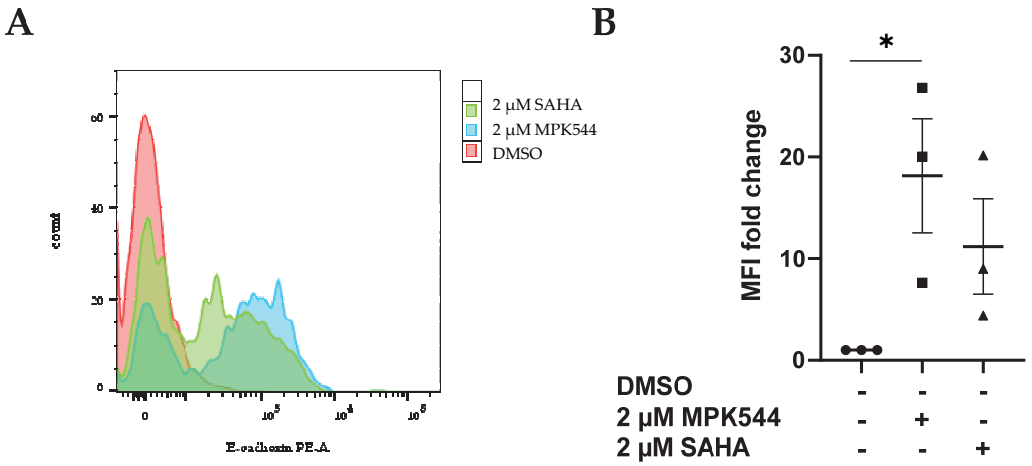


Figure 3.1-4 Expression of E-cadherin in 3D co-culture spheroids after treatment with MPK544 and SAHA. Co-culture spheroids were treated with 2 µM MPK544 or SAHA for 72 h, respectively. Expression of E-cadherin was quantified via flow cytometry. (A) Exemplary overlay histograms for E-cadherin expression after different treatments. (B) Quantification of MFI fold change in E-cadherin expression in co-culture spheroids after treatment with 2 µM MPK544 or SAHA for 72 (control ●; 2 µM MPK544 ▪; 2 µM SAHA). E-cadherin expression was measured in at least 3000 cells. Error bars indicate standard errors of mean (n = 3 independent experiments with * = $p \leq 0.05$.

In PDAC, HDAC 2 has been shown to suppress the expression of the epithelial marker E-cadherin, thereby promoting the EMT and migration [14,32]. To study the effect of **MPK544** on tumor cell invasion, PANC-1 cells were seeded in a matrigel drop which was surrounded by a second matrigel layer based on a method adapted from Hurley et al. (2017) [37]. The spherical invasion assay enables the chemotaxis-independent observation of cancer cell invasion in contrast to conventional transwell assays. The quantification of the number of cells invading the second matrigel layer revealed that 72 h of treatment with TGF-β increased the number of invading cells by 1.6-fold, while

treatment with the subtoxic concentration of 2 µM **MPK544** reduced the number of invading cells by 3-fold compared to control (Figure 3.1-5).

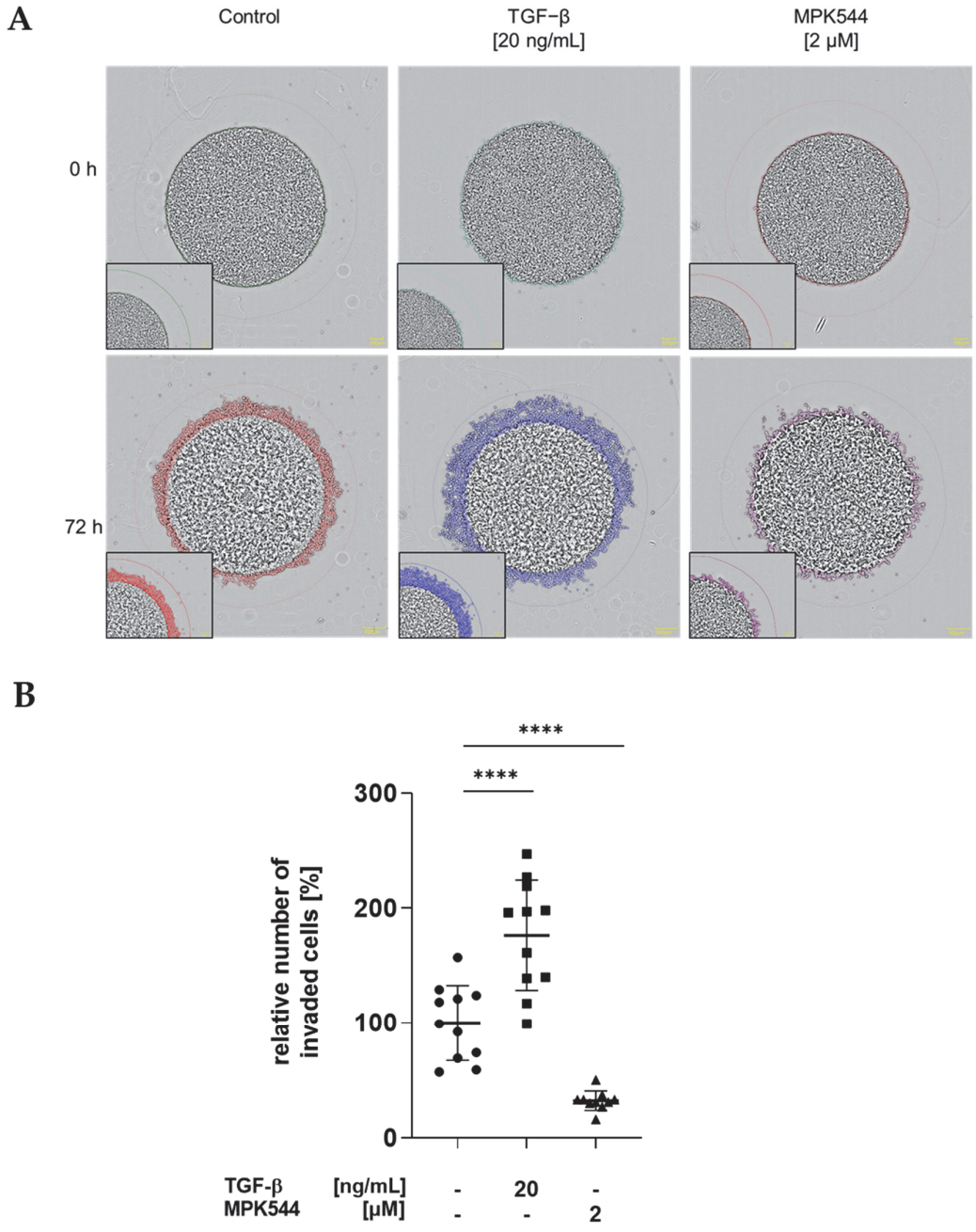


Figure 3.1-5 The invasion of PANC-1 cells into a 3D matrix. (A) PANC-1 cells were mixed in a ratio of 1:1 with matrigel and seeded into a 24-well plate. After 24 h, a second layer of matrigel was applied, and the cells were incubated for 72 h at 37 °C. The invasion of the PANC-1 cells into the second matrigel layer was studied by phase contrast microscopy (control in red; 20 ng/mL TGF-β in purple; 2 µM MPK544 in pink). The invasion assay ran for 72 h, and the area of invaded cells into the surrounding matrigel was visualized (control in red; 20 ng/mL TGF-β in purple; 2 µM MPK544 in pink) and calculated. (B) The quantification of the area of invaded cells upon treatment with 2 µM MPK544 in PANC-1 cells

(control ●; 20 ng/mL TGF- β ▪; 2 µM MPK544). Error bars indicate the standard errors of the mean (n = 3 independent experiments with **** = p ≤ 0.0001).

High expression levels of HDAC 6 have been shown to correlate with resistance to apoptosis [17]. HDAC 2 activity on the other hand regulates cell cycle progression [38]. The commercially available HDAC inhibitors, SAHA and tubastatin A, have been shown to induce apoptosis, as well as cell cycle arrest in the G2/M phase, in different cancer cells, including PANC-1 [39,40,41]. A 48 h treatment with 1 µM MPK544 significantly increased the amount of early apoptotic and dead cells by 2-fold in comparison to 1% DMSO-treated PANC-1 cells (Figure 3.1-6B).

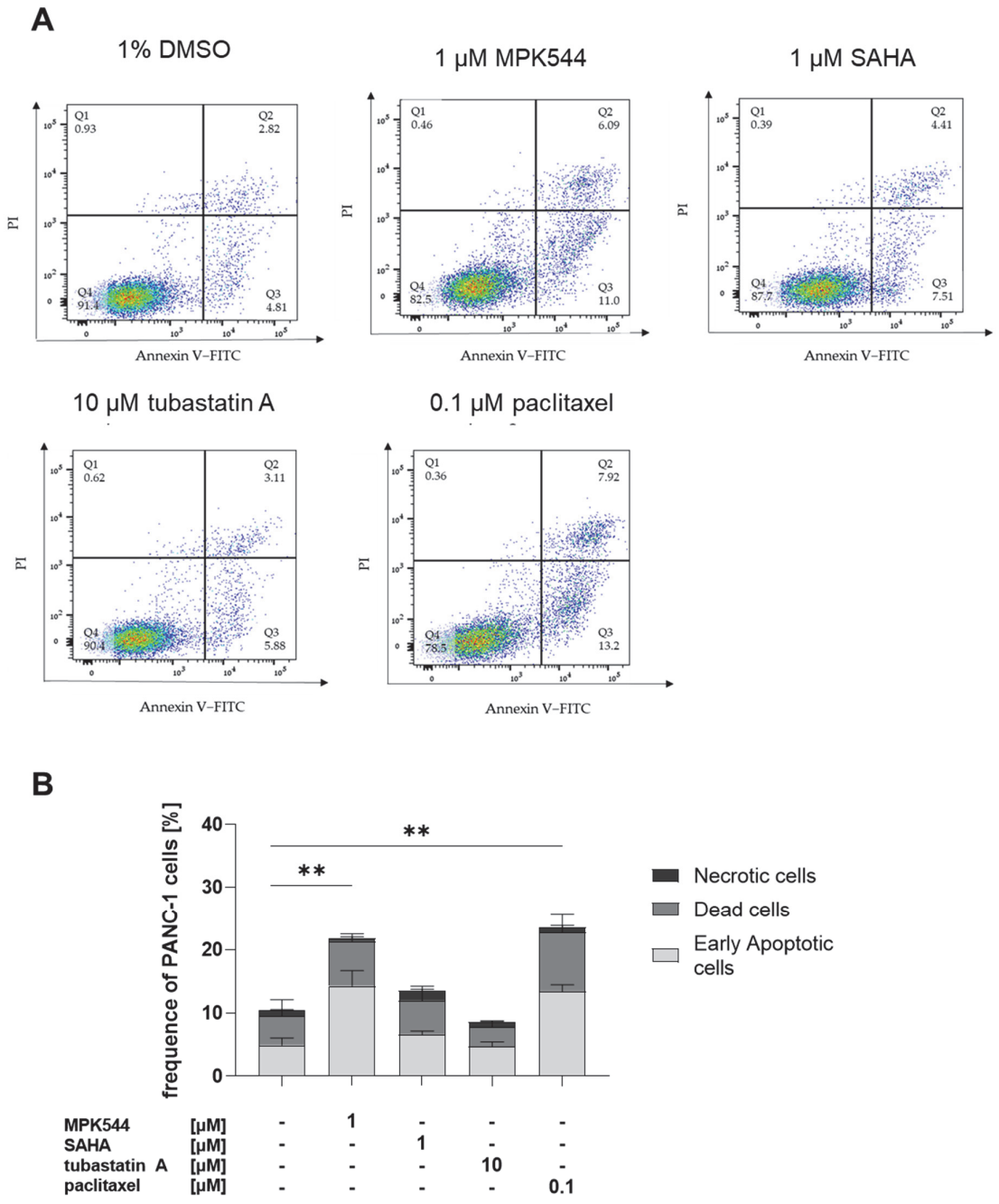


Figure 3.1-6 Induction of apoptosis in PANC-1 cells. Cells were treated with 1 µM MKP544, 1 µM SAHA, 10 µM tubastatin A, or 0.1 µM paclitaxel for 48 h. For detection of apoptosis, cells were stained with Annexin V and PI and analyzed by flow cytometry. (A) Percentage of apoptotic cells treated with MPK544, SAHA, tubastatin A, or paclitaxel are shown in exemplary dot plots. (B) Quantification of apoptotic cells after 48 h of treatment. Apoptosis of at least 10,000 cells was analyzed via flow cytometry. Error bars indicate standard errors of mean (n = 3 independent experiments with ** = $p \leq 0.01$).

Besides the induction of apoptosis, the influence on the cell cycle of PANC-1 cells after 48 h treatment with 1 µM **MPK544**, 1µM SAHA, 10 µM tubastatin A, or 0.1 µM paclitaxel was analyzed. **MPK544** treatment led to a 1.7-fold reduction in the G1 phase and a 1.6-fold increase in the G2 phase (Figure 3.1-7B). Comparable observations were

made for the pan-HDAC inhibitor SAHA and the HDAC6 inhibitor tubastatin A, however without achieving significance (Figure 3.1-7). Treatment with the tubulin inhibitor paclitaxel induced, as expected, cell cycle arrest in the G2/M phase (Figure 3.1-7).

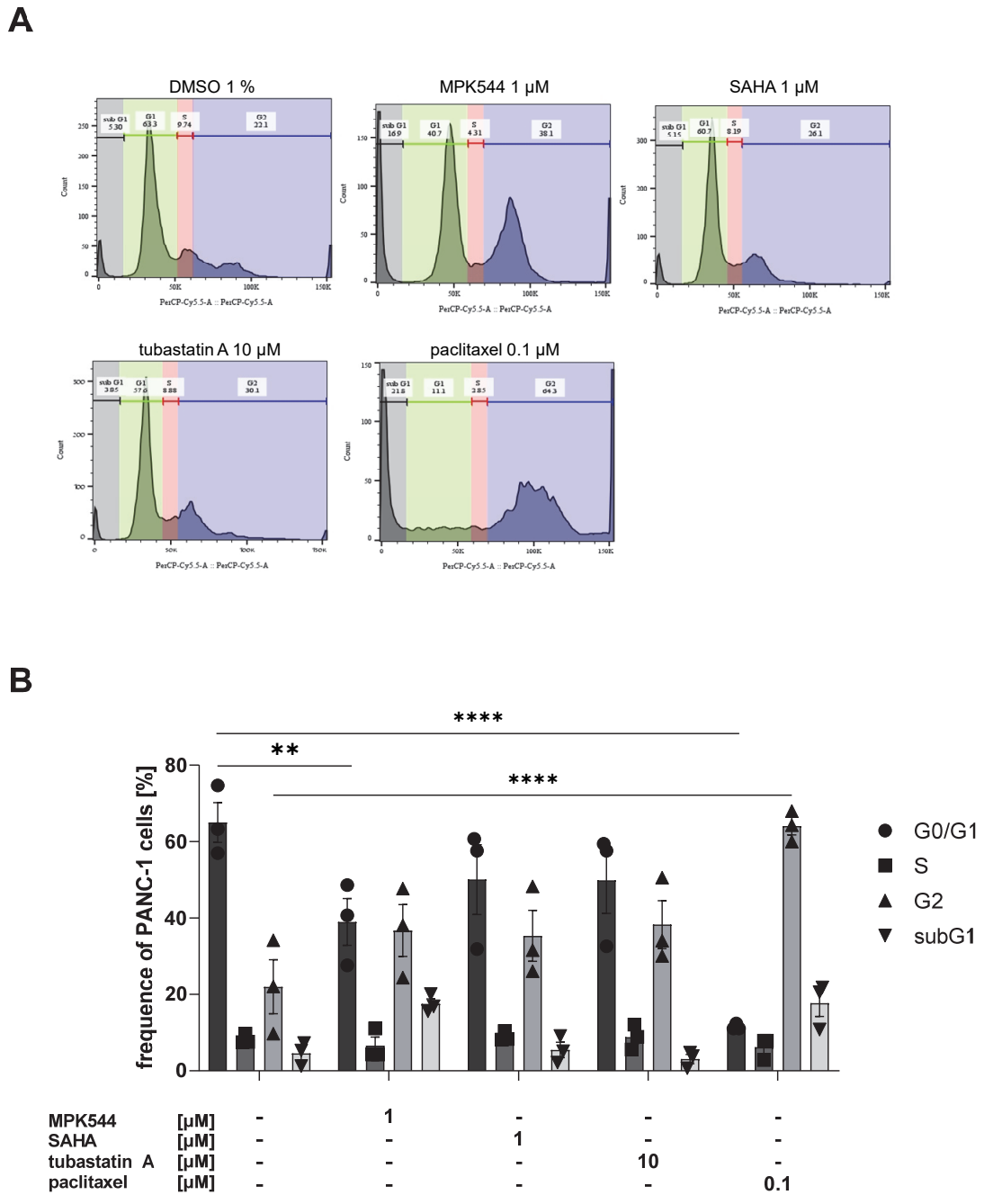


Figure 3.1-7 Cell cycle analysis of PANC-1 cells. Cells were treated with 1 µM MPK544, 1 µM SAHA, 10 µM tubastatin A, or 0.1 µM paclitaxel for 48 h. Cell cycle analysis was performed according to Nicoletti method. (A) Percentage of cells in different cell cycles after treatment with MPK544, SAHA, tubastatin A, or paclitaxel for 48 h is shown in exemplary histograms. (B) Quantification of cell cycle phases. Cell

cycles of at least 10,000 cells were analyzed via flow cytometry. Error bars indicate standard errors of mean (n = 3 independent experiments with ** = $p \leq 0.01$; and **** = $p \leq 0.0001$).

So far, HDACis have failed as monotherapies for solid tumors but have shown the first promising results in combination with chemotherapeutics [42,43]. Therefore, we explored the potential synergism of **MPK544** with the chemotherapeutic drugs gemcitabine and 5-fluorouracil (5-FU) in PANC-1 cells. As shown in Figure 3.1-8, we screened **MPK544** against increasing concentrations of gemcitabine or 5-FU, respectively. Indeed, **MPK544** demonstrates a synergistic interaction at concentrations above the IC50 value of gemcitabine (0.17 µM) (Figure 3.1-8A). However, for 5-FU, no synergistic interaction with **MPK544** could be detected (Figure 3.1-8B). Data were generated using the Bliss synergy analysis [44].

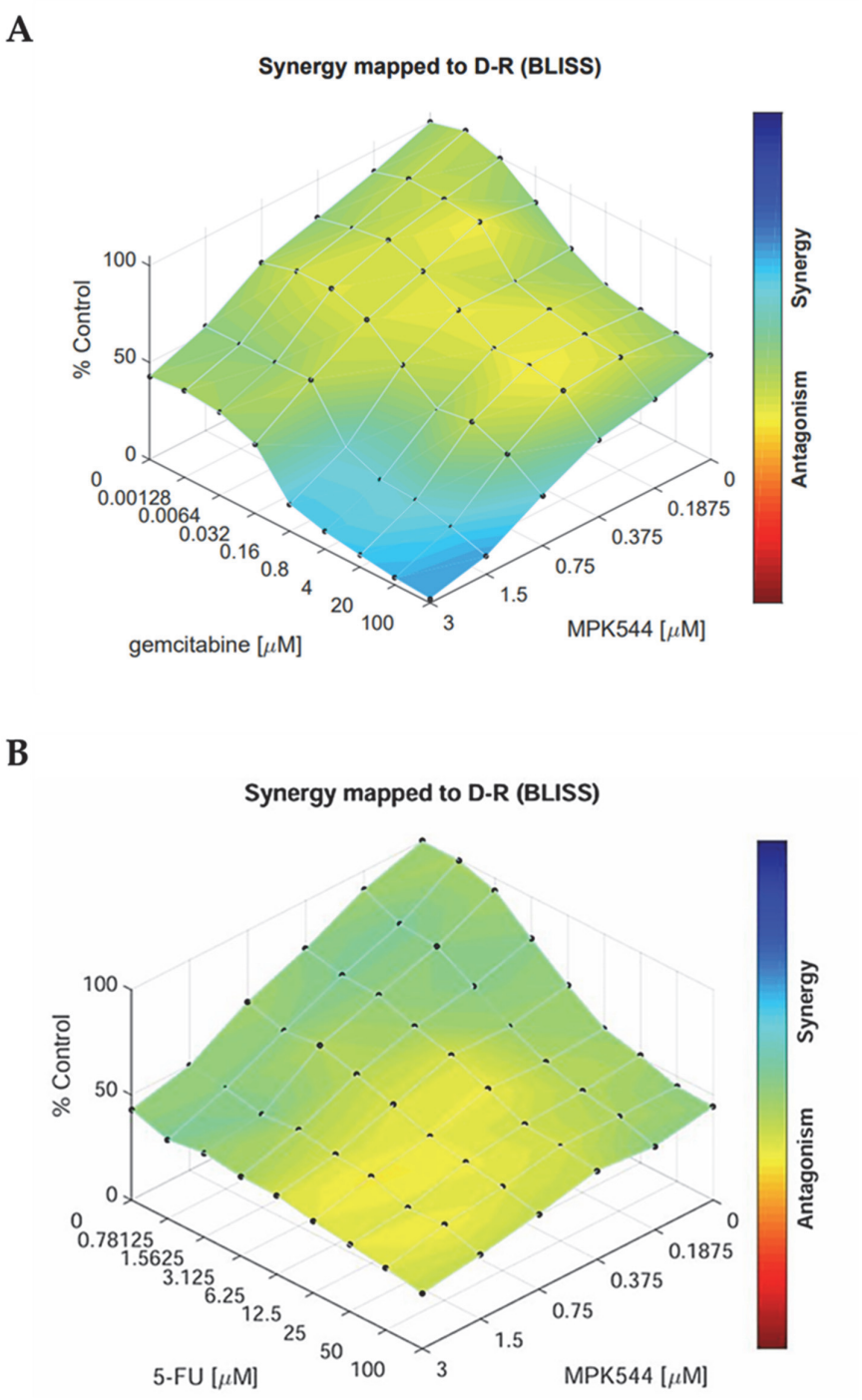


Figure 3.1-8 MPK544 demonstrates a synergistic interaction with the chemotherapeutic drug gemcitabine and no synergistic interaction with 5-fluorouracil (5-FU). A representative Bliss synergy plot of MPK544 with gemcitabine (A) and 5-FU (B) in PANC-1 cells (n = 3) is depicted. The Bliss synergy was analyzed and visualized with the Combenefit software (version 2.021) [44].

HDAC inhibition has gained a lot of attention in the discovery and development of novel anticancer drugs. For example, the HDACi SAHA has been FDA-approved for the treatment of cutaneous T-cell lymphoma [45,46]. In the treatment of PDAC, multiple HDAC inhibitors have demonstrated anti-tumor efficacy in vivo as well as in mouse

models but failed in clinical trials [20,42], presumably indicating that HDACis might not be suitable for monotherapy. For PDAC, HDACis are currently investigated in clinical trials as combination therapies with cytotoxic chemotherapeutics such as gemcitabine [43]. We showed that **MPK544** demonstrates a synergistic interaction with gemcitabine in PANC-1 cells. For 5-FU, however, no synergistic interaction with **MPK544** was detected. Whether this result can be explained with the selected tumor type or the HDAC inhibitor, selectivity needs to be further explored. In this context, it is worth to mention that a recent study showed a synergistic interaction of 5-FU with the pan-HDACi panobinostat in gastric cancer cell types [47].

Furthermore, we investigated the potential of **MPK544** to reverse the mesenchymal phenotype and reduce invasive properties and cell proliferation in PDAC tumor cells. The cytotoxic effect of **MPK544** was characterized in comparison to SAHA and the specific HDAC 6 inhibitor tubastatin A. In 2D, **MPK544** cytotoxic efficacy was superior to SAHA and tubastatin A. Interestingly, the strongest cytotoxic effect of **MPK544** was observed in co-culture spheroids consisting of PSCs and PANC-1 cells. In PDAC, 90% of the solid tumor is composed of PSCs, generating a desmoplastic microenvironment and leading to an increase in stiffness [3]. As shown by Kim et al. (2018), particularly class I HDACs are overexpressed in CAFs, which explains the remarkably robust cytotoxic efficacy of **MPK544** [48]. This must be taken into account with regard to possible toxic side effects that may occur due to the inhibition of class I HDACs.

To generate specific HDAC inhibitors, it is crucial to understand the critical HDAC targets responsible for the therapeutic effect in a particular cancer type. Studies have shown that class I HDACs and HDAC 6 are the most important targets for cytotoxic anti-cancer effects in PDAC [14,49,50]. Specifically, HDAC 2 is associated with high metastatic capacity resulting from the downregulation of E-cadherin [14]. Thus, HDAC 2 inhibition might be associated with a reversion of the mesenchymal phenotype of PDAC tumor cells into an epithelial phenotype, thereby reducing metastatic capacity and increasing sensitivity to chemotherapeutics [43,51]. We were able to confirm this potential by showing a significant upregulation of E-cadherin at both mRNA and protein levels after treatment with **MPK544**. Furthermore, **MPK544** showed a concentration-dependent effect that was superior to SAHA at a concentration of 1 µM after 24 h. Furthermore, in co-culture spheroids, treatment with **MPK544** led to a significant increase in E-cadherin expression. In contrast, tubastatin A did not induce a significant increase in E-cadherin expression in 2D and 3D models, confirming the hypothesis

that HDAC 6 is not involved in the regulation of E-cadherin expression. A key activator of the EMT is the effector cytokine TGF-β which leads to the increased invasion of tumor cells through the downregulation of the epithelial marker E-cadherin [36,52]. Krauß et al. (2022) were able to show that HDAC 2 deactivates the tumor suppressor pathways of TGF-β in PDAC [38]. TGF-β is known to be a potent inducer of the EMT and chemoresistance in PDAC. The most aggressive form of PDAC is classified as a basal-like PDAC which exhibits a TGF-β signature and is enriched in the EMT. Therefore, we investigated whether **MPK544** could reverse the TGF-β-induced EMT. **MPK544** was able to reverse the TGF-β-induced EMT in PANC-1 cells, indicated by the significant upregulation of E-cadherin at the mRNA and protein level. These results are consistent with the findings of Mishra et al. (2017b) showing that the specific class I HDACis domatinostat (4SC-202), entinostat, and mocetinostat were able to reverse the TGF-β-induced EMT [49].

E-cadherin is a calcium-dependent cell adhesion molecule responsible for cell contraction in epithelial tissues. The upregulation of E-cadherin has been shown to be associated with a reduced metastasis rate and invasion of pancreatic cancer cells mediated by the inhibition of HDAC 2. To investigate the invasion capacity, we established a spherical invasion assay adopted from Hurley et al. (2017) [37]. **MPK544** treatment significantly reduced the invasive potential of PANC-1 cells. However, recent studies have revealed that partial EMT (p-EMT) enables the metastasis of circulating tumor cells and is associated with shorter progression-free survival [53,54]. p-EMT may be regulated independently of TGF-β and is therefore fundamentally different from the classical EMT process. In contrast to fully mesenchymal cells, which migrate as individual cells, cells in the p-EMT state migrate in clusters through the vasculature. In future studies, the mechanism by which HDACs regulate p-EMT in PDAC needs to be further investigated.

HDAC inhibition has been shown to affect the cell cycle and induce apoptosis in cancer cells [55]. Our results showed that the inhibition of HDAC 2/6 by **MPK544** resulted in a significant induction of apoptosis and cell cycle shift in the G2/M phase. In agreement with the results of Wang et al. (2012), treatment with the HDAC 6-specific inhibitor tubastatin A showed minimal effects on the cell cycle and the induction of apoptosis [50]. These results support the findings of Krauß et al. (2022) who showed that the depletion of HDAC 2 led to cell cycle arrest at the G2/M phase in murine PDAC [38]. HDAC 6 is a unique member of the HDAC family due to its functionality and

localization. It is primarily localized in the cytoplasm and has two catalytic deacetylase domains [56]. In addition, HDAC 6 has been reported to interact with a wide range of different proteins such as α-tubulin, heat shock protein 90 (Hsp90), ERK1, and many others [57,58]. Through these interactions, HDAC 6 regulates various cellular processes such as proliferation and apoptosis [59]. However, studies have shown that targeting HDAC 6 alone has not led to any significant benefit in solid tumors. Interestingly, several studies have shown that HDAC 6 inhibitors in combination therapy with chemotherapeutics increased the cytotoxic efficacy of the latter [60].

In conclusion, **MPK544** acts by suppressing invasion via upregulating E-cadherin mediated by HDAC 2 blockade and by inducing cell cycle arrest leading to apoptosis via HDAC 6 inhibition. Furthermore, a synergistic interaction of MPK544 with the chemotherapeutic agent gemcitabine could be demonstrated. Overall, these results suggest that HDAC 2/6 inhibitors might represent a novel therapeutic strategy for the treatment for PDAC.

Materials and Methods

Cell Culture

The PANC-1 cell line, acquired from the American Type Culture Collection (ATCC), was cultured in Dulbecco's Modified Eagle's Medium (DMEM) (#41965039, Gibco, Grand Island, NY, USA) supplemented with 10% fetal bovine serum (FBS) (#10270-106, Gibco), as well as 1% penicillin–streptomycin (#15140122, Gibco, Grand Island, NY, USA). Pancreatic stellate cells (PSCs) were provided by Dr. Erkan of Koç University Hospital in Turkey. The ethics committee for the biomedical sciences at KOÇ University granted ethical approval, and all patients consented in writing. Pancreatic stellate cells were obtained from patients diagnosed with ductal adenocarcinoma and cultured in DMEM/F12 (#11320074, Gibco, Grand Island, NY, USA) with 20% fetal bovine serum (FBS) and 1% pen-strep under aseptic conditions. Both cell types were incubated at 37 °C in a humidified atmosphere supplemented with 5% CO_2.

Spheroid Formation

PANC-1 spheroids were formed by adding 5000 PANC-1 cells per well into an ultra-low attachment (ULA)-coated surface plate (#650970, Greiner Bio-One, Kremsmünster, Austria) in DMEM. Co-culture spheroids were generated according to

our previous study [30]. The compound treatment of PANC-1 spheroids and co-culture spheroids was initiated on day 4 following cell seeding.

Cell Viability Assays

Cell viability in both PANC-1 and PSC cells was assessed using the PrestoBlue HS Cell Viability Assay (#P50201, Thermo Scientific, Waltham, MA, USA) in 96-well plates (#655090, Greiner Bio-One, Kremsmünster, Austria), seeding 5000 cells per well for PANC-1 and 2000 cells per well for PSCs. Compounds were incubated for 72 h. Fluorescence values were recorded using the Tecan SPARK instrument (Tecan Group, Männedorf, Switzerland). The cell viability of 3D spheroids was analyzed with the CellTiter-Glo® 3D Cell Viability Assay (#G9681, Promega, Madison, WI, USA) according to the manufacturer's protocol. Luminescence values were measured with the Tecan SPARK instrument (Tecan Group, Männedorf, Switzerland).

Western Blot Analysis

PANC-1 was seeded onto 6-well plates (#657180, Greiner Bio-One, Kremsmünster, Austria) containing 1.8 mL DMEM supplemented with 10% FBS and 1% pen-strep. Cells were treated either with **MPK544**, SAHA, or tubastatin A for 72 h. Cells were lysed with 500 µL of radioimmunoprecipitation assay (RIPA) buffer, along with a protease inhibitor (#11836170001, Roche, Basel, Switzerland) and phosphatase inhibitor (#04906845001, Roche). The BCA protein assay kit (#23227, Thermo Scientific, Waltham, MA, USA) was used to determine protein concentration. After denaturation at 95 °C for 10 min, the proteins were loaded onto a 10% SDS gel and separated using the Biometra Eco-Mini Buffer Tank system (Analytik Jena, Jena, Germany, #846-017-103/017-170). Protein transfer onto a PVDF membrane (BioRad Laboratories, Inc., Hercules, CA, USA, #1620177) was facilitated using the Biometra Fastblot system (#846-015-299 Analytik Jena, Jena, Germany). The membrane was incubated overnight at 4 °C with the following antibodies: E-cadherin (BD Bioscience, Heidelberg, Germany, #610182) and GAPDH (Cell signaling, Danvers, MA, USA, #2118). After three washes with 1x TBS-T, the corresponding secondary antibody labeled with horseradish peroxidase was incubated at room temperature for one hour (Goat anti-rabbit, #31460, Goat anti-mouse #31432, Thermo Fisher Scientific, Waltham, MA, USA). Antibody binding was detected using the SuperSignal West Pico Plus substrate kit (#34577, Thermo Fisher Scientific, Waltham, MA, USA) and

visualized using the ChemStudio 159 imager (#849-97-0928-04, Analytik Jena, Jena, Germany).

Quantitative Real-Time PCR (qRT-PCR)

To determine E-cadherin mRNA levels after treatment with MKP544, the following primers from Eurofins were utilized (Ebersberg, Germany): E-cadherin (forward, 5′ CGAGAGCTACACGTTCACGG-3′, reverse 5′-GGGTGTCGAGGGAAAAATAGG-3′) (Anzai et al. 2017) and GAPDH (forward, 5′-TGCACCACCAACTGCTTAGC-3′; reverse, 5′-GGCATGGACTGTGGTCATGAG-3′). PANC-1 cells were incubated with **MPK544**, SAHA, or tubastatin A for 24 or 72 h. The total RNA was extracted using the RNeasy MiniKit (#74104, Qiagen, Hilden, Germany) as described in the manufacturer's instructions. The determination of the RNA concentration was performed using the Tecan Spark NanoQuant plate (Tecan Group, Männedorf, Switzerland). The cDNA synthesis was conducted with 1 µg of isolated mRNA using the QuantiTect Reverse Transcription Kit (#205311, Qiagen, Hilden, Germany). The qRT-PCR was carried out with 50 ng cDNA using the Luna® Universal qPCR Master Mix (# M3003L, New England BioLabs® Inc., Ipswich, MA, USA). Ct values were calculated with the ΔΔCT method. Sample values were normalized to the housekeeping gene GAPDH (glyceraldehyde 3-phosphate dehydrogenase). Analytical evaluation was performed with the qPCRsoft 4.1 software (Analytic Jena, Jena, Germany).

Spherical Invasion Assay

The invasion assay was adapted from Hurley et al. (2017) [37]. In summary, PANC-1 cells were diluted 1:1 with matrigel (#356230, Corning, Corning, NY, USA). Compounds were applied to the cell suspension in a 24-well plate. The matrigel was allowed to polymerize for 30 min at 37 °C. After a 24 h incubation period, a second matrigel layer was added on top of the first. The invasion of the PANC-1 cells into the second layer of matrigel was studied for 72 h with the CQ1 Confocal Imaging Cytometer (#90ZA00673, Yokogawa, Tokyo, Japan). The invaded number of cells was quantified at 0 h and after 72 h with the CellPathFinder software (version 3.06.06.06, Yokogawa). Machine learning was used to automatically identify and count each invasive cell in the brightfield mode. To capture all cells invaded in the second matrigel layer, the analysis radius was set to 1500 µm.

Immunofluorescence of Whole Spheroids

Spheroids were cultivated for 4 days, followed by 72 h of treatment. The protocol was adapted from Xie et al. (2020), and the spheroids were fixed with 4% paraformaldehyde for 1 h at room temperature [30]. The primary antibody staining process involved permeabilization using 0.25% Triton X-100, followed by blocking with a solution of 0.1% BSA and 0.01% Tween 20 in PBS. Spheroids were incubated with 100 µL of primary antibody solution (Human Ki67/MKI67 (#MAB7617, R&DSystems, Minneapolis, MN, USA), E-cadherin (#610182, BD Biosciences, Franklin Lakes, NJ, USA) for 24 h at 4 °C. The secondary antibody solution (Alexa Flour 647 donkey (H+L) anti-mouse (#A-31571, Invitrogen, Waltham, MA, USA), Alexa Flour 488 donkey (H+L) anti-rabbit (#A-21206, Invitrogen)) including 2 µg/mL DAPI (#D9542, Sigma-Aldrich, Saint Louis, MI, USA) was incubated at 4 °C for 24 h. The clearing process was performed by sequential incubation in six ethanol solutions with an increasing concentration (30%, 50%, 70%, 90%, 96%, and 100%), each for 30 min. A final clearing step involved a benzyl alcohol/benzyl benzoate solution with a 1:2 ratio for 1 h. Afterwards, the spheroids were transferred to an imaging plate (# 89626, ibidi GmbH, Gräfelfing, Germany) and imaged with the CQ1 Confocal Imaging Cytometer (Part Number 90ZA00673, Yokogawa). Z-stacks were obtained with 100 stacks per spheroid (1 slice/µm) and analyzed using the CellPathFinder software.

Flow Cytometry

Co-culture spheroids were generated as described above. Then, 4 days after seeding, spheroids were treated with drug candidates and harvested after 72 h of incubation. After washing with PBS, spheroids were digested into single cell suspension using 500 µL Accumax Cell Dissociation Solution (#ACM-1F, Capricorn Scientific GmbH, Ebsdorfergrund, Germany). The single cell suspensions were transferred onto a 96 V bottom plate (#83.3926, Sarstedt, Nümbrecht, Germany) and stained in Automacs Running Buffer with REA Control (S)-PE (#130-113-438, Miltenyi, Bergisch Gladbach, Germany), E-cadherin-PE (#130-111-992, Miltenyi) antibodies according to manufacture introductions for 10 min at 4 °C. For the analysis of apoptosis and the cell cycle, PANC-1 cells were cultured in 6-well plates. After treatment for 48 h, cells were harvested and washed with PBS. Staining was performed using the Annexin V-FITC/propidium iodide (PI) Apoptosis Detection Kit from Elabscience (#E-CK-A211, Housten, TX, USA) according to the manufacturer’s instructions. For cell cycle

analysis, cells were washed with PBS and suspended in 100 µL of hypotonic buffer (0.1% Triton X-100, 1% sodium citrate, and 0.05 mg/mL PI in double-distilled water). The cells were incubated for 10 min at room temperature. Flow cytometry was performed with the BD FACSLyric flow cytometer (#87135, BD Bioscience, Franklin Lakes, NJ, USA) and analyzed with the FlowJo software (version 10.8.1).

Combinatorial Drug Testing

PANC-1 cells were seeded onto 96-well plates (#655090, Greiner Bio-One, Kremsmünster, Austria). Then, 24 h after seeding, the cells were treated with increasing concentrations in 9 × 6 dose–response matrices. For MPK544, the concentration range was 0.1875 µM up to 3 µM, for gemcitabine from 1.28 nM up to 100 µM, and for 5-fluorouracil (5-FU) from 0.78125 µM up to 100 µM, treated at 1:2, 1:5, and 1:2 dilutions, respectively. Cell viability was monitored after 72 h using the PrestoBlue HS Cell Viability Assay (as described in 4.3.). Bliss synergy scores were determined using the Combenefit synergy analysis software (version 2.021) [44].

Statistical Analysis

GraphPad Prism 8.4.3 software (GraphPad Software, Boston, MA, USA) was utilized for statistical and graphical analysis. The IC50 values were acquired for assessing cell viability through non-linear regression. A one-way analysis of variance (ANOVA, New Providence, NJ, USA) and unpaired *t*-test were employed to scrutinize statistical data, with p-values < 0.05 considered statistically significant.

Supplementary Materials

The following supporting information can be downloaded at https://www.mdpi.com/article/10.3390/ph17060752/s1. References 61,62,63 are cited in Supplementary Material.

Author Contributions

N.E.T., T.K., K.S., and A.D. designed and conceived the experiments. K.S, A.D., J.H. and M.P. conducted the experiments. K.S. and A.D. analyzed the results. Enzyme selectivity data were provided by A.H. and M.U.K. The original manuscript draft was written by K.S. and A.D. The manuscript was edited by K.S. and A.D. and revised by N.E.T., M.U.K., and T.K. Supervision and project conceptual design were conducted

by N.E.T. and T.K. All authors have read and agreed to the published version of the manuscript.

Funding

This work was funded by the Deutsche Forschungsgemeinschaft (DFG, German Research Foundation) 270650915 (Research Training Group GRK 2158 to T.K. and N.E.T., M.U.K. acknowledges financial support from the Deutsche Forschungsgemeinschaft (DFG, German Research Foundation) KA 1942/2-1.

Institutional Review Board Statement

Not applicable.

Informed Consent Statement

Not applicable.

Data Availability Statement

Data is contained within the article and Supplementary Materials.

Acknowledgments

We would like to thank Karin Peter and Nadine Horstick for their excellent technical support throughout this work. Furthermore, we express our gratitude to Michael Schell for his invaluable assistance in devising the CellPathFinder image analysis. We would like to thank the working group of Christoph Suschek, especially Vera Grotheer, for providing the BD FACSLyric flow cytometer.

Conflicts of Interest

The authors declare no conflicts of interest.

References

1. Elrakaybi, A.; Ruess, D.A.; Lübbert, M.; Quante, M.; Becker, H. Epigenetics in Pancreatic Ductal Adenocarcinoma: Impact on Biology and Utilization in Diagnostics and Treatment. *Cancers* **2022**, *14*, 5926. [Google Scholar] [CrossRef] [PubMed]
2. Siegel, R.L.; Miller, K.D.; Fuchs, H.E.; Jemal, A. Cancer statistics, 2022. *CA Cancer J. Clin.* **2022**, *72*, 7–33. [Google Scholar] [CrossRef] [PubMed]

3. Hosein, A.N.; Brekken, R.A.; Maitra, A. Pancreatic cancer stroma: An update on therapeutic targeting strategies. *Nat. Rev. Gastroenterol. Hepatol.* **2020**, *17*, 487–505. [Google Scholar] [CrossRef]

4. Nielsen, M.F.B.; Mortensen, M.B.; Detlefsen, S. Key players in pancreatic cancer-stroma interaction: Cancer-associated fibroblasts, endothelial and inflammatory cells. *World J. Gastroenterol.* **2016**, *22*, 2678–2700. [Google Scholar] [CrossRef]

5. Bulle, A.; Lim, K.-H. Beyond just a tight fortress: Contribution of stroma to epithelial-mesenchymal transition in pancreatic cancer. *Signal Transduct. Target. Ther.* **2020**, *5*, 249. [Google Scholar] [CrossRef] [PubMed]

6. Guo, J.; Wang, S.; Gao, Q. An integrated overview of the immunosuppression features in the tumor microenvironment of pancreatic cancer. *Front. Immunol.* **2023**, *14*, 1258538. [Google Scholar] [CrossRef]

7. Muller, M.; Haghnejad, V.; Schaefer, M.; Gauchotte, G.; Caron, B.; Peyrin-Biroulet, L.; Bronowicki, J.-P.; Neuzillet, C.; Lopez, A. The Immune Landscape of Human Pancreatic Ductal Carcinoma: Key Players, Clinical Implications, and Challenges. *Cancers* **2022**, *14*, 995. [Google Scholar] [CrossRef]

8. Chen, G.; Wu, K.; Li, H.; Xia, D.; He, T. Role of hypoxia in the tumor microenvironment and targeted therapy. *Front. Oncol.* **2022**, *12*, 961637. [Google Scholar] [CrossRef]

9. Xiang, X.-S.; Li, P.-C.; Wang, W.-Q.; Liu, L. Histone deacetylases: A novel class of therapeutic targets for pancreatic cancer. *Biochim. Biophys. Acta Rev. Cancer* **2022**, *1877*, 188676. [Google Scholar] [CrossRef]

10. Singh, T.; Kaur, P.; Singh, P.; Singh, S.; Munshi, A. Differential molecular mechanistic behavior of HDACs in cancer progression. *Med. Oncol.* **2022**, *39*, 171. [Google Scholar] [CrossRef]

11. Kulka, L.A.M.; Fangmann, P.-V.; Panfilova, D.; Olzscha, H. Impact of HDAC Inhibitors on Protein Quality Control Systems: Consequences for Precision Medicine in Malignant Disease. *Front. Cell Dev. Biol.* **2020**, *8*, 425. [Google Scholar] [CrossRef] [PubMed]

12. Barneda-Zahonero, B.; Parra, M. Histone deacetylases and cancer. *Mol. Oncol.* **2012**, *6*, 579–589. [Google Scholar] [CrossRef] [PubMed]

13. Seto, E.; Yoshida, M. Erasers of histone acetylation: The histone deacetylase enzymes. *Cold Spring Harb. Perspect. Biol.* **2014**, *6*, a018713. [Google Scholar] [CrossRef] [PubMed]

14. Laschanzky, R.S.; Humphrey, L.E.; Ma, J.; Smith, L.M.; Enke, T.J.; Shukla, S.K.; Dasgupta, A.; Singh, P.K.; Howell, G.M.; Brattain, M.G.; et al. Selective Inhibition of Histone Deacetylases 1/2/6 in Combination with Gemcitabine: A Promising Combination for Pancreatic Cancer Therapy. *Cancers* **2019**, *11*, 1327. [Google Scholar] [CrossRef] [PubMed]

15. Wawruszak, A.; Kalafut, J.; Okon, E.; Czapinski, J.; Halasa, M.; Przybyszewska, A.; Miziak, P.; Okla, K.; Rivero-Muller, A.; Stepulak, A. Histone Deacetylase Inhibitors and Phenotypical Transformation of Cancer Cells. *Cancers* **2019**, *11*, 148. [Google Scholar] [CrossRef] [PubMed]

16. Krauß, L.; Schneider, C.; Hessmann, E.; Saur, D.; Schneider, G. Epigenetic control of pancreatic cancer metastasis. *Cancer Metastasis Rev.* **2023**, *42*, 1113–1131. [Google Scholar] [CrossRef] [PubMed]

17. Fu, X.-H.; Zhang, X.; Yang, H.; Xu, X.-W.; Hu, Z.-L.; Yan, J.; Zheng, X.-L.; Wei, R.-R.; Zhang, Z.-Q.; Tang, S.-R.; et al. CUDC-907 displays potent antitumor activity against human pancreatic adenocarcinoma in vitro and in vivo through inhibition of HDAC6 to downregulate c-Myc expression. *Acta Pharmacol. Sin.* **2019**, *40*, 677–688. [Google Scholar] [CrossRef] [PubMed]

18. Luu, T. Epithelial-Mesenchymal Transition and its Regulation Mechanisms in Pancreatic Cancer. *Front. Oncol.* **2021**, *11*, 646399. [Google Scholar] [CrossRef] [PubMed]

19. Park, S.J.; Kim, S.-M.; Moon, J.-H.; Kim, J.H.; Shin, J.-S.; Hong, S.-W.; Shin, Y.J.; Lee, D.-H.; Lee, E.Y.; Hwang, I.-Y.; et al. SAHA, an HDAC inhibitor, overcomes erlotinib resistance in human pancreatic cancer cells by modulating E-cadherin. *Tumour Biol.* **2016**, *37*, 4323–4330. [Google Scholar] [CrossRef]

20. Knoche, S.M.; Brumfield, G.L.; Goetz, B.T.; Sliker, B.H.; Larson, A.C.; Olson, M.T.; Poelaert, B.J.; Bavari, A.; Yan, Y.; Black, J.D.; et al. The histone

deacetylase inhibitor M344 as a multifaceted therapy for pancreatic cancer. *PLoS ONE* **2022**, *17*, e0273518. [Google Scholar] [CrossRef]

21. Conroy, T.; Pfeiffer, P.; Vilgrain, V.; Lamarca, A.; Seufferlein, T.; O'Reilly, E.M.; Hackert, T.; Golan, T.; Prager, G.; Haustermans, K.; et al. Pancreatic cancer: ESMO Clinical Practice Guideline for diagnosis, treatment and follow-up. *Ann. Oncol.* **2023**, *34*, 987–1002. [Google Scholar] [CrossRef]
22. Pusceddu, S.; Ghidini, M.; Torchio, M.; Corti, F.; Tomasello, G.; Niger, M.; Prinzi, N.; Nichetti, F.; Coinu, A.; Di Bartolomeo, M.; et al. Comparative Effectiveness of Gemcitabine plus Nab-Paclitaxel and FOLFIRINOX in the First-Line Setting of Metastatic Pancreatic Cancer: A Systematic Review and Meta-Analysis. *Cancers* **2019**, *11*, 484. [Google Scholar] [CrossRef] [PubMed]
23. Thomas, D.; Radhakrishnan, P. Pancreatic Stellate Cells: The Key Orchestrator of The Pancreatic Tumor Microenvironment. *Adv. Exp. Med. Biol.* **2020**, *1234*, 57–70. [Google Scholar] [CrossRef]
24. Cave, D.D.; Di Guida, M.; Costa, V.; Sevillano, M.; Ferrante, L.; Heeschen, C.; Corona, M.; Cucciardi, A.; Lonardo, E. TGF-β1 secreted by pancreatic stellate cells promotes stemness and tumourigenicity in pancreatic cancer cells through L1CAM downregulation. *Oncogene* **2020**, *39*, 4271–4285. [Google Scholar] [CrossRef]
25. Marks, P.A.; Breslow, R. Dimethyl sulfoxide to vorinostat: Development of this histone deacetylase inhibitor as an anticancer drug. *Nat. Biotechnol.* **2007**, *25*, 84–90. [Google Scholar] [CrossRef] [PubMed]
26. Marks, P.A. Discovery and development of SAHA as an anticancer agent. *Oncogene* **2007**, *26*, 1351–1356. [Google Scholar] [CrossRef]
27. McClure, J.J.; Li, X.; Chou, C.J. Advances and Challenges of HDAC Inhibitors in Cancer Therapeutics. *Adv. Cancer Res.* **2018**, *138*, 183–211. [Google Scholar] [CrossRef]
28. Stenzel, K.; Hamacher, A.; Hansen, F.K.; Gertzen, C.G.W.; Senger, J.; Marquardt, V.; Marek, L.; Marek, M.; Romier, C.; Remke, M.; et al. Alkoxyurea-Based Histone Deacetylase Inhibitors Increase Cisplatin Potency in

Chemoresistant Cancer Cell Lines. *J. Med. Chem.* **2017**, *60*, 5334–5348. [Google Scholar] [CrossRef] [PubMed]

29. Negmeldin, A.T.; Pflum, M.K.H. The structural requirements of histone deacetylase inhibitors: SAHA analogs modified at the C5 position display dual HDAC6/8 selectivity. *Bioorg. Med. Chem. Lett.* **2017**, *27*, 3254–3258. [Google Scholar] [CrossRef]

30. Xie, B.; Hänsel, J.; Mundorf, V.; Betz, J.; Reimche, I.; Erkan, M.; Büdeyri, I.; Gesell, A.; Kerr, R.G.; Ariantari, N.P.; et al. Pseudopterosin and O-Methyltylophorinidine Suppress Cell Growth in a 3D Spheroid Co-Culture Model of Pancreatic Ductal Adenocarcinoma. *Bioengineering* **2020**, *7*, 57. [Google Scholar] [CrossRef]

31. Aghdassi, A.; Sendler, M.; Guenther, A.; Mayerle, J.; Behn, C.-O.; Heidecke, C.-D.; Friess, H.; Büchler, M.; Evert, M.; Lerch, M.M.; et al. Recruitment of histone deacetylases HDAC1 and HDAC2 by the transcriptional repressor ZEB1 downregulates E-cadherin expression in pancreatic cancer. *Gut* **2012**, *61*, 439–448. [Google Scholar] [CrossRef]

32. Kaneta, Y.; Sato, T.; Hikiba, Y.; Sugimori, M.; Sue, S.; Kaneko, H.; Irie, K.; Sasaki, T.; Kondo, M.; Chuma, M.; et al. Loss of Pancreatic E-Cadherin Causes Pancreatitis-Like Changes and Contributes to Carcinogenesis. *Cell. Mol. Gastroenterol. Hepatol.* **2020**, *9*, 105–119. [Google Scholar] [CrossRef] [PubMed]

33. Mishra, V.K.; Subramaniam, M.; Kari, V.; Pitel, K.S.; Baumgart, S.J.; Naylor, R.M.; Nagarajan, S.; Wegwitz, F.; Ellenrieder, V.; Hawse, J.R.; et al. Krüppel-like Transcription Factor KLF10 Suppresses TGFβ-Induced Epithelial-to-Mesenchymal Transition via a Negative Feedback Mechanism. *Cancer Res.* **2017**, *77*, 2387–2400. [Google Scholar] [CrossRef]

34. Garajová, I.; Cavazzoni, A.; Verze, M.; Minari, R.; Pedrazzi, G.; Balsano, R.; Gelsomino, F.; Valle, R.D.; Digiacomo, G.; Giovannetti, E.; et al. It Takes Two to Tango: Potential Prognostic Impact of Circulating TGF-Beta and PD-L1 in Pancreatic Cancer. *Life* **2022**, *12*, 960. [Google Scholar] [CrossRef]

35. Principe, D.R.; Timbers, K.E.; Atia, L.G.; Koch, R.M.; Rana, A. TGFβ Signaling in the Pancreatic Tumor Microenvironment. *Cancers* **2021**, *13*, 5086. [Google Scholar] [CrossRef]

36. Alvarez, M.A.; Freitas, J.P.; Mazher Hussain, S.; Glazer, E.S. TGF-β Inhibitors in Metastatic Pancreatic Ductal Adenocarcinoma. *J. Gastrointest. Cancer* **2019**, *50*, 207–213. [Google Scholar] [CrossRef] [PubMed]

37. Hurley, J.D.; Akers, A.T.; Friedman, J.R.; Nolan, N.A.; Brown, K.C.; Dasgupta, P. Non-pungent long chain capsaicin-analogs arvanil and olvanil display better anti-invasive activity than capsaicin in human small cell lung cancers. *Cell Adhes. Migr.* **2017**, *11*, 80–97. [Google Scholar] [CrossRef]

38. Krauß, L.; Urban, B.C.; Hastreiter, S.; Schneider, C.; Wenzel, P.; Hassan, Z.; Wirth, M.; Lankes, K.; Terrasi, A.; Klement, C.; et al. HDAC2 Facilitates Pancreatic Cancer Metastasis. *Cancer Res.* **2022**, *82*, 695–707. [Google Scholar] [CrossRef] [PubMed]

39. Alqosaibi, A.I.; Abdel-Ghany, S. Vorinostat induces G2/M cell cycle arrest in breast cancer cells via upregulation of PTEN. *Eur. Rev. Med. Pharmacol. Sci.* **2023**, *27*, 1503–1511. [Google Scholar] [CrossRef]

40. Niu, J.; Wang, X.; Qu, J.; Mager, D.E.; Straubinger, R.M. Pharmacodynamic modeling of synergistic birinapant/paclitaxel interactions in pancreatic cancer cells. *BMC Cancer* **2020**, *20*, 1024. [Google Scholar] [CrossRef]

41. Urdiciain, A.; Erausquin, E.; Meléndez, B.; Rey, J.A.; Idoate, M.A.; Castresana, J.S. Tubastatin A, an inhibitor of HDAC6, enhances temozolomide–induced apoptosis and reverses the malignant phenotype of glioblastoma cells. *Int. J. Oncol.* **2019**, *54*, 1797–1808. [Google Scholar] [CrossRef] [PubMed]

42. Arnold, N.B.; Arkus, N.; Gunn, J.; Korc, M. The histone deacetylase inhibitor suberoylanilide hydroxamic acid induces growth inhibition and enhances gemcitabine-induced cell death in pancreatic cancer. *Clin. Cancer Res.* **2007**, *13*, 18–26. [Google Scholar] [CrossRef] [PubMed]

43. Roca, M.S.; Moccia, T.; Iannelli, F.; Testa, C.; Vitagliano, C.; Minopoli, M.; Camerlingo, R.; de Riso, G.; de Cecio, R.; Bruzzese, F.; et al. HDAC class I inhibitor domatinostat sensitizes pancreatic cancer to chemotherapy by

targeting cancer stem cell compartment via FOXM1 modulation. *J. Exp. Clin. Cancer Res.* **2022**, *41*, 83. [Google Scholar] [CrossRef] [PubMed]

44. Di Veroli, G.Y.; Fornari, C.; Wang, D.; Mollard, S.; Bramhall, J.L.; Richards, F.M.; Jodrell, D.I. Combenefit: An interactive platform for the analysis and visualization of drug combinations. *Bioinformatics* **2016**, *32*, 2866–2868. [Google Scholar] [CrossRef] [PubMed]

45. Shustov, A.; Coiffier, B.; Horwitz, S.; Sokol, L.; Pro, B.; Wolfson, J.; Balser, B.; Eisch, R.; Popplewell, L.; Prince, H.M.; et al. Romidepsin is effective and well tolerated in older patients with peripheral T-cell lymphoma: Analysis of two phase II trials. *Leuk. Lymphoma* **2017**, *58*, 2335–2341. [Google Scholar] [CrossRef] [PubMed]

46. O'Connor, O.A.; Horwitz, S.; Masszi, T.; van Hoof, A.; Brown, P.; Doorduijn, J.; Hess, G.; Jurczak, W.; Knoblauch, P.; Chawla, S.; et al. Belinostat in Patients with Relapsed or Refractory Peripheral T-Cell Lymphoma: Results of the Pivotal Phase II BELIEF (CLN-19) Study. *J. Clin. Oncol.* **2015**, *33*, 2492–2499. [Google Scholar] [CrossRef] [PubMed]

47. Wu, Y.; Li, C.S.; Meng, R.Y.; Jin, H.; Chai, O.H.; Kim, S.M. Regulation of Hippo-YAP/CTGF signaling by combining an HDAC inhibitor and 5-fluorouracil in gastric cancer cells. *Toxicol. Appl. Pharmacol.* **2024**, *482*, 116786. [Google Scholar] [CrossRef] [PubMed]

48. Kim, D.J.; Dunleavey, J.M.; Xiao, L.; Ollila, D.W.; Troester, M.A.; Otey, C.A.; Li, W.; Barker, T.H.; Dudley, A.C. Suppression of TGFβ-mediated conversion of endothelial cells and fibroblasts into cancer associated (myo)fibroblasts via HDAC inhibition. *Br. J. Cancer* **2018**, *118*, 1359–1368. [Google Scholar] [CrossRef]

49. Mishra, V.K.; Wegwitz, F.; Kosinsky, R.L.; Sen, M.; Baumgartner, R.; Wulff, T.; Siveke, J.T.; Schildhaus, H.-U.; Najafova, Z.; Kari, V.; et al. Histone deacetylase class-I inhibition promotes epithelial gene expression in pancreatic cancer cells in a BRD4- and MYC-dependent manner. *Nucleic Acids Res.* **2017**, *45*, 6334–6349. [Google Scholar] [CrossRef] [PubMed]

50. Wang, G.; He, J.; Zhao, J.; Yun, W.; Xie, C.; Taub, J.W.; Azmi, A.; Mohammad, R.M.; Dong, Y.; Kong, W.; et al. Class I and class II histone deacetylases are

potential therapeutic targets for treating pancreatic cancer. *PLoS ONE* **2012**, *7*, e52095. [Google Scholar] [CrossRef]

51. Gruber, W.; Peer, E.; Elmer, D.P.; Sternberg, C.; Tesanovic, S.; Del Burgo, P.; Coni, S.; Canettieri, G.; Neureiter, D.; Bartz, R.; et al. Targeting class I histone deacetylases by the novel small molecule inhibitor 4SC-202 blocks oncogenic hedgehog-GLI signaling and overcomes smoothened inhibitor resistance. *Int. J. Cancer* **2018**, *142*, 968–975. [Google Scholar] [CrossRef] [PubMed]
52. Hahn, S.; Oh, B.J.; Kim, H.; Han, I.W.; Shin, S.H.; Kim, G.; Jin, S.-M.; Kim, J.H. Anti-cancer effects of metformin in a 3D co-culture model of pancreatic ductal adenocarcinoma. *Am. J. Cancer Res.* **2023**, *13*, 1806–1825. [Google Scholar] [PubMed]
53. Semaan, A.; Bernard, V.; Kim, D.U.; Lee, J.J.; Huang, J.; Kamyabi, N.; Stephens, B.M.; Qiao, W.; Varadhachary, G.R.; Katz, M.H.; et al. Characterisation of circulating tumour cell phenotypes identifies a partial-EMT sub-population for clinical stratification of pancreatic cancer. *Br. J. Cancer* **2021**, *124*, 1970–1977. [Google Scholar] [CrossRef] [PubMed]
54. Aiello, N.M.; Kang, Y. Context-dependent EMT programs in cancer metastasis. *J. Exp. Med.* **2019**, *216*, 1016–1026. [Google Scholar] [CrossRef] [PubMed]
55. Hoffmann, M.J.; Meneceur, S.; Hommel, K.; Schulz, W.A.; Niegisch, G. Downregulation of Cell Cycle and Checkpoint Genes by Class I HDAC Inhibitors Limits Synergism with G2/M Checkpoint Inhibitor MK-1775 in Bladder Cancer Cells. *Genes* **2021**, *12*, 260. [Google Scholar] [CrossRef] [PubMed]
56. Kaur, S.; Rajoria, P.; Chopra, M. HDAC6: A unique HDAC family member as a cancer target. *Cell. Oncol.* **2022**, *45*, 779–829. [Google Scholar] [CrossRef]
57. Kutil, Z.; Skultetyova, L.; Rauh, D.; Meleshin, M.; Snajdr, I.; Novakova, Z.; Mikesova, J.; Pavlicek, J.; Hadzima, M.; Baranova, P.; et al. The unraveling of substrate specificity of histone deacetylase 6 domains using acetylome peptide microarrays and peptide libraries. *FASEB J.* **2019**, *33*, 4035–4045. [Google Scholar] [CrossRef]

58. Wu, J.-Y.; Xiang, S.; Zhang, M.; Fang, B.; Huang, H.; Kwon, O.K.; Zhao, Y.; Yang, Z.; Bai, W.; Bepler, G.; et al. Histone deacetylase 6 (HDAC6) deacetylates extracellular signal-regulated kinase 1 (ERK1) and thereby stimulates ERK1 activity. *J. Biol. Chem.* **2018**, *293*, 1976–1993. [Google Scholar] [CrossRef]

59. Zheng, Y.; Yang, X.; Wang, C.; Zhang, S.; Wang, Z.; Li, M.; Wang, Y.; Wang, X.; Yang, X. HDAC6, modulated by miR-206, promotes endometrial cancer progression through the PTEN/AKT/mTOR pathway. *Sci. Rep.* **2020**, *10*, 3576. [Google Scholar] [CrossRef]

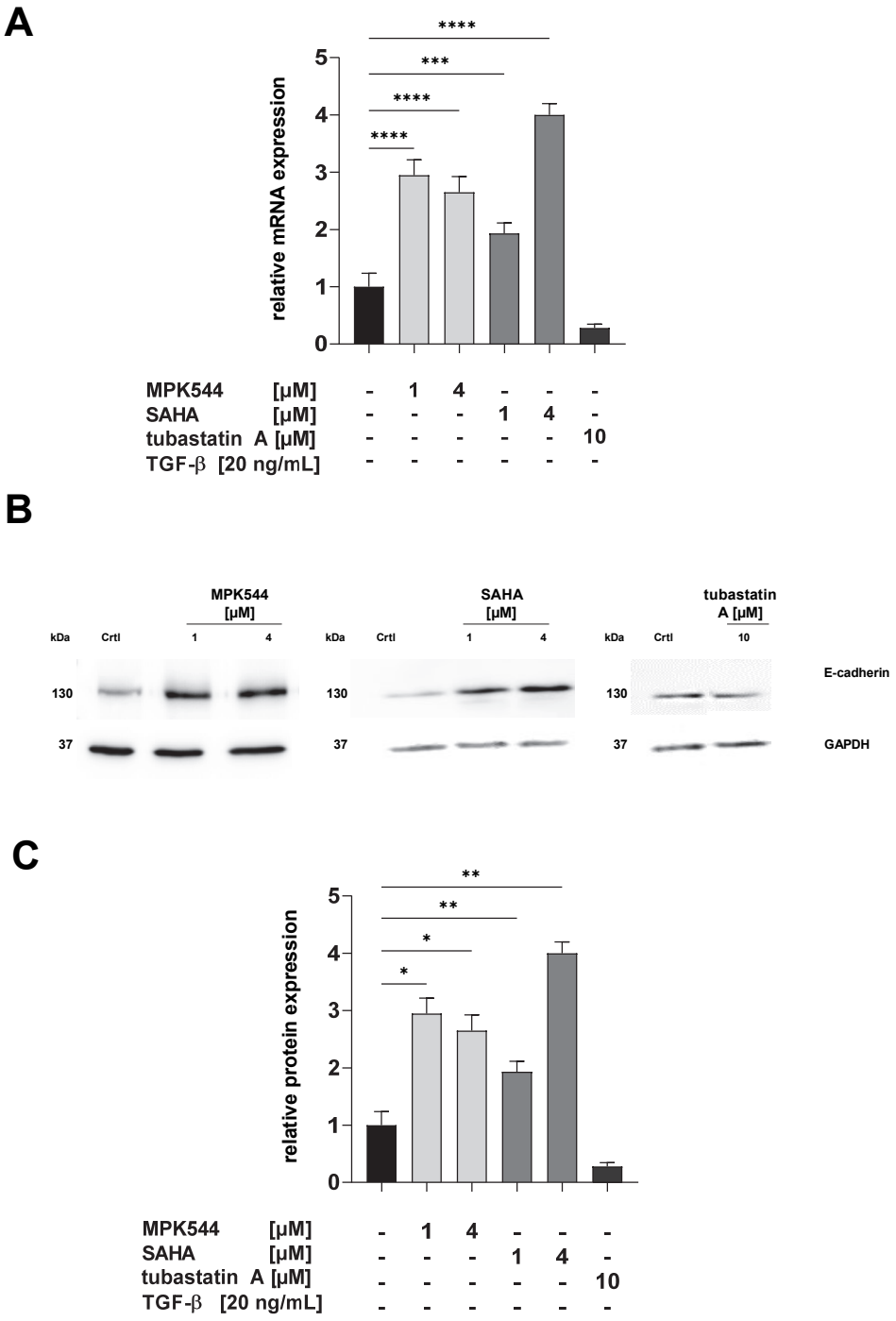
60. Yoo, J.; Jeon, Y.H.; Lee, D.H.; Kim, G.W.; Lee, S.W.; Kim, S.Y.; Park, J.; Kwon, S.H. HDAC6-selective inhibitors enhance anticancer effects of paclitaxel in ovarian cancer cells. *Oncol. Lett.* **2021**, *21*, 201. [Google Scholar] [CrossRef]

61. Olah, G.A.; Fung, A.P. Hexahydro-2-(1H)-Azocinone. *Org. Synth.* **2003**, *63*, 188. [Google Scholar]

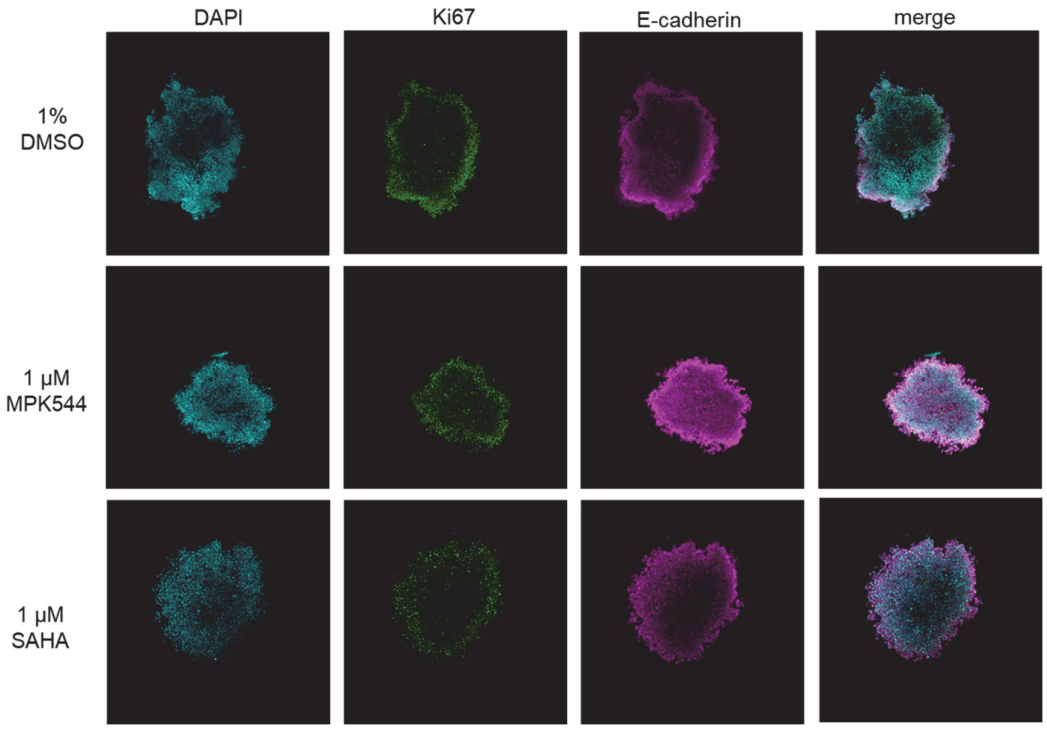
62. Giovannini, A.; Savoia, D.; Umani-Ronchi, A. Organometallic ring-opening reactions of N-acyl and N-alkoxycarbonyl lactams. Synthesis of cyclic imines. *J. Org. Chem.* **1989**, *54*, 228–234. [Google Scholar] [CrossRef]

63. Ugwuegbulam, C.O.; Foy, J.E. Process for the Preparation of Anti-Malarial Drugs. U.S. Patent 6,479,660, 12 November 2002. [Google Scholar]

3.1.1 Supplementary Information



Supplementary Figure 3.1-1 Upregulation of E-cadherin expression in PANC-1 cells. PANC-1 cells were treated with MPK544, SAHA and tubastatin A for 72 h. mRNA levels of E-cadherin in PANC-1 cells were analyzed by qRT-PCR (A) and at the protein level by western blot (B, C). Representative western blots are shown (B). Error bars indicate the standard errors of the mean (of at least three independent experiments, with * = $p \leq 0.05$; ** = $p \leq 0.01$; *** = $p \leq 0.001$; and **** = $p \leq 0.0001$).



Supplementary Figure 3.1-2 E-cadherin expression in PANC-1 spheroids after 72h of treatment with MPK544 or SAHA. DAPI-staining of nuclei (405 nm); staining of the proliferation marker Ki67 (488 nm); staining of E-cadherin (647 nm); merging of all three channels. Imaging of spheroids with the CQ1 High-Content Spinning Disk System (Yokogawa Electric Corporation). IC50 values for PANC-1 spheroids are 2.17µM for SAHA and 2.20 µM for MPK544.

3.2 Modelling of the multicellular tumor microenvironment of pancreatic ductal adenocarcinoma (PDAC) on a fit-for-purpose biochip for preclinical drug discovery

Alina Deipenbrock *[a], Ben Eric Wilmes [a], Thomas Sommermann [b], Nader Abdo [b], Kyra Moustakas [a], Martin Raasch[b], Knut Rennert [b], and Nicole E. Teusch [a]

[a] Institute of Pharmaceutical Biology and Biotechnology, Heinrich-Heine-University Düsseldorf, Universitätsstr. 1, 40225 Düsseldorf, Germany. E-mail: Nicole.Teusch@hhu.de

[b] Dynamic42 GmbH, Jena, Germany

Published in: *Lab on a chip*

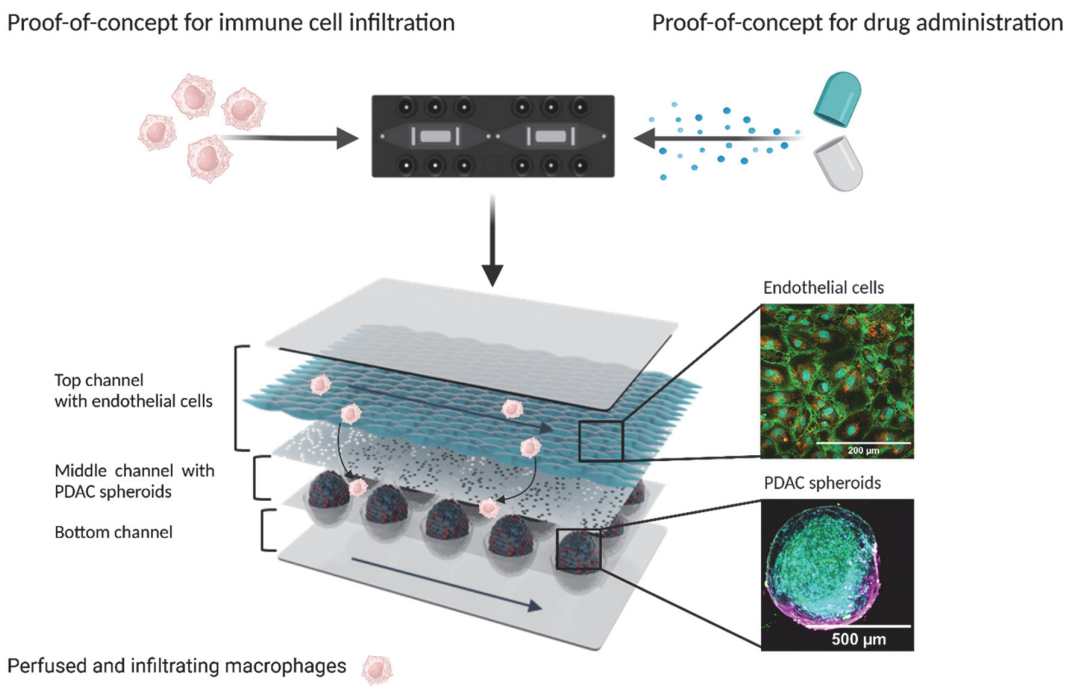
DOI: 10.1039/d4lc01016g

Own contributions to the manuscript: 75%

- Conceptualization of the experiments (50%) together with Nicole Teusch
- Methodology (100%), Investigation (70%), Validation (90%), Data curation (100%), Formal analysis (100%), and Visualization (80%) of the following experiments:
    - Establishment of cultivation of PDAC spheroids and HUVEC on the biochip via immunofluorescence, viability assay, and FITC dextran assay (90%) together with Kyra Moustakas
    - Analysis of drug treatment on the biochip via immunofluorescence, viability assay, and FITC dextran assay (100%)
    - Perfusion with monocytes and characterization of macrophage differentiation (100%)
    - Characterization of monocyte infiltration via immunofluorescence into the co-culture spheroids (50%) together with Ben E. Wilmes
- Writing and drafting the manuscript (85%) together with Nicole Teusch

Abstract

Pancreatic ductal adenocarcinoma (PDAC) is the most common and lethal form of pancreatic cancer. One major cause for a fast disease progression is the presence of a highly fibrotic tumor microenvironment (TME) mainly composed of cancer-associated fibroblasts (CAF), and various immune cells, especially tumor-associated macrophages (TAM). To conclusively evaluate drug efficacy, it is crucial to develop in vitro models that can recapitulate the cross talk between tumor cells and the surrounding stroma. Here, we constructed a fit-for-purpose biochip platform which allows the integration of PDAC spheroids (composed of PANC-1 cells and pancreatic stellate cells (PSC)). Additionally, the chip design enables dynamic administration of drugs or immune cells via a layer of human umbilical vein endothelial cells (HUVEC). As a proof-of-concept for drug administration, vorinostat, an FDA-approved histone deacetylase inhibitor for cutaneous T-cell lymphoma (CTCL), subjected via continuous flow for 72 h, resulted in a significantly reduced viability of PDAC spheroids without affecting vascular integrity. Furthermore, dynamic perfusion with peripheral mononuclear blood cells (PBMC)-derived monocytes resulted in an immune cell migration through the endothelium into the spheroids. After 72 h of infiltration, monocytes differentiated into macrophages which polarized into the M2 phenotype. The polarization into M2 macrophages persisted for at least 168 h, verified by expression of the M2 marker CD163 which increased from 72 h to 168 h, while the M1 markers CD86 and HLA-DR were significantly downregulated. Overall, the described spheroid-on-chip model allows the evaluation of novel therapeutic strategies by mimicking and targeting the complex TME of PDAC.



Introduction

Pancreatic ductal adenocarcinoma (PDAC) is a highly aggressive cancer type with a five-year survival rate of 13% [1–3]. Early metastases, late diagnosis and therapy resistance are known factors of the low survival rates of patients with PDAC. To date, cytotoxic chemotherapy with the combinatory regimen FOLFIRINOX (leucovorin, 5-fluoruracil, irinotecan and oxaliplatin) or, if intolerable, the combination of gemcitabine and capecitabine represents the first line treatment for patients who are not eligible for surgical resection [4].

In PDAC, the tumor microenvironment (TME) is characterized by a large cellular heterogeneity. The main cell types within the tumor stroma include pancreatic stellate cells (PSC), and a variety of immune cells that form a highly fibrotic and immunosuppressive TME [5,6].

During tumorigenesis, PSC convert into cancer-associated fibroblasts (CAF), which exhibit a myofibroblast-like phenotype and constitute approximately 90% of the TME [7,8]. CAF secrete large amounts of extracellular matrix (ECM) components such as fibronectins, collagens and hyaluronic acid, responsible for the dense and stiff TME [9] forming a mechanical barrier surrounding the tumor lesions [8,10,11]. Additionally,

activated PSC release factors like interleukin-6 (IL-6), interleukin-10 (IL-10), CXCL12 transforming growth factor-beta (TGF-β), macrophage colony-stimulating factor (M-CSF), and vascular endothelial growth factor (VEGF), which are described for their involvement in immunosuppression, epithelial-mesenchymal transition (EMT), or angiogenesis [12–14]. For example, the release of M-CSF promotes the differentiation of monocytes into M2 macrophages [15]. The initiation of angiogenesis through the release of proangiogenic factors like VEGF leads to the generation of atypical and multibranched vessels that, however, collapse under the high interstitial pressure within the PDAC TME, resulting in a leaky and dysfunctional vasculature which then ultimately leads to a hypovascular and hypoxic tumour phenotype [16]. Importantly, a poor vascular supply also limits the delivery of chemotherapeutic agents into the tumor tissue [17]. Overall, the highlighted relevance of CAF in the tumor-stroma crosstalk leading to a highly desmoplastic milieu on one hand, with limited drug delivery on the other hand, underlines the need for novel preclinical 3D TME models [6].

In addition to CAF, the PDAC TME encompasses a variety of immune cell types and is abundantly infiltrated by tumor-associated macrophages (TAM). Macrophages are traditionally classified into two phenotypically and functionally distinct subsets: the immunogenic M1 phenotype and the immunosuppressive M2 phenotype. Recent research has highlighted the dynamic and versatile nature of TAM phenotypes [18] and in the case of PDAC, TAM are mainly polarized towards a M2 phenotype (*i.e.* $CD163^+$) [19,20]. In fact, a high infiltration of $CD163^+$ macrophages is associated with a lower overall survival rate in PDAC patients [21,22]. TAM contribute to tumor progression by enhancing both, chemoresistance and immunosuppression, as well as promoting acinar-to-ductal metaplasia through the secretion of tumor necrosis factor α (TNFα) and the activation of matrix metalloproteinases (MMPs) [23–26]. TAM macrophages release different mediators that lead to the activation of signaling pathways in tumor cells like PI3K/Akt, JAK/STAT or others subsequently contributing to chemoresistance [27–29]. Studies in mice showed that depletion of macrophages or blocking macrophage recruitment *via* the CC-chemokine ligand 2 (CCL2) axis can restore the sensitivity for gemcitabine or FOLFIRINOX, confirming the important role for M2 macrophages with respect to current and future therapeutic strategies [30–32]. Characteristic for their immunosuppressive behavior, M2 macrophages secret anti-inflammatory cytokines and chemokines such as IL-10, IL-6, IL-1-RA, CXCL7 and CCL2 which promote exhaustion of cytotoxic $CD8^+$ T-cells on one hand [24,33] and

drive the differentiation of $CD4^+$ T-cells towards Th2, Th17 and regulatory T-cells (Treg), widely known for their immunosuppressive and tumor promoting functions [34,35]. Furthermore, TAM inhibit the anti-tumor activity of cytotoxic $CD8^+$ T-cells by expressing immune checkpoint inhibitor ligands, such as PD-L1 and Dectin-1, on their surface [36,37]. Additionally, TAM induce the expression of these checkpoint inhibitors on tumor cells, directly contributing to the immune escape of cancer cells [38].

In vitro modelling of the complex cellular interplay within the PDAC TME is technically and scientifically challenging as conventional two-dimensional (2D) tumor cell culture settings are inadequate in mimicking cell–cell and cell–matrix interactions, spatial orientation, physicochemical stiffness as well as nutrient and oxygen gradients [39]. This limitation significantly reduces the prediction of therapeutic efficacy in 2D tumor cell monolayers in general and for PDAC in particular. Thus, to achieve more physiologically relevant and conclusive *in vitro* models, to date, multicellular tumor spheroids (MCTS), patient-derived organoids (PDO), and microfluidic devices represent the cutting edge for preclinical tumor models focussing on TME modulation [40]. MCTS were first described by Kunz-Schughart *et al.* in 2001, who generated spheroids composed of breast cancer cells and fibroblasts [41]. Since then, a variety of MCTS, composed of cancer cells combined with one or more stromal cell types, have been established for various malignancies, including pancreatic cancer [42–47]. However, these simplistic models were mainly generated with pancreatic cancer cell lines, CAF and one type of ECM components like collagens or Matrigel [42,45,46]. A few MCTS also include other important stroma cell types, such as endothelial cells[44] or TAM [48]. The incorporation of monocytes into PDAC MCTS demonstrates the ability of *in vitro* spheroids models to differentiate monocytes into macrophages and to polarize them towards an M2 phenotype [48–50]. An alternative to MCTS are PDO, which are generated from patient-derived tumor cells offering the opportunity to study molecular/cellular heterogeneity and directly mimic individual patient's biology [51]. However, spheroid and organoid models have inherent limitations, including the lack of a functional vasculature prohibiting the investigation of a dynamic drug or immune cells application route [52].

Recent advances in microfluidic technologies have facilitated the development of tumor-on-chip systems, which enable the 3D culture of multiple cell types under flow conditions [53]. In addition, a microfluidic system enables the dynamic application of drugs. Dynamic drug administration *via* microfluidic systems surpasses traditional

static dosing by enabling controlled release of therapeutics over extended periods or with variable concentrations, thereby more closely mimicking natural pharmacokinetics [54–56].

In the context of PDAC, different tumor-on-chip models have been developed over the past decade to investigate various aspects of the TME and its influence on drug response [57–63]. Examples for simplified models incorporated PDAC tumor cells and CAF into microfluidic chips to study the crosstalk between stromal and pancreatic cancer cells but lack the addition of immune and endothelial cells [57,61]. Other previously described models allow high throughput drug screening, but still do not include macrophages or a vasculature [55,59]. However, these models demonstrate that the dynamic administration of drugs influences their cytotoxic impact on PDAC spheroids [55]. This enhances our understanding of drug uptake and distribution in tumor models by providing new insights into how dynamic dosing regimens can improve treatment responses. Other chip models encompass patient-derived pancreatic tumor cells [60,62,63]. However, compared to our approach described here, these models also miss either an endothelial layer [60] or integrated immune cells [62,63]. The most complex PDAC model described so far was set up in a three-compartment chip with patient-derived PDAC organoids at the bottom, PSC in the middle and an endothelial tube at the top, which was perfused with peripheral blood mononuclear cells (PBMC) [58]. However, this model is missing a continuous flow.

Here, we report a novel PDAC-on-chip model incorporating relevant hallmarks of the desmoplastic and immunosuppressive TME allowing dynamic drug administration as well as immune cell infiltration *via* a continuous flow. This microfluidic biochip model combines MCTS composed of PANC-1 cells and PSC with a newly designed biochip incorporating an endothelial layer of human umbilical vein endothelial cells (HUVEC). Despite of the existing shear stress, an intact vasculature in the presence of MCTS could be established, allowing drug delivery *via* the endothelial layer. We previously reported that treatment with vorinostat, an FDA-approved drug for cutaneous T-cell lymphoma (CTCL), also known as suberoylanilide hydroxamic acid (SAHA),[64] displays a cytotoxic effect on 3D PDAC spheroids generated from PANC-1 cells and PSC [65]. Here, we show that treatment with vorinostat delivered *via* a continuous flow through an endothelial layer composed of HUVEC reduced spheroid viability, while not significantly compromising the integrity of the endothelial layer. Additionally, our system is amenable to study immune cell infiltration as demonstrated by perfused

monocytes which successfully infiltrated the spheroids and differentiated into macrophages. The polarization into M2 macrophages started 96 h after the infiltration and lasted for at least 168 h.

Experimental

Biochip design and fabrication

Biochips were manufactured by Dynamic42 GmbH (Jena, Germany) from injection-molded polybutylene terephthalate (PBT) base bodies. The biochip harbors two chambers each consisting of 3 vertically stacked channels (top = TOP, middle = MID, bottom = BOT) equipped with individual inlets and outlets in luer-format. Channels on the top and the bottom side of the biochip are sealed by a poly carbonate (PC) bonding foil and separated on the inside from MID channel by porous membranes which serve as culture surface for cells. The total channel volumes, including inlets and outlets, are 290 µL (TOP), 390 µl (MID) and 270 µL (BOT). The interfacing membrane of top to middle channel is made of 12 µm thick polyethylene terephthalate (PET) with 8 µm pores at a density of 1×10^6 cm^{-2} (Sabeu, Radeberg, Germany) and has a surface area of 1.32 cm^2. The second interfacing membrane from the middle to the bottom channel is made of PC with 2 µm pores at a pore density of 1×10^6 cm^{-2}, and has a surface area of 0.61 cm^2 and is imprinted with 25 microcavities with a diameter of 800 µm (300 Microns, Karlsruhe, Germany).

Cell culture

The PANC-1 cell line, acquired from the American Type Culture Collection (ATCC), was cultured in Dulbecco's modified Eagle's medium (DMEM) (#41965039, Gibco Grand Island, NY, USA) supplemented with 10% fetal bovine serum (FBS) (#10270-106, Gibco), and 1% penicillin–streptomycin (pen-strep) (#15140122, Gibco). PSC were provided by Dr. Erkan of Koç University Hospital in Turkey. The ethics committee for the biomedical sciences at KOÇ University granted ethical approval, and all patients consented in writing. PSC were obtained from patients diagnosed with ductal adenocarcinoma, and cultured in DMEM/F12 (#11320074, Gibco) with 20% FBS and 1% pen–strep under aseptic conditions. HUVEC (University Hospital, Jena, Germany) were cultured in ECGM (# CC-3156, Lonza, Basel, Switzerland) supplemented with ECGM SingleQuots (#CC-4176) and 1% pen–strep. All cell types were incubated at 37 °C with 5% CO_2.

Isolation of monocytes

Peripheral blood mononuclear cells (PBMC) were isolated from buffy coats, obtained from anonymized healthy donors (Düsseldorf University Hospital, Germany) approved for *in vitro* research, using the Ficoll-Paque density gradient method. The buffy coats were mixed with D-PBS and layered on top of Histopaque (#10771, Sigma-Aldrich). After centrifugation at 850 × *g* for 20 minutes (with 0 acceleration and deceleration) a ring of PBMCs was obtained. PBMCs were collected and incubated for 10 minutes in ammonium chloride solution for red blood cell lysis. After washing with D-PBS the cell number was determined. $CD14^+$ monocytes were isolated from PBMC by magnetic activated cell sorting (MACS) using monocyte-specific anti-CD14 monoclonal antibodies conjugated to paramagnetic microbeads (#130-097-052, Miltenyi Biotec, Bergisch Gladbach, Germany) according to the manufacture's protocol and the MidiMACS separator (#130-042-302, Miltenyi Biotec). Monocytes were cultured in RPMI (#21875-034, Gibco) supplemented with 10% FBS and 1% pen–strep at a concentration of 1×10^6 cells per mL.

Spheroid formation

The generation of co-culture spheroids, consisting of PANC-1 and PSC cells, was performed as previously described by Xie *et al.* [45]. Briefly, 1×10^4 cells per mL PANC-1 cells and 2×10^4 cells per mL PSC were combined in DMEMF12. Collagen-I (#A1048301, Gibco, Waltham, MA USA) was added to a final concentration of 0.1 mg mL^{-1}. The cell suspension was transferred to an ultra-low attachment coated 96-well plate (#650970, Greiner Bio-One) and cultivated at 37 °C and 5% CO_2. For the generation of PANC-1 spheroids 1500 PANC-1 cells in 50 µL DMEM with 2.5% (v/v) Matrigel (#356230, Corning, NY, USA) were added into a well of an ultra-low attachment coated 96-well plate (#650970, Greiner Bio-One) and centrifuged at 1500 rpm for 5 min. Spheroids were transferred into the biochip 4 days after seeding.

HUVEC cultivation in and integration of 3D spheroids into the chip

The membrane in the TOP channel was coated with collagen-I (#A1048301, Gibco, Waltham, MA USA). 150 000 HUVEC were seeded on the coated membrane in the TOP channel. Following daily media exchange with 250 µL EGM-2 in the TOP channel, HUVEC were cultivated for 4 days in the chip. 4 days old spheroids were collected in a 1.5 mL tube. A minimum of 20 spheroids were loaded into the microcavities of the

MID channel. The spheroids were cultivated on the biochip in 70% EGM-2 mixed with 30% DMEMF12 and 2.5% (v/v) Matrigel.

Perfusion of the biochip

For perfusion of the biochip the TOP and BOT channel of the biochip were individually connected *via* tubing to a peristaltic pump (Ismatec™ IPC 4 Peristaltic Pump, # ISM930A, Masterflex, Barrington, IL, USA). Each tubing system includes a PHarMed BPT thermoplastic elastomer 2-stop tube (ISMATEC, Wertheim, Germany), filled with 250 µL medium and a medium reservoir (MoBiTec, Göttingen, Germany), filled with 750 µL of medium. The TOP and the BOT channel were perfused with a flow rate of 25 µL min^{-1} for 72 h at 37 °C and 5% CO_2. The MID channel harbouring tumor spheroids was non-perfused and closed using standard luer-plugs (Mobitec, Göttingen, Germany).

Cell viability

The CellTiter-Glo® 3D cell viability assay (#G9681, Promega, Madison, WI, USA) was used to analyze the cell viability of 3D spheroids. Cell viability of HUVEC, PANC-1 and PSC cell, was determined using the PrestoBlue HS Cell Viability Assay (#P50201, Thermo Scientific, Waltham, MA, USA) 10 000 HUVEC, 5000 PANC-1 and 2000 PSC were seeded per well in 96-well plates (#655090, Greiner Bio-One). Compound treatment was performed 24 h after seeding, for 72 h. Fluorescence values were recorded using the Tecan SPARK instrument (Tecan Group, Switzerland).

Immunofluorescence (IF) staining of the HUVEC layer

The biochip was cut open on the TOP side and the interfacing membrane between TOP and MID channel was detached from the chip using a standard lab scalpel (#11566, Swann Morton, Sheffiel, United Kingdom) and placed in a well of a 24-well plate prefilled with 500 µL D-PBS. The membrane was fixed for 15 minutes with 4% paraformaldehyde (PFA) (#0964.1, Sigma-Aldrich, Saint Louis, MI, USA) solution (in D-PBS) and then blocked for 30 minutes with 0.1% saponin and 3% normal donkey serum (NDS) in D-PBS at room temperature (RT). The membrane was incubated overnight at 4 °C with 50 µL of primary antibody solution (VE-cadherin (# AF938, R&D Systems), von Willebrand factor (#A0082, Agilent, Santa Clara, CA, USA)). The secondary antibody solution (Alexa Fluor 546 (donkey anti-rabbit antibody, Invitrogen), Alexa Fluor 488 (donkey anti-goat antibody, Invitrogen, Waltham, MA, USA), 2 µg

mL^{-1} DAPI (#D9542, Sigma-Aldrich,)) was prepared in PBS containing 0.1% saponin and 3% NDS, and the membrane was incubated in 50 µL in the dark for 1 hour at RT. The membrane was mounted on a glass slide with fluorescence mounting medium (#GM30411-2, Agilent Technologies, Santa Clara, CA, USA), dried overnight and imaged with the CQ1 High-Content Spinning Disk System (part number 90ZA00673, Yokogawa, Tokyo, Japan). The cell viability staining was performed according to manufacturer instructions using the Viability Kit (#L3224, Invitrogen, Carlsbad, CA, USA). Briefly, HUVEC on the membrane were incubated for 30 min in PBS containing calcein-AM and ethidium homodimer-1. Afterwards, the membrane was washed with PBS and fixed with 4% PFA. The membrane was mounted on a glass slide with fluorescence mounting medium, dried overnight and imaged with the CQ1 High-Content Spinning Disk System (Part Number 90ZA00673, Yokogawa).

Immunofluorescence staining of spheroids

Spheroids were collected with a pipette from the biochip after 72 h and stained according to the MACS clearing Kit (#130-126-719, Miltenyi Biotec). Briefly, the spheroids were fixed with 4% PFA for 1 hour at RT. Following 6 h of permeabilization the spheroids were incubated with 100 µL of primary antibody solution (Human Ki67/MKI67 (#MAB7617, R&DSystems, Minneapolis, MN, USA), α-SMA (#19245S, Cell Signal, Danvers, MA, USA), pan-cytokeratin (#130-133-439, Miltenyi Biotec), CD45 (#130-110-638, Miltenyi Biotec), CD163 (#130-112-286, Miltenyi Biotec)) for 24 h at 4 °C. The secondary antibody solution (Alexa Flour 647 donkey (H + L) anti-mouse (#A-31571, Invitrogen), Alexa Flour 488 donkey (H + L) anti-rabbit (#A-21206, Invitrogen)) including 2 µg mL^{-1} DAPI (#D9542, Sigma-Aldrich) was incubated at 4 °C for 24 h. The clarification process was carried out by successive incubation in three ethanol solutions of increasing concentration (50%, 70% and 100%), each containing 2% Tween. The incubation was initially carried out for 2 h each (for the 50% and 70% ethanol concentrations) and finally in the presence of 100% ethanol overnight. The final step was clearing for 6 h with the clearing solution. Afterwards, the spheroids were transferred to an imaging plate (# 89626, ibidi GmbH) and imaged with the CQ1 High-Content Spinning Disk System (Part Number 90ZA00673, Yokogawa). 3D images were visualized using the 3D viewer plugin [66] in in the Fiji Software [67].

Quantitative real-time PCR (qRT-PCR)

To determine the cytokine expression of PANC-1, PSC, co-culture spheroids and PANC-1 spheroids a qRT-PCR was performed. The following primers were utilized to determine the mRNA levels of TNF-α, IL-8 and IL-6: glyceraldehyde-3-phosphate dehydrogenase (GAPDH) (forward, 5′-TGCACCACCAACTGCTTAGC-3′; reverse, 5′-GGCATGGACTGTGGTCATGAG-3′), TNF-α (forward 5′-CCCTGCTGCACTTTGGAGTG-3′; reverse 5′-CGGGGTTCGAGAAGATGAT-3′), IL-6 (forward 5′-GGCACTGGCAGAAAACAACC-3′; reverse 5′-GCAAGTCTCCTCATTGAATCC-3′), and IL-8 (forward 5′-ACTGAGAGTGATTGAGAGTGGAC-3′; reverse 5′-AACCCTCTGCACCCAGTTTTC-3′). PANC-1, PSC, co-culture spheroids and PANC-1 spheroids were cultivated for 72 h in 3D medium. The qRT-PCR was performed as previously described by us.[65] The ΔΔCt method was used to calculate the Ct values. Sample data were normalized to the housekeeping gene GAPDH. Quantitative analysis was conducted using qPCRsoft 4.1 software (Analytik Jena, Jena, Germany).

Permeability characterization of the HUVEC layer

Fluorescein isothiocyanate–dextran (FITC–dextran, Merck) with an average molecular weight of 3–5 kDa was used to assess the barrier permeability of the HUVEC layer. Therefore, medium in both channels was replaced by prewarmed PBS. A volume of 250 µL 0.1 mg mL^{-1} FITC–dextran solution in PBS was added in the TOP channel. The chips were incubated for 1 h at 37 °C and 5% CO_2 allowing FITC–dextran to permeate through the cell layer. After the incubation the solutions from the TOP, MID and BOT channel were collected separately and transferred into a 96 well plate. All steps were performed protected from light. The fluorescence values were measured with the Tecan SPARK instrument (Tecan Group, Switzerland). FITC–dextran concentrations were calculated from a standard curve obtained from the 0.1 mg mL^{-1} stock solution.

Drug adsorption

A circular perfusion setup consisting of tubing and a 1 mL reservoir was connected to both the upper and lower channel of an empty, sterilized and coated biochip. All channels, tubing and reservoirs were filled with ECGM containing indicated levels of vorinostat and 1 : 1000 DMSO. Upper and lower channel were perfused with 25 µl min^{-1}, at 37 °C and 5% CO_2. After 24 h media in the perfusion setup was pooled and

vorinostat levels were quantified using LCMS. Controls were incubated for 24 h at 37 °C in glass vials.

LCMS analysis

Ultra-high-performance liquid chromatography (LCMS) coupled with high resolution mass spectrometry was carried out using a Thermo (Bremen, Germany) UltiMate HPG-3400 RS binary pump, WPS-3000 auto sampler which was set to 10 °C and which was equipped with a 25 µL injection syringe and a 100 µL sample loop. The column was kept at 25 °C within the column compartment TCC-3200. Chromatography column Thermo Accucore® C-18 RP (100 × 2.1 mm; 2.6 µm) was run at a constant flow rate of 0.4 mL min^{-1} using a gradient (ESI‡ Table S1) (time in min/concentration eluent B in %) – 0/0; 0.2/0; 8/100; 11/100; 11.1/0; 12.0/0 (ESI‡ Table S1). Eluent A was water, with 2% acetonitrile and 0.1% formic acid. Eluent B was pure acetonitrile.

Mass spectra were recorded with Thermo QExactive plus orbitrap mass spectrometer coupled to a heated electrospray source (HESI). Column flow was switched at 0.5 min from waste to the MS and at 11.5 min again back to the waste, to prevent source contamination. For monitoring two full scan modes were selected with the following parameters. Polarity: positive; scan range: 100 to 1500 *m*/*z*; resolution: 70 000; AGC target: 3×10^6; maximum IT: 200 ms. General settings: sheath gas flow rate: 60; auxiliary gas flow rate 20; sweep gas flow rate: 5; spray voltage: 3.0 kV; capillary temperature: 320 °C; S-lens RF level: 90; auxiliary gas heater temperature: 400 °C; acquisition time frame: 0.5–11.5 min. For negative mode, all values were kept instead of the spray voltage which was set to 2.5 kV.

Flow cytometry of infiltrated macrophages

The time course of the polarization of monocytes after infiltration into the co-culture spheroids was analyzed with flow cytometry. For this, co-culture spheroids were collected 24 h, 48 h, 72 h, 96 h, and 168 h after infiltration with PBMC-derived monocytes. After spheroid digestion with Accutase (#A1110501, Gibco), the cells were stained with the following antibodies according to manufactures instructions; CD163-PE (#130-112-286, Miltenyi Biotec), CD11b-VioBlue (#130-110-616, Miltenyi Biotec), CD86-APC (#130-116-161, Miltenyi Biotec), CD45-VioGreen (#130-110-638, Miltenyi Biotec), HLA-DR-PEVio770 (#130-111-944, Miltenyi Biotec). Flow cytometry was performed using the CytoFlex (Beckman-Coulter, Brea, CA, USA) flow cytometer. The

data were analysed with the CytExpert software (version 10.10.0, Beckman-Coulter, Brea, CA, USA).

Statistical analysis

For statistical and graphical analysis, the GraphPad Prism 8.4.3 software (GraphPad Software, Boston, MA, USA) was used. The IC_{50} values were determined by non-linear regression to assess cell viability. One-way analysis of variance (ANOVA) and unpaired *t*-test were used to test the statistical data, with *p*-values ≤ 0.05 considered statistically significant.

Results and discussion

Design of the PDAC on chip model

The Dynamic42 BC003 biochip was developed for organ-on-chip applications integrating spheroids or organoids in a perfused system. Designs were fine-tuned for injection moulding using the CAD software SolidWorks. Each biochip consists of two independent chambers (Figure 3.2-1A). Individual chambers are comprised of three vertically stacked channels which can all be separately loaded and perfused using the respective inlets and outlets (Figure 3.2-1A and B). Channels are separated by two porous membranes with the lower membrane carrying 25 microcavities with a diameter of 800 µm for spheroid insertion. Channel dimensions of MID channel are at least 1 mm throughout the whole biochip to support non-destructive spheroid loading of spheroids up to 800 µm in diameter. In the PDAC setup, a confluent layer of HUVEC is generated on the membrane in the TOP channel and perfused at 25 µL min^{-1} to mimic the vascular flow (Figure 3.2-1B-D). A minimum of 20 PDAC-spheroids are inserted into the microcavities of the MID channel, which is then sealed with plugs. The microcavities of the MID channel project into the BOT channel. The BOT channel is also perfused at 25 µL min^{-1} to improve nutrient availability for spheroids. Importantly, spheroids are shielded from flow and shear forces by the porous microcavity membrane. Reservoirs are inserted into both perfused inlets to keep cell culture medium available and to simultaneously serve as bubble traps.

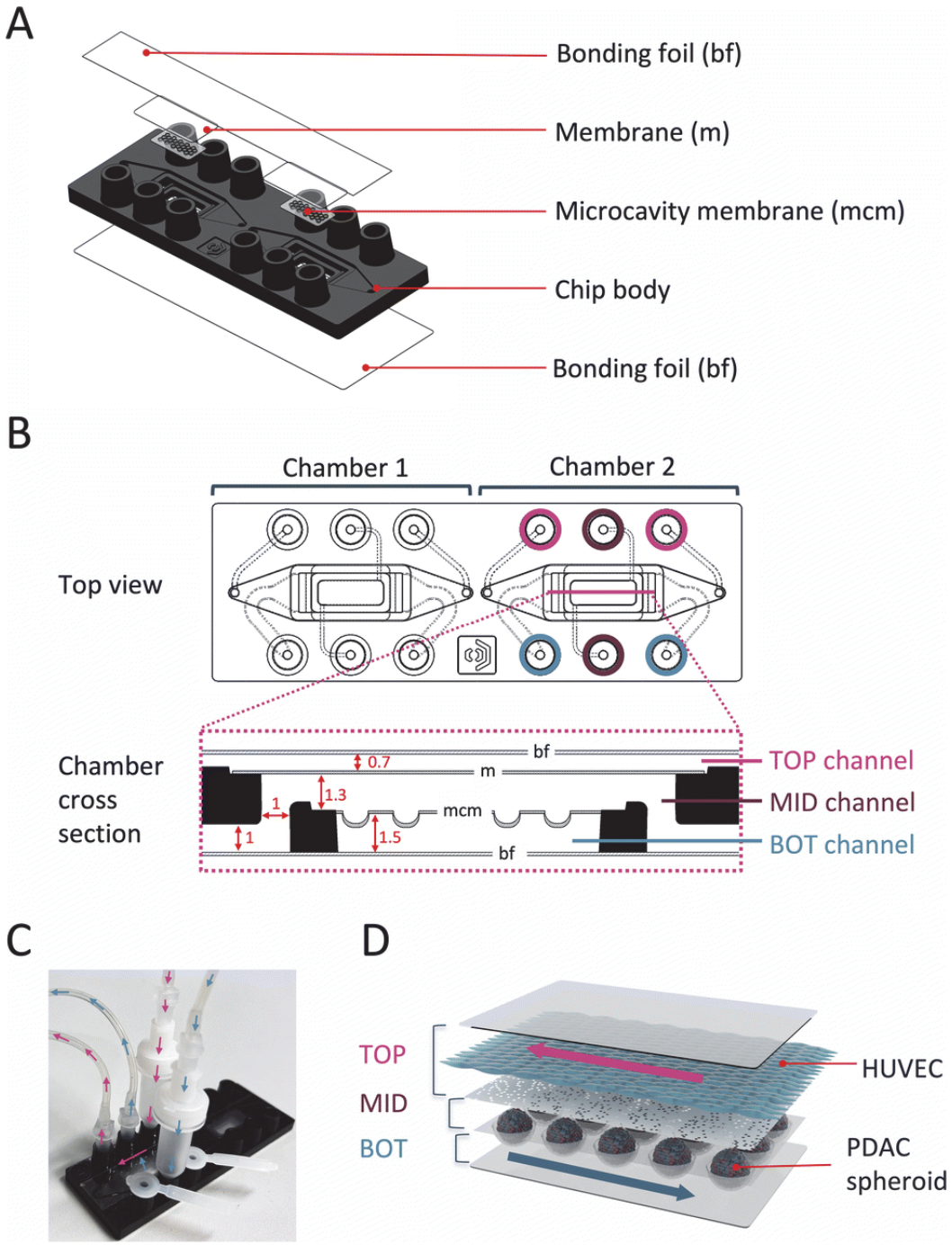


Figure 3.2-1 Design of the biochip. (A) Exploded view of the chip (B) translucent view of the chip. The upper panel shows the TOP view with underlying channels in dotted lines. Coloured circles indicate the location of ports for TOP (TOP), middle (MID) and bottom (BOT) channels. The lower panel shows a cross section of a chamber at the indicated position. The position of the bonding foil (BF), the membrane pore size of 8 µm (M) and microcavity membrane pore size of 2 µm (MCM) are indicated. Red numbers depict the channel height at the bottlenecks (red arrows) in millimeters. (C) Perfusion setup for the PDAC model. The tubing connects ports of the TOP and the BOT channel to create two independent perfusion circles. The MID channel is sealed. Arrows indicate the media flow direction in the TOP (magenta) and

the BOT (blue) channel during perfusion. (D) Schematic illustration of the PDAC model. Arrows depict the flow direction in the TOP (magenta) and the BOT (blue) channel.

The potential of adsorption of small molecules is a challenge in many biochip systems due to their large surface area, additional tubing systems and non-favourable biochip base body material [68]. To test drug retention in the biochip made of PBT and described here, media containing 0.5–10 µM of vorinostat was either perfused through the TOP and BOT channel of the biochip or incubated in glass vials. After 24 h, the vorinostat concentration in the perfused chip was determined by LCMS. Notably, irrespective of the starting concentration, perfused and non-perfused controls did not show any significant loss of vorinostat levels over input, confirming that vorinostat is neither degraded in nor adsorbed to the biochip surface (Table 3.2-1).

Table 3.2-1 Absorption data of vorinostat in the biochip

Starting concentration vorinostat [µM]	**Measured vorinostat concentration [µM] after 24h in the biochip**
0.5	0.693 ± 0.094
1	1.017 ± 0.191
5	5.131 ± 0.109
10	10.149 ± 0.182

Spheroid viability in the biochip

To analyze potential effects on the viability of PDAC spheroids cultivated in the biochip under continuous or controlled perfusion, a total of 25 PDAC mono- or co-culture spheroids were loaded into the respective microcavities within the MID channel (Figure 3.2-2A). Immunofluorescence staining confirmed that PANC-1 mono-spheroids and co-culture spheroids maintain their structure in the biochip, with the latter keeping its subcellular composition of a fibrotic shell of PSC surrounding a core of PANC-1 cells [45] (Figure 3.2-2B). Evaluating spheroid viability after 72 h of cultivation without a continuous flow (so-called “static condition”) revealed a decrease in viability by 44% in the co-culture spheroids and by 59% in the PANC-1 spheroids in the biochip compared to a cultivation setting in a 96-well plate (Figure 3.2-2C). Importantly, the viability of the PDAC spheroids significantly increased under flow conditions in the chip from 56% to 78% in co-culture spheroids and from 41% to 91% in PANC-1 spheroids, respectively.

Notably, a direct viability comparison of spheroids cultured in the presence of a continuous flow of 25 µL min^{-1} and spheroids cultured in 96-well plate still revealed a significant decrease in cell viability in co-culture spheroids of 22% but only a slight decrease in PANC-1 spheroids of 9%. The reduced viability observed under static conditions on the chip may be attributed to the spheroid-to-medium volume ratio, the MID channel contains 250 µL of medium for 25 spheroids, equating to 10 µL per spheroid, in contrast to the 100 µL per spheroid provided in the microtiter plate conditions. A total of 1500 µL of medium is supplied through the MID channel and the perfusion system in the BOT channel for 25 spheroids, amounting to 60 µL per spheroid. In conclusion, this indicates that our microfluidic system provides efficient nutrient supply and is suitable for the cultivation of both spheroid types under microfluidic conditions.

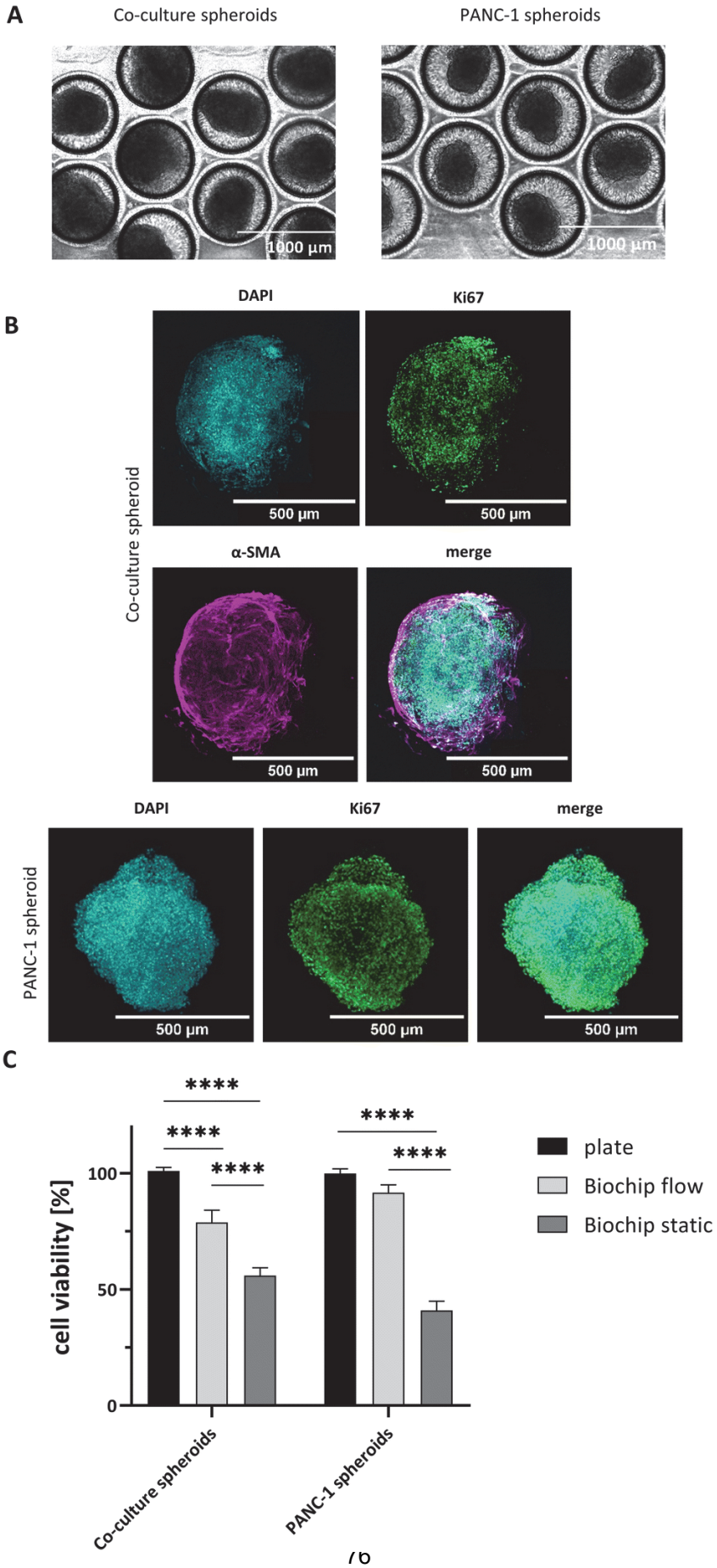

A
Co-culture spheroids
PANC-1 spheroids
1000 µm
1000 µm
B
DAPI
Ki67
Co-culture spheroid
500 µm
500 µm
α-SMA
merge
500 µm
500 µm
DAPI
Ki67
merge
PANC-1 spheroid
500 µm
500 µm
500 µm
C
****
****
****
****
****
cell viability [%]
100
50
0
plate
Biochip flow
Biochip static
Co-culture spheroids
PANC-1 spheroids

Figure 3.2-2 Cultivation of spheroids on the biochip. (A) Co-culture spheroids and PANC-1 spheroids loaded into the microcavities of the biochip. Images are taken via bright field microscopy after loading of the spheroids. Scale is 1000 µm. (B) If staining of 3D PANC-1 and co-culture spheroids after 72 h cultivation on the biochip shown as maximum intensity projection (MIP) of a Z-stack. DAPI-staining of nuclei (blue); staining of the proliferation marker Ki67 (green); staining of fibroblast marker α-SMA (purple); merging of all three channels. Scale bar is 500 µm. (C) Investigation of cell viability of 3D spheroids after 72 h cultivation on biochip either under flow or static conditions in comparison to the cultivation in a 96-well plate. Error bars indicate the standard errors of the mean of at least three independent experiments, with **** = $p \leq 0.0001$.

Cultivation of HUVEC in the biochip

Tumor vascularization plays a pivotal role in facilitating immune cell infiltration, nutrient and oxygen supply and drug delivery [6]. Consequently, integrating a perfusable vasculature into *in vitro* TME models is essential for accurately recapitulating the *in vivo* vascular transport dynamics of immune cells, and drugs into the tumor [69]. As demonstrated in Figure 3.2-3, HUVECs were seeded into the TOP channel in the chip and cultured under static conditions for 4 days until full confluency was achieved. HUVECs were either cultivated for further 72 h in the presence of a continuous flow of 25 µL min^{-1} or without any flow. After 72 h of cultivation, under static or under flow conditions, a tight endothelial barrier was established, as confirmed by the expression of the endothelial markers Willebrand factor (vWF) and adherence junction marker vascular endothelial (VE-) cadherin (Figure 3.2-3). Furthermore, assessment of the macromolecular permeability of the endothelial layer (Supplementary Figure 3.2-1) revealed that the barrier permeability is not influenced by cultivation under flow conditions. In the presence of co-culture spheroids and under flow conditions, the endothelial cells failed to maintain a tight endothelial layer (Supplementary Figure 3.2-2) whereas the endothelial layer remained unaffected under static conditions (Supplementary Figure 3.2-2) suggesting that the increased viability of the spheroids under flow conditions sensitize endothelial cells to cells stress. Previous studies show that the expression of the proinflammatory cytokines TNF-α, IL-8 and IL-6, which are also secreted by co-culture spheroids (Supplementary Figure 3.2-3) might impact endothelial adherence [58]. Indeed, the addition of conditioned medium obtained from the supernatant of co-culture spheroids resulted in an increase of loose connections between the HUVEC cells (Supplementary Figure 3.2-4), arguing that spheroids secrete soluble factors, like TNF-α, IL-8 and IL-6 (Supplementary Figure 3.2-3), which impair the HUVEC layer integrity under flow conditions.

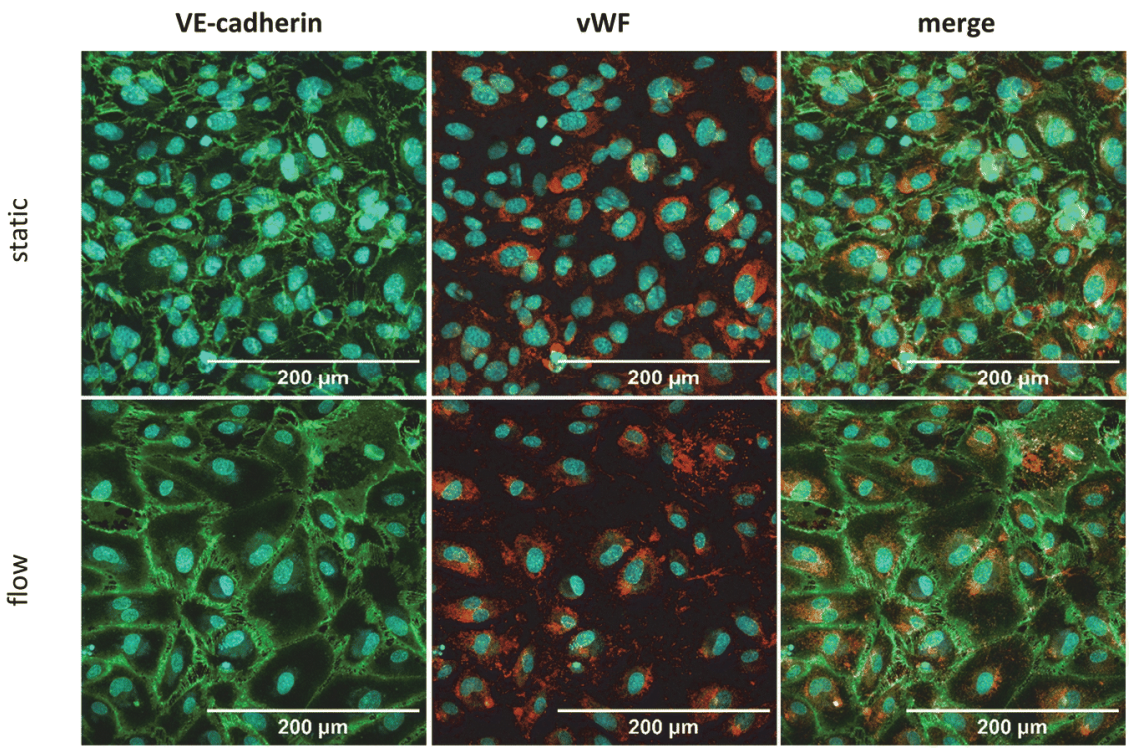


Figure 3.2-3 Cultivation of HUVEC on the biochip. HUVEC were cultivated for 72 h under static (upper row) or flow (bottom row) conditions. The endothelial markers VE-cadherin (green), von Willebrand factor (vWF) (red) and the nuclear dye DAPI (blue) were stained. Shown as MIP of a Z-stack. Scale bar is 200 µm.

Massive ECM secretion by CAF within the PDAC TME creates a dense and stiff mechanical barrier around the tumor cells [69]. Absence of such barrier might enhance negative effects of the tumor on the endothelium. To recreate this mechanical barrier in our model, 2.5% Matrigel was introduced into the MID channel embedding the spheroids. In addition, as illustrated in Figure 3.2-4, the incorporated Matrigel restored vascular stability under perfusion in the presence of both, co-culture spheroids and PANC-1 spheroids (Figure 3.2-4). Furthermore, a quantitative permeability assessment of the HUVEC layer confirms that the addition of Matrigel significantly restored the barrier permeability under flow conditions (Supplementary Figure 3.2-1). These results are in line with other PDAC-on-chip platforms with incorporated HUVEC-based vasculature, which also achieved an intact endothelial layer by embedding the tumor cells or organoids in Matrigel [58,63,70].

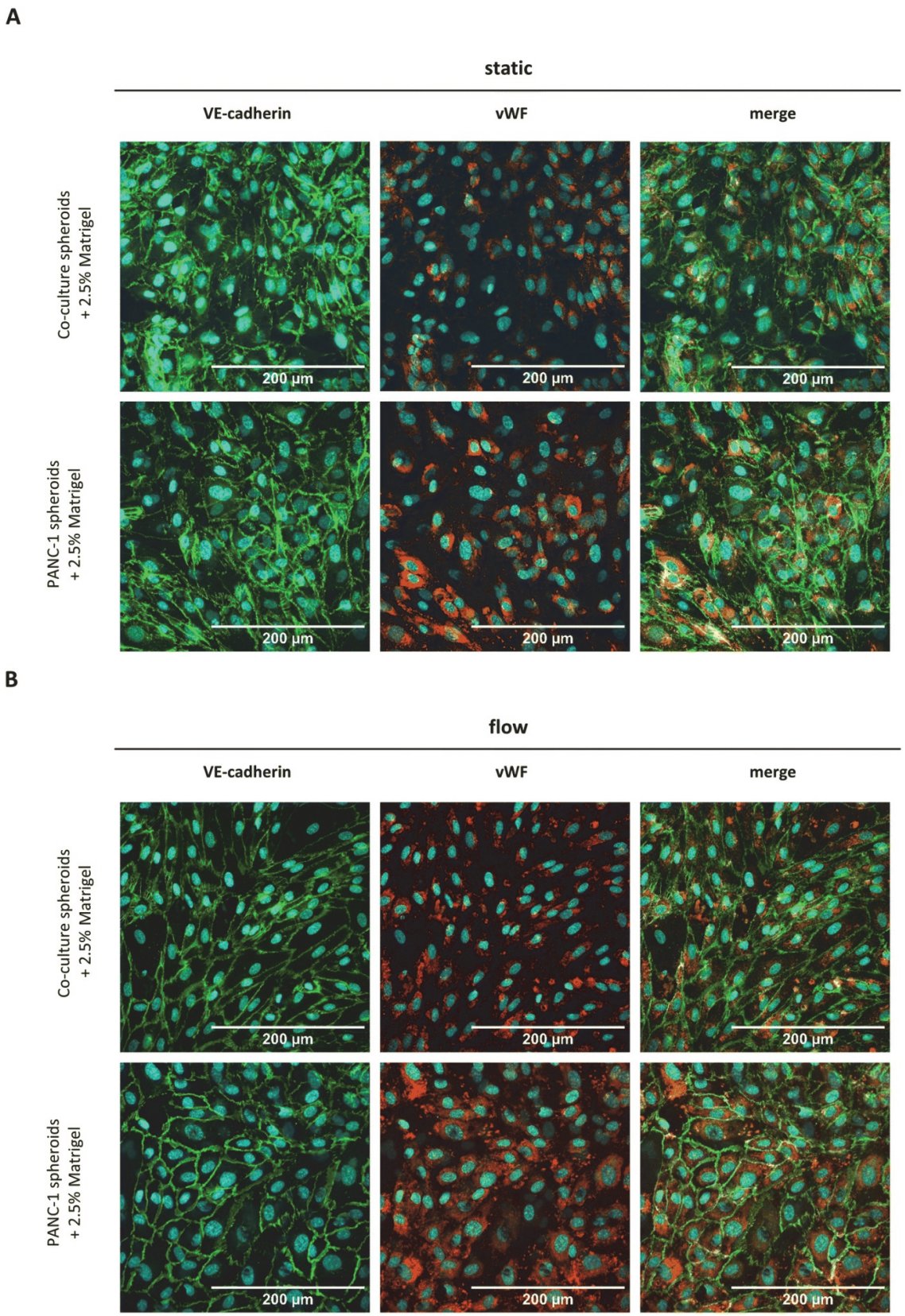


Figure 3.2-4 Rescue strategy for HUVEC layer in the presence of pdac spheroids. The vasculature remains stable under static (A) and flow (B) with an addition of 2.5% matrigel both in the presence of co-culture spheroids (upper row) as well as in the presence of PANC-1 spheroids (bottom row). Stained

the endothelial markers VE-cadherin (green), von Willebrand factor (vWF) (red) and the nuclear dye DAPI (blue) were stained. Shown as MIP of a Z-stack. Scale bar is 200 µm.

Proof-of-concept for a dynamic drug administration

A dynamic application of drugs through a microfluidic system offers an improved simulation of the *in vivo* drug transport and can significantly influence treatment responses, as initially demonstrated for PDAC by Schuster et al. [55]. The histone deacetylase inhibitor vorinostat, approved for the treatment of CTCL, exhibits cytotoxic effects on cells that overexpress class I histone deacetylases (HDACs) and HDAC6 [64]. This effect has been demonstrated across various malignancies, including pancreatic ductal adenocarcinoma (PDAC), [71] while sparing healthy cells [64]. As demonstrated by our previous work, the histone deacetylase inhibitor vorinostat, also known as suberoylanilide hydroxamic acid (SAHA), exhibits a cytotoxic effect on co-culture spheroids with an IC_{50} value of 0.85 µM [65]. In contrast, an IC_{50} value of 5.7 µM was determined for HUVECs (Supplementary Table 3.2-2). This cell type dependent efficacy difference opens a treatment window for targeting 3D PDAC spheroids without affecting the viability of endothelial cells. Thus, concentrations of 1.5, 2.5 or 3.5 µM SAHA were introduced *via* a flow of 25 µL min^{-1} in the TOP channel. After a treatment period of 72 h, the vasculature integrity (Figure 3.2-5A) and the co-culture spheroids viability (Figure 3.2-5B) were assessed, respectively. Analysis of the expression of the endothelial markers VE-cadherin and vWF indicated that the integrity of the endothelial layer was unaffected at SAHA concentrations up to 2.5 µM (Figure 3.2-5A). These results were verified by a live dead staining of the HUVEC layer (Supplementary Figure 3.2-5) and a barrier integrity test (Figure 3.2-5C), confirming no significant increase in FITC dextran leakage upon treatment with 1.5 or 2.5 µM SAHA, but a slight leakage increase of 11.5% compared to 9.9% for the untreated control after treatment with 3.5 µM SAHA. In contrast to its impact on endothelial cells, SAHA treatment significantly impaired the viability of the co-culture spheroids by 41% or 49% at concentrations of 2.5 µM and 3.5 µM, respectively (Figure 3.2-5B). In conclusion, our model allows administration of drug candidates *via* an intact vasculature under flow conditions while significantly and selectively effecting spheroid viability.

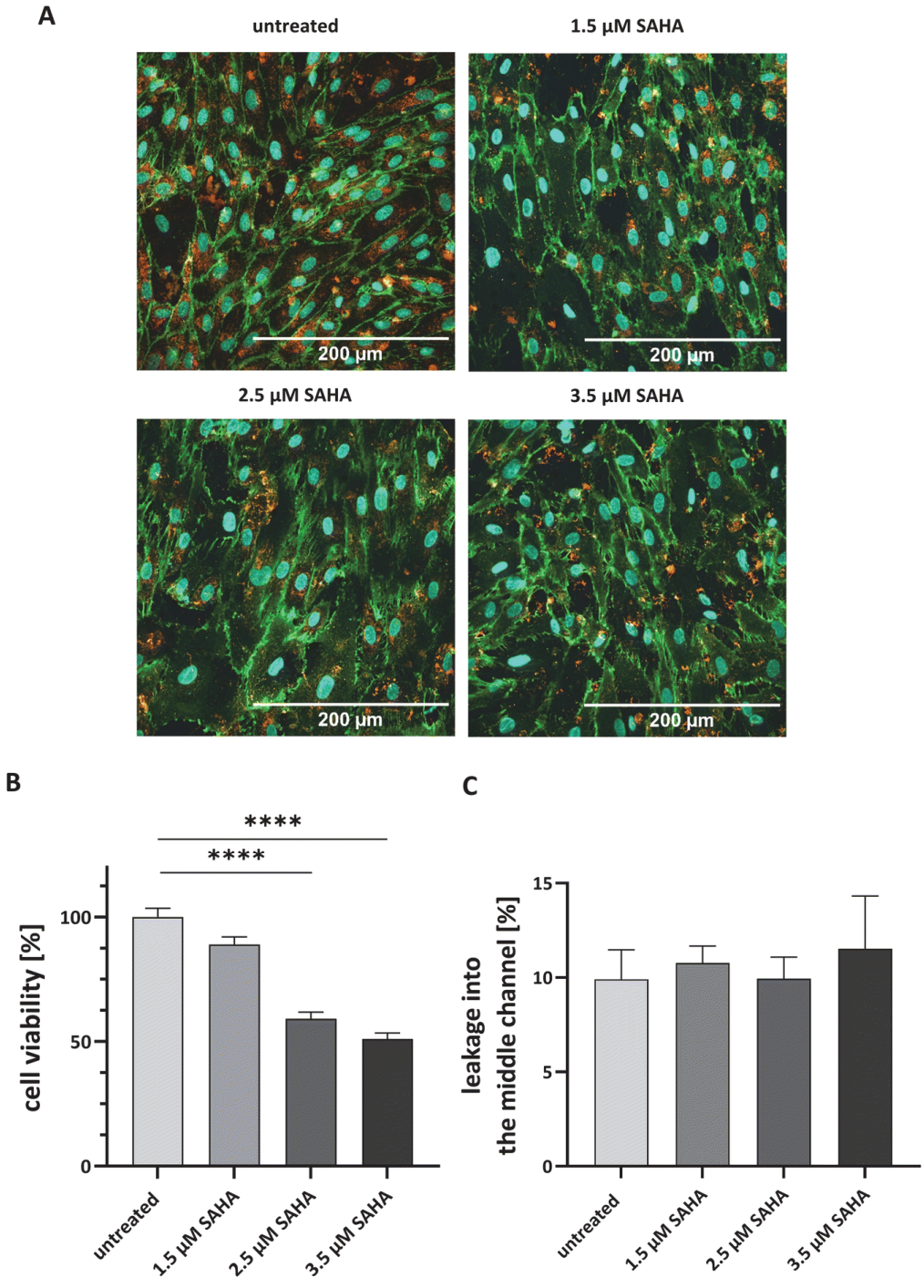


Figure 3.2-5 Dynamic administration of the HDAC inhibitor SAHA in the PDAC biochip model. (A) Investigation of the influence of increasing SAHA concentrations on the vasculature integrity. VE-cadherin (green), von Willebrand factor (red) as marker of the endothelial cells, DAPI for staining the cell nuclei (blue). Shown as MIP of a Z-stack. Scale 200 µm. (B) Investigation of the viability of the 3D PDAC spheroids in the biochip in the presence of SAHA after 72 h administration (with **** = $p \leq 0.0001$). (C) Permeability assay of HUVEC layer after treatment with SAHA for 72 h. FITC dextran assay was performed to measure the barrier integrity of the HUVEC layer after 72 h treatment with 1.5, 2.5, or 3.5 µm SAHA. FITC dextran solution was added into the top channel. After 1 h the leakage into the mid channel was determined via fluorescence measurement.

Integration and spatial distribution of macrophages

TAM which have been shown to be significantly associated with a poor overall survival rate in PDAC patients [72] are described as $CD163^+$ M2-polarized [19]. Overall, $CD163^+$ M2 macrophages represent an immunosuppressive and pro-fibrotic cell type [19] that is also reported to release mediators which activate different pathways in tumor cells like PI3K/Akt, JAK/STAT or others, subsequently contributing to chemoresistance [27,73,74]. Since TAM polarization is the result of the crosstalk between tumor cells and CAF through the secretion of different signaling molecules, like IL-4, TGF-β, or M-CSF, [19,25,74] we integrated PBMC-derived monocytes into our PDAC biochip model to investigate the polarization into TAM.

To this end, we perfused primary PBMC-derived monocytes for 72 h through the top channel of the biochip. As shown by the positive signal of the leucocyte marker CD45 (Figure 3.2-6A), the monocytes significantly infiltrated the co-culture spheroids (Figure 3.2-6A). Notably, primary monocytes also infiltrate PANC-1 spheroids, where they distribute evenly in the whole spheroid (Supplementary Figure 3.2-6). Furthermore, analysis of CD163 expression of integrated monocytes indicate that PDAC spheroids polarize integrated macrophages towards an M2 phenotype. Indeed, when compared to unstimulated monocytes, expression of CD163 increased by 1.9-fold within 72 h of infiltration of co-culture spheroids under flow (Figure 3.2-6B). Notably, polarization persisted in the co-culture spheroids for up to 168 h as indicated by CD163 upregulation (Supplementary Figure 3.2-7). Simultaneously, the M1 markers CD86 and HLA-DR are significantly downregulated when compared to monocytes before infiltrating the spheroids (Figure 3.2-6B) indicating the that the polarization is triggered by the integration. These results are in line with the findings from Madsen *et al.* (2021) [49].

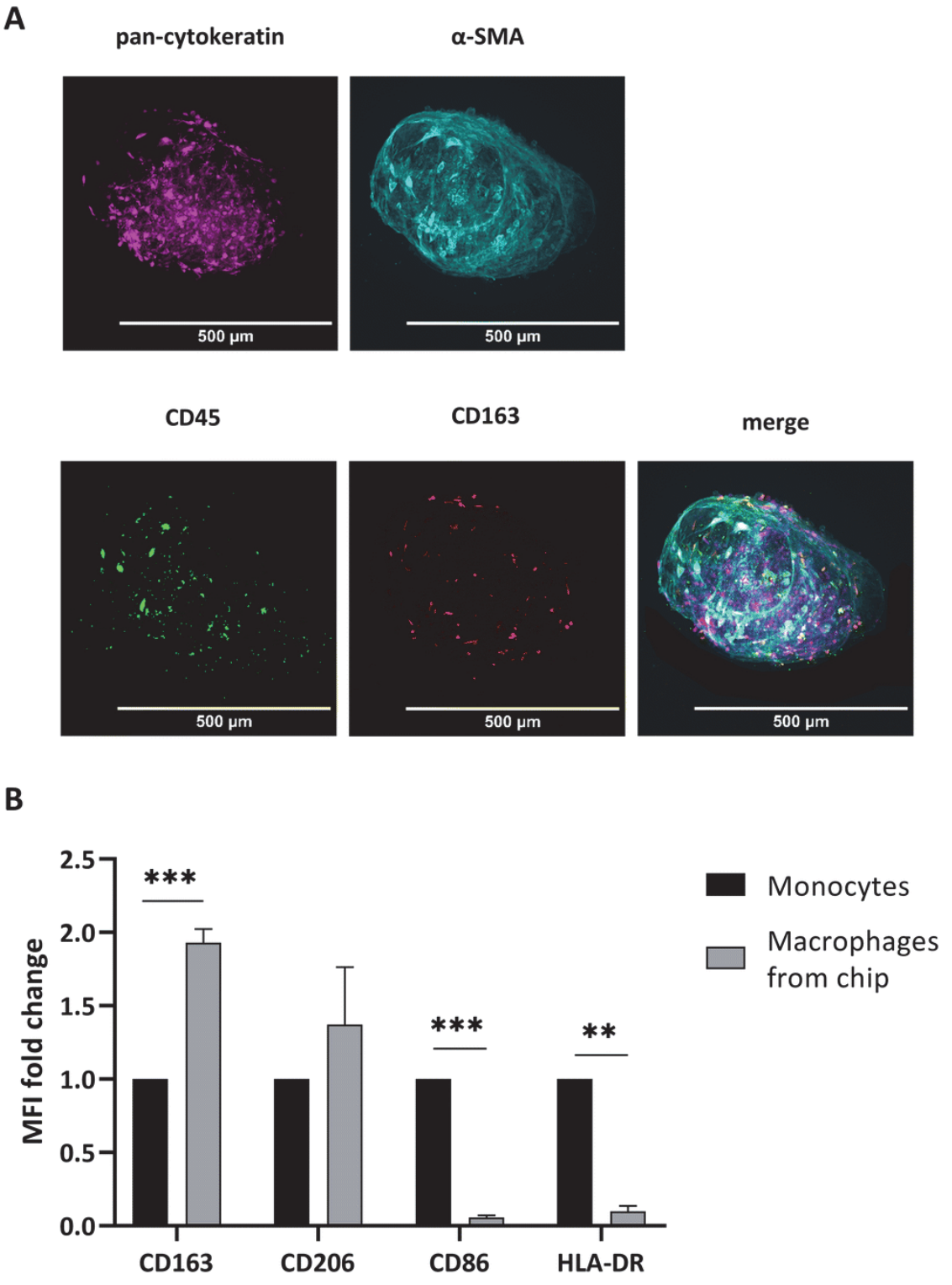


Figure 3.2-6 Polarization of monocytes after perfusion in the biochip. (A) If staining of co-culture spheroids after perfusion with primary monocytes over the endothelial layer. Co-culture spheroids were seeded into the biochip and primary monocytes were perfused over the endothelial layer in the TOP channel. After 72 h of perfusion the co-culture spheroids were stained for the tumor cell marker pan-cytokeratin (purple), the fibroblast marker α-SMA (blue), the immune cell marker CD45 (green), and the M2 marker CD163 (red); merging of all four channels. Shown as MIP of a Z-stack. Scale bar is 500 µm. (B) Marker characterization of polarized macrophages. Polarization after infiltration into co-culture spheroids was analyzed by flow cytometry 72 h after perfusion with monocytes in the biochip.

Macrophages identified as $CD11b^+$ and $CD45^+$ were analyzed for surface expression of CD163, CD206, CD86, and HLA-DR. Infiltrated cells were compared to unstimulated monocytes as controls. Error bars indicate the standard errors of the mean of three independent experiments, with ** = $p \leq 0.01$; *** = $p \leq 0.005$.

To investigate the spatial distribution of the infiltrated macrophages in the co-culture spheroids, a 3D image of a whole spheroid was generated and digitally divided into two halves (Figure 3.2-7A). As demonstrated in Figure 3.2-7 B and in the ESI† Video S1, the infiltrated macrophages preferably localize in the fibrotic shell part of the co-culture spheroids. These findings show, that our *in vitro* model despite of its simplicity is able to recreate the spatial distribution of macrophages in PDAC patients, where M2 macrophages are significantly enriched in the stromal part of the TME [75]. It is currently hypothesized that the secretion of multiple cytokines and chemokines, like IL-10, GM-CSF, IL-4 or IL-33 by pancreatic cancer cells and other cell types of the TME, especially CAF and T helper cells 2 (Th2), can mainly trigger the polarization of TAM towards a M2 phenotype in PDAC [19,25]. For example, activation of the epidermal growth factor receptor (EGFR)/AKT/cAMP signaling pathway through cancer cell secreted REG4 enhances the expression of CD163, CD206 and IL-10 [76].

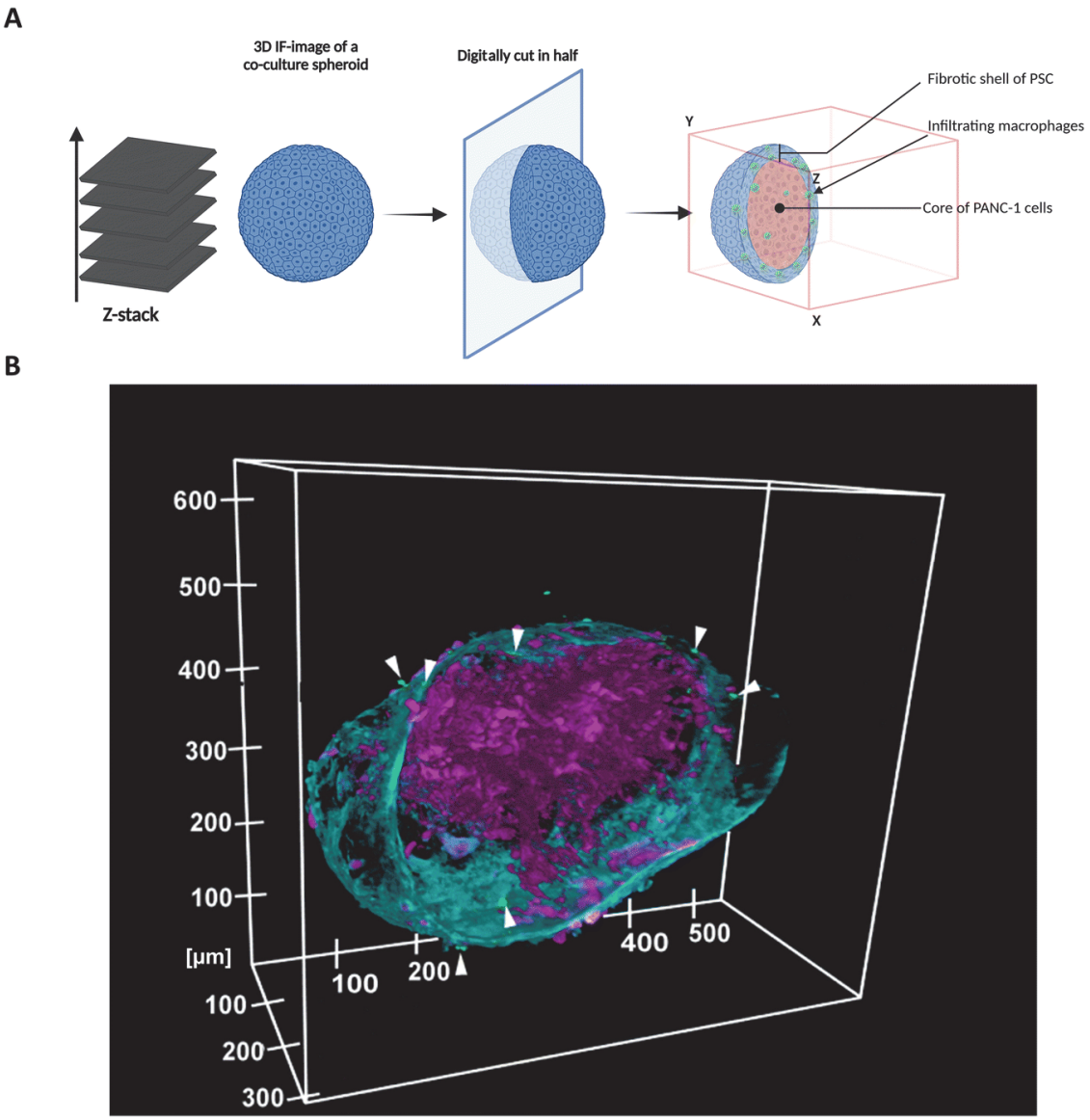


Figure 3.2-7 Spatial distribution of infiltrated monocytes. (A) 3D-rendered confocal Z-stack image of a monocyte-infiltrated spheroid, consisting of 300 slices each 1 µm per step, visualized using image software Fiji with the 3D viewer plugin. For enhanced clarity, the spheroid was spatially cut in half, allowing better visualization of the fibrotic shell, the core of PANC-1 cells and the spatial distribution of infiltrating macrophages. Created in biorender. (B) Fluorescent 3D image of the halved spheroid. Scale bars in 100 µm steps are provided, and the spatial orientation of the halved section is indicated. If staining for the tumor cell marker pan-cytokeratin (purple), the fibroblast marker α-SMA (blue), the and the M2 marker CD163 (green) merged in one image. White arrows indicate $CD163^{+}$ signals.

Overall, the reported findings open a path for more in-depth characterization of macrophage polarization in the presence of different drugs screened in the here described PDAC-on-chip model. In conclusion, our microfluidic biochip is applicable to investigate dynamic monocytes infiltration *via* a vascular layer and the polarization towards M2 in the spheroids. In future studies, the implementation and integration of

additional relevant immune cell types present in the TME of PDAC [5], such as Treg, cytotoxic T-cells or natural killer cells, appears necessary to investigate the cell-specific influence on drug treatments.

Conclusions

In summary, we developed a novel tumor-on-chip model to mimic the microenvironment of PDAC. Tumor-on-chip models play a crucial role in advancing our understanding of tumor-TME interactions, particularly in evaluating therapeutic efficacy. In this study, we developed an innovative microfluidic PDAC model integrating a perfusable endothelial layer with multicellular tumor spheroids (MCTS) consisting of PANC-1 cancer cells and PSC embedded within an ECM. This model provides an initial proof-of-concept for controlled drug administration and immune cell infiltration.

These initial optimizations represent foundational steps in enhancing this approach. By reliably simulating key processes such as vascular transport, immune cell polarization, and drug delivery, this model facilitates a deeper exploration of potential drug synergies, the incorporation of more complex multicellular structures by introducing additional immune and non-immune cell types, and the comprehensive study of the direct and indirect effects on the entire TME. This includes evaluating aspects like spatial immune cell polarization, cytotoxic activity, and drug resistance mechanisms. Ultimately, this advanced PDAC model offers a powerful platform for identifying promising new drug candidates, thereby reducing the reliance on animal models and improving translational potential for clinical applications.

Data availability

Data are available upon request.

Conflicts of interest

M. R. and K. R. hold equity in Dynamic42 GmbH. All other authors have no conflict of interest to declare.

Acknowledgements

This work was supported by a grant to N. E. T. and M. R. by the Bundesministerium für Bildung und Forschung (grant number 16LW0306K). We express our gratitude to

Michael Schell and Fredrik Wieland for their invaluable assistance in devising the CellPathFinder image analysis. Moreover, we would like to thank the working group of Rüdiger Sorg at Heinrich Heine University Düsseldorf and Nico Überschaar at Friedrich Schiller University Jena for providing the Cytoflex flow cytometer and performing the LCMS analysis, respectively.

Notes and references

1. R. L. Siegel , K. D. Miller , N. S. Wagle and A. Jemal , *Ca-Cancer J. Clin.*, 2023, **73** , 17 —48 Search PubMed ULB Volltext .
2. R. L. Siegel , A. N. Giaquinto and A. Jemal , *Ca-Cancer J. Clin.*, 2024, **74** , 12 —49 CrossRef PubMed ULB Volltext .
3. F.Bray, M.Colombet, J. F.Aitken, A.Bardot, S.Eser, J.Galceran, M.Hagenimana, T.Matsuda, L.Mery, M.Piñeros, I.Soerjomataram, E.de Vries, C.Wiggins, Y.-J.Won, A.Znaor and J.Ferlay, Cancer Incidence in Five Continents, Vol. XII, https://ci5.iarc.who.int (accessed 01.10.2024, 2024).
4. T. Conroy , P. Pfeiffer , V. Vilgrain , A. Lamarca , T. Seufferlein , E. M. O'Reilly , T. Hackert , T. Golan , G. Prager , K. Haustermans , A. Vogel and M. Ducreux , *Ann. Oncol.*, 2023, **34** , 987 —1002 CrossRef CAS PubMed ULB Volltext .
5. M. H. Sherman and G. L. Beatty , *Annu. Rev. Pathol.*, 2023, **18** , 123 —148 CrossRef CAS PubMed ULB Volltext .
6. C. Hartupee , B. M. Nagalo , C. Y. Chabu , M. Z. Tesfay , J. Coleman-Barnett , J. T. West and O. Moaven , *Front. Immunol.*, 2024, **15** , 1287459 CrossRef CAS PubMed ULB Volltext .
7. L. N. Barrera , A. Evans , B. Lane , S. Brumskill , F. E. Oldfield , F. Campbell , T. Andrews , Z. Lu , P. A. Perez-Mancera , T. Liloglou , M. Ashworth , M. Jalali , R. Dawson , Q. Nunes , P. A. Phillips , J. F. Timms , C. Halloran , W. Greenhalf , J. P. Neoptolemos and E. Costello , *Cancer Res.*, 2020, **80** , 2861 —2873 CrossRef CAS PubMed ULB Volltext .
8. J. Norton , D. Foster , M. Chinta , A. Titan and M. Longaker , *Cancers*, 2020, **12** , 1347 CrossRef CAS PubMed ULB Volltext .

9. Y. Wu , C. Zhang , K. Jiang , J. Werner , A. V. Bazhin and J. G. D'Haese , *Front. Oncol.*, 2020, **10** , 621937 CrossRef PubMed .

10. A. Morgan , M. Griffin , L. Kameni , D. C. Wan , M. T. Longaker and J. A. Norton , *Biology*, 2023, **12** , 1044 CrossRef CAS PubMed .

11. P. P. Provenzano , C. Cuevas , A. E. Chang , V. K. Goel , D. D. Von Hoff and S. R. Hingorani , *Cancer Cell*, 2012, **21** , 418 — 429 CrossRef CAS PubMed .

12. R. Ajina and L. M. Weiner , *Pancreas*, 2020, **49** , 1014 — 1023 CrossRef CAS PubMed .

13. D. Thomas and P. Radhakrishnan , *Adv. Exp. Med. Biol.*, 2020, **1234** , 57 — 70 CrossRef CAS PubMed .

14. Y. Ju , D. Xu , M. M. Liao , Y. Sun , W. D. Bao , F. Yao and L. Ma , *npj Precis. Oncol.*, 2024, **8** , 199 CrossRef PubMed .

15. A. Zhang , Y. Qian , Z. Ye , H. Chen , H. Xie , L. Zhou , Y. Shen and S. Zheng , *Cancer Med.*, 2017, **6** , 463 —470 CrossRef CAS PubMed .

16. M. C. Whittle and S. R. Hingorani , *Gastroenterology*, 2019, **156** , 2085 — 2096 CrossRef CAS PubMed .

17. H. Y. Tanaka , T. Nakazawa , A. Enomoto , A. Masamune and M. R. Kano , *Cancers*, 2023, **15** , 724 CrossRef CAS PubMed .

18. M. Locati , G. Curtale and A. Mantovani , *Annu. Rev. Pathol.*, 2020, **15** , 123 — 147 CrossRef CAS PubMed .

19. S. Yang , Q. Liu and Q. Liao , *Front. Cell Dev. Biol.*, 2020, **8** , 607209 Search PubMed .

20. H. Hu , J.-J. Hang , T. Han , M. Zhuo , F. Jiao and L.-W. Wang , *Tumor Biol.*, 2016, **37** , 8657 —8664 CrossRef CAS PubMed .

21. G. Atanasov , C. Pötner , G. Aust , K. Schierle , C. Dietel , C. Benzing , F. Krenzien , M. Bartels , U. Eichfeld , M. Schmelzle , M. Bahra , A. Pascher and G. Wiltberger , *Onco Targets Ther*, 2018, **9** , 29715 — 29726 Search PubMed .

22. R. Zhang , Q. Liu , J. Peng , M. Wang , T. Li , J. Liu , M. Cui , X. Zhang , X. Gao , Q. Liao and Y. Zhao , *J. Cancer*, 2020, **11** , 2371 —2381 CrossRef CAS PubMed .

23. Y. Yang , Z. Guo , W. Chen , X. Wang , M. Cao , X. Han , K. Zhang , B. Teng , J. Cao , W. Wu , P. Cao , C. Huang and Z. Qiu , *Mol. Ther.*, 2021, **29** , 1226 —1238 CrossRef CAS PubMed .

24. A. R. Poh and M. Ernst , *Cancers*, 2021, **13** , 2860 CrossRef CAS PubMed .

25. H. J. Lin , Y. Liu , K. Caroland and J. Lin , *Cancers*, 2023, **15** , 3507 CrossRef CAS PubMed .

26. G. Y. Liou , H. Döppler , B. Necela , M. Krishna , H. C. Crawford , M. Raimondo and P. Storz , *J. Cell Biol.*, 2013, **202** , 563 —577 CrossRef CAS PubMed .

27. S. Wang , J. Wang , Z. Chen , J. Luo , W. Guo , L. Sun and L. Lin , *Npj Precis. Oncol.*, 2024, **8** , 31 CrossRef PubMed .

28. B. Deswal , U. Bagchi and S. Kapoor , *Anti-Cancer Agents Med. Chem.*, 2024, **24** , 146 —156 CrossRef CAS PubMed .

29. J. Zhang , J. Song , S. Tang , Y. Zhao , L. Wang , Y. Luo , J. Tang , Y. Ji , X. Wang , T. Li , H. Zhang , W. Shao , J. Sheng , T. Liang and X. Bai , *Cell Rep.*, 2023, **42** , 112620 CrossRef CAS PubMed .

30. K. Kuwada , S. Kagawa , R. Yoshida , S. Sakamoto , A. Ito , M. Watanabe , T. Ieda , S. Kuroda , S. Kikuchi , H. Tazawa and T. Fujiwara , *J. Exp. Clin. Cancer Res.*, 2018, **37** , 307 CrossRef CAS PubMed .

31. T. M. Nywening , B. A. Belt , D. R. Cullinan , R. Z. Panni , B. J. Han , D. E. Sanford , R. C. Jacobs , J. Ye , A. A. Patel , W. E. Gillanders , R. C. Fields , D. G. DeNardo , W. G. Hawkins , P. Goedegebuure and D. C. Linehan , *Gut*, 2018, **67** , 1112 —1123 CrossRef CAS PubMed .

32. S. M. Buchholz , R. G. Goetze , S. K. Singh , C. Ammer-Herrmenau , F. M. Richards , D. I. Jodrell , M. Buchholz , P. Michl , V. Ellenrieder , E.

Hessmann and A. Neesse , *Cancers*, 2020, **12** , 1978 CrossRef CAS PubMed ULB Volltext .

33. C. Zheng , J. Wang , Y. Zhou , Y. Duan , R. Zheng , Y. Xie , X. Wei , J. Wu , H. Shen , M. Ye , B. Kong , Y. Liu , P. Xu , Q. Zhang and T. Liang , *Cell Rep.*, 2024, **43** , 114088 CrossRef CAS PubMed ULB Volltext .

34. D. Daley , V. R. Mani , N. Mohan , N. Akkad , G. Pandian , S. Savadkar , K. B. Lee , A. Torres-Hernandez , B. Aykut , B. Diskin , W. Wang , M. S. Farooq , A. I. Mahmud , G. Werba , E. J. Morales , S. Lall , B. J. Wadowski , A. G. Rubin , M. E. Berman , R. Narayanan , M. Hundeyin and G. Miller , *J. Exp. Med.*, 2017, **214** , 1711 —1724 CrossRef CAS PubMed ULB Volltext .

35. F. Pratticò and I. Garajová , *Curr. Oncol.*, 2024, **31** , 4241 — 4260 CrossRef PubMed ULB Volltext .

36. E. M. Palsson-McDermott , L. Dyck , Z. Zasłona , D. Menon , A. F. McGettrick , K. H. G. Mills and L. A. O'Neill , *Front. Immunol.*, 2017, **8** , 1300 CrossRef PubMed ULB Volltext .

37. D. Daley , V. R. Mani , N. Mohan , N. Akkad , A. Ochi , D. W. Heindel , K. B. Lee , C. P. Zambirinis , G. S. B. Pandian , S. Savadkar , A. Torres-Hernandez , S. Nayak , D. Wang , M. Hundeyin , B. Diskin , B. Aykut , G. Werba , R. M. Barilla , R. Rodriguez , S. Chang , L. Gardner , L. K. Mahal , B. Ueberheide and G. Miller , *Nat. Med.*, 2017, **23** , 556 — 567 CrossRef CAS PubMed ULB Volltext .

38. M. Tsukamoto , K. Imai , T. Ishimoto , Y. Komohara , Y. I. Yamashita , S. Nakagawa , N. Umezaki , T. Yamao , Y. Kitano , T. Miyata , K. Arima , H. Okabe , Y. Baba , A. Chikamoto , T. Ishiko , M. Hirota and H. Baba , *Cancer Sci.*, 2019, **110** , 310 —320 CrossRef CAS PubMed ULB Volltext .

39. B. Gündel , X. Liu , M. Löhr and R. Heuchel , *Front. Cell Dev. Biol.*, 2021, **9** , 741162 CrossRef PubMed ULB Volltext .

40. O. E. Atat , Z. Farzaneh , M. Pourhamzeh , F. Taki , R. Abi-Habib , M. Vosough and M. El-Sibai , *Hum. Cell*, 2022, **35** , 23 — 36 CrossRef CAS PubMed ULB Volltext .

41. L. A. Kunz-Schughart , P. Heyder , J. Schroeder and R. Knuechel , *Exp. Cell Res.*, 2001, **266** , 74 —86 CrossRef CAS PubMed .

42. H. Y. Tanaka , T. Kurihara , T. Nakazawa , M. Matsusaki , A. Masamune and M. R. Kano , *Biomaterials*, 2020, **251** , 120077 CrossRef CAS PubMed .

43. M. J. Ware , V. Keshishian , J. J. Law , J. C. Ho , C. A. Favela , P. Rees , B. Smith , S. Mohammad , R. F. Hwang , K. Rajapakshe , C. Coarfa , S. Huang , D. P. Edwards , S. J. Corr , B. Godin and S. A. Curley , *Biomaterials*, 2016, **108** , 129 —142 CrossRef CAS PubMed .

44. G. Lazzari , V. Nicolas , M. Matsusaki , M. Akashi , P. Couvreur and S. Mura , *Acta Biomater.*, 2018, **78** , 296 —307 CrossRef CAS PubMed .

45. B. Xie , J. Hänsel , V. Mundorf , J. Betz , I. Reimche , M. Erkan , I. Büdeyri , A. Gesell , R. G. Kerr and N. P. Ariantari , *et al.*, *Bioengineering*, 2020, **7** , 57 CrossRef CAS PubMed .

46. X. Liu , B. Gündel , X. Li , J. Liu , A. Wright , M. Löhr , G. Arvidsson and R. Heuchel , *Transl. Oncol.*, 2021, **14** , 101107 CrossRef CAS PubMed .

47. G. Giustarini , G. Teng , A. Pavesi and G. Adriani , *Front. Oncol.*, 2023, **13** , 1156769 CrossRef CAS PubMed .

48. N. Bidan , G. Dunsmore , M. Ugrinic , M. Bied , M. Moreira , C. Deloménie , F. Ginhoux , C. Blériot , M. de la Fuente and S. Mura , *Drug Delivery Transl. Res.*, 2024, **14** , 2085 —2099 CrossRef CAS PubMed .

49. N. H. Madsen , B. S. Nielsen , S. L. Nhat , S. Skov , M. Gad and J. Larsen , *Pathogens*, 2021, **10** , 969 CrossRef CAS PubMed .

50. J. Kuen , D. Darowski , T. Kluge and M. Majety , *PLoS One*, 2017, **12** , e0182039 CrossRef PubMed .

51. A. Zeöld , G. O. Sándor , A. Kiss , A. Soós , T. Tölgyes , A. Bursics , Á. Szűcs , L. Harsányi , Á. Kittel , A. Gézsi , E. I. Buzás and Z. Wiener , *Cell. Mol. Life Sci.*, 2021, **78** , 3005 —3020 CrossRef PubMed .

52. A. Sontheimer-Phelps , B. A. Hassell and D. E. Ingber , *Nat. Rev. Cancer*, 2019, **19** , 65 —81 Search PubMed .

53. M. Geyer and K. Queiroz , *Front. Cell Dev. Biol.*, 2021, **9** , 761807 CrossRef PubMed .

54. H. Xu , J. Wen , J. Yang , S. Zhou , Y. Li , K. Xu , W. Li and S. Li , *Cell Commun. Signaling*, 2024, **22** , 515 CrossRef PubMed .

55. B. Schuster , M. Junkin , S. S. Kashaf , I. Romero-Calvo , K. Kirby , J. Matthews , C. R. Weber , A. Rzhetsky , K. P. White and S. Tay , *Nat. Commun.*, 2020, **11** , 5271 CrossRef CAS PubMed .

56. Y. Zhu , D. Jiang , Y. Qiu , X. Liu , Y. Bian , S. Tian , X. Wang , K. J. Hsia , H. Wan , L. Zhuang and P. Wang , *Bioact. Mater.*, 2024, **39** , 59 —73 CrossRef CAS .

57. V. Sgarminato , S. L. Marasso , M. Cocuzza , G. Scordo , A. Ballesio , G. Ciardelli and C. Tonda-Turo , *Biomater. Sci.*, 2023, **11** , 208 —224 RSC .

58. M. Geyer , L. M. Gaul , S. L. D Agosto , V. Corbo and K. Queiroz , *Front. Immunol.*, 2023, **14** , 1155085 Search PubMed .

59. M. Geyer , D. Schreyer , L. M. Gaul , S. Pfeffer , C. Pilarsky and K. Queiroz , *Cell Death Discovery*, 2023, **9** , 20 Search PubMed .

60. M. R. Haque , C. R. Wessel , D. D. Leary , C. Wang , A. Bhushan and F. Bishehsari , *Microsyst. Nanoeng.*, 2022, **8** , 36 Search PubMed .

61. C. R. Drifka , K. W. Eliceiri , S. M. Weber and W. J. Kao , *Lab Chip*, 2013, **13** , 3965 —3975 Search PubMed .

62. D. Gioeli , C. J. Snow , M. B. Simmers , S. A. Hoang , R. A. Figler , J. A. Allende , D. G. Roller , J. T. Parsons , J. D. Wulfkuhle , E. F. Petricoin , T. W. Bauer and B. R. Wamhoff , *Lab Chip*, 2019, **19** , 1193 —1204 RSC .

63. F. L. Lai Benjamin , X. Lu Rick , Y. Hu , H. L. Davenport , W. Dou , E. Y. Wang , N. Radulovich , M. S. Tsao , Y. Sun and M. Radisic , *Adv. Funct. Mater.*, 2020, **30** , 2000545 CrossRef PubMed .

64. P. A. Marks and R. Breslow , *Nat. Biotechnol.*, 2007, **25** , 84 —90 CrossRef CAS PubMed .

65. K. Schiedlauske , A. Deipenbrock , M. Pflieger , A. Hamacher , J. Hänsel , M. U. Kassack , T. Kurz and N. E. Teusch , *Pharmaceuticals*, 2024, **17** , 752 CrossRef CAS PubMed ULB Volltext .

66. B. Schmid , J. Schindelin , A. Cardona , M. Longair and M. Heisenberg , *BMC Bioinf.*, 2010, **11** , 274 CrossRef PubMed ULB Volltext .

67. J. Schindelin , I. Arganda-Carreras , E. Frise , V. Kaynig , M. Longair , T. Pietzsch , S. Preibisch , C. Rueden , S. Saalfeld , B. Schmid , J. Y. Tinevez , D. J. White , V. Hartenstein , K. Eliceiri , P. Tomancak and A. Cardona , *Nat. Methods*, 2012, **9** , 676 —682 CrossRef CAS PubMed ULB Volltext .

68. S. B. Campbell , Q. Wu , J. Yazbeck , C. Liu , S. Okhovatian and M. Radisic , *ACS Biomater. Sci. Eng.*, 2021, **7** , 2880 — 2899 CrossRef CAS PubMed ULB Volltext .

69. W. J. Ho , E. M. Jaffee and L. Zheng , *Nat. Rev. Clin. Oncol.*, 2020, **17** , 527 — 540 CrossRef PubMed ULB Volltext .

70. Y. Bi , V. S. Shirure , R. Liu , C. Cunningham , L. Ding , J. M. Meacham , S. P. Goedegebuure , S. C. George and R. C. Fields , *Integr. Biol.*, 2020, **12** , 221 — 232 CrossRef PubMed ULB Volltext .

71. X. S. Xiang , P. C. Li , W. Q. Wang and L. Liu , *Biochim. Biophys. Acta, Rev. Cancer*, 2022, **1877** , 188676 CrossRef CAS PubMed ULB Volltext .

72. M. Yu , R. Guan , W. Hong , Y. Zhou , Y. Lin , H. Jin , B. Hou and Z. Jian , *Cancer Manage. Res.*, 2019, **11** , 4041 — 4058 CrossRef PubMed ULB Volltext .

73. G. D'Errico , M. Alonso-Nocelo , M. Vallespinos , P. C. Hermann , S. Alcalá , C. P. García , L. Martin-Hijano , S. Valle , J. Earl , C. Cassiano , L. Lombardia , J. Feliu , M. C. Monti , T. Seufferlein , L. García-Bermejo , P. Martinelli , A. Carrato and B. Sainz , *Oncogene*, 2019, **38** , 5469 — 5485 CrossRef PubMed ULB Volltext .

74. Z. Hussain , T. Bertran , P. Finetti , E. Lohmann , E. Mamessier , G. Bidaut , F. Bertucci , M. Rego and R. Tomasini , *Cell Commun. Signaling*, 2024, **22** , 1 CrossRef CAS PubMed ULB Volltext .

75. S. A. Väyrynen , J. Zhang , C. Yuan , J. P. Väyrynen , A. Dias Costa , H. Williams , V. Morales-Oyarvide , M. C. Lau , D. A. Rubinson , R. F. Dunne , M. M. Kozak , W. Wang , D. Agostini-Vulaj , M. G. Drage , L. Brais , E. Reilly , O. Rahma , T. Clancy , J. Wang , D. C. Linehan , A. J. Aguirre , C. S. Fuchs , L. M. Coussens , D. T. Chang , A. C. Koong , A. F. Hezel , S. Ogino , J. A. Nowak and B. M. Wolpin , *Clin. Cancer Res.*, 2021, **27** , 1069 — 1081 CrossRef PubMed .

76. X. Ma , D. Wu , S. Zhou , F. Wan , H. Liu , X. Xu , X. Xu , Y. Zhao and M. Tang , *Oncol. Rep.*, 2016, **35** , 189 —196 CrossRef CAS PubMed .

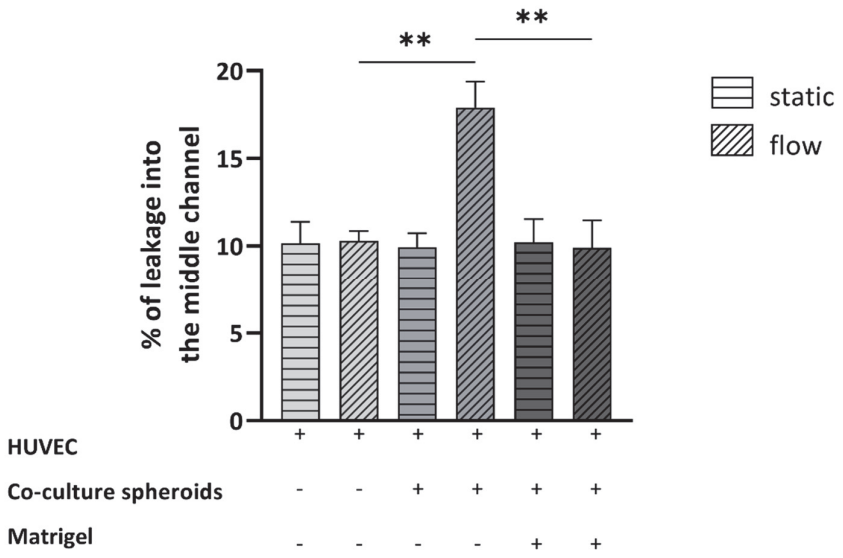
Footnote

1. † Electronic supplementary information (ESI) available. See DOI: https://doi.org/10.1039/d4lc01016g

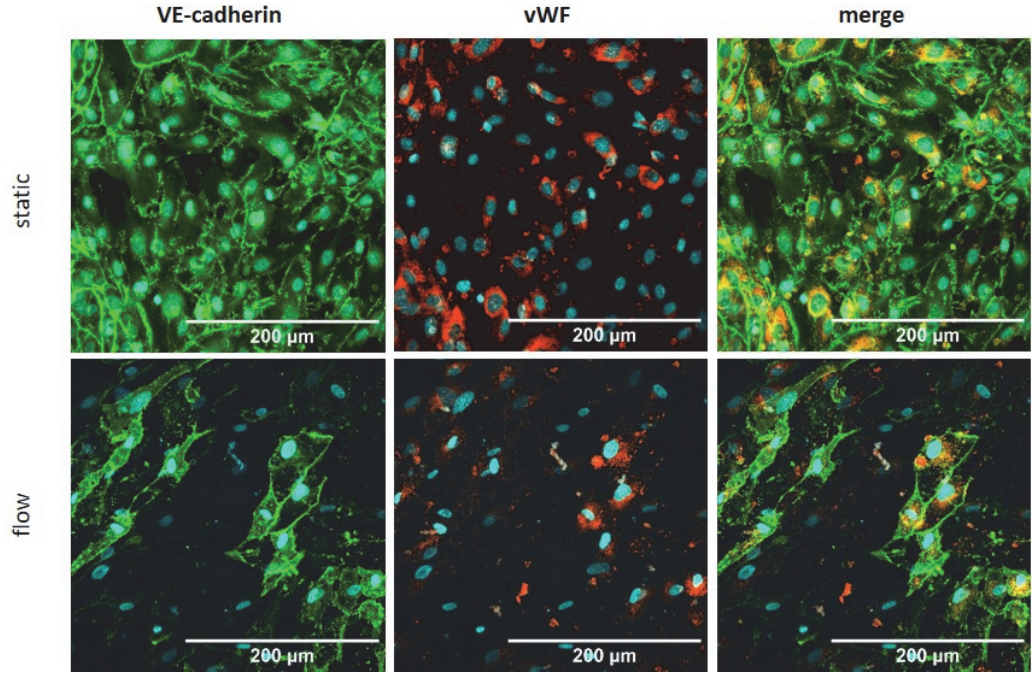
3.2.1 Supplementary Information

Supplementary Table 3.2-1 Gradient for UHPLC / HRMS measurement.

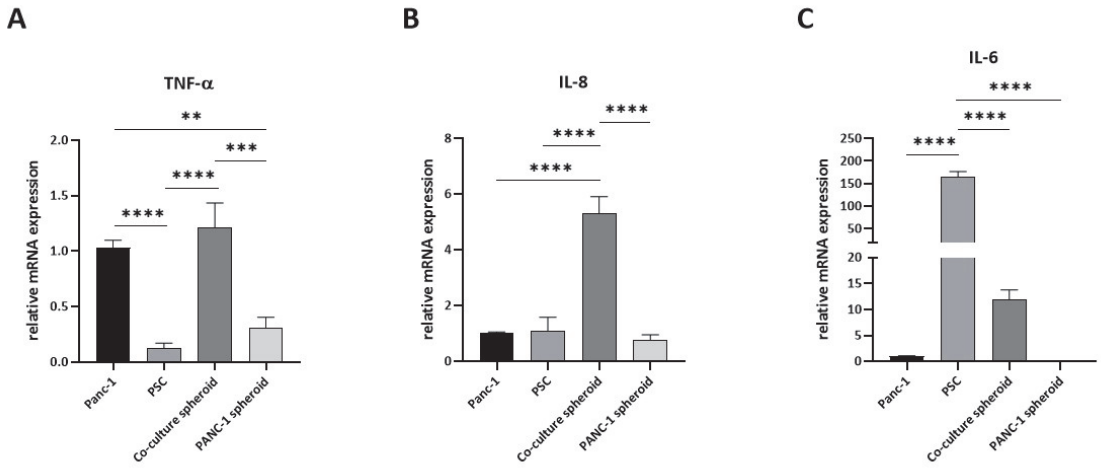
TIME [MIN]	SOLVENT B [%]
0	0
0.2	0
8.0	100
11.0	100
11.1	0
12.0	0



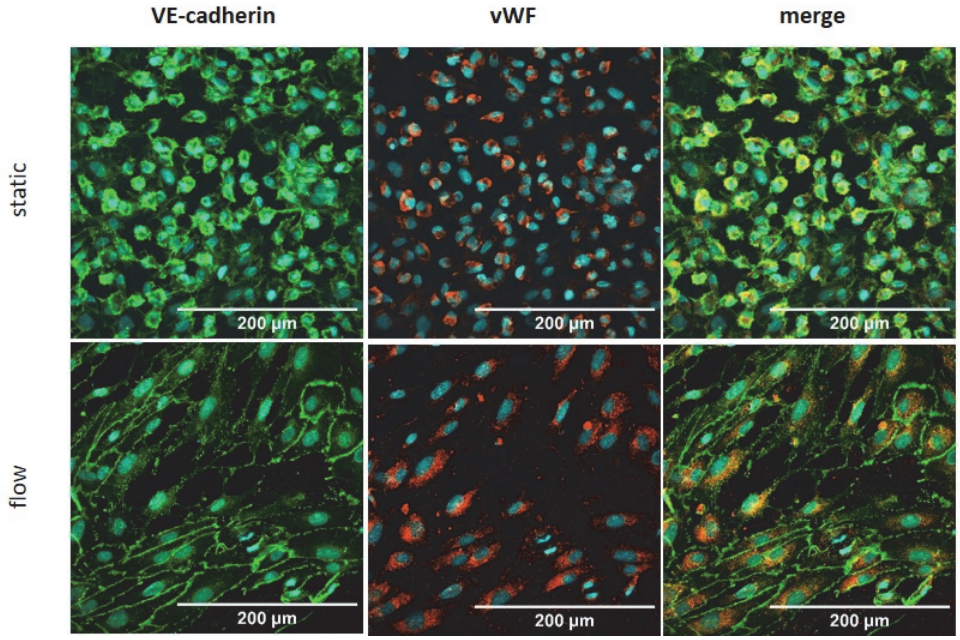
Supplementary Figure 3.2-1. Permeability assay of HUVEC layer. FITC dextran assay was performed to measure the barrier integrity of the HUVEC layer after 72 h under static or flow conditions and in the presence or absence of co-culture spheroids, with or without the addition of Matrigel. FITC dextran solution was added into the top channel. After 1 h the leakage into the middle channel was determined via fluorescence measurement. Error bars indicate the standard errors of the mean of three independent experiments, with **= $p \leq 0.01$.



Supplementary Figure 3.2-2. Integrity of the vasculature consisting of HUVEC in the presence of co-culture spheroids in the biochip after 72 h. The vasculature remains stable in the presence of the co-culture spheroids under static conditions (top row). In the presence of the spheroids and under flow conditions, the endothelial cells do not show a stable vasculature (bottom row). The endothelial markers VE-cadherin (green), von Willebrand factor (vWF; red) and the nuclear dye DAPI (blue) were stained. Representative image of several random field images. Scale bar is 200 µm.



Supplementary Figure 3.2-3 Cytokine expression in PANC-1 cells, PSC cells, co-culture spheroids and PANC-1 spheroids. PANC-1 cells, PSC cells, co-culture spheroids and PANC-1 spheroids were cultivated for 72h in 3D medium. mRNA levels of TNF-α (A), IL-8 (B), and IL-6 (C) were analyzed by qRT-PCR. Error bars indicate standard errors of mean (of at least three independent experiments, with; ** = p ≤ 0.01; *** = p ≤ 0.001; and **** = p ≤ 0.0001).

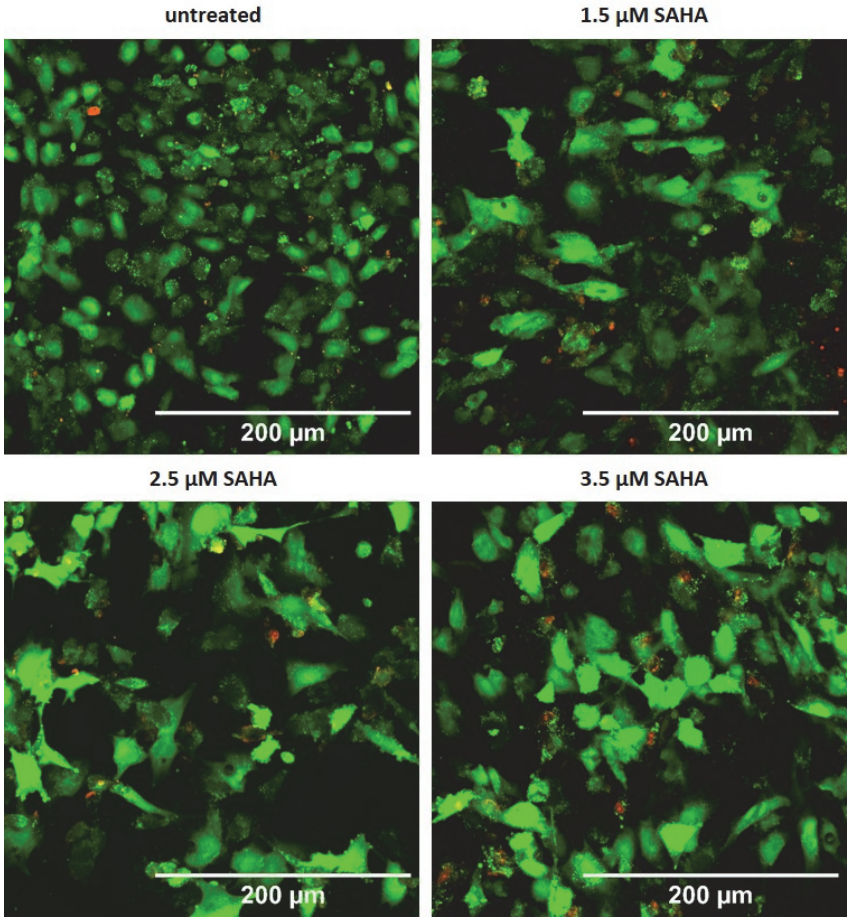


Supplementary Figure 3.2-4 Cultivation of HUVEC in the biochip. HUVEC were cultivated in the presence of conditioned media from co-culture spheroids for 72 h under static (top row) or flow (bottom row) conditions. The endothelial markers vascular endothelial (VE-) cadherin (green), von Willebrand factor (vWF; red) and the nuclear dye DAPI (blue) were stained. Representative image of several random field images. Scale bar is 200 µm.

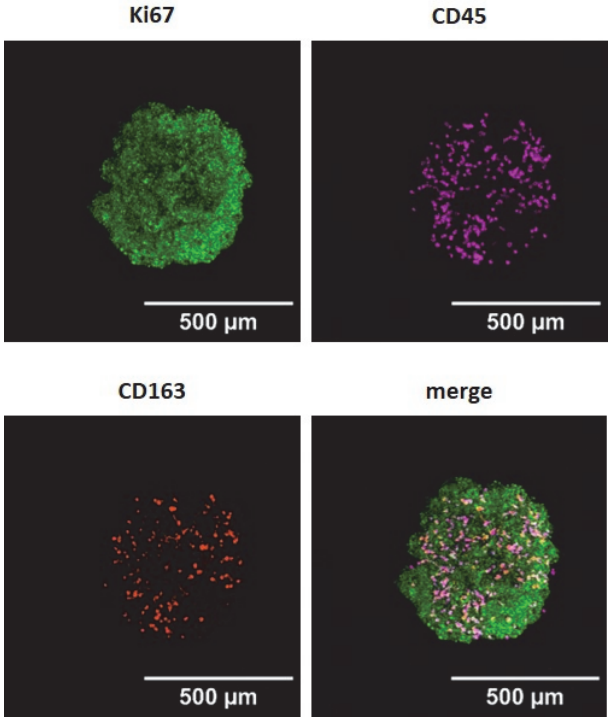
Supplementary Table 3.2-2 The cytotoxic efficacy of the HDAC inhibitor vorinostat represented by the respective IC50 values in 2D HUVEC cultures as well as in 3D PANC-1 spheroids and co-culture

spheroids after 72 h incubation. The arithmetic means and their respective standard deviations of three independent experiments are depicted.

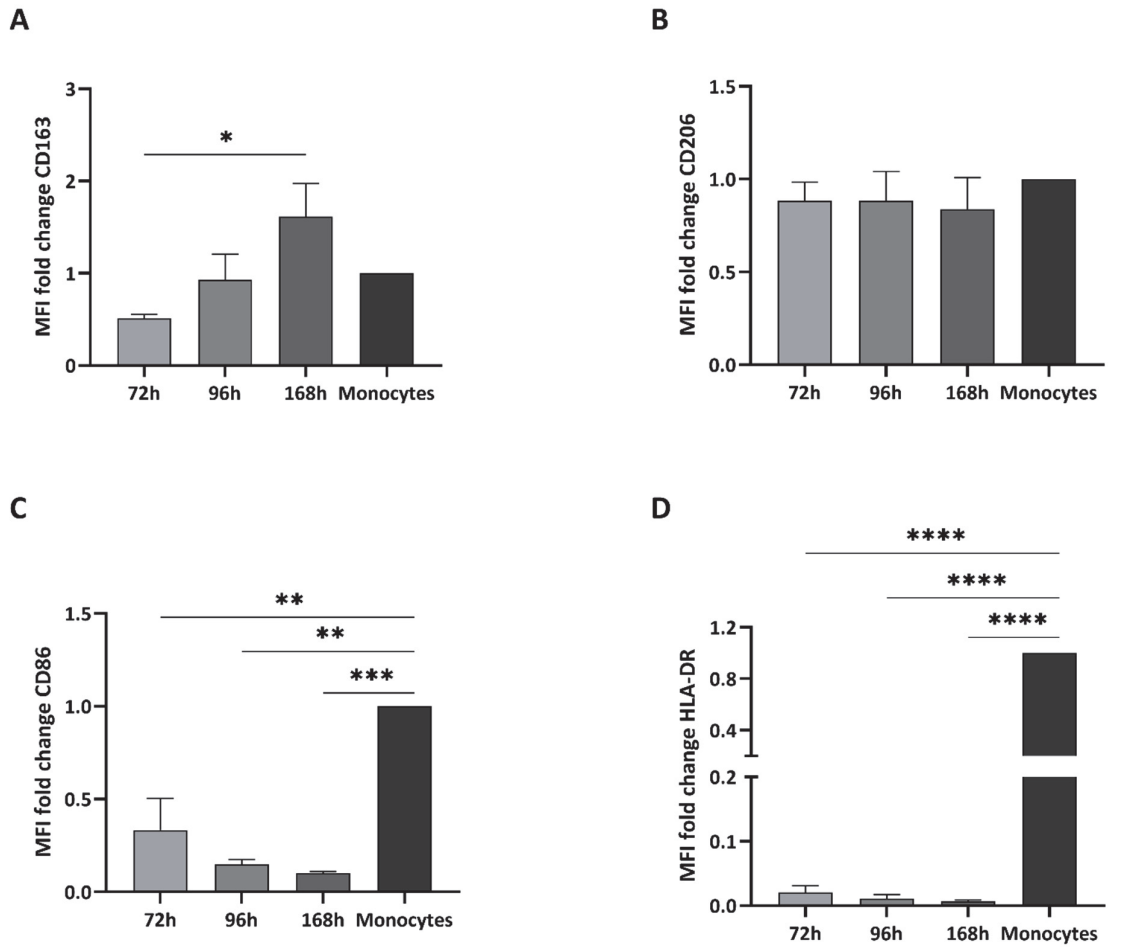
Cell type	IC_{50} in µM
HUVEC	5.70 ± 0.49
PANC-1 spheroid	2.08 ± 0.32
Co-culture spheroid	0.85 ± 0.25



Supplementary Figure 3.2-5 Live / Dead staining of HUVEC layer after treatment with SAHA. HUVECs were stained with Calcein (green) and Ethidium homodimer-1(red) after 72 h treatment with 1.5, 2.5 or 3.5 µM SAHA, untreated cells served as control. Green staining shows viable cells, red staining indicates dead cells. Representative image of several random field images. Scale bar is 200 µm.



Supplementary Figure 3.2-6 IF staining of PANC-1 spheroids after addition of primary monocytes. PANC-1 spheroids were seeded into 96-well plates and primary monocytes were added at day 4 of the cultivation. After 72 h of co-cultivation the PANC-1 spheroids were stained for the tumor cell marker Ki67 (green), the immune cell marker CD45 (purple), and the M2 marker CD163 (red); merging of all channels. Shown as maximum intensity projection MIP of a z-Stack. Scale is 500 µm.



Supplementary Figure 3.2-7 Time course of macrophage polarization after infiltration of the co-culture spheroids. $CD14^+$ monocytes were added to 4-day-old spheroids and were analyzed by flow cytometry 72 h, 96 h, and 168 h after infiltration. Macrophages identified as $CD11b^+$ and $CD45^+$ were analyzed for surface expression of (A) CD163, (B) CD206, (C) CD86, and (D) HLA-DR. Infiltrated cells were compared to unstimulated monocytes as controls. Error bars indicate the standard errors of the mean of three independent experiments, with * = $p \leq 0.05$; ** = $p \leq 0.01$; ***= $p \leq 0.005$; **** = $p \leq 0.0001$.

3.2.2 Additional unpublished data

TAM have been identified as key contributors to the development of chemoresistance in PDAC [196]. By secreting cytokines such as TGF-β and IL-10, they activate anti-apoptotic signaling pathways (e.g. PI3K/Akt, JAK/STAT) tumor cells [122, 196]. These interactions protect tumor cells from the cytotoxic impact of chemotherapy [131, 197, 198]. Consequently, incorporating M2 macrophages into preclinical drug-testing models is vital to accurately reflect this protective mechanism when assessing the efficacy of chemotherapeutic agents. As shown in Figure 3.2-8 the incorporation of M2 macrophages into our co-culture spheroid model significantly reduces the cytotoxic effect of paclitaxel in a dose dependent manner.

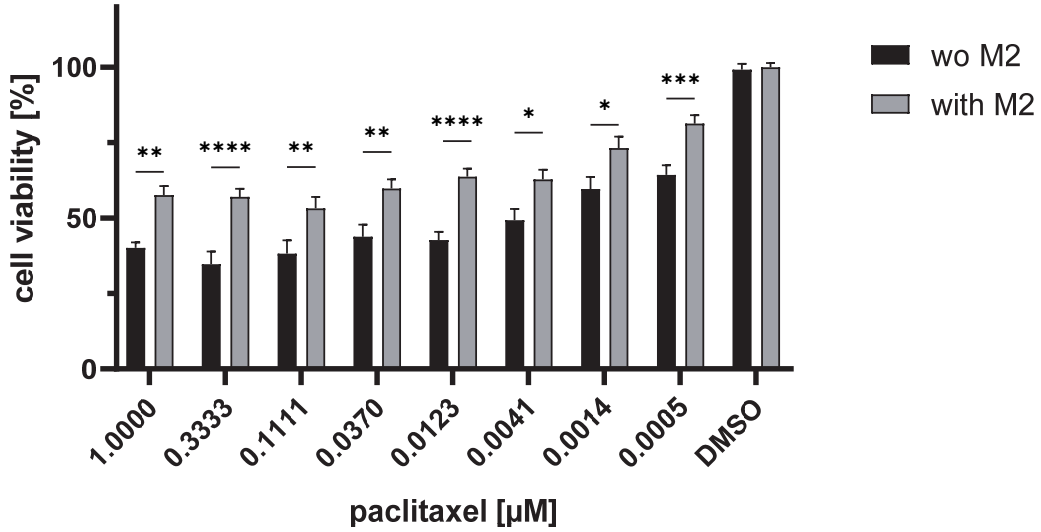


Figure 3.2-8 Effect of macrophages on chemosensitivity. PBMC-derived monocytes were differentiated towards M2 macrophages for 7 days. M2 macrophages were added to co-culture spheroids 24 h after seeding the spheroids. Co-culture spheroids with or without (wo) M2 macrophages were treated on day four of the spheroid culture for 72 h. Cell viability was determined using the Cell Titer Glo Assay. Viability was normalized against the corresponding DMSO control. Error bars indicate the standard errors of the mean of three independent experiments, with * = $p \leq 0.05$; ** = $p \leq 0.01$; ***= $p \leq 0.005$; **** = $p \leq 0.0001$.

3.3 Targeting stroma-mediated T-cell exclusion and functional exhaustion in pancreatic ductal adenocarcinoma (PDAC) through CXCR4 and PD-1 blockade

Alina Deipenbrock[1], Lina Hofer[1], Ben E. Wilmes[1], Timur Cetin[2], Martin Hoffmann[2], Irene Esposito[3], Dirk Weyhe[2], Johannes Stegmaier[4], and Nicole E. Teusch[1]*

[1]Heinrich-Heine-Universität Düsseldorf, Institute of Pharmaceutical Biology and Biotechnology, Düsseldorf, North Rhine-Westphalia, Germany

[2]Carl von Ossietzky Universität Oldenburg, University Hospital for Visceral Surgery, PIUS-Hospital Oldenburg, Oldenburg, Lower Saxony, Germany

[3]University Hospital Düsseldorf, Institute of Pathology, Düsseldorf, North Rhine-Westphalia, Germany

[4]Heinrich-Heine-Universität Düsseldorf, Center for Digital Medicine, Group Machine Learning for Medical Data, Düsseldorf, North Rhine-Westphalia, Germany

* Correspondence: Corresponding Author nicole.teusch@hhu.de

Keywords: Pancreatic ductal adenocarcinoma, Tumor microenvironment, T-cell exhaustion, T-cell exclusion, Immune checkpoints, CXCR4, PD-1, Patient-derived spheroids

Submitted to and currently und revision: Front. Immunol. - Cancer Immunity and Immunotherapy

Own contributions to the manuscript: 90%

- Conceptualization of the experiments (60%) together with Nicole Teusch
- Methodology (100%), Investigation (90%), Validation (100%), Data curation (100%), Formal analysis (100%), and Visualization (100%) of the following experiments:
    - Characterization of T-cells in PDAC patients (80%) together with Ben E. Wilmes
    - Characterization of T-cells after infiltration into PANC-1 spheroids (100%)
    - Immunofluorescence staining to analyze T-cell infiltration into PANC-1 spheroids (100%)
    - Establishment of patient-derived cell lines (80%) together with Lina Hofer

  - Establishment of patient-derived spheroids (100%)
  - Characterization of T-cells after infiltration into patient-derived spheroids (100%)
  - Immunofluorescence staining to analyze T-cell infiltration into co-culture spheroids and PDS after AMD3100 treatment (50%) quantification performed by Johannes Stegmaier
  - qPCR and flow cytometry to analyze the effect of pembrolizumab treatment on effector molecule expression (100%)
- Writing and drafting the manuscript (85%) together with Nicole Teusch

Abstract

Background: Pancreatic ductal adenocarcinoma (PDAC) is one of the deadliest malignancies to date and characterized by a unique immunosuppressive and highly desmoplastic tumor microenvironment (TME). These features drive profound T-cell dysfunction and maintain high resistance to current immunotherapy. By recapitulating the complex 3D architecture of human PDAC, we demonstrate the key immunosuppressive mechanisms that drive T-cell dysfunction within the tumor microenvironment.

Method: 3D PDAC spheroids—generated from PANC-1 cells alone or together with primary pancreatic stellate cells (PSC)—were infiltrated with primary human T-cells from healthy donors, allowing controlled analysis of T-cell infiltration, activation, and checkpoint regulation. Furthermore, patient-derived spheroids (PDS) composed of primary tumor cells and cancer-associated fibroblasts were infiltrated with autologous T-cells.

Results: Infiltrated T-cells exhibited a pronounced exhaustion signature, including strong upregulation of PD-1, LAG-3, and CTLA-4, closely mirroring the phenotype of tumor-infiltrating lymphocytes (TIL) isolated from PDAC patient samples. Incorporation of pancreatic stellate cells (PSC) generated a fibrotic barrier around the tumor cells that markedly restricted T-cell infiltration, modeling the desmoplastic TME characteristic of PDAC. From a mechanistic perspective, stromal CXCL12–CXCR4 enhanced T-cell exclusion: pharmacological CXCR4 blockade with AMD3100 significantly enhanced T-cell infiltration into PSC-containing spheroids. Furthermore, treatment with the anti-PD-1 monoclonal antibody pembrolizumab partially restored the effector cell function of T-cells within the 3D system. These results demonstrate that

this minimalistic platform is capable of capturing complex, cytokine- and stroma-driven immunomodulation typically observed only in advanced organoid or in vivo systems. Crucially, key immunological features—including T-cell exhaustion, stromal exclusion, and therapeutic responsiveness—were fully reproduced in PDS. PDS reproduced patient-specific T-cell suppression patterns and therapeutic responses, underscoring the translational relevance of the platform.

Conclusion: Together, our findings identify critical determinants of T-cell dysfunction in PDAC and introduce a versatile, animal-free 3D model that powerfully captures hallmark immune-evasion mechanisms in PDAC. This system provides a scalable and mechanistically faithful tool for dissecting TME-driven immune suppression and for accelerating the functional evaluation of immunotherapeutic strategies, including patient-tailored approaches.

Introduction

Pancreatic ductal adenocarcinoma (PDAC) is one of the most lethal malignancies, with a five-year survival rate of only about 13% [1, 2]. Late diagnosis, a high metastatic potential, and a heterogeneous tumor microenvironment (TME) are key contributors to this poor prognosis [1, 3]. The PDAC TME consists of various cell types, including immune cells, endothelial cells, neuronal cells and cancer-associated fibroblasts (CAF) [4-6]. CAF promote the tumor progression through the release of immunosuppressive cytokines and chemokines like TGF-β, CXCL10, and CXCL12, and produce large amounts of extracellular matrix (ECM), resulting in a dense and desmoplastic stroma [4, 7].

In addition to CAF, the PDAC TME contains diverse immune cell populations, however, these are predominantly immunosuppressive, including tumor associated macrophages (TAM), myeloid-derived suppressor cells (MDSC), and regulatory T-cells (Treg). TAM are mainly polarized towards the immunosuppressive M2 phenotype contributing to tumor progression by enhancing immunosuppression and chemoresistance [8, 9]. MDSC impair T-cell function directly by upregulating programmed death-ligand 1 (PD-L1) to inhibit T-cell activation, and indirectly via an IL-10 dependent release of TGF-β, driving the expansion of Treg [10, 11]. Treg ($FoxP3^+$, $CD4^+$, $CD25^+$) secrete the anti-inflammatory cytokines IL-10 and TGF-β and express the checkpoint molecule cytotoxic T-lymphocyte-associated protein 4 (CTLA-4), thereby inhibiting effector T-cell function and polarization of TAM towards M2 [12]. Treg

inversely correlate with $CD8^+$ T-cell infiltration and are associated with poor clinical outcomes [13]. Treg activate a tolerogenic phenotype in dendritic cells, characterized by downregulation of the costimulatory molecules CD86 and CD40, MHC class II, and IFN-γ, leading to suppressed activation of $CD8^+$ T-cells [10]. Accordingly, elevated Treg frequencies are considered a negative prognostic biomarker in PDAC [12, 13]. Besides Treg, $CD4^+$ T helper (Th) cells are largely polarized toward a Th2 phenotype, promoting immunosuppression through the release of anti-inflammatory cytokines such as IL-4 and IL-13, which polarize anti-inflammatory M2 macrophages and support tumor cell metabolism through increased glycolysis via JAK-STAT signaling [14, 15]. In addition, $CD4^+$ Th17 cells have also been described in the TME of PDAC patients, where they are associated with a poorer prognosis by promoting the formation of pancreatic intraepithelial neoplasia (PanIN) and enhancing the stem cell properties of tumor cells [10, 16, 17]. Th17 secrete IL-17, which increases fibrosis, neovascularization, and myeloid cell recruitment, enhancing survival and growth of tumor cells through the activation of the gp130-JAK2-STAT3 pathway [17-19]. Cytotoxic lymphocytes ($CD8^+$ T-cells, (CTL)) are crucial for the elimination of tumor cells, mediating killing through the secretion of granzyme B, perforin, IFN-γ, and TNF-α, or of mediating FasL-induced apoptosis [12]. In PDAC, however, effector T-cells are largely excluded from the TME and confined to the periphery within the stroma-rich areas surrounding the tumor [12]. This exclusion is driven by the CAF-derived chemokine CXCL12, which acts as a specific ligand for the G protein-coupled receptor CXCR4 in T-cells, promoting their chemotactic migration into stroma-rich areas [20, 21]. Furthermore, T-cells in the PDAC TME exhibit an exhausted phenotype characterized by increased expression of checkpoint molecules, reduced proliferative capacity, and diminished effector function [12, 22, 23]. Key checkpoint molecules elevated in these T-cells include programmed cell death protein-1 (PD-1), lymphocyte-activation gene 3 (LAG-3), and cytotoxic T-lymphocyte-associated protein 4 (CTLA-4) [24, 25]. PD-1 engages its ligands PD-L1 and PD-L2, expressed on tumor cells and other TME-resident T-cells, attenuating T-cell activation and promoting T-cell apoptosis [26]. CTLA-4 competes with CD28 for binding to B7 ligands on antigen-presenting cells, thereby preventing co-stimulatory signaling required for full T-cell activation and driving an immunosuppressive state [27, 28]. LAG-3 interacts with MHC class II molecules, interfering with effective T-cell receptor (TCR) signaling and dampening T-cell activation [29]. Collectively, these mechanisms reduce effector

function of $CD4^+$ T-cells and impair the cytotoxic activity of $CD8^+$ T-cells against tumor cells [28, 29].

Advances in immunotherapy have focused on reactivating tumor-infiltrating T-cells, by blocking checkpoint molecules with monoclonal antibodies [11, 30]. The first FDA approved immune checkpoint inhibitor (ICI) was the CTLA-4 blocker ipilimumab for metastatic melanoma in 2011 [31]. Since then, numerous ICI targeting CTLA-4, PD-1, or PD-L1, including pembrolizumab, nivolumab, durvalumab, atezolizumab, and avelumab, have been approved for various malignancies, such as non-small cell lung cancer, urothelial carcinoma, Hodgkin lymphoma, and hepatocellular carcinoma. [32-37]. In PDAC, several ICI have been or are currently under clinical investigation, including the PD-1 inhibitors nivolumab or pembrolizumab, the PD-L1 inhibitor durvalumab, and the CTLA-4 inhibitor ipilimumab [38-41]. However, as monotherapy, these antibodies have failed to demonstrate an increase in overall survival (OS) and progression free survival (PFS) compared to chemotherapy and led to grade 3 treatment-related adverse events in up to 55% of the patients [26, 42-44]. To overcome this limited efficacy, multiple clinical trials have evaluated ICI in combination with other therapeutics. These include combination with standard chemotherapy regimens (FOLFIRINOX or gemcitabine plus nab-paclitaxel) alongside pembrolizumab, nivolumab, ipilimumab, or durvalumab [45-47], as well as combinations with PARP-inhibitors [48, 49], or TME-modulating agents such as the CXCR4 antagonist motixafortide (BL-8040), an indoleamine 2,3-dioxygenase 1 [IDO1] inhibitor [50, 51], and a focal adhesion kinase (FAK) inhibitor [52]. To date, no broadly effective immunotherapeutic strategy is available for the vast majority of PDAC patients with microsatellite-stable tumors, although pembrolizumab is FDA-approved and effective for the rare (1.2%) microsatellite instability-high (MSI-H) and deficient mismatch repair (dMMR) patient subset [26, 53, 54].

To elucidate mechanisms underlying T-cell dysfunction in the PDAC TME, we examine the composition, spatial localization, and functional state of tumor-infiltrating lymphocytes in PDAC patients. Clinical analyses have frequently reported an altered $CD4^+/CD8^+$ T-cell ratio in both the tumor microenvironment and in peripheral blood from PDAC patients [12, 55]. The TME is often characterized by a relative enrichment of $CD4^+$ T-cell subsets, including Th2-polarized and regulatory Treg, alongside a reduced cytotoxic $CD8^+$ T-cell compartment [12]. In the peripheral blood, an increased

expansion of regulatory and memory $CD4^+$ T-cell populations has been described [55]. The overall increased CD4/CD8 ration is less consistent compared to the TME and the shift is associated more with an increase of specific $CD4^+$ subpopulations (e.g. Treg) rather than a reduction of CD8 T-cells. [55]. This suggest a systemic shift towards a CD4 dominant immunity, however it remains unclear how the peripheral immune alterations reflect the intratumoral T-cell composition. In addition, tumor-infiltrating T-cells commonly exhibit elevated expression of multiple inhibitory receptors, including PD-1, CTLA-4, and LAG-3, indicative of an exhausted phenotype [24]. We therefore investigate the effect of infiltration into PDAC spheroids on T-cell checkpoint expression. Beyond functional exhaustion, spatial immune exclusion represents another hallmark of the PDAC microenvironment. Cytotoxic T-cells are frequently restricted to stromal regions or the tumor periphery, while the tumor core remains poorly infiltrated [20]. This phenomenon has been attributed in part to the dense desmoplastic stroma and the activity of CAF, which can promote T-cell exclusion via the CXCL12–CXCR4 axis [21]. By mimicking the spatial composition of the TME we analyzed the role of CAF on the infiltration of T-cells.

While these immunologic alterations have been well documented, they have been predominantly studied in isolation in patient tumor samples, mouse models and in vitro models [56-58]. Conventional 2D models and classic patient-derived organoids lack the spatial organization and cellular composition of the TME and are therefore of limited value for investigation of T-cell infiltration and immunotherapeutic response. As a result, the interplay between checkpoint molecule upregulation, the accumulation of Treg, and the stroma-mediated exclusion of T-cells, and how these collectively contribute to immunotherapy resistance in PDAC remains poorly understood. Therefore, we aim to recapitulate these key immunosuppressive mechanisms simultaneously to drive T-cell dysfunction within the TME using the complex 3D architecture of human PDAC. This model is designed to recapitulate various mechanisms of immune evasion in PDAC, thereby providing a more predictive platform for the analysis of immunotherapeutic treatments and patient-specific responses as current *in vitro* models.

Material and Methods

Cell culture

The PANC-1 cell line was obtained from the American Type Culture Collection (ATCC) and maintained in Dulbecco's Modified Eagle Medium (DMEM; #41965039, Gibco, Grand Island, NY, USA) supplemented with 10% fetal bovine serum (FBS; #10270-106, Gibco) and 1% penicillin–streptomycin (Pen-Strep; #15140122, Gibco). Pancreatic stellate cells (PSC) were kindly provided by Dr. Erkan (Koç University Hospital, Turkey). Ethical approval for the use of PSC was obtained from the Biomedical Sciences Ethics Committee of Koç University, and written informed consent was received from all participating patients. PSC were isolated from individuals diagnosed with pancreatic ductal adenocarcinoma and cultured in DMEM/F12 medium (#11320074, Gibco) containing 20% FBS and 1% Pen-Strep under sterile conditions. All cell cultures were maintained at 37 °C and 5% CO_2.

Isolation of T-cells

Peripheral blood mononuclear cells (PBMC) were isolated from buffy coats obtained from anonymized healthy donors (Düsseldorf University Hospital, Germany) who had provided material approved for in vitro research. Autologous T-cells from PDAC patients were isolated in the same manner from patient's PBMC. The isolation was performed using a Ficoll-Paque density gradient centrifugation method. Briefly, buffy coats were diluted with D-PBS and carefully layered over Histopaque (#10771, Sigma-Aldrich, St. Louis, MO, USA). Following centrifugation at 850 × g for 20 min with minimal acceleration and deceleration, the PBMC layer was collected. To remove residual erythrocytes, cells were incubated for 10 min in ammonium chloride lysis buffer, then washed with Dulbecco's Phosphate Buffered Saline (D-PBS), and the cell count was determined.

T-cells were subsequently isolated from PBMC using Magnetic-Activated Cell Sorting (MACS) with biotinylated CD4 (#130-113-224, Miltenyi Biotec, Bergisch Gladbach, Germany) and CD8 (#130-110-676, Miltenyi Biotec) antibodies, followed by anti-biotin microbeads (#130-090-485, Miltenyi Biotec) according to the manufacturer's instructions, employing the MidiMACS separator (#130-042-302, Miltenyi Biotec). The purified T-cells were maintained in RPMI medium (#21875-034, Gibco) supplemented with 10% FBS, 1% penicillin–streptomycin, and 50 ng/mL IL-2 (#11340025,

ImmunoTools, Friesoythe, Germany). For T-cell activation and expansion, CD3/CD28 Dynabeads (#11161D, Thermo Fisher Scientific, Waltham, MA, USA) were added at a 1:2 bead-to-cell ratio.

Isolation and cultivation of patient-derived tumor cells, T-cells and CAF

PDAC tissue and full blood were obtained during resection at Pius-Hospital Oldenburg, Germany. The use of human tissue samples was approved by the ethics committee at Carl von Ossietzky University Oldenburg and confirmed by Heinrich Heine University Düsseldorf (study number 2022-058). All patients provided written informed consent prior to tissue collection. Clinicopathological characteristics of the included PDAC patients are summarized in Supplementary Table 2.3-1. All patients underwent surgical resection without prior neoadjuvant treatment. For tissue dissociation, the tumor specimen was washed in DPBS supplemented with 2% (v/v) FBS, and carefully trimmed to remove residual adipose tissue. The remaining tumor tissue was finely minced into fragments smaller than 1 cm^3 and enzymatically digested in 15 mL of digestion solution, containing 0.6 mg/mL Collagenase IV (#17104-019 Gibco), 0.1 mg/mL DNAse (#10104159001 Roche, Basel, Switzerland) and 2% FBS in RPMI (#21875-034 Gibco) at 37 °C with constant agitation for 45–60 min. The resulting suspension was filtered through a 70 µm cell strainer, and remaining tissue fragments were mechanically dissociated using a syringe plunger. The filter was rinsed with DPBS containing 2% FBS, and the cell suspension was centrifuged at 550 g for 7 min. The cell pellet was resuspended in DMEMF12 containing 10% FBS for tumor cell cultivation and 20% FBS for CAF cultivation. Pure cell lines were obtained via differential trypsinization [59]. Characterization of patient-derived cells was performed via immunofluorescence staining. Cancer cell were stained for vimentin (#sc-6260, Santa Cruz Biotechnology, Dallas, TX, USA), pan-cytokeratin (#130-133-439, Miltenyi Biotec), cytokeratin 7 (#130-115-446, Miltenyi Biotec), E-cadherin (#130-111-992, Miltenyi Biotec), CD44 (#130-113-900, Miltenyi Biotec), Epcam (#14-9326-82, Thermo Fisher), Ki67 (#MAB7617, R&D Systems, Minnneapolis, MN, USA), and N-cadherin (#ab98952, Abcam, Cambridge, England). Patient-derived CAF were immunofluorescence labeled for αSMA (#19245S, Cell Signaling, Danvers, MA, USA). For flow cytometric analysis of the T-cells from the tumor tissue, immune cells were isolated from the digested tumor tissue using MACS with biotinylated CD45 (#130-110-630, Miltenyi Biotec,) antibodies, followed by anti-biotin microbeads (#130-090-485,

Miltenyi Biotec) according to the manufacturer's instructions. Isolated immune cells were stained for FACS analysis as stated below.

Spheroid formation

For the generation of mono-culture spheroids composed of PANC-1 cells, further referred to as PANC-1 spheroids, 1500 PANC-1 cells in 50 µL DMEM with 2.5% (v/v) Matrigel (#356230, Corning, NY, USA) were added into an ultra-low attachment coated 96-well plate (#650970, Greiner Bio-One, Kremsmünster, Austria) and centrifuged at 1500 rpm for 5 min. Co-culture spheroids were generated according to our previous protocol [60]. Patient-derived spheroids (PDS) composed of patient-derived tumor cells and primary CAF accordingly.

Immunofluorescence staining of tumor slices

Formalin-fixed, paraffin-embedded (FFPE) PDAC tumor sections (1.5 µm) were kindly generated at the Institute of Pathology from the University Hospital Düsseldorf. All samples were anonymized and their use was approved by the ethics committee of the Heinrich Heine University Düsseldorf (study number 2022-2170). Tissue sections were deparaffinized using xylene and a graded ethanol series, followed by antigen retrieval in Tris(hydroxymethyl)aminomethane–ethylenediaminetetraacetic acid (Tris-EDTA) buffer (pH 9) for 15 min at 100 °C. After washing in Tris-buffered saline containing Tween 20 (TBS-T), sections were blocked for 1 h at 20 °C in phosphate-buffered saline (PBS) supplemented with 5% bovine serum albumin (BSA) and 0.01% Tween 20. Primary and secondary antibodies were diluted in blocking buffer and incubated with the sections for 1 h at 20 °C in the dark. Following incubation, slides were washed, mounted using fluorescence mounting medium (#GM30411-2, Agilent Technologies, Santa Clara, CA, USA), and allowed to dry overnight. Image acquisition was performed using the CellVoyager™ CQ1 High-Content Imaging System (#90ZA00673, Yokogawa Electric Corporation, Musashino, Japan).

Quantitative analysis of tumor slices

FFPE tissue sections of 10 PDAC patients form the Institute of Pathology from the University Hospital Düsseldorf were subjected to immunofluorescence staining for CD4 and CD8, followed by nuclear counterstaining with DAPI. 40 images per patient were captured at 40× magnification, with Z-stacks acquired to ensure accurate detection of cellular structures across all focal planes.

Image analysis was performed using CellProfiler (version 4.2.8 Supplementary Figure2.3-1). To improve segmentation accuracy, individual image planes were analyzed instead of maximum-intensity projections, thereby preserving spatial resolution and minimizing signal overlap in densely packed areas. Nuclei were identified based on DAPI staining using a deep learning-based segmentation approach. Specifically, the Cellpose algorithm was applied via a CellProfiler plugin to enable accurate instance segmentation of individual nuclei despite variable staining intensity and high tissue density [61]. Following nuclear segmentation, the expression of cell-associated markers was determined by quantifying the CD4 and CD8 fluorescence signals in the vicinity of each nucleus. Cells were classified as $CD4^+$ or $CD8^+$ based on marker-specific thresholds for fluorescence intensity, which

Immunofluorescence staining of spheroids

Spheroids were stained according to the MACS Clearing Kit protocol (#130-126-719, Miltenyi Biotec). Briefly, spheroids were fixed in 4% paraformaldehyde (PFA) for 1 h at room temperature (RT). Following fixation, samples were permeabilized for 6 h prior to incubation with 100 µL of primary antibody solution containing CD4 (#ab133616, Abcam), α-SMA (#19245S, Cell Signaling), pan-cytokeratin (#130-133-439, Miltenyi Biotec), CD8 (#130-110-815, Miltenyi Biotec) or CD45 (#130-110-638, Miltenyi Biotec) for 24 h at 4 °C. Subsequently, spheroids were incubated with the secondary antibody solution comprising Alexa Fluor 647 donkey (H+L) anti-mouse (#A-31571, Invitrogen) and Alexa Fluor 488 donkey (H+L) anti-rabbit (#A-21206, Invitrogen), Alexa Flour 405 donkey (H+L) anti mouse (#A-48257, Invitrogen) supplemented with 2 µg/mL DAPI (#D9542, Sigma-Aldrich), for 24 h at 4 °C. Optical clearing was performed by sequential incubation in ethanol solutions of increasing concentration (50%, 70%, and 100%) containing 2% Tween, each for 2 h, with the final 100% step carried out overnight. This was followed by incubation in clearing solution for 6 h. Cleared spheroids were then transferred to an imaging plate (#89626, ibidi GmbH, Gräfelfing, Germany) and imaged using the CQ1 High-Content Spinning Disk System (#90ZA00673, Yokogawa). 3D images were visualized using the 3D viewer plugin [61] in in the Fiji Software [62].

Quantitative real-time PCR (qRT-PCR)

To assess chemokine and effector molecule expression, quantitative real-time PCR (qRT-PCR) was performed on T-cells, PANC-1 cells, pancreatic stellate cells (PSC),

PANC-1 spheroids, co-culture spheroids, as well as patient-derived tumor cells, cancer-associated fibroblasts (CAF), and corresponding spheroids. The following primers were utilized to determine the mRNA levels of CXCL12, CXCR4, IFN-γ, Granzyme B, Perforin and glyceraldehyde-3-phosphate dehydrogenase (GAPDH) (forward, 5'-TGCACCACCAACTGCTTAGC-3'; reverse, 5'-GGCATGGACTGTGGTCATGAG-3'), CXCL12 (forward 5´-CTCAACACTCCAAACTGTGCCC-3´; reverse 5´- CTCCAGGTACTCCTGAATCCAC-3´), CXCR4 (forward 5´- CTCCTCTTTGTCATCACGCTTCC -3´; reverse 5´-GGATGAGGACACTGCTGTAGAG-3´), IFN-γ (forward 5´-GAGTGTGGAGACCATCAAGGAAG -3´; reverse 5´- TGCTTTGCGTTGGAC ATTCAAGTC -3´), Granzyme B (forward 5´- CGACAGTACCATTGAGTTGTGCG -3´; reverse 5´- TTCGTCCATAGGAGACAATGCCC-3´), Perforin (forward 5´- ACT CAC AGG CAG CCA ACT TTG C -3´; reverse 5´- CTCTTGAAGTCAGGGTGCAGCG-3´). 2D cell lines were cultivated for 72 h and spheroids for 96 h in RPMI medium. The qRT-PCR was performed as previously described by us [63]. Relative gene expression was calculated using the ΔΔCt method, with normalization to the housekeeping gene GAPDH. Quantitative data analysis was conducted using qPCRsoft 4.1 software (Analytik Jena, Jena, Germany).

Flow cytometry of T-cells

Checkpoint molecule expression in T-cells was analyzed by flow cytometry. PDAC spheroids and patient-derived spheroids were collected following infiltration with either PBMC-derived T-cells or autologous T-cells. Subsequently, spheroids were enzymatically dissociated into single-cell suspensions using Accutase (A1110501, Gibco). Cells were subsequently stained according to the manufacturers' protocols using the following fluorochrome-conjugated antibodies: CD45-VioGreen (#130-110-638, Miltenyi Biotec), CD8-FITC (#130-110-815, Miltenyi Biotec), CD4-VioBright-V600 (#130-129-579, Miltenyi Biotec), CD25-APC (#130-113-284, Miltenyi Biotec), CD69-VioBlue (#130-112-799, Miltenyi Biotec), CD223-APCVio770 (#130-130-284, Miltenyi Biotec), CD279-PerCP 5.5 (#367410, BioLegend, San Diego, CA, USA), CD3-AF700 (#367410, BioLegend), CD152-PEVio770 (#130-130-455, Miltenyi Biotec). Data acquisition was performed using a Cytek® Northern Lights flow cytometer (Cytek Biosciences, Fremont, CA, USA), and subsequent analyses were carried out with FlowJo software (version 10.9.0; BD, Ashland, OR, USA).

Semi-automatic spheroid analysis pipeline

Initially the three-channel raw image data (Supplementary Figure 3.3-2A) were split into individual files per channel are denoted as nuclei (nucleus marker DAPI), T-cells (CD45 T-cell marker) and shell (fibroblast marker α-SMA) in the subsequent paragraphs. All three channels were normalized using a quantile-based normalization strategy by stretching the intensity range to the 0.01 and 0.99 quantiles and clipping values to a range of [0,1] (Supplementary Figure 3.3-2B). T-cells were segmented using the TWANG algorithm [64] using the parameters σ_min=3,σ_max=4 for the Laplacian-of-Gaussian Scale-Space Maximum Intensity Projection (LoGSSMP). To suppress false positive detections in the background, only detections with an average intensity exceeding μ+2σ were kept, where μ is the mean intensity and σ is the standard deviation of the LoGSSMP intensity. The TWANG segmentation parameters were set to σ_grad=3,σ_kernel=2,r^s=1.3. Exemplary results of the detection are depicted in Supplementary Figure 3.3-2C.

The shell interior region was segmented in a semi-automatic fashion. A dedicated graphical user interface was used to annotate selected slices of the shell image channel. In the lateral image orientation (XY), annotations were performed at slice intervals of 25 and polygons were manually drawn along the inner edge of the interface between interior and surrounding shell in slices where the interior was properly visible. To faithfully reconstruct the 3D shape, two additional orthogonal views that were located in the center of the lateral annotations were annotated. Finally, the polygon points of all slice annotations were used to compute the 3D convex hull that served as an approximation of the interior region of the spheroid (Supplementary Figure 3.3-2D).

For the final quantifications, T-cells were assigned either to the inside of the spheroid or to the outside region. If a T-cell's segmentation intersected more than 50% with the semi-automatically created shell images, it was counted to the interior region, otherwise to the outside region and in addition to the absolute counts, the fraction of inside vs. outside T-cells was measured in percent. To further characterize the localization of the T-cells with respect to the spheroid center, the Euclidean distance of each T-cell to the centroid of the shell's interior region was computed and plotted as separate normalized histograms of the distance distributions of the inside and the outside T-cells (Supplementary Figure 3.3-2E).

Statistical analysis

For statistical and graphical analysis, the GraphPad Prism 8.0.2 software (GraphPad Software, Boston, MA, USA) was used. One-way analysis of variance (ANOVA) and unpaired t-test were used to test the statistical data, with p-values ≤ 0.05 considered statistically significant.

Results

To investigate the intratumoral distribution of T-cell subsets, immunofluorescence staining for CD8 and CD4 was performed on PDAC patient tumor slices. As shown in Figure 3.3-1A, B, a higher abundance of $CD4^+$ T-cells than $CD8^+$ T-cells was observed. Image based analysis of tumor slices from 10 PDAC patients was performed to quantify the CD4 and CD8 frequencies (Supplementary Figure 2.3-1). As shown in Figure 1C, the frequency of $CD4^+$ T-cells was 4.3-fold elevated compared to $CD8^+$ T-cells.

To validate these observations in fresh PDAC samples, flow cytometric analysis was conducted to determine the frequencies of $CD4^+$ and $CD8^+$ T-cells isolated from either tumor tissue or peripheral blood of five PDAC patients. Consistent with the immunofluorescence data, tumor-derived samples exhibited a significantly elevated frequency of $CD4^+$ T-cells, corresponding to a 2.6-fold increase relative to $CD8^+$ T-cells. Notably, a similar shift in the CD4/CD8 ratio toward $CD4^+$ T-cell predominance was detected in peripheral blood mononuclear cells (PBMC) from the same patients, with a 3.5-fold increase. To exclude age-related effects as a potential confounding factor, PBMC from age-matched healthy donors were analyzed. As shown in Figure 3.3-1D, PBMC from the control cohort displayed a 2.6-fold higher frequency of $CD8^+$ T-cells compared to PDAC patients, indicating that the altered CD4/CD8 ratio is associated with disease status rather than with age.

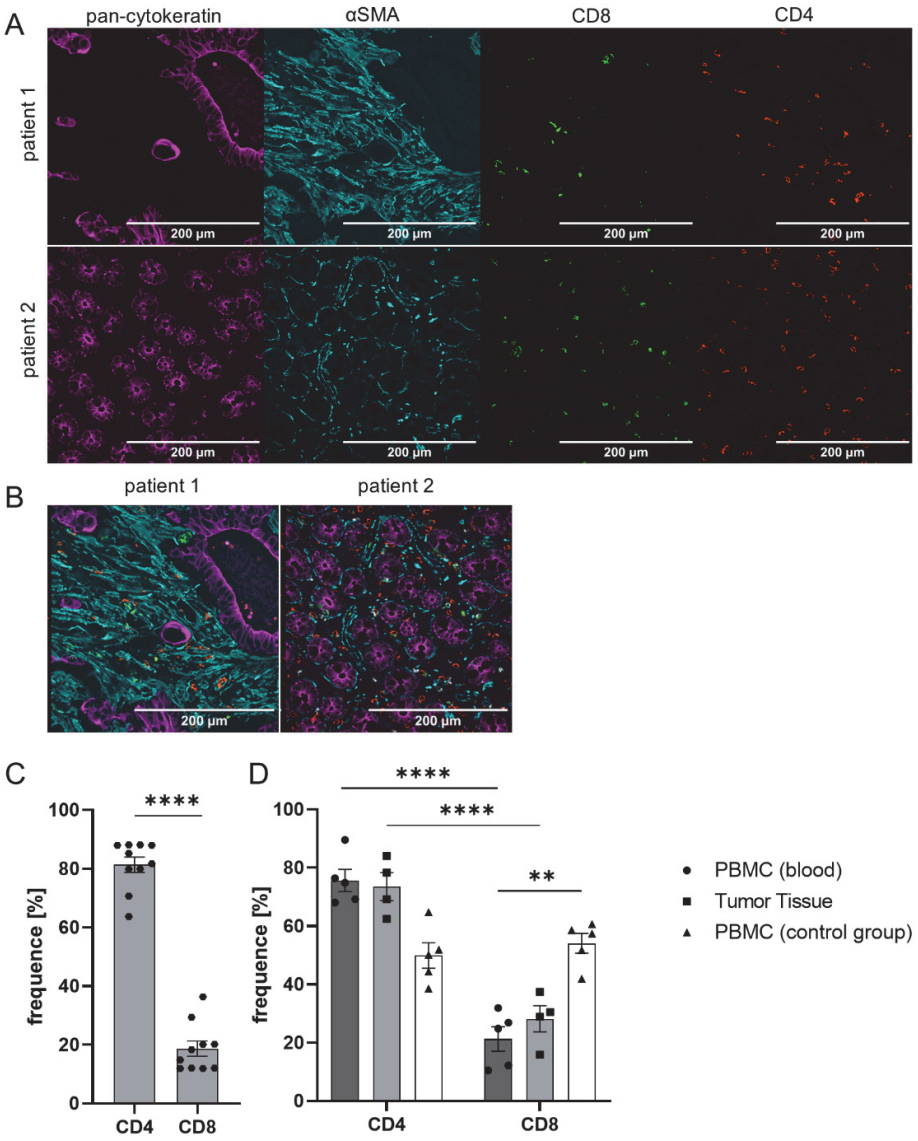


Figure 3.3-1 Intratumoral T-cell distribution and frequency in PDAC patients. Shown are two representative immunofluorescence staining of two tumor slices from PDAC patients with individual channels (A) alongside a merge of all fluorescence channels (B). Stained are the tumor cell marker pan-cytokeratin (magenta), the fibroblast marker alpha-smooth-muscle-actin (αSMA, cyan), and the T-cell markers CD8 (green) and CD4 (red). Scalebar: 200 µm. (C) Quantification of $CD4^+$ and $CD8^+$ percentages in tumor infiltrating lymphocytes (TIL). Percentages of $CD4^+$ and $CD8^+$ were quantified in tumor slices from 10 PDAC patients conducting image-based analysis. (D) Frequency plot of CD4 and CD8 percentages in PBMC and TIL. Frequency of $CD4^+$ and $CD8^+$ T-cells isolated from the blood of patients or the tumor tissue was analyzed via flow cytometry. PBMC from age-matched healthy donors served as a control group. Error bars indicate the standard errors of the mean of five independent patients, with ** = p≤0.01, **** = p ≤ 0.0001.

Beyond exclusion of cytotoxic T-cells, the TME of PDAC actively promotes T-cell exhaustion, which is characterized by the upregulation of immune checkpoint molecules and impaired T-cell function [25]. To evaluate the exhaustion status of T-cells, checkpoint molecule expression was analyzed by flow cytometry in T-cells isolated from tumor tissue and peripheral blood of PDAC patients. As shown in Figure

3.3-2, tumor-infiltrating T-cells exhibited a significantly increased expression of immune checkpoint molecules compared to peripheral blood-derived T-cells from the same patients. In $CD4^+$ T-cells (Figure 3.3-2A) expression levels of CTLA-4, PD-1, and LAG-3 were elevated by 2.4-fold, 5.7-fold, and 2.3-fold, respectively, relative to $CD4^+$ T-cells from PBMC. A comparable expression pattern was observed in $CD8^+$ T-cells, with a 2.4-fold increase in CTLA-4, a 2.4-fold increase in PD-1, and a 1.8-fold increase in LAG-3 expression (Figure 3.3-2B).

In addition, tumor-infiltrating $CD8^+$ T-cells displayed a 2.6-fold higher expression of the activation marker CD69 compared to their peripheral counterparts (Figure 3.3-2B). Collectively, these findings highlight the pronounced dysfunctional phenotype acquired by T-cells within the PDAC tumor microenvironment.

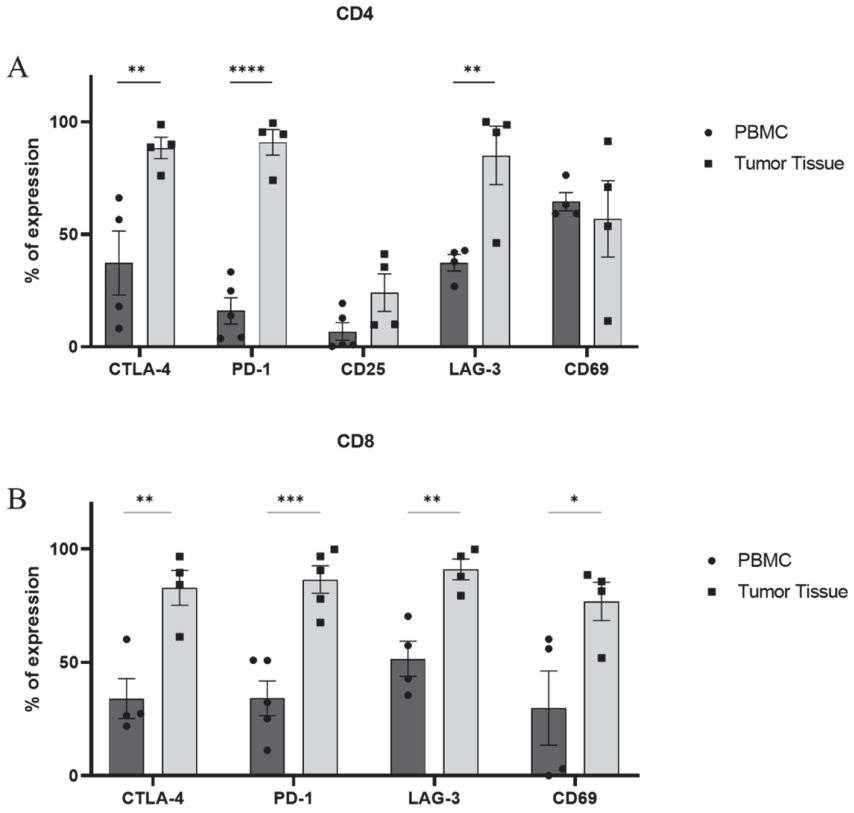


Figure 3.3-2 Checkpoint expression in T-cells isolated from the blood or the tumor tissue of PDAC patients. Checkpoint expression in $CD4^+$ (A) and $CD8^+$ (B) T-cells isolated from the blood or the tumor tissue of PDAC patients was analyzed by flow cytometry. T-cells identified as $CD3^+$ and $CD45^+$ were analyzed for surface expression of CTLA-4, PD-1, LAG-3 and CD69. T-cells isolated from the tumor tissue were compared to T-cells isolated from the blood. Error bars indicate the standard errors of the mean of four independent patients, with ** = $p \leq 0.01$; *** = $p \leq 0.005$; **** = $p \leq 0.0001$.

To enable the functional evaluation of novel immunotherapeutic strategies for PDAC, it is essential to recapitulate the immunosuppressive mechanisms operating within the

TME in vitro. We therefore established a simplified, human 3D spheroid platform designed mimic T-cell checkpoint upregulation and immune exclusion observed in PDAC patients.

PANC-1 spheroids composed of PANC-1 tumor cells alone or in combination with PSC were generated and infiltrated with $CD3^+$ T-cells isolated from healthy donor PBMC for 72 h. As shown in Figure 3.3-3, T-cell infiltration into both spheroid types resulted in a pronounced induction of immune checkpoint expression. In $CD4^+$ T-cells (Figure 3.3-3A), co-culture spheroids induced a 2.4-fold increase in CTLA-4, a 7.5-fold increase in PD-1, and a 1.4-fold increase in LAG-3 expression, whereas PANC-1 spheroids induced corresponding increases of 3.5-fold (CTLA-4), 6.2-fold (PD-1), and 1.3-fold (LAG-3). In $CD8^+$ T-cells (Figure 3.3-3B), co-culture spheroids led to a 3.7-fold increase in PD-1, and a 1.4-fold increase in LAG-3 expression, while PANC-1 spheroids induced corresponding increases 3.6-fold (PD-1), and 1.3-fold (LAG-3). No significant upregulation of CTLA-4, or CD69 was observed in $CD8^+$ T-cells under these conditions. Collectively, these data demonstrate that despite its simplicity, the co-culture 3D PDAC model robustly reproduces key features of checkpoint upregulation observed in infiltrating T-cells in PDAC tumors (Figure 3.3-2). Furthermore, the frequency of $FoxP3^+$ $CD25^+$ in $CD4^+$ T-cells increased 3.4-fold following infiltration into PANC-1 spheroids and 3.0-fold in co-culture spheroids, indicating an expansion of immunosuppressive regulatory T-cell populations (Figure 3.3-3C).

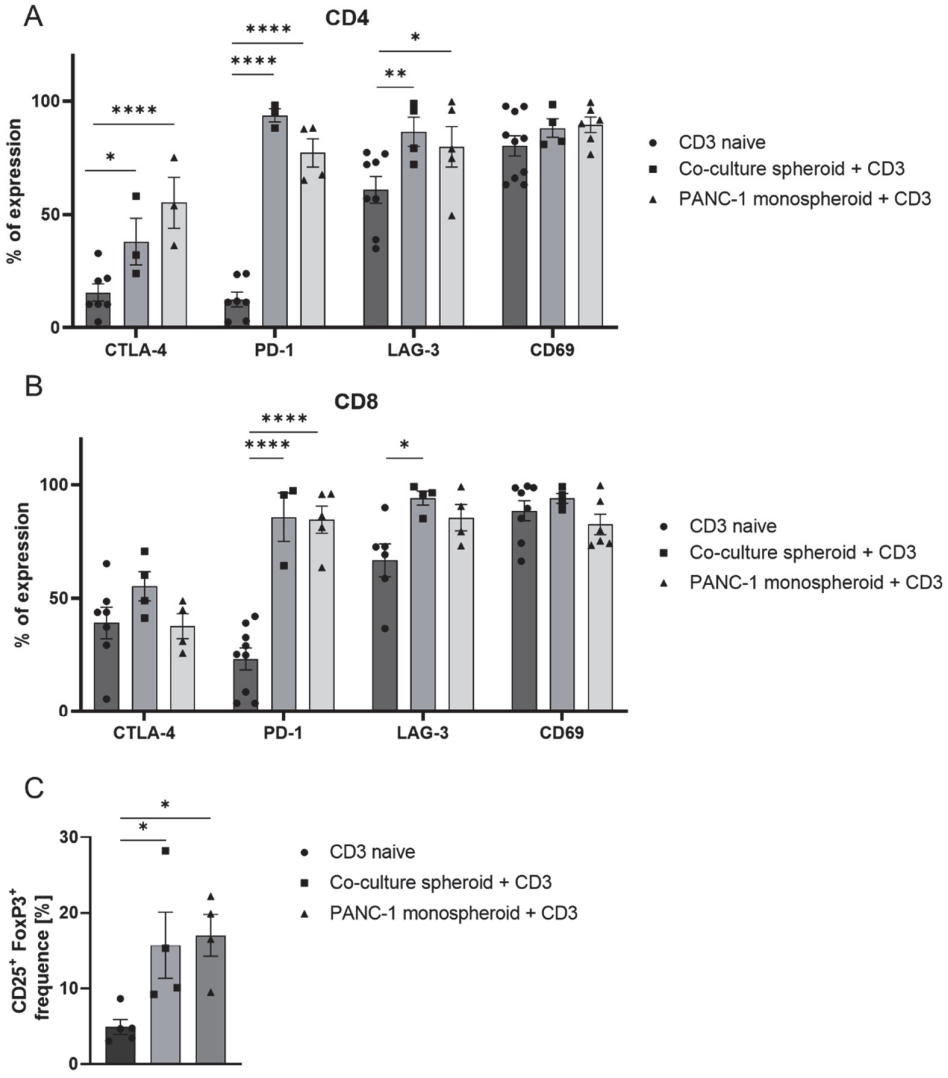


Figure 3.3-3 Checkpoint expression in T-cells after co-cultivation with PANC-1 spheroids. Checkpoint expression in $CD4^+$ (A) and $CD8^+$ (B) T-cells after co-cultivation with PANC-1 spheroids was analyzed by flow cytometry. PANC-1 spheroids were generated prior to infiltration with $CD3^+$ T-cell, isolated from PBMC from healthy donors. T-cells infiltration was performed for 72 h with either co-culture spheroids or PANC-1 monospheroids. T-cells identified as $CD3^+$ and $CD45^+$ were analyzed for surface expression of CTLA-4, PD-1, LAG-3 and CD69. Naïve T-cells isolated from the blood of healthy donors served as control. (C) Frequence of $CD25^+$ $FoxP3^+$ $CD4^+$ T-cells. Frequence of $CD25^+$ $FoxP3^+$ in $CD4^+$ T-cells was analyzed after 72 h of infiltration. Naïve T-cells isolated from the blood of healthy donors served as control. Error bars indicate the standard errors of the mean of at least three independent experiments from three different donors, with * = p≤0.05; ** = p≤0.01; **** = p ≤ 0.0001.

CAF are considered to be key mediators of T-cell exclusion in the PDAC TME through secretion of the chemokine CXCL12, which binds the chemokine receptor CXCR4 on T-cells sequestering them within the peritumoral stroma [21]. To assess whether this stromal-driven immune exclusion could be recapitulated in vitro, T-cell infiltration was compared between PANC-1 monospheroids and PSC-containing co-culture spheroids.

As illustrated in Figure 3.3-4, T-cells efficiently and homogeneously infiltrated monospheroids. In contrast, in PSC-containing co-culture spheroids, T-cells predominantly accumulated at the stromal outer layer, failing to penetrate the spheroid core. These findings indicate that stromal fibroblasts establish both a physical and functional barrier, restricting T-cell infiltration.

Consistent with this observation, expression analysis demonstrated significantly elevated CXCL12 levels in PSC and PSC-containing spheroids compared with PANC-1 tumor cells (Supplementary Figure 3.3-3). In parallel, CXCR4 expression was enriched on $CD3^+$ T-cells, indicating a CXCL12–CXCR4 axis–dependent mechanism underlying T-cell retention at the stromal compartment.

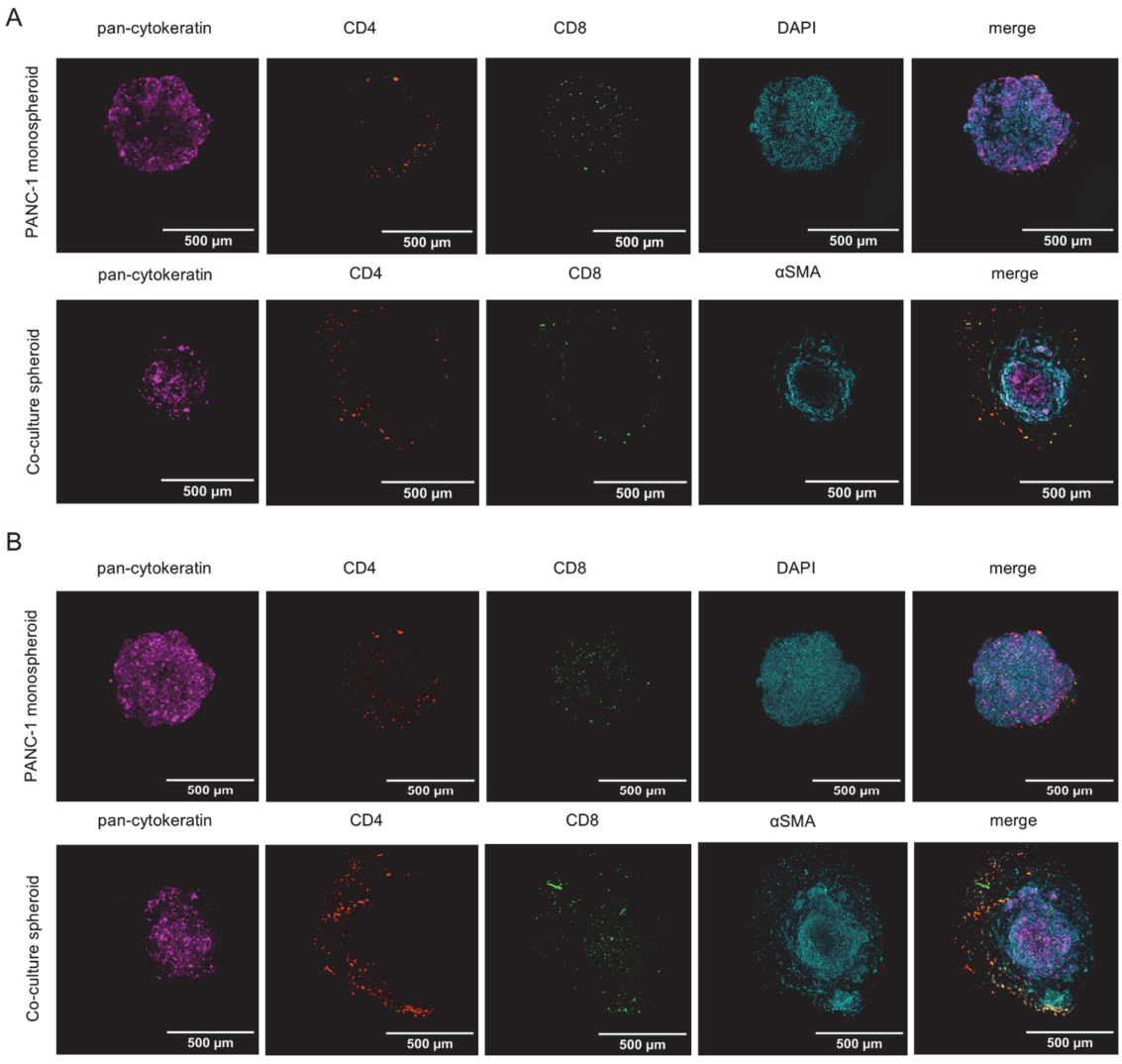


Figure 3.3-4 T-cell infiltration into PANC-1 spheroids. Shown are representative immunofluorescence images of PANC-1 spheroids with $CD3^+$ T-cells. PANC-1 monospheroids or co-culture spheroids containing PSC were infiltrated with $CD3^+$ T-cells isolated from PBMC from healthy donors for 72 h. Spheroids were stained for pan-cytokeratin (tumor cells, purple), CD4 (green), CD8 (red), and either

nuclei or α-SMA (fibroblast) (blue). Representative single optical sections from a z-stack (A) and maximum intensity projections (MIP) of the complete z-stack (B) for the single channels alongside a merge of all fluorescence channels are shown. Scale bar, 500 µm; magnification, 10x.

Patient-derived systems provide higher translational relevance by preserving tumor heterogeneity, authentic stromal signaling, and autologous immune interactions that cannot be captured by conventional cell line–based models. Therefore, a patient-derived spheroid (PDS) model was established, composed of patient-derived tumor cells and CAF, and subsequently infiltrated with autologous T-cells. Primary tumor cells were characterized by immunofluorescence staining using established tumor cell markers [59], while CAF identity was confirmed by α-SMA expression (Supplementary Figure 3.3-4). As shown in Figure 3.3-5, patient-derived tumor cells and CAF self-assemble into co-culture spheroids in a manner comparable to the cell line-based model, resulting in the formation of a distinct fibrotic shell surrounding a tumor cell-rich core. Maximum intensity projections are provided in Supplementary Figure 3.3-5. Notably, compared to the cell line–based model, the fibrotic stromal compartment was even more pronounced in the patient-derived system.

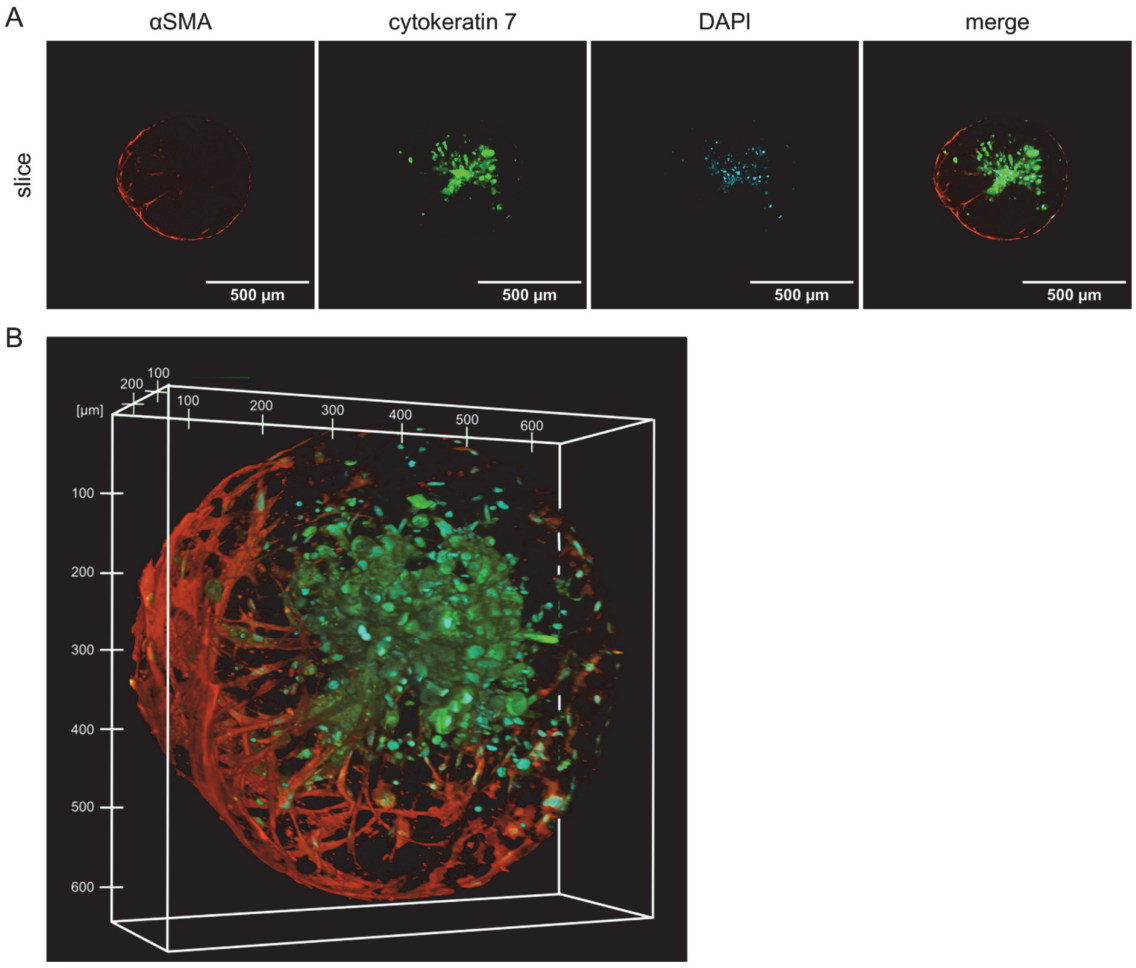


Figure 3.3-5 Composition of patient-derived spheroids (PDS). (A) Spheroids composed of patient-derived tumor cells and patient-derived CAF were generated for four days. Spheroids were stained with the fibroblast marker α-SMA (red), the tumor cell marker cytokeratin 7 (green), and the nuclei (blue). Shown are representative single optical sections from a z-stack for the single channels alongside a merge of all fluorescence channels. Scale bar, 500 µm; magnification, 10×. (B) 3D-rendered confocal Z-stack image of a patient derived spheroid, consisting of 300 slices each 0.5 µm per step, visualized using Image Software Fiji with the 3D Viewer plugin. For enhanced clarity, the spheroid was spatially cut in half, allowing better visualization of the fibrotic shell, the nuclei and the tumor cells. The spatial orientation of the section is indicated. Scale bar are 100 µm steps. Magnification 20x.

Furthermore, T-cells were largely restricted from infiltrating the tumor cell core by the fibrotic shell (Figure 3.3-6A), thereby recapitulating the T-cell exclusion previously observed in the cell line-based co-culture spheroids These findings are further supported by elevated CXCL12 expression in patient-derived CAF and patient-derived spheroids compared to primary tumor cells (Supplementary Figure 3.3-3B).

In addition to immune exclusion, increased expression of immune checkpoint molecules was observed upon T-cell infiltration (Figure 3.3-6B, C). In infiltrated $CD4^+$ T-cells, PD-1 expression increased 6.0-fold, and LAG-3 expression increased 1.9-fold. The upregulation of CTLA-4 and CD69 did not reach statistical significance in $CD4^+$ T-

cells. In $CD8^+$ T-cells, PD-1 and LAG-3 expression increased 3.5-fold and 2.1-fold, respectively, whereas CTLA-4 and CD69 did not show significant changes. Collectively, these results recapitulate the checkpoint molecule expression signature previously observed in tumor infiltrating T-cells (Figure 3.3-2). Furthermore, the frequence of $FoxP3^+$ $CD25^+$ $CD4^+$ T-cells increased 7.3-fold upon infiltration into PDS (Figure 3.3-6D), indicating an expansion of the regulatory T-cell populations.

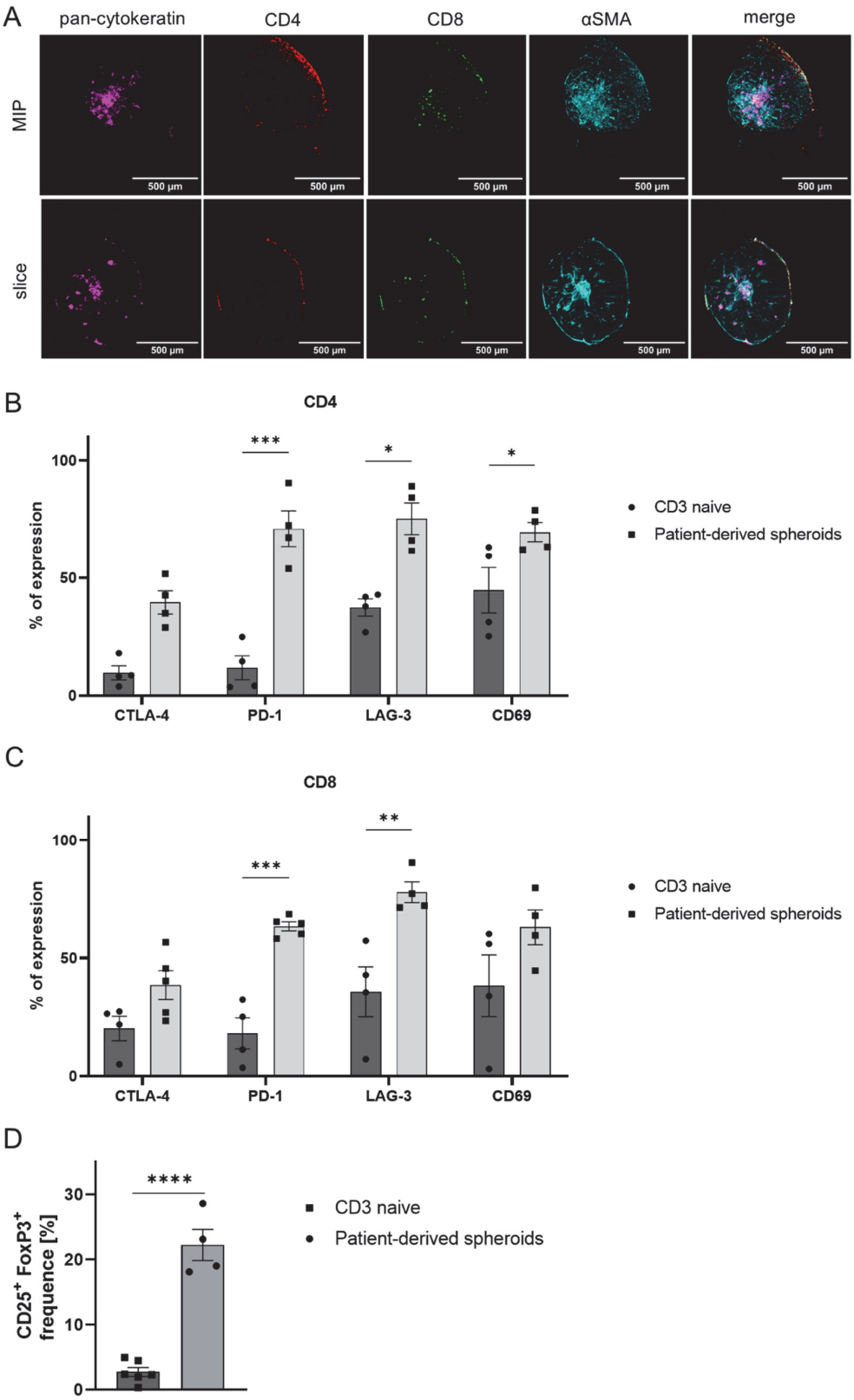


Figure 3.3-6 T-cell infiltration into patient-derived spheroids (PDS). (A) Representative immunofluorescence images of PDS following infiltration with autologous $CD3^+$ T-cells. Spheroids composed of patient-derived tumor cells and patient-derived CAF were infiltrated with autologous $CD3^+$

T-cells isolated from PBMC from the same PDAC patient for 72 h. Spheroids were stained for pan-cytokeratin (tumor cells, purple), CD4 (green), CD8 (red), and α-SMA (fibroblast) (blue). Representative maximum intensity projections (MIP) from a whole z-Stack and single optical sections from a z-stack for the single channels alongside a merge of all fluorescence channels are shown. Scale bar, 500 µm; magnification, 10×. (B, C) Checkpoint expression in T-cells after 72 h infiltration in PDS. Checkpoint expression in $CD4^+$ (B) and $CD8^+$ (C) T-cells after infiltration in PDS were analyzed by flow cytometry. T-cells identified as $CD3^+$ and $CD45^+$ were analyzed for surface expression of CTLA-4, PD-1, LAG-3 and CD69. (D) Frequence of $CD25^+$ $FoxP3^+$ $CD4^+$ T-cells. Frequence of $CD25^+$ $FoxP3^+$ in $CD4^+$ T-cells was analyzed after 72 h of infiltration. Autologous naïve T-cells isolated from the blood of the same patient served as a control. Error bars indicate the standard errors of the mean of at least four independent experiments with * = p≤0.05; ** = p≤0.01; ** = p≤0.001; **** = p ≤ 0.0001.

To overcome T-cell exclusion, several preclinical studies have applied CXCR4 antagonists, such as AMD3100, to disrupt the CXCL12–CXCR4 axis, thereby enhancing T-cell infiltration into the TME [21, 51, 67]. Moreover, Bockorny et al. demonstrated in a clinical trial that pharmacological CXCR4 inhibition increased intratumoral T-cell infiltration in PDAC patients [51].

To assess whether this phenomenon could be recapitulated in our models, co-culture spheroids and PDS were treated with AMD3100 for 24 h immediately following T-cell addition. As shown in Figure 3.3-7B, AMD3100 treatment resulted in increased T-cell infiltration into the co-culture spheroids. Notably, T-cells displayed a more homogeneous spatial distribution throughout the spheroid rather than being restricted to the fibrotic shell. A comparable effect was observed in patient-derived spheroids in the presence of autologous T-cells (Figure 3.3-7C). Quantitative image analysis was performed to determine the frequency of T-cells within the tumor core (Supplementary Figure 3.3-2). The analysis further confirmed a significant enhancement of T-cell infiltration upon CXCR4 blockade in both co-culture spheroids and PDS compared to untreated controls (Figure 3.3-7D, E). In the co-culture spheroids, the percentage of T-cells in the tumor cell core increased from 3.0% to 16.2% (±2.65%) following treatment with AMD3100 (**Fehler! Verweisquelle konnte nicht gefunden werden.D)**. In the PDS, the proportion of T-cells infiltrating the tumor core increased from 2.3% to 6.7 % (±1.75%) (**Fehler! Verweisquelle konnte nicht gefunden werden.E).**

Collectively, these findings indicate that inhibition of the CXCR4–CXCL12 axis effectively restores T-cell infiltration into the tumor cell region, further supporting the role of CAF-driven CXCL12 signaling as a clinically relevant mechanism of immune exclusion in PDAC.

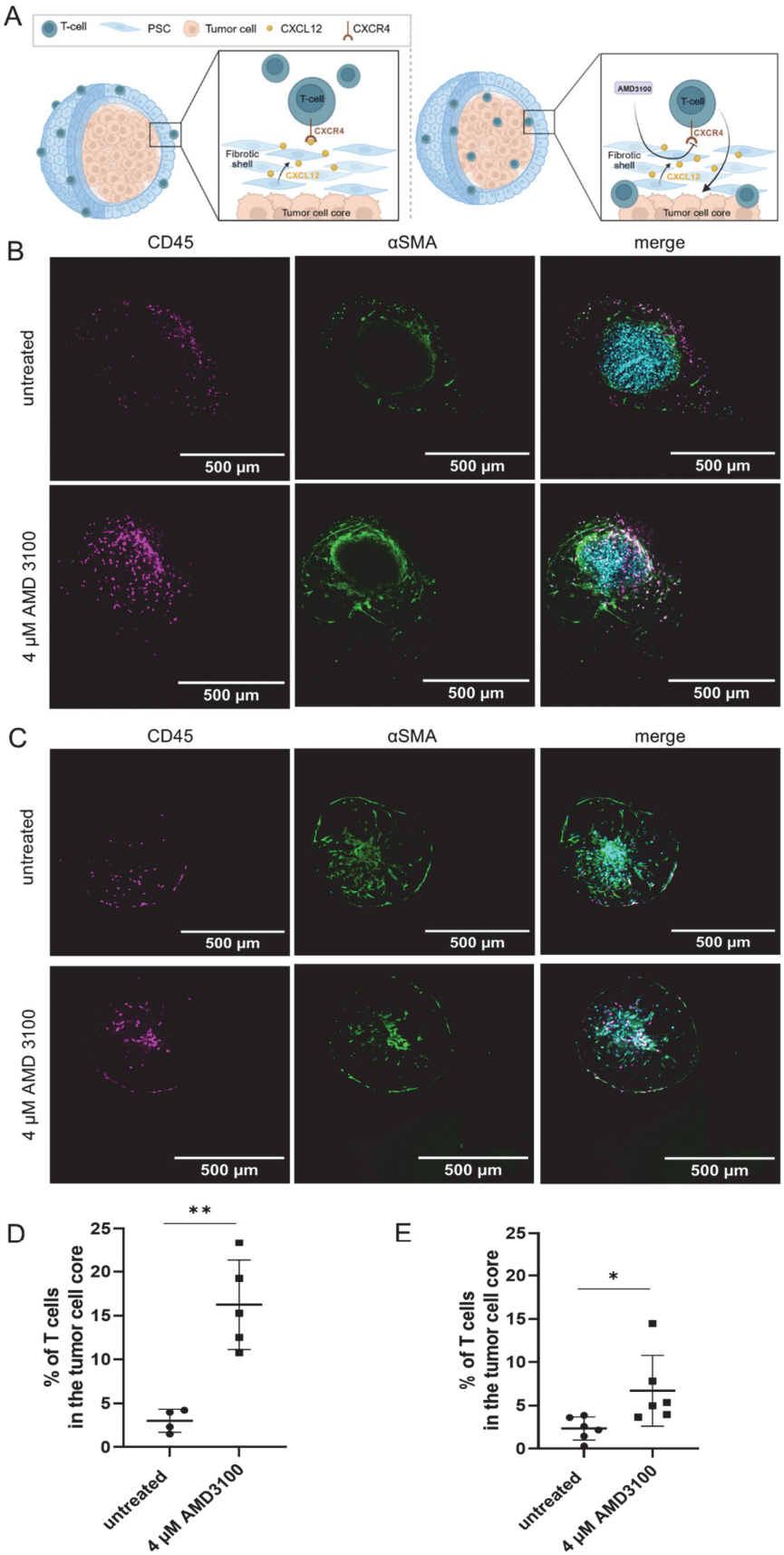

A
T-cell
PSC
Tumor cell
CXCL12
CXCR4
Fibrotic shell
Tumor cell core
AMD3100
B
CD45
αSMA
merge
untreated
4 µM AMD 3100
500 µm
C
D
E
% of T cells in the tumor cell core
**
*
untreated
4 µM AMD3100

Figure 3.3-7 T-cell infiltration in co-culture spheroids and PDS after AMD3100 treatment. (A) Schematic illustration of the mechanistic interaction of AMD3100 on T-cell infiltration. Created with BioRender. Representative IF staining of co-culture spheroids (B) and PDS (C) after infiltration with $CD3^+$ T-cells and treatment with AMD3100 for 24 h. Co-culture spheroids were infiltrated with $CD3^+$ T-cells isolated from healthy donors PBMC for 24 h. PDS were infiltrated with autologous T-cells derived from patients´ PBMC. Treatment with 4 µM AMD3100 was added directly after T-cell addition and performed for 24 h. Spheroids were stained for the T-cell marker CD45 (purple), the nuclei (blue), and the fibroblast marker α-SMA (green). Representative images of on layer of a z-stack (B, C) are displayed. Scale bar is 500 µm and the magnification 10x. (D, E) Quantification of the T-cell infiltration after treatment with AMD3100. The spheroids were divided into a shell region and a tumor cell core region based on the α-SMA signal. T-cells were associated with the core or shell region. Displayed are the percentage of T-cells in the tumor core region with or without 4 µM AMD 3100 treatment in co-culture spheroids (D) and PDS (E). Data represent the standard error of the mean of at least three independent experiments. Statistical significance is indicated as $*p \leq 0.05$, $**p \leq 0.01$.

Counteracting T-cell dyfunction and restoring effector function through immune checkpoint blockade targeting PD-1 has been widely employed to disrupt PD-1 engagement with its ligands [26]. However, in PDAC, clinical application of ICI, including the anti–PD-1 monoclonal antibody pembrolizumab, has demonstrated limited therapeutic benefit, with the exception of the small group of MSI-H/dMMR patients [26, 39, 48, 51, 54].

To evaluate the functional impact of PD-1 blockade in our 3D PDAC models, we quantified IFN-γ, Granzyme B and perforin mRNA expression in infiltrating T-cells following 72 h of pembrolizumab treatment. As shown in Figure 3.3-8A, treatment with 1 µg/mL and 10 µg/mL pembrolizumab resulted in a 1.6-fold and 2.0-fold increase in IFN-γ mRNA expression, respectively, in T-cells infiltrating PANC-1 spheroids. In contrast, T-cells infiltrating co-culture spheroids containing PSC did not exhibit a significant increase in IFN-γ expression upon PD-1 blockade. In PDS pembrolizumab induced a 5.0-fold and 3.4-fold increase in IFN-γ expression at 1 µg/mL and 10 µg/mL, respectively. Furthermore, treatment with pembrolizumab enhanced the expression of cytotoxic effector molecules in PDS. Granzyme B expression (Figure 3.3-8B) increased 2.6-fold following treatment with 1 µg/mL and 2.5-fold with 10 µg/mL pembrolizumab, while perforin expression (Figure 3.3-8C) was elevated 2.8-fold and 4.7-fold at the corresponding concentrations. In contrast, Granzyme B and perforin expression were not significantly altered in T-cells infiltrating PANC-1 or co-culture spheroids upon treatment. Flow cytometric analysis revealed increased expression of the effector molecules IFN-γ and Granzyme B in stimulated $CD8^+$ T cells following co-culture with PDS (Supplementary Figure 2.3-6). The frequency of IFN-γ^+ $CD8^+$ T cells increased from 12.5% to 17.2%, while granzyme B expression increased from 65.0% to 70.6% (Supplementary Figure 2.3-6A, B). Perforin expression showed a tendency

towards increased expression; however, this difference did not reach statistical significance (Supplementary Figure 2.3-6C). To determine whether these effects were attributable to altered PD-1 surface expression, flow cytometric analysis were performed following 72 h of treatment. As illustrated in Supplementary Figure 3.3-7 pembrolizumab did not affect PD-1 surface levels in either $CD4^+$ or $CD8^+$ T-cells. These findings indicate that the observed increase in effector molecule expression results from functional PD-1 blockade rather than modulation of PD-1 receptor expression.

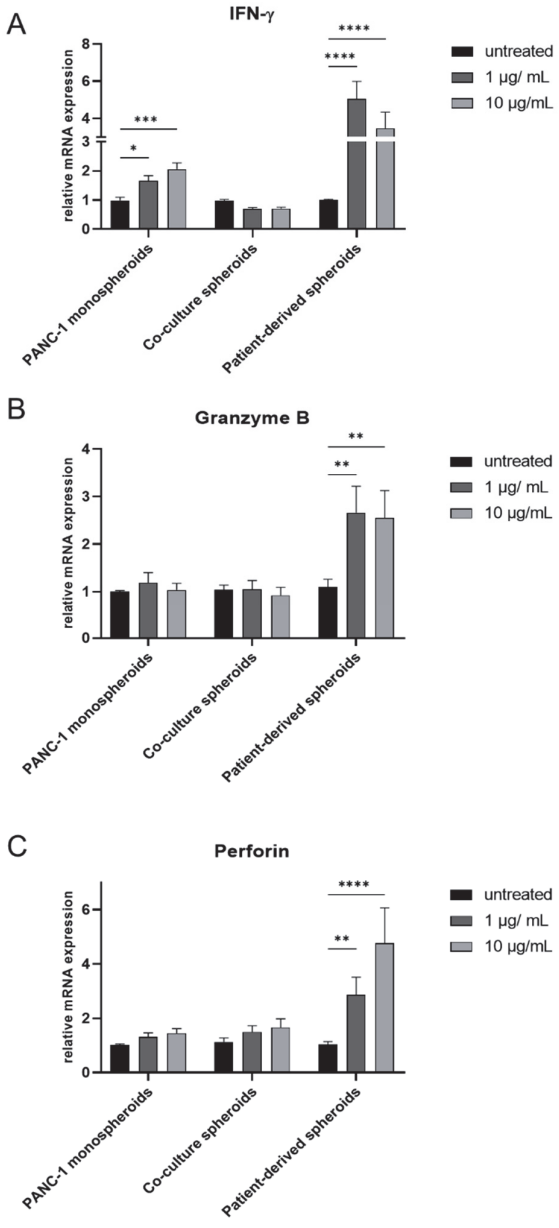


Figure 3.3-8 IFN-γ, Granzyme B and perforin expression following treatment with pembrolizumab. PDAC spheroids were infiltrated with $CD3^+$ T-cells isolated from PBMC from healthy donors or, in the case of

patient-derived spheroids (PDS), with autologous patient-derived PBMC. Pembrolizumab (1 µg/mL or 10 µg/mL) was added at the time of T-cell infiltration and maintained for 72 h. IFN-γ (A), Granzyme B (B) and perforin (C) mRNA expression was quantified by RT–qPCR. Data represent the mean ± SEM of three independent experiments. Statistical significance is indicated as *p ≤ 0.05, **p ≤ 0.01, ***p ≤ 0.001, and ****p ≤ 0.0001.

Discussion

T-cell dysfunction within the TME of PDAC is multifactorial and emerges from the interplay of multiple immunosuppressive mechanisms. Central processes are the accumulation of immunosuppressive Treg, a shift towards a $CD4^+$-dominant immune profile, the stromal-mediated exclusion of effector T-cells from the tumor core, and a pronounced upregulation of multiple immune checkpoint molecules, including LAG-3, CTLA-4, and PD-1 [3, 12]. Together, these mechanisms form a spatially and functionally distinct immune microenvironment that limits effective T-cell infiltration and promotes a functionally exhausted phenotype [12]. In line with these reports, we observed a shift in the CD4/CD8 ratio toward $CD4^+$ T-cells within the TIL, supporting the hypothesis of preferential accumulation of $CD4^+$ subsets in the TME of PDAC. Furthermore, consistent with previous studies tumor-infiltrating T-cells exhibited a significant upregulation of the immune checkpoint molecules CTLA-4, LAG-3, and PD-1[26, 68].

In line with the findings of Rodríguez et al. [55], we also detected an increased frequency of $CD4^+$ T-cells in the peripheral blood of PDAC patients compared to age-matched healthy donors. Our data, derived from matched tumor tissue and peripheral blood samples from the same patients, provide evidence for a coordinated shift toward a $CD4^+$-dominant immune profile at both systemic and intratumoral levels, suggesting a bidirectional interaction between tumor-derived immunomodulatory signals and systemic immune cell composition. To the best of our knowledge, this is the first study to directly demonstrate such a parallel alteration in the TME and peripheral blood within individual PDAC patients. However, the mechanistic relationship between these compartments remains to be elucidated further.

By recapitulating the basic spatial and stromal architecture of the PDAC TME in our PANC-1 spheroid models, we were able to reproduce key mechanisms underlying T-cell dysfunction observed in patients, including checkpoint upregulation, increased Treg frequencies, and stromal-mediated exclusion of T-cells. However, as PANC-1

spheroids lack an autologous T-cell response, we infiltrated patient-derived spheroids (PDS) with autologous T-cells. In contrast to previously described patient-derived organoids, our approach includes CAF-mediated stromal compartments, recapitulating T-cell–stromal interactions including the named hallmarks of T-cell dysfunction in PDAC [56, 69, 70]. Here, we demonstrate that infiltration of autologous T-cells into PDS results in a pronounced upregulation of immune checkpoint molecules, increased accumulation of Treg, and spatial restriction of T-cells to the stromal compartment. Importantly, our study highlights a progressive increase in physiological relevance across the applied in vitro models. This difference likely reflects the increasing restoration of stromal complexity across the models, whereby CAF-derived signaling and spatial organization critically shape T-cell access and functional activation [71]. In contrast, PDS more closely resemble the complexity of the human PDAC tumor microenvironment by preserving patient-specific stromal architecture, tumor heterogeneity, and autologous immune interactions. Consequently, functional T-cell responses were most pronounced and most clinically aligned in the PDS model, suggesting that stromal complexity and cellular origin critically determine the extent of immunological modulation. This further emphasize the relevance of autologous, patient-derived systems for evaluating patient-specific responses to cell-based therapeutic approaches for PDAC.

It has been demonstrated that T-cell exclusion from the tumor core in PDAC is mediated by CAF via CXCL12–CXCR4 signaling [21]. To overcome this mechanism, the FDA-approved CXCR4 antagonist AMD3100 has been employed in several studies, which collectively demonstrated increased T-cell infiltration in vitro, in vivo, and in clinical trials [21, 51, 67, 72]. These findings underscore the translational relevance of the CXCL12–CXCR4 axis as a key driver of stromal-mediated T-cell exclusion in PDAC. In our model, disruption of the CXCL12–CXCR4 axis with AMD3100 reduced chemokine-driven T-cell retention and thereby significantly increased T-cell infiltration into the tumor core region in both co-culture spheroids and PDS. In PDS, this effect was less pronounced compared to that in PANC-1 co-culture spheroids. The reduced proportion of T-cells within the tumor core in PDS likely reflects a migration-restrictive effect imposed by the denser fibrotic stromal compartment, which limits T-cell penetration despite chemokine axis blockade. However, this structural organization more accurately reflects the spatial architecture of the PDAC TME in vivo, in which the fibrotic component can comprise up to 80% of the TME [6].

ICI represent an effective strategy to counteract T-cell exhaustion and restore effector function [11]. In PDAC, several ICI have been evaluated in both monotherapy and combination regimens [11, 26, 53]. However, their clinical efficacy has remained very limited, with the exception of the rare (approximately 1.2%) MSI-H/dMMR patient subgroup, in which pembrolizumab has been approved by the FDA [54]. Here, we demonstrate an increased expression of the effector molecules IFN-γ, Granzyme B, and perforin in autologous T-cells infiltrating PDS following pembrolizumab treatment. As reported by James et al., this effect is patient-dependent and warrants further investigation in additional PDAC patients using established PDS models [73]. In contrast, no significant changes in Granzyme B or perforin expression were observed in T-cells infiltrating cell line–based spheroids. For IFN-γ, only T-cells infiltrating PANC-1 spheroids exhibited an increase upon treatment with pembrolizumab. These findings are consistent with those of Daunke et al., who, using cell line–based PDAC spheroids, similarly observed no significant effect of pembrolizumab on effector molecule expression [74]. Taken together, these results support the hypothesis that blockade of the PD-1/PD-L1 axis alone is insufficient to overcome the complex immunosuppressive TME in PDAC [53]. In this context, our study provides a basis for further investigations into the efficacy of ICI in physiologically relevant preclinical PDAC models. Novel checkpoint targets such as LAG-3, T-cell immunoglobulin and mucin domain-containing protein 3 (TIM-3), and T-cell immunoreceptor with Ig and ITIM domains (TIGIT) are currently under investigation [11], and may enhance therapeutic efficacy when used as combinatorial co-inhibitory targets alongside PD-1/PD-L1-directed therapies.

Overall, our findings underscore that immune evasion in PDAC is driven by both T-cell exclusion and checkpoint-associated T-cell dysfunction. Importantly, the CXCL12–CXCR4 axis and PD-1 signaling appear to contribute to distinct yet complementary mechanisms of immunosuppression. While CXCR4-mediated signaling presumably limits T-cell infiltration into the tumor microenvironment, PD-1 signaling contributes to impaired T-cell effector function. Consequently, a combined targeted intervention on the PD-1/PD-L1 signaling pathway and the CXCR4–CXCL12 axis could represent a promising strategy to overcome key mechanisms of immune evasion in PDAC by simultaneously enhancing T-cell infiltration and restoring cytotoxic activity. To support this concept, Bockorny et al. clinically evaluated the combination of the CXCR4 antagonist motixafortide with pembrolizumab and reported increased intratumoral T-

cell infiltration, as well as an overall response rate of 32% and a median duration of response of 7.8 months [51]. Our 3D co-culture model provides a suitable platform for combinatorial drug testing and could facilitate further investigation of the potential synergistic effects of PD-1 blockade and CXCR4 inhibition in PDAC.

We acknowledge that this study has several limitations, which highlight important directions for future research. First, the inclusion of a relatively small patient cohort (n = 5) may limit the robustness and generalizability of our findings. Further studies should include larger patient cohorts to validate the patient-derived findings of this study and to investigate the heterogeneity of patient-specific responses. Nevertheless, our results are consistent with those reported in larger patient cohorts [23, 24]. Second, we present initial proof-of-concept data for PDS as a novel experimental platform and for the CXCR4-CXCL21 axis as one putative therapeutic approach for ICI co-treatment. Further studies incorporating a larger number of patient-specific models will be required to evaluate patient-specific response differences. Furthermore, a more comprehensive investigation of the signaling pathways underlying the distinct mechanisms of T-cell dysfunction including transcriptomic analysis may enable the identification of novel therapeutic targets beyond the CXCR4-CXCL12 axis to overcome immune suppression in PDAC. To this end, the incorporation of additional cellular components of the TME including other immune cell types or neuronal structures will be essential [75].

Overall, our results support a multifaceted and spatially organized model of T-cell dysfunction in PDAC, in which immune evasion arises from the coordinated interplay of multiple mechanisms rather than isolated signaling pathways. Immune dysfunction is not driven by a single dominant process but instead emerges from the interaction of stromal-mediated T-cell exclusion via the CXCL12–CXCR4 axis, immune checkpoint upregulation leading to functional exhaustion, and the accumulation of regulatory T-cell populations that further reinforce immunosuppression [6, 76]. Within this framework, CAF act as central orchestrators by shaping both the physical architecture of the TME and its immunological landscape [5, 6]. This spatial and functional compartmentalization not only restricts T-cell infiltration but also limits effective effector function, thereby contributing to the pronounced resistance of PDAC to current immunotherapeutic strategies [76].

In summary, we identified key determinants of T-cell dysfunction in PDAC, including immune checkpoint upregulation, stromal exclusion, and the accumulation of regulatory T-cells. Despite its simplicity, our 3D models are able to recapitulate these hallmark mechanisms of immune evasion in PDAC, providing a scalable and robust tool for studying TME-driven immunosuppression and functional characterization of immunotherapeutic approaches. However, additional experimental patient-derived models recapitulating both the complex spatial organization and the full functional and multicellular complexity of the TME are essential to dissect these interconnected mechanisms and to evaluate future therapeutic strategies for PDAC.

Conflict of Interest

The authors declare that there is no conflict of interest.

Author Contributions

N.E.T. and A.D. designed and conceived the experiments. A.D., L.H. and B.E.W. conducted the experiments. A.D. analyzed the results. Tumor slices were provided by I.E.. Primary tumor tissue samples and blood were provided by D.W. and T.C.. T-cell infiltration quantification was performed by J.S. The original manuscript draft was written by A.D. The manuscript was edited by A.D. and N.E.T and finally revised by N.E.T., I.E., J.S., D.W. and T.C.. Supervision and project conceptual design were conducted by N.E.T. Resources were provided by N.E.T., I.E., D.W. and J.S.. All authors have read and agreed to the published version of the manuscript.

Funding

This work was supported by a grant to N.E.T by the Bundesministerium für Bildung und Forschung, Technologie und Raumfahrt (BMFTR) (grant number 16LW0306K).

Acknowledgments

We express our gratitude he working group of Klaus Pfeffer at Heinrich Heine University Düsseldorf a for providing the Cytek flow cytometer.

Supplementary Material

Supplementary Table 2.3-1. Clinicopathological characteristics of the PDAC patient cohort included in this study.

Supplementary Figure 2.3-1. Workflow for quantification of $CD4^+$ and $CD8^+$ T cells in PDAC tissue slices

Supplementary Figure 2.3-2. Overview of the semi-automatic spheroid analysis pipeline

Supplementary Figure 2.3-3. CXCL12 and CXCR4 expression

Supplementary Figure 2.3-4. Characterization of primary patient-derived cells

Supplementary Figure 2.3-5. Composition of patient-derived spheroids (PDS)

Supplementary Figure 2.3-6. IFN-γ, Granzyme B and perforin protein expression following treatment with pembrolizumab

Supplementary Figure 2.3-7. Effect of pembrolizumab treatment on PD-1 surface expression.

Data Availability Statement

Data are available upon request.

Generative AI statement

The author(s) declared that generative AI was not used in the creation of this manuscript.

References

1. Mack, S., et al., Pancreatic Cancer: Epidemiology, Risk Factors, and Prevention. Onco, 2025. 5(3): p. 37.

2. Siegel, R.L., et al., Cancer statistics, 2025. CA Cancer J Clin, 2025. 75(1): p. 10-45.

3. Hartupee, C., et al., Pancreatic cancer tumor microenvironment is a major therapeutic barrier and target. Front Immunol, 2024. 15: p. 1287459.

4. Wu, Y., et al., The Role of Stellate Cells in Pancreatic Ductal Adenocarcinoma: Targeting Perspectives. Front Oncol, 2020. 10: p. 621937.

5. Thomas, D. and P. Radhakrishnan, Pancreatic Stellate Cells: The Key Orchestrator of The Pancreatic Tumor Microenvironment. Adv Exp Med Biol, 2020. 1234: p. 57-70.

6. Bräutigam, K., et al., Tumor immune microenvironment in pancreatic ductal adenocarcinoma revisited - Exploring the "Space". Cancer Lett, 2025. 622: p. 217699.

7. Norton, J., et al., Pancreatic Cancer Associated Fibroblasts (CAF): Under-Explored Target for Pancreatic Cancer Treatment. Cancers (Basel), 2020. 12(5).

8. Weizman, N., et al., Macrophages mediate gemcitabine resistance of pancreatic adenocarcinoma by upregulating cytidine deaminase. Oncogene, 2014. 33(29): p. 3812-9.

9. Yang, S., Q. Liu, and Q. Liao, Tumor-Associated Macrophages in Pancreatic Ductal Adenocarcinoma: Origin, Polarization, Function, and Reprogramming. Front Cell Dev Biol, 2020. 8: p. 607209.

10. Huber, M., et al., The Immune Microenvironment in Pancreatic Cancer. Int J Mol Sci, 2020. 21(19).

11. Thankachan, S.V., et al., Tumor Microenvironment: Recent Advances in Immunotherapies of Pancreatic Cancer. Medicina (Kaunas), 2025. 61(10).

12. Goulart, M.R., et al., T cells in pancreatic cancer stroma. World J Gastroenterol, 2021. 27(46): p. 7956-7968.

13. Protti, M.P. and L. De Monte, Immune infiltrates as predictive markers of survival in pancreatic cancer patients. Front Physiol, 2013. 4: p. 210.

14. Kerk, S.A., et al., Metabolic networks in mutant KRAS-driven tumours: tissue specificities and the microenvironment. Nat Rev Cancer, 2021. 21(8): p. 510-525.

15. Dey, P., et al., Oncogenic KRAS-Driven Metabolic Reprogramming in Pancreatic Cancer Cells Utilizes Cytokines from the Tumor Microenvironment. Cancer Discov, 2020. 10(4): p. 608-625.

16. Wang, S., Z. Li, and G. Hu, Prognostic role of intratumoral IL-17A expression by immunohistochemistry in solid tumors: a meta-analysis. Oncotarget, 2017. 8(39): p. 66382-66391.

17. Hegde, S., et al., Dendritic Cell Paucity Leads to Dysfunctional Immune Surveillance in Pancreatic Cancer. Cancer Cell, 2020. 37(3): p. 289-307.e9.

18. Liu, W., X. Wang, and W. Wu, Role and functional mechanisms of IL-17/IL-17R signaling in pancreatic cancer (Review). Oncol Rep, 2024. 52(5).

19. McAllister, F., et al., Oncogenic Kras activates a hematopoietic-to-epithelial IL-17 signaling axis in preinvasive pancreatic neoplasia. Cancer Cell, 2014. 25(5): p. 621-37.

20. Ene-Obong, A., et al., Activated pancreatic stellate cells sequester CD8+ T cells to reduce their infiltration of the juxtatumoral compartment of pancreatic ductal adenocarcinoma. Gastroenterology, 2013. 145(5): p. 1121-32.

21. Garg, B., et al., NFκB in Pancreatic Stellate Cells Reduces Infiltration of Tumors by Cytotoxic T Cells and Killing of Cancer Cells, via Up-regulation of CXCL12. Gastroenterology, 2018. 155(3): p. 880-891.e8.

22. Papalampros, A., et al., Unique Spatial Immune Profiling in Pancreatic Ductal Adenocarcinoma with Enrichment of Exhausted and Senescent T Cells and Diffused CD47-SIRPα Expression. Cancers (Basel), 2020. 12(7).

23. Wan, S., et al., Tumor infiltrating T cell states and checkpoint inhibitor expression in hepatic and pancreatic malignancies. Front Immunol, 2023. 14: p. 1067352.

24. Yousuf, S., et al., Spatially Resolved Multi-Omics Single-Cell Analyses Inform Mechanisms of Immune Dysfunction in Pancreatic Cancer. Gastroenterology, 2023. 165(4): p. 891-908.e14.

25. Saka, D., et al., Mechanisms of T-Cell Exhaustion in Pancreatic Cancer. Cancers (Basel), 2020. 12(8).

26. Balsano, R., et al., Pancreatic Ductal Adenocarcinoma and Immune Checkpoint Inhibitors: The Gray Curtain of Immunotherapy and Spikes of Lights. Curr Oncol, 2023. 30(4): p. 3871-3885.

27. Chen, L., Co-inhibitory molecules of the B7-CD28 family in the control of T-cell immunity. Nat Rev Immunol, 2004. 4(5): p. 336-47.

28. Li, H.B., Z.H. Yang, and Q.Q. Guo, Immune checkpoint inhibition for pancreatic ductal adenocarcinoma: limitations and prospects: a systematic review. Cell Commun Signal, 2021. 19(1): p. 117.

29. Long, L., et al., The promising immune checkpoint LAG-3: from tumor microenvironment to cancer immunotherapy. Genes Cancer, 2018. 9(5-6): p. 176-189.

30. Ju, Y., et al., Barriers and opportunities in pancreatic cancer immunotherapy. NPJ Precis Oncol, 2024. 8(1): p. 199.

31. Hodi, F.S., et al., Improved survival with ipilimumab in patients with metastatic melanoma. N Engl J Med, 2010. 363(8): p. 711-23.

32. Wang, J., T. Yang, and J. Xu, Therapeutic Development of Immune Checkpoint Inhibitors. Adv Exp Med Biol, 2020. 1248: p. 619-649.

33. Dang, T.O., et al., Pembrolizumab for the treatment of PD-L1 positive advanced or metastatic non-small cell lung cancer. Expert Rev Anticancer Ther, 2016. 16(1): p. 13-20.

34. Kim, J., et al., The Cancer Genome Atlas Expression Subtypes Stratify Response to Checkpoint Inhibition in Advanced Urothelial Cancer and Identify a Subset of Patients with High Survival Probability. Eur Urol, 2019. 75(6): p. 961-964.

35. Kasamon, Y.L., et al., FDA Approval Summary: Nivolumab for the Treatment of Relapsed or Progressive Classical Hodgkin Lymphoma. Oncologist, 2017. 22(5): p. 585-591.

36. Kudo, M., Targeted and immune therapies for hepatocellular carcinoma: Predictions for 2019 and beyond. World J Gastroenterol, 2019. 25(7): p. 789-807.

37. Arafat Hossain, M., A comprehensive review of immune checkpoint inhibitors for cancer treatment. Int Immunopharmacol, 2024. 143(Pt 2): p. 113365.

38. Tsujikawa, T., et al., Evaluation of Cyclophosphamide/GVAX Pancreas Followed by Listeria-Mesothelin (CRS-207) with or without Nivolumab in Patients with Pancreatic Cancer. Clin Cancer Res, 2020. 26(14): p. 3578-3588.

39. Katz, M.H.G., et al., Multicenter randomized controlled trial of neoadjuvant chemoradiotherapy alone or in combination with pembrolizumab in patients with resectable or borderline resectable pancreatic adenocarcinoma. J Immunother Cancer, 2023. 11(12).

40. Gross, N.E., et al., Phosphodiesterase-5 inhibition collaborates with vaccine-based immunotherapy to reprogram myeloid cells in pancreatic ductal adenocarcinoma. JCI Insight, 2024. 9(18).

41. O'Reilly, E.M., et al., Durvalumab With or Without Tremelimumab for Patients With Metastatic Pancreatic Ductal Adenocarcinoma: A Phase 2 Randomized Clinical Trial. JAMA Oncol, 2019. 5(10): p. 1431-1438.

42. Sharma, P., et al., Efficacy and tolerability of tremelimumab in patients with metastatic pancreatic ductal adenocarcinoma. Journal of Clinical Oncology. 36(4_suppl): p. 470-470.

43. Brahmer, J.R., et al., Safety and activity of anti-PD-L1 antibody in patients with advanced cancer. N Engl J Med, 2012. 366(26): p. 2455-65.

44. Royal, R.E., et al., Phase 2 trial of single agent Ipilimumab (anti-CTLA-4) for locally advanced or metastatic pancreatic adenocarcinoma. J Immunother, 2010. 33(8): p. 828-33.

45. Kalyan, A., et al., Ipilimumab and gemcitabine for advanced pancreas cancer: A phase Ib study. 2016, American Society of Clinical Oncology.

46. Ma, J., et al., Immune checkpoint inhibitors combined with chemotherapy for the treatment of advanced pancreatic cancer patients. Cancer Immunol Immunother, 2020. 69(3): p. 365-372.

47. Weiss, G.J., et al., Phase Ib/II study of gemcitabine, nab-paclitaxel, and pembrolizumab in metastatic pancreatic adenocarcinoma. Invest New Drugs, 2018. 36(1): p. 96-102.

48. Reiss, K.A., et al., Niraparib plus nivolumab or niraparib plus ipilimumab in patients with platinum-sensitive advanced pancreatic cancer: a randomised, phase 1b/2 trial. Lancet Oncol, 2022. 23(8): p. 1009-1020.

49. Pishvaian, M.J., et al., A Phase I/II Study of Veliparib (ABT-888) in Combination with 5-Fluorouracil and Oxaliplatin in Patients with Metastatic Pancreatic Cancer. Clin Cancer Res, 2020. 26(19): p. 5092-5101.

50. Naing, A., et al., Abstract CT177: Epacadostat plus durvalumab in patients with advanced solid tumors: preliminary results of the ongoing, open-label, phase I/II ECHO-203 study. Cancer Research, 2018. 78(13_Supplement): p. CT177-CT177.

51. Bockorny, B., et al., BL-8040, a CXCR4 antagonist, in combination with pembrolizumab and chemotherapy for pancreatic cancer: the COMBAT trial. Nat Med, 2020. 26(6): p. 878-885.

52. Wang-Gillam, A., et al., Phase I study of defactinib combined with pembrolizumab and gemcitabine in patients with advanced cancer. 2018, American Society of Clinical Oncology.

53. Al-Khinji, A., et al., Immune checkpoint inhibitors in pancreatic adenocarcinoma: a systematic review and meta analysis of clinical outcomes. Front Oncol, 2025. 15: p. 1569884.

54. Marabelle, A., et al., Pembrolizumab in microsatellite-instability-high and mismatch-repair-deficient advanced solid tumors: updated results of the KEYNOTE-158 trial. Nat Cancer, 2025. 6(2): p. 253-258.

55. Rodriguez, E., et al., In-depth immune profiling of peripheral blood mononuclear cells in patients with pancreatic ductal adenocarcinoma reveals discriminative immune subpopulations. Cancer Sci, 2024. 115(7): p. 2170-2183.

56. Lahusen, A., et al., A pancreatic cancer organoid-in-matrix platform shows distinct sensitivities to T cell killing. Sci Rep, 2024. 14(1): p. 9377.

57. Ajina, R. and L.M. Weiner, T-Cell Immunity in Pancreatic Cancer. Pancreas, 2020. 49(8): p. 1014-1023.

58. Blise, K.E., et al., Machine Learning Links T-cell Function and Spatial Localization to Neoadjuvant Immunotherapy and Clinical Outcome in Pancreatic Cancer. Cancer Immunol Res, 2024. 12(5): p. 544-558.

59. Chai, C., et al., Establishment and characterization of the PDAC-X3 cell line: a novel Chinese-origin pancreatic ductal adenocarcinoma cell line. Human Cell, 2024. 37(5): p. 1578-1592.

60. Xie, B.H., J.; Mundorf, V.; Betz, J.; Reimche, I.; Erkan, M.; Büdeyri, I.; Gesell, A.; Kerr, R.G.; Ariantari, N.P.; et al, Pseudopterosin and O-Methyltylophorinidine Suppress Cell Growth in a 3D Spheroid Co-Culture Model of Pancreatic Ductal Adenocarcinoma. Bioengineering, 2020.

61. Schmid, B., et al., A high-level 3D visualization API for Java and ImageJ. BMC Bioinformatics, 2010. 11: p. 274.

62. Schindelin, J., et al., Fiji: an open-source platform for biological-image analysis. Nat Methods, 2012. 9(7): p. 676-82.

63. Schiedlauske, K., et al., Novel Histone Deacetylase (HDAC) Inhibitor Induces Apoptosis and Suppresses Invasion via E-Cadherin Upregulation in Pancreatic Ductal Adenocarcinoma (PDAC). Pharmaceuticals, 2024. 17(6): p. 752.

64. Stegmaier, J., et al., Fast segmentation of stained nuclei in terabyte-scale, time resolved 3D microscopy image stacks. PLoS One, 2014. 9(2): p. e90036.

65. Sharma, P., et al., Primary, Adaptive, and Acquired Resistance to Cancer Immunotherapy. Cell, 2017. 168(4): p. 707-723.

66. Yang, X., et al., Targeting Proliferating Tumor-Infiltrating Macrophages Facilitates Spatial Redistribution of CD8(+) T Cells in Pancreatic Cancer. Cancers (Basel), 2022. 14(6).

67. Feig, C., et al., Targeting CXCL12 from FAP-expressing carcinoma-associated fibroblasts synergizes with anti-PD-L1 immunotherapy in pancreatic cancer. Proc Natl Acad Sci U S A, 2013. 110(50): p. 20212-7.

68. Brouwer, T.P., et al., Local and systemic immune profiles of human pancreatic ductal adenocarcinoma revealed by single-cell mass cytometry. J Immunother Cancer, 2022. 10(7).

69. Boilève, A., et al., Organoids for Functional Precision Medicine in Advanced Pancreatic Cancer. Gastroenterology, 2024. 167(5): p. 961-976.e13.

70. Morceau, F., et al., Pancreatic Cancer Organoids: Modeling Disease and Guiding Therapy. Cancers (Basel), 2025. 17(23).

71. Deipenbrock, A., et al., Modelling of the multicellular tumor microenvironment of pancreatic ductal adenocarcinoma (PDAC) on a fit-for-purpose biochip for preclinical drug discovery. Lab Chip, 2025.

72. Gok Yavuz, B., et al., Cancer associated fibroblasts sculpt tumour microenvironment by recruiting monocytes and inducing immunosuppressive PD-1(+) TAMs. Sci Rep, 2019. 9(1): p. 3172.

73. James, T.N., et al., Organoid Modeling of the Tumor Immune Microenvironment. Cell, 2018. 175(7): p. 1972-1988.e16.

74. Daunke, T., et al., Expression and role of the immune checkpoint regulator PD-L1 in the tumor-stroma interplay of pancreatic ductal adenocarcinoma. Front Immunol, 2023. 14: p. 1157397.

75. Shakiba, M. and D.A. Tuveson, Macrophages and fibroblasts as regulators of the immune response in pancreatic cancer. Nat Immunol, 2025. 26(5): p. 678-691.

76. Mercanti, L., et al., PDAC, the Influencer Cancer: Cross-Talk with Tumor Microenvironment and Connected Potential Therapy Strategies. Cancers (Basel), 2023. 15(11).

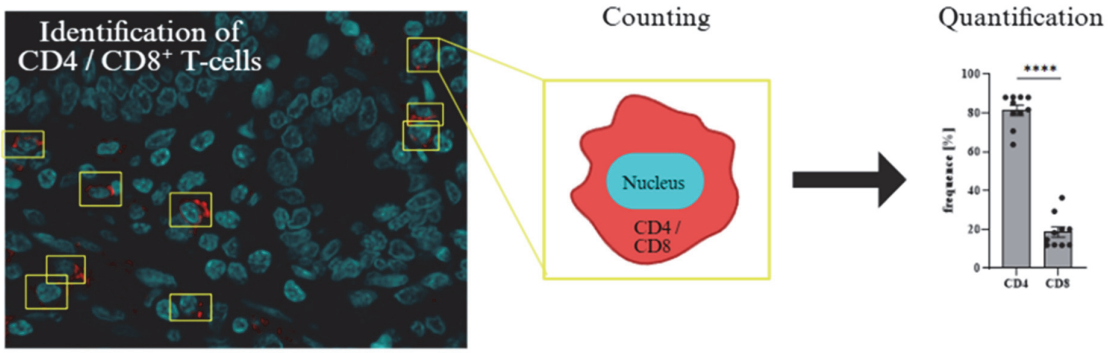
3.3.1 Supplementary Information

2.3.1.1 **Supplementary Figures and Tables**

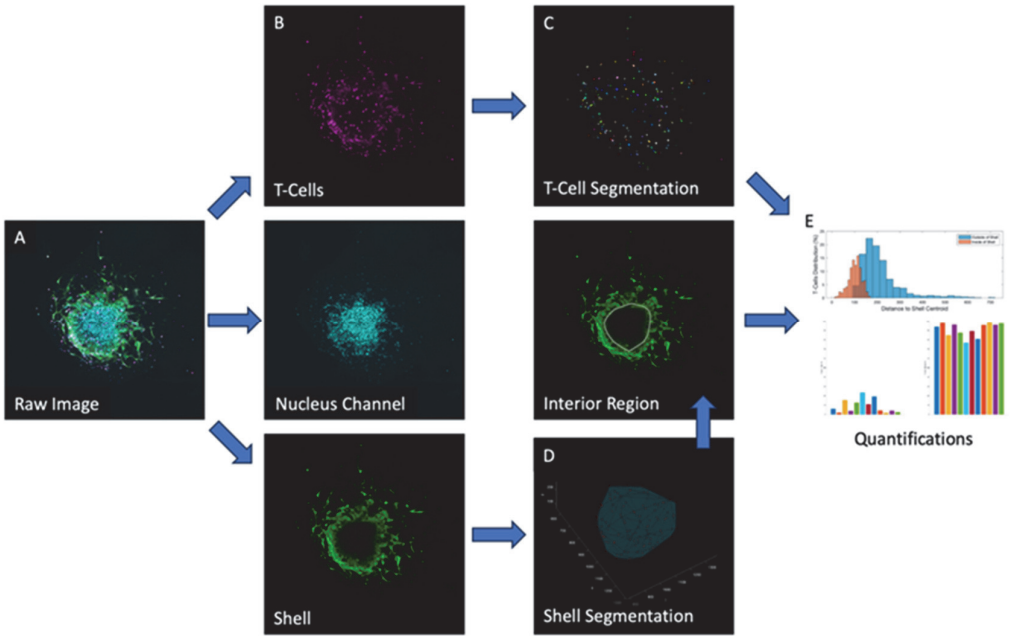
Supplementary Table 3.3-1 Clinicopathological characteristics of the PDAC patient cohort included in this study.

Patient	Grading	UICC-stadium	Neoadjuvant treatment	Surgical resection
1	G3 high grade	IV	No	Yes
2	G2 low grade	IB	No	Yes
3	G3 high grade	IIB	No	Yes
4	G2 low grade	IIB	No	Yes
5	G3 high grade	IB	No	Yes

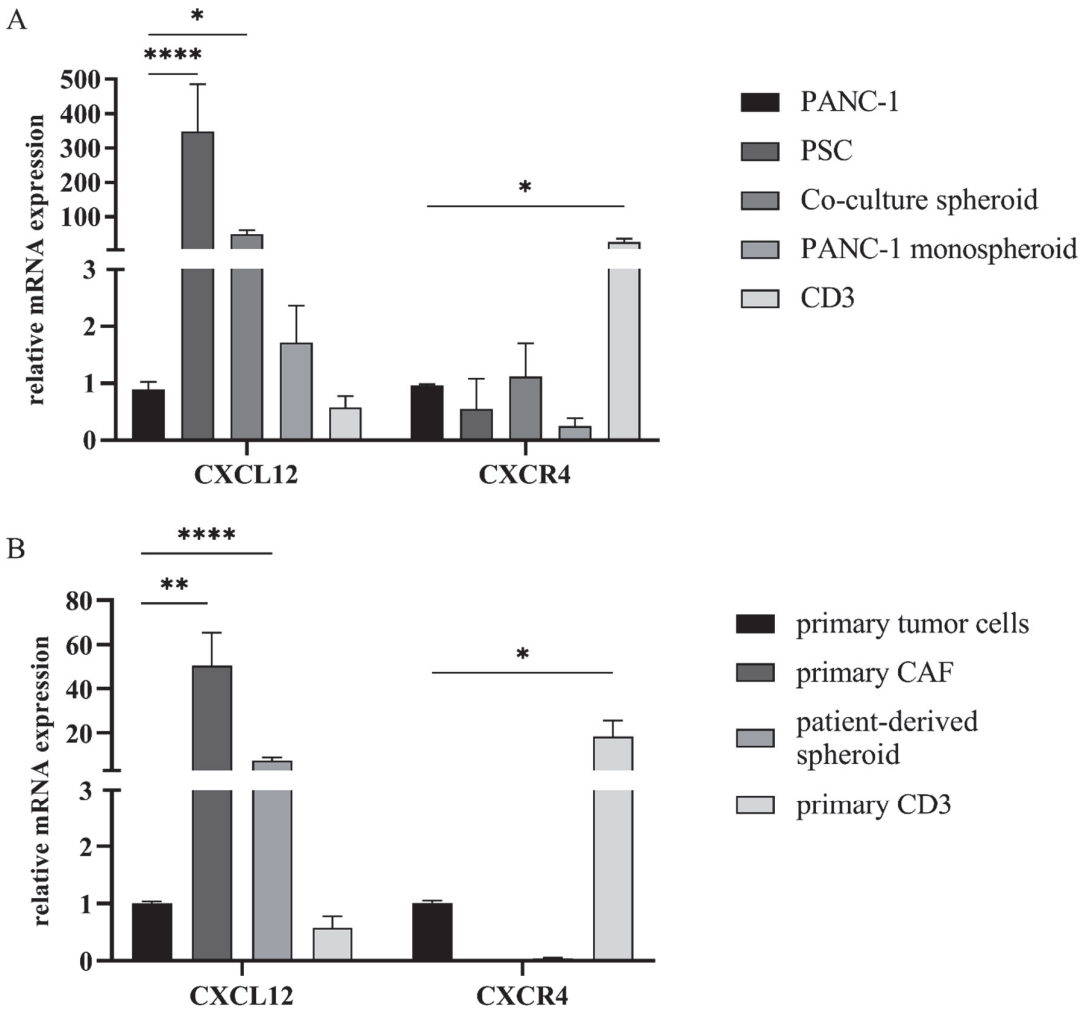
Supplementary Figures



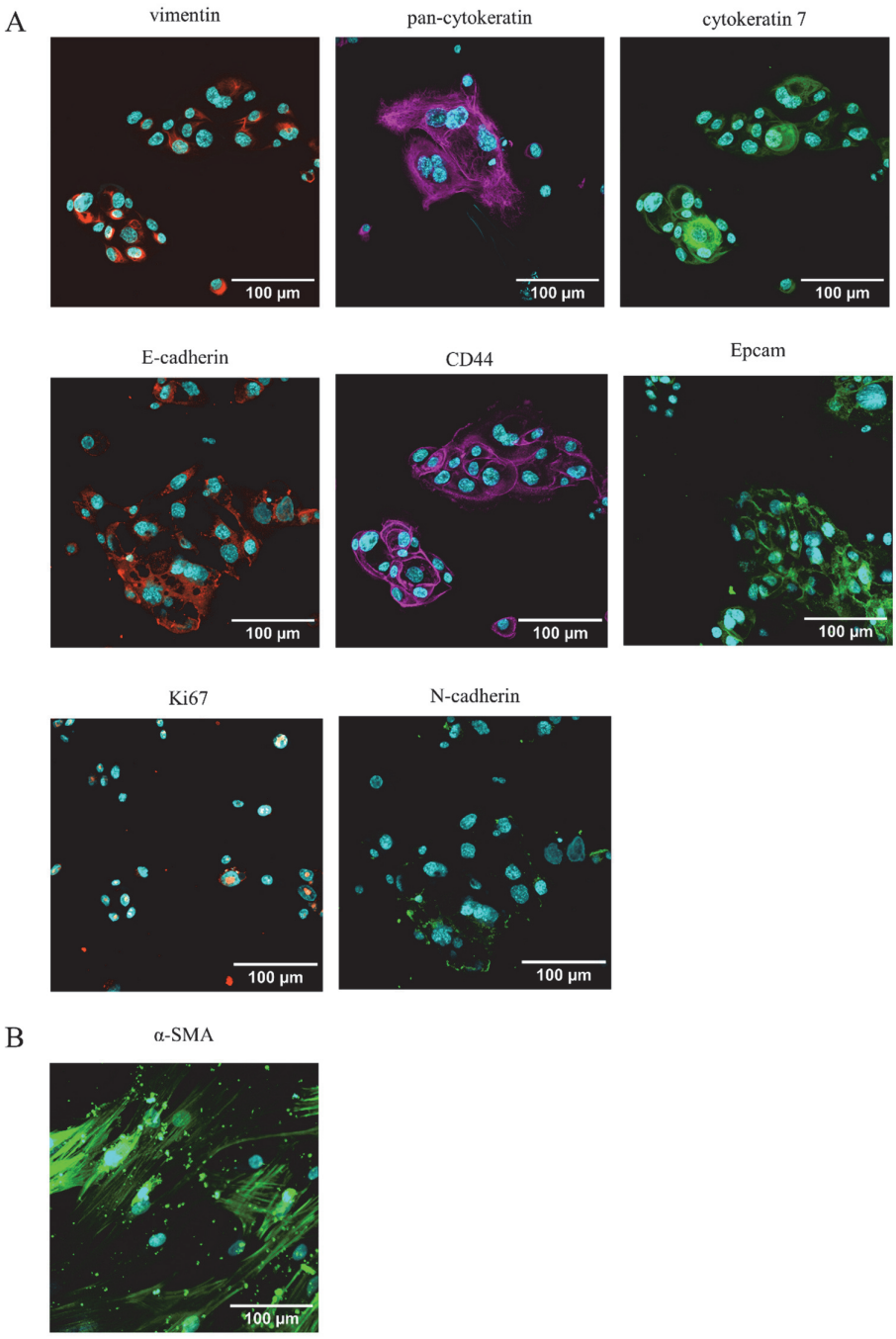
Supplementary Figure 2.3-1 Workflow for quantification of $CD4^+$ and $CD8^+$ T cells in PDAC tissue slices. Formalin-fixed paraffin-embedded (FFPE) tissue slices were subjected to immunofluorescence staining for CD4 and CD8, followed by nuclear counterstaining with DAPI. Individual nuclei were segmented based on DAPI staining, and CD4/CD8 fluorescence intensity was quantified in the vicinity of each nucleus. Cells were classified as $CD4^+$ or $CD8^+$ according to predefined marker-specific fluorescence intensity thresholds applied uniformly across all samples. The total number of $CD4^+$ and $CD8^+$ T cells was quantified per image and summarized for each patient. The schematic illustrates representative identification of $CD4^+$/$CD8^+$ T cells, nucleus-based cell assignment, and subsequent quantification of T-cell subset frequencies. Created with BioRender.



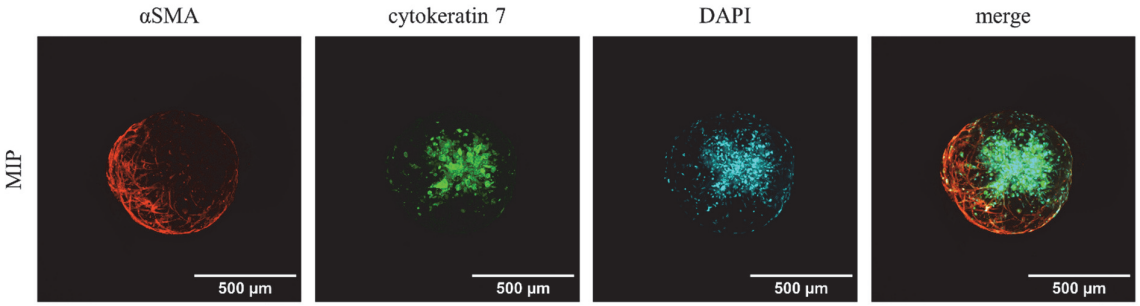
Supplementary Figure 3.3-2 Overview of the semi-automatic spheroid analysis pipeline. Three-channel raw images (A) were separated by channel and quantile normalized (B). The TWANG segmentation algorithm was used for instance segmentation of the T-cells (C). The shell's interior region was manually defined using a graphical user interface (D) and T-cell segmentations were associated with the interior/exterior region, respectively, based on their overlap with the manually defined interior region. Quantifications include distance distributions of T-cells from the interior centroid as well as absolute counts and occurrence frequencies of T-cells in the interior/exterior regions (E).



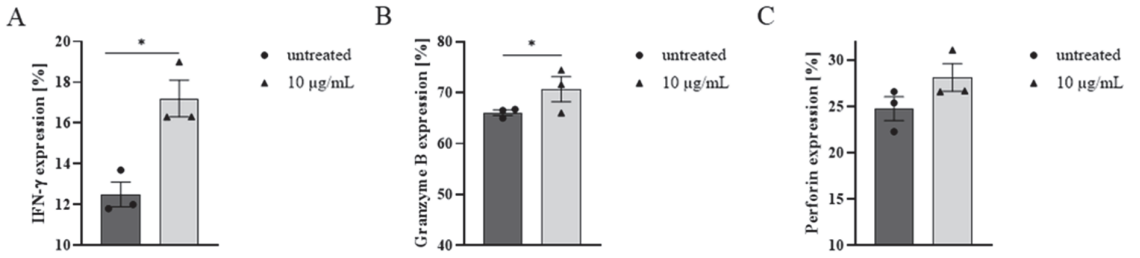
Supplementary Figure 3.3-3 CXCL12 and CXCR4 expression. mRNA Expression levels of CXCL12 and CXCR4 were analyzed by RT-PCR. (A) Comparison of different mRNA levels in PANC-1, PSC, Co-culture spheroids, PANC-1 monospheroids, and naïve CD3 T-cells isolated from healthy donors PBMC. (B) Expression of CXCL12 and CXCR4 mRNA levels in patient-derived tumor cells, CAF, patient-derived spheroids and CD3 T-cells isolated form the patients PBMC. Error bars indicate the standard errors of the mean of three independent experiments, with * = p≤0.05; ** = p≤0.01; **** = p ≤ 0.0001.



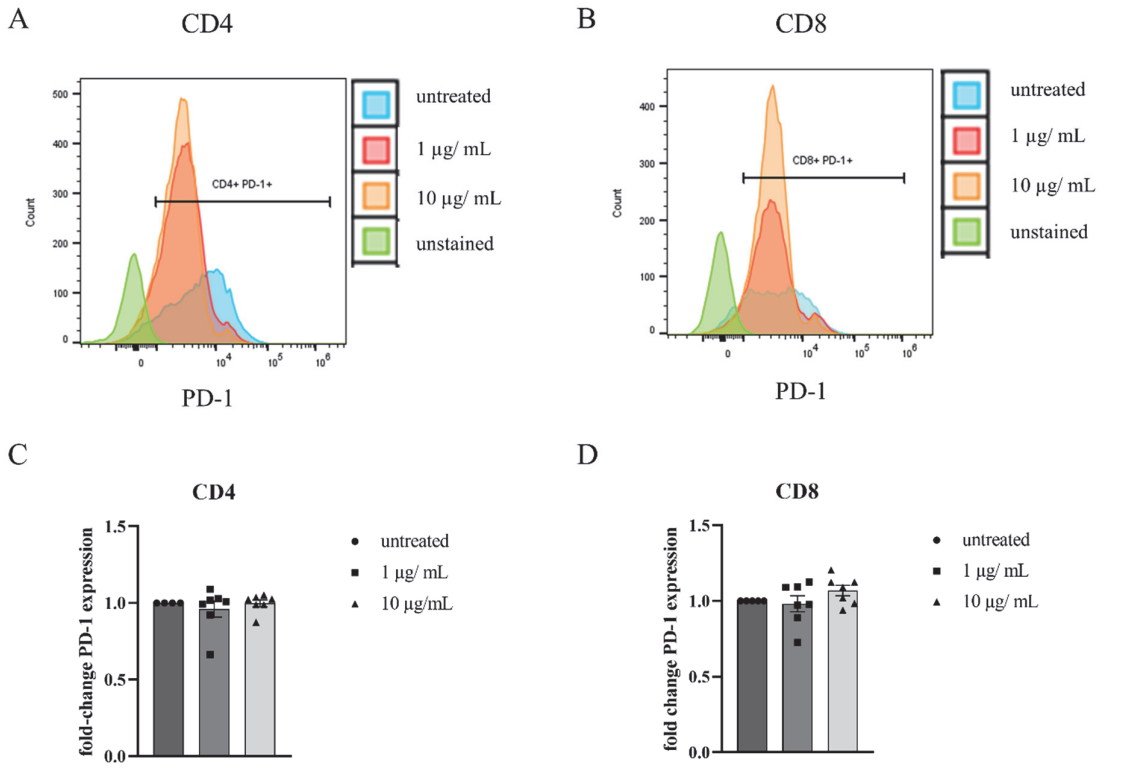
Supplementary Figure 3.3-4 Characterization of primary patient-derived cells. Representative immunofluorescence images are shown. (A) Primary tumor cells were isolated form primary PDAC tumor tissue. Expression of tumor cell markers was analyzed conducting immunofluorescence staining. The following markers were co-stained with the nuclei (blue): vimentin, pan cytokeratin, cytokeratin 7, E-cadherin, CD44, Epcam, Ki67, and N-cadherin. (B) Immunofluorescence staining of primary CAF for the fibroblast marker α-SMA (green) and the nuclei (blue). Magnification 40x, scale bar 100 µm.



Supplementary Figure 3.3-5 Composition of patient-derived spheroids (PDS). Representative immunofluorescence images of a PDS are shown. Spheroids composed of patient derived tumor cells and patient derived CAF were generated and stained for the fibroblast marker α-SMA (red), the and the tumor cell marker cytokeratin 7 (green), and the nuclei (blue) Shown are representative maximum intensity projections (MIP) from a whole z-stack for the single channels alongside a merge of all fluorescence channels. Scale bar, 500 µm; magnification, 10×.



Supplementary Figure 2.3-6 IFN-γ, Granzyme B and perforin protein expression following treatment with pembrolizumab. Patient-derived spheroids were infiltrated with $CD3^+$ T-cells isolated from autologous patient-derived PBMC. Pembrolizumab (10 µg/mL) was added at the time of T-cell infiltration and maintained for 72 h. IFN-γ (A), Granzyme B (B) and perforin (C) expression in $CD8^+$ T-cells were quantified by flow cytometry. Data represent the mean ± SEM of three independent experiments. Statistical significance is indicated as *$p \leq 0.05$.



Supplementary Figure 3.3-7 Effect of pembrolizumab treatment on PD-1 surface expression. PANC-1 spheroids were generated prior to infiltration with $CD3^+$ T-cells isolated from peripheral blood mononuclear cells (PBMC) of healthy donors. Pembrolizumab (1 µg/mL or 10 µg/mL) was added at the time of T-cell infiltration and maintained for 72 h. Representative flow cytometry histograms depicting PD-1 surface expression in $CD4^+$ (A) and $CD8^+$ (B) T-cells following 72 h of pembrolizumab treatment. Quantitative analysis of PD-1 expression in $CD4^+$ (C) and $CD8^+$ (D) T-cells after 72 h of treatment. Untreated spheroids served as controls.

Supplementary Methods

Cytokine Expression

T-cell cytokine expression was assessed following a 6 h restimulation with 500 ng/mL ionomycin and 5 ng/mL Phorbol 12-myristate 13-acetate (PMA (#J63916.MCR, Thermo Scientific)). Brefeldin A (#HY-16592-5mg, MedChem Express) was added during the stimulation period to allow intracellular accumulation of cytokines. After restimulation, cells were stained for the surface markers CD3, CD4, and CD8, followed by intracellular staining for IFN-γ (#130-114-021, Miltenyi Biotec), perforin (#130-130-854, Miltenyi Biotec), and granzyme B (#130-116-654, Miltenyi Biotec) prior to flow cytometric analysis.

4 Unpublished data

The following chapters contain additional unpublished datasets, which were generated as part of this dissertation in the process of developing an immunocompetent 3D PDAC biochip model.

4.1 Implementation of T-cells into the biochip model

By replicating the key structural and stromal features of the PDAC TME in our PANC-1-based spheroid co-culture model, we were able to reproduce key features of the T-cell dysfunction observed in patients, including the upregulation of immune checkpoint molecules and the stromal exclusion of T-cells [139, 152]. To investigate whether these observations were consistent under dynamic conditions, we perfused T-cells derived from PBMC over an endothelial layer in our biochip model.

4.1.1 Infiltration of T-cells into PDAC spheroids under perfusion on the biochip

As shown in Figure 4.1-1 PBMC-derived T-cells demonstrate active migration from the perfusion flow into the PANC-1 spheroids. While T-cells are uniformly distributed throughout PANC-1 monospheroids, their infiltration into co-culture spheroids is significantly reduced and appears restricted to the fibrotic stroma. These findings validate the biochip model´s ability to recapitulate active T-cell recruitment under flow conditions, while successfully mimicking the stroma-mediated immune exclusion from the tumor core previously observed in static cultures.

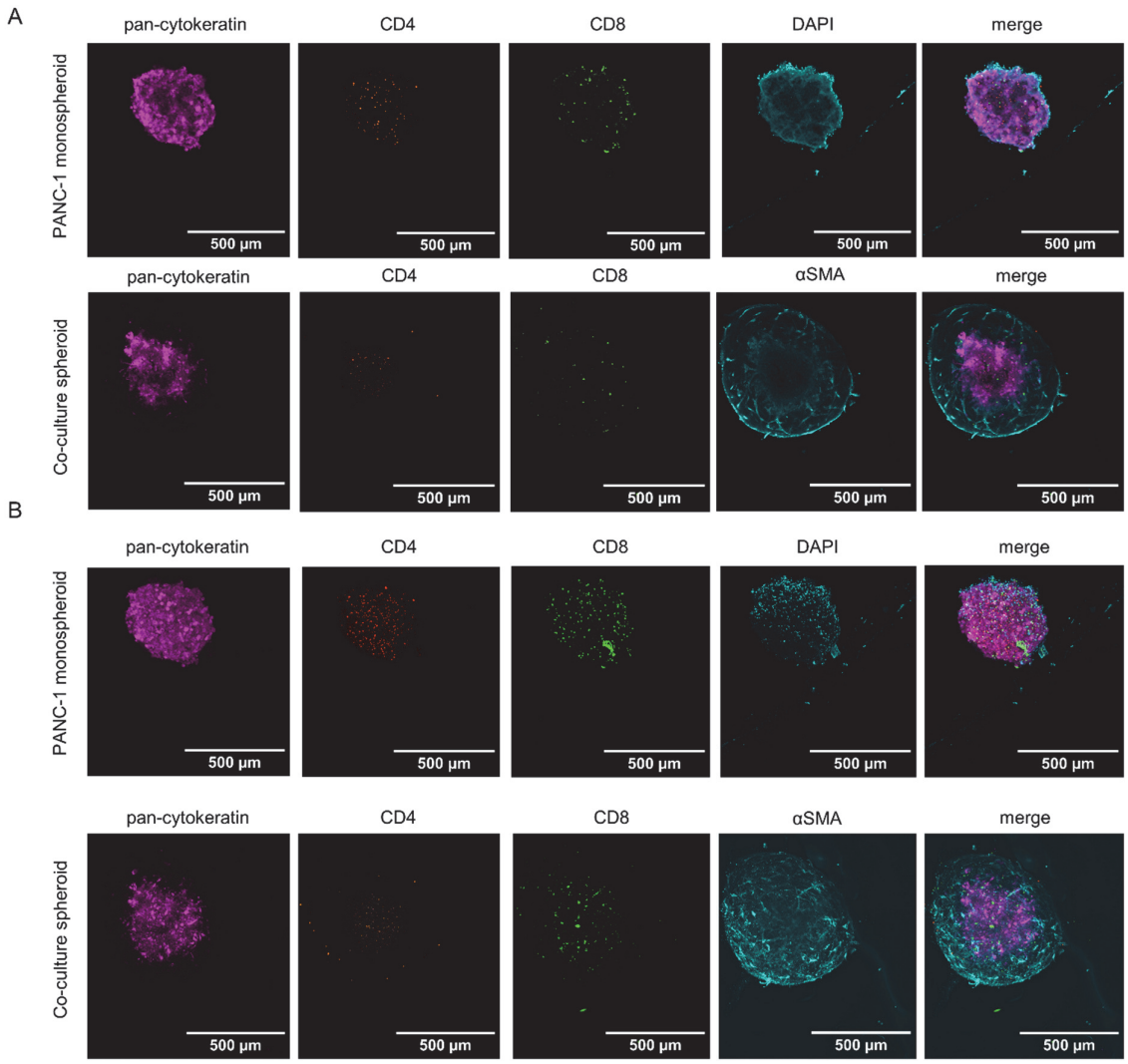


Figure 4.1-1 T-cell infiltration in PANC-1 spheroids on chip. Shown are representative immunofluorescence images of PANC-1 spheroids infiltrated with $CD3^+$ T-cells. PANC-1 monospheroids or co-culture spheroids containing PSC were perfused with $CD3^+$ T-cells isolated from PBMC from healthy donors for 72 h. Spheroids were stained for pan-cytokeratin (tumor cells, purple), CD4 (red), CD8 (green), and either nuclei or α-SMA (fibroblast) (blue). Representative single optical sections from a z-stack (A) and maximum intensity projections (MIP) of the complete z-stack (B) for the single channels alongside a merge of all fluorescence channels are shown. Scale bar, 500 µm; magnification, 10x.

4.1.2 Checkpoint expression of infiltrated T-cells after perfusion on the biochip

To determine whether the infiltrated T-cells from the biochip exhibit the same dysfunctional phenotype as those in static cultures, checkpoint expression was analyzed by flow cytometry. In $CD4^+$ T-cells, a significant upregulation of CTLA-4 (4.5-fold and 4.0-fold) and LAG-3 (1.5-fold and 1.5-fold) was observed in co-culture and PANC-1 monospheroids, whereas PD-1 expression increased significantly (7.1-fold) only in $CD4^+$ T-cells from co-culture spheroids (Figure 4.1-2A). Conversely, the

activation marker CD69 remained unchanged by infiltration in both spheroid models (Figure 4.1-2A). Within the $CD8^+$ T-cell population, PD-1 levels were significantly elevated upon infiltration in both PANC-1 models (3.8-fold and 2.0-fold), while LAG-3 expression showed an upward trend without reaching statistical significance Figure 4.1-2B). The expression levels of CD69 and CTLA-4 showed no significance changes (Figure 4.1-2B).

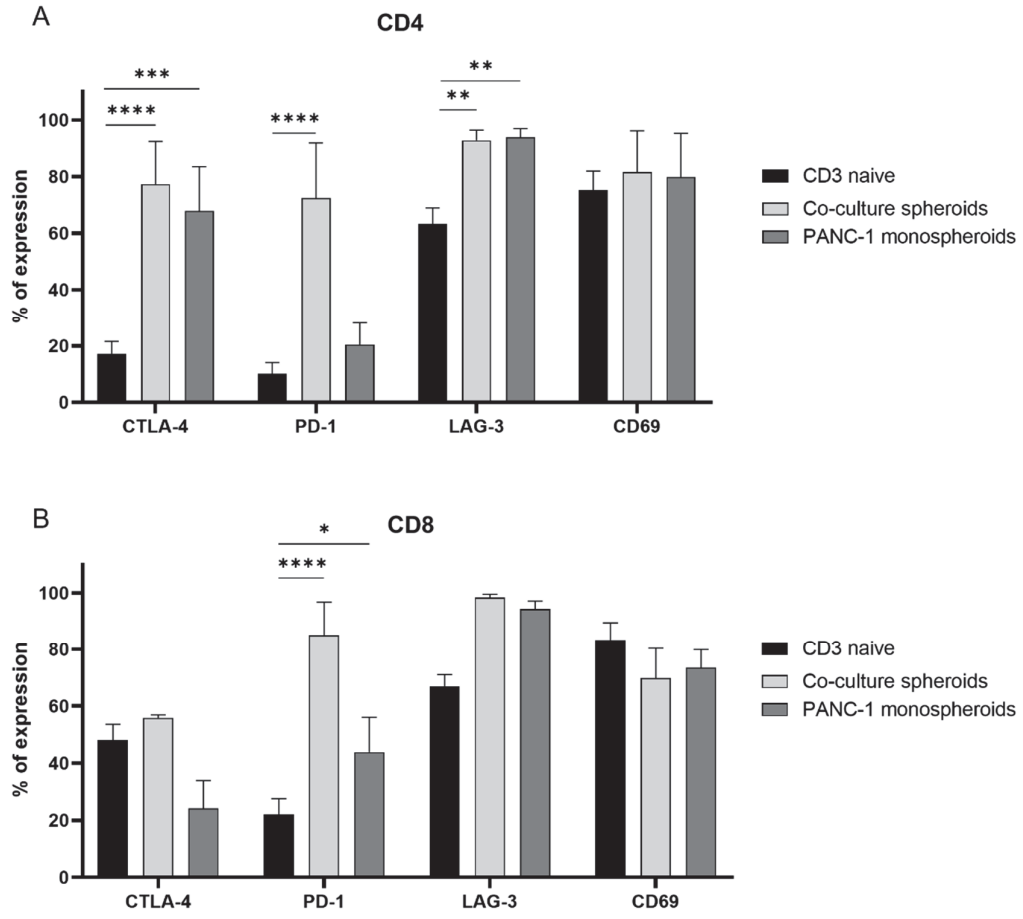


Figure 4.1-2 Checkpoint expression in T-cells after infiltration on the biochip. Checkpoint expression in $CD4^+$ (A) and $CD8^+$ (B) T-cells after perfusion on the biochip was analyzed by flow cytometry. PANC-1 spheroids were generated prior to loading on the biochip and perfusion with $CD3^+$ T-cell, isolated from PBMC from healthy donors. T-cells perfusion was performed for 72 h on either co-culture spheroids or PANC-1 monospheroids. T-cells identified as $CD3^+$ and $CD45^+$ were analyzed for surface expression of CTLA-4, PD-1, LAG-3 and CD69. Naïve T-cells isolated from the blood of healthy donors served as control. Naïve T-cells isolated from the blood of healthy donors served as control. Error bars indicate the standard errors of the mean of at least three independent experiments from three different donors, with * = $p \leq 0.05$; ** = $p \leq 0.01$; *** = $p \leq 0.001$; **** = $p \leq 0.0001$.

4.2 Material and Methods

This chapter contains the material and methods of all additional unpublished data (3.2.2) and unpublished data (4.1) presented in this work.

4.2.1 Material

4.2.1.1 Suppliers and their locations

Table 4.2-1 Suppliers and their locations

Supplier	Headquarter
ATCC	Manassas, Virginia, USA
BD	Ashland, Oregon, USA
BioCat	Heidelberg, Germany
BioLegend	San Diego, California, USA
Carl Roth GmbH + Co.KG	Karlsruhe, Germany
Corning	Corning, New York, USA
Cytek Biosciences	Fremont, California, USA
Dynamic42	Jena, Germany
Gibco	Grand Island, New York, USA
GraphPad Software, Inc.	San Diego, California, USA
Greiner Bio-One	Kremsmünster, Austria
ImmunoTools	Friesoythe, Germany
Ismatec	Wertheim, Germany
Lonza	Basel, Switzerland
Masterflex	Barrington, IL, USA
Miltenyi Biotec	Bergisch Gladbach, Germany
MoBiTec	Göttingen, Germany
PHC Europe B. V	Breda, Netherlands
Promega	Madison, Wisconsin, USA
Santa Cruz Biotechnology	Dallas, Texas, USA
Sigma-Aldrich	Darmstadt, Germany
Tecan Group	Männedorf, Switzerland
Thermo Fisher Scientific	Waltham, Massachusetts, USA
Yokogawa	Musashino, Japan

4.2.1.2 Chemicals

Table 4.2-2 Chemicals

Chemical	Supplier	Catalog number
Dimethyl sulfoxide (DMSO)	Roth	A994.1
Trypan Blue Stain (0.4%)	Gibco	15250061

4.2.1.3 Buffer and Solutions

Table 4.2-3 Buffer

Buffer	Supplier	Catalog number
CellTiter-Glo® 3D Cell Viability Assay	Promega	G9681
Dulbecco's phosphate buffered saline (D-PBS) (1x)	PAN Biotec	P04-36500
Histopaque	Sigma-Aldrich	10771

4.2.1.4 Cell culture medium, supplements, and reagents

Table 4.2-4 Basic cell culture medium, supplements, and reagents

Media/ reagent/ supplement	Supplier	Catalog number
Accutase	Gibco	A1110501
Collagen-1 (rat-tail)	Gibco	A1048301
Dulbecco's phosphate buffered saline (D-PBS) (1x)	PAN Biotec	P04-36500
Dulbecco's Modified Eagle Medium (DMEM)	Gibco	41965039
Dulbecco's Modified Eagle Medium/F-12 (DMEM F12)	Gibco	11320074
Fetal Bovine Serum (FBS)	Gibco	11573397
Matrigel	Corning	356231
Pen-Strep	Gibco	15140122
RPMI 1640	Gibco	21875-034
Trypsin EDTA 0.25%	Thermo Fisher Scientific	25200056
Trypsin EDTA 0.05%	Thermo Fisher Scientific	25300062

Table 4.2-5 Commercially available cell culture medium and supplements

Media/ supplement	Supplier	Catalog number
Endothelial Cell Basal Medium-2 (ECBM)	Lonza	CC-3156
EGM-2 Single Quots	Lonza	CC-4176

Table 4.2-6 Cell culture medium composition

Media composition for	Media composition
PANC-1	DMEM FBS (10%) Pen-Strep (1%)
PSC	DMEM F12 FBS (20%) Pen-Strep (1%)
HUVEC	ECBM EGM-2 single Quots Pen-Strep (1%)
Co-culture spheroids	RPMI FBS (10%) Pen-Strep (1%) Collagen-1 (0.1 mg/mL)
Macrophage differentiation	RPMI FBS (10%) Pen-Strep (1%) M-CSF 100 ng/mL
T-cell	RPMI FBS (10%) Pen-Strep (1%)
Biochip top channel	ECBM EGM-2 single Quots without hydrocortison Pen-Strep (1%)
Biochip middle channel	30% T-cell medium 70% Biochip top channel medium 2.5% (v/v) Matrigel
Biochip bottom channel	30% T-cell medium 70% Biochip top channel medium

4.2.1.5 Cytokines, growth factors and treating compounds

Table 4.2-7 Cytokines and growth factors

Agent	Supplier	Catalog number
rhIL-2	ImmunoTools	11340025
M-CSF	ImmunoTools	11343113

Table 4.2-8 Treating compounds

Agent	Supplier	Catalog number
Dynabeads™ Human T-Activator CD3/CD28 for T-Cell Expansion and Activation	Thermo Scientific	11161D
paclitaxel	Santa Cruz Biotechnology	sc-201439

4.2.1.6 Commercially available kits

Table 4.2-9 Commercially available kits

Kit	Supplier	Catalog number
MACS clearing Kit	Miltenyi Biotec	130126-719

Antibodies

Table 4.2-10 Primary antibodies

Antibody	Conjugate	Species	Application	Supplier	Catalog number
α-SMA		Mouse	Immunofluorescence	Cell Signaling	19245S
CD3	Alexa Flour (AF)700	Mouse	Flow cytometry (1:50)	BioLegend	317340
CD4	Biotin	recombinant	MACS Isolation (1:500)	Miltenyi Biotec	130-113-224
CD4	VioBright V600	recombinant	Flow cytometry (1:50)	Miltenyi Biotec	130-129-579
CD8	Biotin	recombinant	MACS Isolation (1:500)	Miltenyi Biotec	130-110-676
CD8	FITC	recombinant	Flow cytometry (1:50)	Miltenyi Biotec	130-110-815
CD14	microbeads	recombinant	MACS Isolation	Miltenyi Biotec	130-097-052
CD25	APC	recombinant	Flow cytometry (1:50)	Miltenyi Biotec	130-113-284
CD45	VioGreen	recombinant	Flow cytometry (1:50)	Miltenyi Biotec	130-110-638
CD69	VioBlue	recombinant	Flow cytometry (1:50)	Miltenyi Biotec	130-112-799
CD152 (CTLA-4)	PE-Vio770	recombinant	Flow cytometry (1:50)	Miltenyi Biotec	130-130-455

CD223 (LAG-3)	APC-Vio770	recombinant	Flow cytometry (1:50)	Miltenyi Biotec	130-130-284
CD279 (PD-1)	PerCP-Cy5.5	mouse	Flow cytometry (1:50)	BioLegend,	367410
pan-cytokeratin	VioR667	recombinant	Immunofluorescence	Miltenyi Biotec	130-133-439

Table 4.2-11 Secondary antibodies

Antibody	**Conjugate**	**Species**	**Application**	**Supplier**	**Catalog number**
Biotin	microbeads	recombinant	MACS Isolation (1:50)	Miltenyi Biotec	130-090-485
Anti-mouse	AF 405	donkey	Immunofluorescence	Invitrogen	A-48257
Anti-rabbit	AF 546	donkey	Immunofluorescence	Invitrogen	A-10040

Consumables

Table 4.2-12 Consumables

Consumable	**Supplier**	**Catalog number**
0.5 mL tube	Sarstedt	72.699
1.5 mL tube	Sarstedt	72.690.001
2 mL tube	Sarstedt	72.691
96-well plate with ultra-low-attachment (ULA) surface	Greiner	650970
Biochip BC003	Dynamic42	BC003_8_PET_MC
Cell counting slides	BioCat	L12001
Cell culture plate, 6 well, surface: Standard, flat base	Sarstedt	83.3920
Luer-plugs	MoBiTec	MOB-M3002
LS Colums	Miltenyi Biotec	130-042-401
Medium reservoir	MoBiTec	MOB-M1002
Serological pipette (5 mL)	Sarstedt	86.1253.025
Serological pipette (10 mL)	Sarstedt	86.1254.025
Serological pipette (25 mL)	Sarstedt	86.1685.020
T75 flask	Sarstedt	83.3910.002
Tube (15 mL)	Sarstedt	62.554.502
Tube (50 mL)	Sarstedt	62.547.254

Devices

Table 4.2-13 Devices

Device	Supplier
CellVoyager™ CQ1 Benchtop High-Content Analysis System	Yokogawa
Centrifuge 5425 R	Eppendorf
Centrifuge 5430 R	Eppendorf
Centrifuge 5804 R	Eppendorf
CO_2 Incubator	PHC Europe B. V
Cytek® Northern Lights FACS	Cytek Biosciences,
Ismatec™ IPC 4 Peristaltic Pump	Masterflex
LUNA-II™ Automated Cell Counter	Eppendorf
MidiMACS separator	Miltenyi Biotec
Tecan Spark microplate reader	Tecan Group

4.2.2 Methods

4.2.2.1 Immune cell isolation from buffy coats

Peripheral blood mononuclear cells (PBMC) were isolated from buffy coats obtained from anonymized healthy donors (Düsseldorf University Hospital, Germany) approved for *in vitro* research. PBMC were separated using Ficoll-based density gradient centrifugation. Briefly, buffy coats were diluted with D-PBS, carefully layered onto Histopaque, and centrifuged at 850 × g for 20 min without acceleration or brake. The interphase containing PBMC was collected and subjected to erythrocyte lysis using ammonium chloride solution for 10 min. Cells were subsequently washed with D-PBS and counted.

$CD14^+$ monocytes were isolated from PBMC by magnetic-activated cell sorting (MACS) using anti-CD14 monoclonal antibody–conjugated paramagnetic microbeads according to the manufacturer's instructions and separated using a MidiMACS separator. Purified monocytes were cultured in RPMI 1640 medium supplemented with 10% FBS and 1% pen–strep at a density of 1×10^6 cells/mL.

T-cells were subsequently isolated from PBMC by MACS. Briefly, cells were labeled with biotinylated anti-CD4 and anti-CD8 antibodies, followed by incubation with anti-biotin microbeads, according to the manufacturer's instructions. Cell separation was performed using a MidiMACS separator. Purified T-cells were cultured in RPMI 1640

medium supplemented with 10% FBS, 1% penicillin–streptomycin, and 50 ng/mL Interleukin-2. CD3/CD28 Dynabeads were added at a bead-to-cell ratio of 1:2 for activation and expansion.

4.2.2.2 Cell cultivation

The human pancreatic cancer cell line PANC-1 was obtained from the American Type Culture Collection (ATCC) and cultured in DMEM supplemented with 10% FBS and 1% penicillin–streptomycin.

PSC were kindly provided by Dr. Erkan (Koç University Hospital, Turkey). Ethical approval for the use of PSC was granted by the Biomedical Sciences Ethics Committee of Koç University, and written informed consent was obtained from all donors. PSC were isolated from patients diagnosed with pancreatic ductal adenocarcinoma and maintained in DMEM/F12 medium supplemented with 20% FBS and 1% penicillin–streptomycin under sterile conditions.

HUVEC (University Hospital Jena, Germany) were cultured in Endothelial Cell Growth Medium supplemented with ECGM SingleQuots and 1% penicillin–streptomycin. All cell cultures were maintained at 37 °C in a humidified incubator with 5% CO_2.

4.2.2.3 Differentiation of M2 macrophages

Monocytes were differentiated into M2 macrophages over the course of 7 days. Therefore, 1 x 10^6 cells/mL were seeded into 6-well plates in RPMI medium supplemented with M-CSF. Medium was changed after 3 and 6 days and supplemented with fresh M-CSF. After 7 days of cultivation M2 macrophages were detached with 0.05% trypsin and used for further experiments.

4.2.2.4 Spheroid generation

PANC-1 monospheroids were generated from 3 × 10^4 cells/mL PANC-1 cells seeded into ULA-plates with 2.5% (v/v) Matrigel and centrifuged for 5 min at 1500 rpm. Co-culture spheroids composed of PANC-1 cells and PSC were generated as previously described by Xie et al. [2]. Briefly, PANC-1 cells (1 × 10^4 cells/mL) and PSC (2 × 10^4 cells/mL) were combined in DMEM/F12 medium. Collagen I was added to a final concentration of 0.1 mg/mL to facilitate spheroid formation. The cell suspension was seeded into ULA 96-well plates and cultured at 37 °C in a humidified atmosphere containing 5% CO_2.

4.2.2.5 Implementation of cells into the biochip

The membrane of the top channel was coated with collagen I. Subsequently, 1.5×10^5 HUVEC were seeded onto the coated membrane. Cells were maintained for 4 days with daily medium exchange using 250 µL endothelial growth medium (EGM-2) in the top channel to allow the formation of a confluent endothelial layer.

Four-day-old spheroids were collected into 1.5 mL tubes, and at least 20 spheroids were loaded into the microcavities of the middle channel. Spheroids were cultured on-chip in a medium consisting of 70% EGM-2, 30% RPMI, and 2.5% (v/v) Matrigel.

4.2.2.6 Perfusion of the biochip

For perfusion experiments, the top and bottom channels were independently connected via tubing to a peristaltic pump. Each circuit comprised a PharMed® BPT thermoplastic elastomer 2-stop tube prefilled with 250 µL medium and connected to a medium reservoir containing 750 µL medium. The top channel was perfused at a flow rate of 10 µL/min for 72 h containing 1 x 10^6 T-cells /mL. The bottom channel was perfused at a flow rate of 25 µL/min for 72 h at 37 °C in a humidified atmosphere with 5% CO_2. The middle channel containing the tumor spheroids remained non-perfused and was sealed using standard Luer plugs.

4.2.2.7 Cell viability assay

Cell viability of 3D spheroids was assessed using the CellTiter-Glo assay according to the manufacturer's instructions. M2 macrophages were added 24 h after spheroid seeding. On day 4 of the spheroid culture paclitaxel treatment was added for 72 h. After 72 h of treatment the CellTiter-Glo assay was performed to measure the cell viability. Luminescence signals were measured using the Tecan Spark microplate reader.

4.2.2.8 Flow cytometry analysis

Checkpoint molecule expression in T-cells was evaluated by flow cytometry. PDAC spheroids were harvested following infiltration with PBMC-derived T-cells. Spheroids were dissociated into single-cell suspensions using Accutase.

Cells were stained according to the manufacturers' instructions with the following fluorochrome-conjugated antibodies: CD45–VioGreen, CD8–FITC, CD4–VioBright V600, CD25–APC, CD69–VioBlue, CD223 (LAG-3)–APC-Vio770, CD279 (PD-1)–PerCP-Cy5.5, CD3–AF700 (BioLegend), and CD152 (CTLA-4)–PE-Vio770.

Data acquisition was performed using a Cytek® Northern Lights flow cytometer (Cytek Biosciences, Fremont, CA, USA), and data were analyzed with FlowJo software (version 10.9.0; BD, Ashland, OR USA).

4.2.2.9 Immunofluorescence staining of spheroids

Spheroid staining was performed using the MACS clearing kit according to manufacturer's instructions. Briefly, spheroids were fixed in 4% PFA for 1 h at RT, followed by a 6 h permeabilization step. Samples were then incubated for 24 h at 4 °C with 100 µL of primary antibody solution targeting CD4, a-SMA, pan-cytokeratin and CD8. This was followed by a 24 h incubation at 4 °C with a secondary antibody cocktail containing Alexa-Flour 546 anti-rabbit and Alexa Flour 405 anti-mouse, and 2 µg/mL DAPI for monospheroids. For optical clearing, spheroids underwent dehydration through an ethanol gradient (50%, 70%, and 100% with 2% Tween), with a final overnight 100% ethanol step, followed by 6 h in clearing solution. Finally, cleared spheroids were transferred to an ibidi imaging plate and visualized using the CQ1 High-Content Spinning Disk System.

5 Discussion

5.1 Interactions between the tumor and the TME as drivers of PDAC progression and therapy resistance

PDAC is characterized by marked resistance to standard chemotherapeutic agents and novel treatment strategies, which is attributable to tumor-intrinsic mechanisms and those mediated by the TME [26, 106]. Although the presence of oncogenic KRAS driver mutations and the loss of key tumor suppressor genes, including TP53, SMAD4, and CDKN2A, are well characterized in tumor initiation and progression, they are insufficient to fully explain the marked treatment resistance observed in patients [26, 30]. Instead, tumor progression and response to therapy are strongly influenced by the spatial organization and dynamic interactions between tumor cells and the various compartments of the TME [107, 199].

In the context of factors intrinsic to tumor cells, aberrant epigenetic regulation leads to the dysregulation of various signaling pathways, which in turn promotes cell proliferation, survival, and invasiveness [100]. The results presented in this study support this concept, as pharmacological inhibition of HDAC by known and novel HDAC inhibitors induced apoptosis and reduced the invasive potential of PDAC tumor cells [101], as indicated by the upregulation of the epithelial marker E-cadherin. However, while molecular insights are crucial, the efficacy of such approaches is fundamentally altered by the surrounding microenvironment [106].

In addition to factors inherent to tumor cells, the TME is a key driver of tumor growth and treatment resistance [107, 200]. Both, CAF and the ECM create a highly desmoplastic and dense stroma that surrounds the tumor cells [110]. Furthermore, they secrete a variety of signaling molecules that influence the recruitment and function of immune cells, thereby promoting the immunosuppressive TME [107, 111]. The 3D model of the co-spheroids used in this study consists of an inner core of tumor cells surrounded by a distinct fibrotic layer. [161]. For the first time, we were able to further improve physiological relevance, introducing immune competence through the infiltration of monocytes a T-cells. Consistent with the immunosuppressive TME of PDAC [61, 130], the infiltrated monocytes polarized toward an M2 phenotype, while the infiltrated T-cells exhibited a dysfunctional phenotype, accompanied by significant upregulation of various checkpoint molecules.

To investigate the active recruitment and modulation of immune cells in an environment that mimics conditions in patients more precisely, we developed an immunocompetent biochip model that enables the dynamic perfusion of immune cells across an endothelial layer. Here, we demonstrated that, in this dynamic environment, infiltrating monocytes were polarized toward a pro-tumoral M2 phenotype, and checkpoint expression was upregulated on infiltrating T-cells. In summary, the replication of these diverse aspects - from epigenetic regulation to dynamic immunomodulation - in a single *in vitro* model is of crucial importance for preclinical drug development. It enables the evaluation of the efficacy of novel therapeutic strategies for PDAC by replicating the tumor-intrinsic and TME-driven mechanisms that contribute to tumor progression and treatment resistance [201].

5.2 Epigenetic remodeling in PDAC

A critical process in the progression of PDAC is the invasion of tumor cells and the formation of metastases. This process is driven by EMT of tumor cells [96]. EMT is controlled by epigenetic regulation, particularly by HDAC [96]. The results of this study showed that a novel HDAC inhibitor and an FDA-approved drug effectively induced apoptosis, but more importantly, triggered the reversal of EMT, characterized by the upregulation of the epithelial marker E-cadherin. In conventional 2D cultures, this is typically observed as a molecular shift [202]. However, integrating these findings into our 3D spheroid and biochip model allows us to investigate the physiological relevance of this observation.

Unlike 2D monolayers, 3D models allow for cell-cell and cell-matrix interactions [165]. E-cadherin is a cell adhesion molecule whose expression restores cell-cell contact and thereby counteracts the invasive potential of tumor cells [203]. Consistent with this concept, we were able to demonstrate reduced invasion in PDAC tumor cells following treatment with HDACi in a 3D invasion assay. This emphasizes the superiority of 3D models in capturing the functional consequences of molecular EMT markers, which often remain masked in 2D layers due to a lack of spatial organization [165].

In addition to their invasive potential, the sensitivity of tumor cells to chemotherapeutic agents is also influenced by their epithelial or mesenchymal state [133]. As the mesenchymal phenotype increases, sensitivity to chemotherapeutic agents decreases [133]. Therefore, HDACi are currently being investigated in clinical trials in combination with chemotherapeutic agents to restore the sensitivity of PDAC tumor cells to systemic

treatment with chemotherapeutic agents [96, 103]. In line with these approaches, we observed synergistic effects of the novel HDACi MPK544 with the chemotherapeutic agent gemcitabine, which may have been facilitated by increased chromatin accessibility. However, in combination with 5-FU, no synergistic effect was observed for the combination with MPK544 in the selected model. This underscores that the epigenetic priming effect is highly drug-specific and requires further investigation in other cell models or with other HDACi.

The use of multicellular 3D models is crucial for evaluating the cytotoxicity and selectivity of HDACi, as HDACs are expressed in all cells and do not act selectively on tumor cells. In the context of PDAC, it should be noted that CAF have also been shown to overexpress Class I HDAC molecules [204]. To investigate the cytotoxic potential of the FDA-approved pan-inhibitor SAHA in a more physiologically relevant model, we applied it in our biochip model. This enabled a dynamic application that mimics transient drug exposure, allowing for a more nuanced assessment of the therapeutic window [180, 182]. In our co-culture spheroids, we observed a concentration-dependent increase in cytotoxicity, while the endothelial barrier remained intact up to the second-highest concentration. These results suggest that our biochip model is suitable for investigating differential cytotoxicity and allows for a more nuanced assessment of safety profiles than is possible with static models [182]. However, further studies are needed to evaluate more selective therapies and combination therapies in this setting. This study provides a proof-of-concept for further drug testing in the biochip model.

Taken together, epigenetic priming by HDACi may contribute to restoring sensitivity to chemotherapeutic agents in PDAC. To evaluate the physiological effect and selectivity of HDACi it is necessary to use multicellular 3D models. Application of a biochip furthermore provides the transient drug exposure and an endothelial barrier further increasing the translation of the results. However, further research is needed to optimize the therapeutic window and minimize off-target effects.

5.3 The desmoplastic stroma as a barrier to chemotherapy

As previously described, HDACi can restore the sensitivity of tumor cells to chemotherapeutic agents; however, clinical practice shows that HDACi and other therapies have only limited efficacy [101]. This is largely attributed to the complex and dense stroma in PDAC patients, which actively impedes drug transport and

biomechanically neutralizes the cytotoxic potential of the drugs [106, 159]. As mentioned above, PSC contribute significantly to the desmoplastic stroma by producing large amounts of ECM [112]. This not only acts as a physical barrier but also increases interstitial pressure, leading to collapsed and dysfunctional vessels, as well as hypoxic conditions, thereby significantly limiting the penetration and efficacy of therapeutic agents [120]. Our biochip model reproduces these stromal characteristics through the implementing the established co-culture model. As demonstrated in a previous study, the cytotoxic capacity of chemotherapeutic agents such as gemcitabine is significantly reduced in this model [161]. The patient-derived spheroids (PDS) established in this study represent a novel approach exhibiting an even more pronounced fibrotic layer that more closely resembles the tumor-stroma distribution found in PDAC patients, where the stroma accounts for up to 85% of the cell mass [106]. This potentially further increases resistance to commonly used chemotherapeutic agents such as gemcitabine or FOLFIRINOX. Further research is needed to assess the role of the fibrotic layer in resistance to chemotherapy.

Another key component of the desmoplastic stroma is TAM. It has been reported that TAM contribute to the immunosuppressive TME and enhance chemoresistance in PDAC [196]. They secrete various cytokines such as TGF-β and IL-10, which induce anti-apoptotic signaling pathways such as PI3K/Akt, JAK/STAT, or others in tumor cells [122, 196]. In doing so, they effectively protect tumor cells from the cytotoxic effects of chemotherapeutic agents [131, 197, 198]. The addition of M2 macrophages to preclinical models for drug testing is therefore crucial to account for the protective effect of macrophages when evaluating the cytotoxicity of active compounds. Here, we demonstrated that the dynamic perfusion of PBMC-derived monocytes in our biochip model resulted in the infiltration of PDAC spheroids by monocytes, followed by their differentiation and polarization into M2 macrophages characterized by the expression of CD11b, CD68, and CD163. This underscores the ability of our simplified model to replicate the active recruitment of monocytes and their subsequent polarization into M2 macrophages, as observed in patients [122]. Significantly, the presence of these M2 macrophages made the spheroids in the co-culture less sensitive to the chemotherapeutic agent paclitaxel. The chemoprotective role of M2 macrophages observed in our spheroid co-culture model is consistent with findings from transgenic mouse models, in which macrophage depletion significantly increased the sensitivity of PDAC tumors to chemotherapeutic agents [135]. However, mouse models often rely

on species-specific signaling, particularly in tumor-immune interactions, whereas our model is composed entirely of human cells and can be adapted into a fully patient-derived model. This is particularly relevant for the interaction between tumor cells and macrophages, as xenograft models face ligand-receptor incompatibilities [162], whereas our model, based entirely on human cells, avoids these issues.

As previously mentioned, spatial organization has a significant impact on cell-cell signaling [154]. Therefore, understanding the spatial organization of the TME is crucial for the development of translational *in vitro* models. Several studies have shown that M2 macrophages accumulate in the fibrotic region of the TME in PDAC patients [106, 205]. We were able to demonstrate that our model replicates this localization within the fibrotic layer of the co-culture spheroids. In contrast, macrophages distributed evenly throughout the entire spheroid when infiltrated into spheroids consisting exclusively of PANC-1 tumor cells. Other spheroid models containing macrophages often lack the fibrotic component or are unable to replicate the three-dimensional distribution, which limits their ability to mimic the spatial architecture of the TME in patients and consequently reduces their translational relevance [173, 174].

In summary, recreating the desmoplastic stroma is a critical factor in the development of translational *in vitro* models for drug testing. CAF and M2 macrophages significantly influence the cytotoxic potential of chemotherapeutic agents and their ability to penetrate tumor tissue [106, 130]. Therefore, it is necessary to replicate not only the cellular composition but also the spatial architecture in order to mimic the protective effect exerted by the desmoplastic stroma in PDAC patients. Our model can replicate both the spatial organization and the functional polarization of M2 macrophages within the stroma.

5.4 Overcoming the T-cell exclusion and dysfunction

To overcome the limitations and serious side effects of systemic therapy, promising advances have been made in immunotherapies for various types of cancer. In PDAC, however, clinical outcomes of immunotherapies, including ICIs and CAR-T cells, have remained poor, except for a small subgroup of MSI-H/dMMR patients [6, 85]. This limited efficacy can be attributed to severe T-cell dysfunction within the PDAC TME, which is driven by the interplay of multiple immunosuppressive mechanisms. Key factors include stroma-mediated exclusion of T-cells from the tumor core, the accumulation of immunosuppressive Tregs, an elevated CD4/CD8 ratio, and increased

expression of various immune checkpoint molecules such as PD-1, CTLA-4, and LAG-3 [141, 206]. This leads to limited T-cell infiltration and promotes a functionally exhausted phenotype, which contributes to the immunosuppressive TME of PDAC [114, 141]. By analyzing TIL from PDAC tumor tissue, we were able to demonstrate upregulation of checkpoint molecules and a shift in the CD4/CD8 ratio in favor of $CD4^+$ T-cells. These results support the findings of previous studies, which demonstrated an accumulation of $CD4^+$ T-cells and pronounced expression of the checkpoint molecules PD-1, LAG-3, and CTLA-4 in TIL from PDAC patients [141, 154].

In addition to the increase in $CD4^+$ cells in TIL, we also observed a higher frequency of $CD4^+$ T-cells in the corresponding PBMC of PDAC patients compared to age-matched healthy donor controls. These findings support the results reported by Rodriguez et al., who demonstrated a shift in the CD4/CD8 ratio toward a CD4-dominant immune profile in the PBMC of PDAC patients [151]. Through the analysis of matched tumor tissue and PBMC from the same patients, our data revealed a shift toward a $CD4^+$-dominant immune profile at both the systemic and intratumoral levels. This coordinated change suggests a possible bidirectional interaction between tumor-derived immunomodulatory signals and systemic immune composition [151]. To the best of our knowledge, this study provides the first evidence of such parallel immune changes in both compartments in individual PDAC patients. However, the mechanistic basis linking these systemic and local immune changes remains to be further elucidated.

By replicating the key structural and stromal features of the PDAC TME in our PANC-1-based spheroid co-culture model, we were able to reproduce key features of the T-cell dysfunction observed in patients, including the upregulation of immune checkpoint molecules, the accumulation of Treg cells, and the stromal exclusion of T-cells [141, 153]. To investigate whether these observations were consistent under dynamic conditions, we perfused T-cells derived from PBMC through an endothelial layer in our biochip model. The biochip results suggest active recruitment of T-cells from the perfusion into the co-cultured spheroids. However, infiltration was restricted to the fibrotic compartment of the spheroids, underscoring that the limited T-cell infiltration is stroma-mediated [106]. Furthermore, the infiltrated T-cells exhibited pronounced expressions of checkpoint molecules.

To overcome the limitation of missing patient-specific immune interactions in this system, the PDS were subsequently infiltrated with autologous T-cells. Unlike conventional approaches using patient-derived organoids [175], our model includes a CAF compartment, thereby enabling the investigation of tumor-stroma-immune interactions that are characteristic of PDAC [107]. In this setting, the infiltration of autologous T-cells into PDS led to pronounced checkpoint upregulation in the infiltrating T-cells, increased accumulation of Tregs, and spatial confinement of T-cells to the stromal region of the PDS.

Across the various *in vitro* systems employed, a gradual increase in physiological relevance was observed. This development is driven by the gradual restoration of stromal complexity, with signals originating from CAF and spatial organization critically regulating T-cell infiltration and function [105, 107]. In particular, PDS more accurately reflect the complexity of the human PDAC TME by preserving patient-specific stromal architecture, tumor heterogeneity, and autologous immune interactions. Accordingly, T-cell responses in this model were not only more pronounced but also better aligned with clinical observations, suggesting that both stromal composition and cellular origin are critical factors in immune modulation [177]. These results emphasize the importance of autologous, patient-derived systems for evaluating individualized responses to immunotherapeutic strategies in PDAC.

5.4.1 Targeting stomal-mediated T-cell exclusion through CXCR4 antagonism

Stroma-mediated T-cell exclusion in PDAC has been attributed to CXCL12 signaling from CAF via their CXCR4 receptor [207]. It has been shown that pharmacological modulation of this axis using the CXCR4 antagonist AMD3100 enhances T-cell infiltration in various experimental settings, including in vitro systems, in vivo models, and early clinical trials [83, 117, 208]. Consistent with these reports, disruption of CXCL12-CXCR4 signaling in our models led to a significant increase in T-cell infiltration into the tumor core of both co-culture spheroids and PDS. However, the magnitude of this effect was lower in PDS compared to PANC-1-based co-culture spheroids. This observation likely reflects the presence of a more compact and fibrotic stromal compartment in PDS, which acts as an additional physical barrier to T-cell migration even in the context of chemokine axis inhibition. Importantly, this structural constraint more closely resembles the situation in patients, where the desmoplastic stroma can account for up to 80% of the tumor mass [106].

5.4.2 Targeting T-cell dysfunction through PD-1 blockade

ICI therapy is an established strategy for restoring T-cell effector function by counteracting exhaustion. In PDAC, however, clinical responses to ICI therapy have been largely disappointing, with significant efficacy limited to the small group of patients with MSI-H/dMMR tumors for whom pembrolizumab is approved [85, 86]. In our study, pembrolizumab treatment enhanced the expression of effector molecules, including IFN-γ, granzyme B, and perforin, in autologous T-cells infiltrating PDS. Consistent with previous reports, this response appeared to be patient-dependent, underscoring the need for further studies in larger patient cohorts [209]. In contrast, T-cells infiltrating cell line-based spheroids showed minimal or no changes in granzyme B and perforin expression, and only a moderate increase in IFN-γ was observed in PANC-1 monospheroids. These results are consistent with previous studies using similar models, which also reported limited responsiveness to PD-1 blockade in *in vitro* systems [210].

Taken together, these results support the hypothesis that inhibition of the PD-1/PD-L1 axis alone is insufficient to overcome the multifaceted immunosuppressive microenvironment in PDAC [85]. Instead, effective therapeutic strategies likely require combinatorial approaches targeting multiple immunoregulatory pathways. In this context, emerging checkpoint molecules such as LAG-3, TIM-3, and TIGIT are currently being investigated, as they may offer additional opportunities to enhance antitumor immunity when combined with PD-1-targeted therapies [61, 85].

Overall, our results support a model in which T-cell dysfunction in PDAC results more from the coordinated interplay of multiple spatially organized immunosuppressive mechanisms than from a single dominant signaling pathway. Our data suggests that stroma-mediated T-cell exclusion via the CXCL12-CXCR4 axis, the upregulation of immune checkpoint molecules associated with functional exhaustion, and the accumulation of regulatory T-cell populations act in concert to establish a highly immunosuppressive microenvironment. In this context, CAF emerge as key regulators that integrate structural and immunological aspects of the TME. By shaping both the physical architecture and the chemokine landscape, they not only restrict T-cell infiltration into the tumor core but also indirectly impair effector function. This spatial and functional compartmentalization of immune responses provides a mechanistic explanation for the limited efficacy of current immunotherapeutic strategies in PDAC.

5.5 Translational relevance of the immunocompetent PDAC model

PDAC is a multifaceted disease characterized by the complex interplay between tumor-intrinsic and TME-driven mechanisms [2, 30, 106]. Simple preclinical models such as monospheroids or PDO cannot replicate this complex interplay, as they consist largely of tumor cells alone [163, 175]. While these models allow for the investigation of tumor-intrinsic mechanisms and, in the case of PDO, the replication of the primary tumor's genetic heterogeneity, they fail to capture the cellular complexity of the TME [175]. Consequently, these models are limited in their translational relevance, as several studies have demonstrated the critical role of the desmoplastic TME in response to therapy [120, 135, 174]. The data from this study support these findings by highlighting the influence of the desmoplastic stroma on sensitivity to paclitaxel and the restriction of immune cell infiltration, particularly the infiltration of effector T-cells. Furthermore, capturing not only the cellular composition but also the spatial architecture directly contributes to the translational relevance of preclinical models, as cell-cell and cell-matrix interactions are influenced by their spatial localization within the TME. Comparison of the spatial architecture in our simplified model showed that the localization of M2 macrophages and T-cells, as well as fibroblasts, as found in primary tumors, was replicated [106, 152]. This increases the translational relevance of our model compared to other preclinical models that fail to capture this aspect [168, 190, 211]. Furthermore, the results demonstrate that our 3D co-culture model, despite its simplicity, can capture several key features of immune evasion and thus enables a mechanistic investigation of tumor-immune interactions.

While cell line-based models are useful tools for investigating general mechanisms occurring in PDAC, they are of limited suitability for predicting patient-specific responses [163]. The current gold standard for personalized medicine are PDO [212]. These are developed directly from the tumor tissue and preserve cancer-intrinsic features, including the genetic, transcriptomic, proteomic and epigenetic alterations of the primary tumor [212, 213]. While they are powerful for investigation of tumor-intrinsic mediated resistance to chemotherapeutics and biomarker discovery, they lack the incorporation of TME factors, that as elucidated before, can significantly influence the treatment response [212, 213]. Therefore, we have developed a fully patient-derived model that allows for infiltration with autologous T-cells while preserving the spatial organization and cellular composition of cell line-based spheroids. Importantly, the infiltration of autologous T-cells into PDS induced an exhausted-like phenotype *ex vivo*,

highlighting the ability of this model to reproduce clinically relevant mechanisms of immune suppression in PDAC. Furthermore, the response of patient-specific immune cells can be evaluated under treatment with immunomodulatory drugs such as ICI. The data suggest that this simplified model is capable of replicating several immunosuppressive mechanisms observed in PDAC patients, making it a highly predictive model. Furthermore, it stands out from other *in vitro* models, which primarily replicate individual mechanisms of immune evasion in PDAC, thereby limiting their predictive power [175, 213].

Despite their complexity, spheroid models still lack a key aspect: physiological perfusion and endothelial barriers. These aspects are important for dynamic drug delivery and for studying the recruitment of immune cells into the TME. Advances in microfluidics have led to the development of tumor-on-chip models that enable dynamic drug delivery and perfusion with immune cells [186]. Several on-chip models have been described for PDAC; however, these typically lack either key components of the TME, such as CAF or immune cells, or consist of separate channels that isolate the various components of the TME from one another [183, 186, 214]. The biochip model used in this study enables the dynamic perfusion of drugs and immune cells while maintaining the spatial and cellular composition of the TME within a single channel, allowing for direct cell-cell and cell-matrix interactions between tumor cells and CAF. The results shown here are consistent with a study by Adnan et al., who used a chip model containing PDO, fibroblasts, monocytes, and T-cells, and demonstrated that the stromal component (monocytes and fibroblasts) significantly influenced the response to chemotherapeutic agents as well as T-cell recruitment and effector function [215]. These findings underscore the relevance of multicellular patient-derived on-chip platforms as a step forward towards translational drug testing and personalized medicine.

To this date GEMM and PDX remain the gold standard for preclinical drug evaluation and chemoresistance modelling [177, 191]. While they offer the advantage of representing a living organism, enabling the study of systemic drug effects, they frequently fall short in mimicking human specific pathobiological responses, and the complex immune-tumor interactions found in PDAC patients [191]. Despite advancements in genetical modifications and the use of humanized models (incorporating patient-derived tissue and PBMC), animal models remain exceptionally time-consuming, costly, and ethically sensitive [177, 191].

In alignment with the 3R principal (Replacement, Reduction, and Refinement) the regulatory landscape is shifting. The FDA released the “U.S. Food and Drug Administration Modernization Act 2.0” in 2022, which marked a pivotal change by removing the strict legal requirement for animal testing, instead permitting validated animal-free methods to fulfill safety assessments prior to human trials [216].

This shift highlights the urgent need for highly translational *in vitro* models in PDAC research [212]. The biochip model presented in this study provides a significant progression from static 3D spheroids to a dynamic environment. By integrating drug perfusion and immune cell circulation, the system captures the spatial architecture of the TME, as well as its intrinsic immunomodulatory properties. Furthermore, the PDS approach described here enables for investigation of personalized responses towards immunotherapies and other targeted therapies. Consequently, this study directly supports the 3R principle regarding reduction and replacement of animal testing [217]. By simulating human-specific tumor-immune-stroma interactions und physiological relevant conditions *in vitro*, this model provides a viable alternative to animal experiments. Unlike 2D cultures or immune-deficient mice, our system maintains the fibrotic architecture and immune dynamics necessary to generate clinically relevant data [165, 177]. Due to its high reproducibility and scalability, this platform allows for rapid screening of therapeutic candidates. By identifying ineffective compounds or adverse immune responses early in the development pipeline, it has the potential to significantly reduce the number of animals required for subsequent late-stage preclinical validation [218].

Despite the significant translational potential and alignment of this platform with the 3Rs principles, the multifaced nature of PDAC and systemic complexity of a human PDAC patient is not fully reflected in *in vitro* systems. While our model bridges the gap between static cultures and animal models, limitations remain that must be addressed to further refine its predictive power.

5.6 Limitations and future perspectives

The transition from static 3D cultures to a dynamic on-chip system and the development of PDS, marks a significant step forward to more translational *in vitro* systems for PDAC. However, the aim to model the complexity of PDAC also presents new technical and biological challenges. To ensure a comprehensive evaluation of the

results, it is crucial to acknowledge the limitations inherent of the current setup and to discuss how they can be addressed in future developments.

Regarding the biological limitations, the current model incorporates tumor cells, CAF, and either TAM or T-cells. However, the TME in PDAC patients is characterized by a far greater cellular diversity [61, 159]. Specifically, other immunosuppressive populations such as MDSC, significantly impair the effector function of T-cells and were not represented here [61, 120]. Moreover, the presence of M2 macrophages is key for the immunosuppressive TME; therefore, the simultaneous inclusion of both pro- and anti-inflammatory immune populations is crucial for a more nuanced evaluation of immunotherapies [177, 196].

Beyond the immune landscape, neuronal cells are increasingly emerging as an important component of the TME, contributing not only to tumor recurrence but also engaging in a complex neuronal-immune cross talk that remains unexplored in this setup [108]. Similarly, CAF are recognized as a highly heterogenous population with distinct functional subtypes. While the fibroblasts used in this study primarily express α-SMA, characterizing them as myCAF, responsible for the production of ECM molecules, incorporating other CAF subtypes, such as iCAF and apCAF, would allow for a more comprehensive investigation of their specific roles in therapeutic resistance [106, 110, 111].

In addition to cellular complexity, the physiochemical environment needs to be further refined. In the current model, the extreme hypoxia and nutrient deprivation characteristic of PDAC are not fully recapitulated, although they are key drivers of metabolic reprogramming and contribute to immune exhaustion [185, 201]. Furthermore, while myCAF and the added ECM components contribute to matrix deposition, the specific biomechanical stiffness and interstitial pressure of the native PDAC tissue, that increases the physical barrier for drug delivery and immune cell infiltration, is only partially captured [219]. It should also be noted that the use of PBMC-derived immune cells from healthy donors in the cell line-based model may not fully reflect the patient specific immune response. Therefore, our PDS model employing autologous T-cells is already a development to overcome this limitation.

Ultimately, while increasing the number of cell types and environmental factors enhances the model's physiological relevance, it also raises the analytical complexity. Striking a balance between a comprehensive biological representation and the precise,

mechanistic evaluation of individual cell-cell interactions remains one of the primary challenges for future developments of this platform.

Beyond the biological constraints, the current setup presents several inherent technical challenges. One primary limitation is the high cell requirement, particularly regarding immune cells, which complicates the evaluation of multiple therapeutic strategies and hinders high-throughput analysis, especially in a patient-specific context [180]. In this regard, the PDS model serves as a more streamlined, minimalistic platform for initial drug screening, while the biochip acts as a sophisticated validation platform for the most promising candidates.

Moreover, the sheer complexity of the biochip system is both time- and cost-intensive, requiring a significant amount of hands-on time to manage multiple cell types simultaneously. This high level of hands-on work inherently increases the risk of user-to-user variability. Furthermore, while the biochip was specifically engineered to incorporate PDAC spheroids, its unique dimensions and flow dynamics differ significantly from other microfluidic models described in the literature [182, 184, 186]. This lack of architectural standardization poses a challenge when comparing experimental outcomes across different on-chip platforms.

A significant analytical constraint is the incompatibility with high-resolution live-cell imaging. The integration of the PET micro-cavity membrane, while providing essential structural support and biocompatibility, contributes to substantial light scattering due to its material thickness and refractive properties [220]. Combined with the overall dimensions of the biochip, this results in suboptimal optical quality, particularly for confocal imaging. Consequently, the investigation of immune cell infiltration and polarization is largely restricted to endpoint analyses using fixed samples. To partially overcome this, the system allows for continuous supernatant sampling throughout the experiment. This enables longitudinal monitoring of secreted signaling molecules and provides an indirect assessment of cell viability, offering insights into the dynamic processes occurring within the TME despite these imaging limitations.

Future iterations of the biochip design and refinements in cellular composition offer significant potential to overcome the current system´s constraints. Integrating PDS directly into the biochip will enable the study of patient-specific responses under dynamic conditions, effectively bypassing the limitations of non-autologous immune models. Furthermore, the simultaneous incorporation of TAM and T-cells will facilitate

a more predictive evaluation of the synergistic effects between conventional chemotherapeutics and immunotherapies [215].

An intriguing alternative to *in vitro* generated MCTS is the *ex vivo* cultivation of tumor tissue fragments [221, 222]. These fragments largely preserve the original heterogeneity and spatial architecture of the primary tumor [221, 222]. While their use is currently hampered by a limited lifespan *ex vivo*, integrating these fragments into an on-chip environment, which more closely mimics the physiological and biomechanical conditions of the native TME, could extend their viability and allow for prolonged dynamic drug testing.

From a technical standpoint, transitioning from a vertical to a horizontal channel architecture, as seen in other microfluidic platforms, would significantly enhance optical accessibility and enable high-resolution live-cell imaging [220]. Additionally, downsizing the chips dimensions would reduce the required cell numbers while maintaining the spatial integrity of the model, thereby increasing its feasibility for patient-specific applications. The integration of real time pH and O_2 sensors would further expand the analytical depth by providing continuous readouts of metabolic state within the microenvironment [180, 220].

Another critical factor for clinical translation is the periodicity of treatment. Transitioning from single-dose applications to long-term cultivation under cyclical chemotherapeutic regiments would better reflect the clinical reality of PDAC patients and allow for the study of acquired resistance mechanisms [182, 218]. Moreover, the platform is ideally suited for evaluating combination therapies, such as dual ICI or the paring of chemotherapy with targeted agents. Beyond traditional approaches, the biochip also provides a robust framework for investigating novel cell-based therapies, including CAR-NK cells or CAR-macrophages, which are currently undergoing early clinical investigation for PDAC [92-94].

Beyond the local microenvironment, the formation of early metastases, particularly in the liver, remains a therapeutic hurdle in PDAC [2]. A limitation of the current biochip model is its inability to capture systemic multi-organ interactions, thereby lacking the capacity to model the metastatic cascade. To address this, the development of multi-organ-on-chip systems represents a vital future direction [223, 224]. By interconnecting various organ-specific modules through a common perfusion system, these platforms allow for physiological crosstalk between the primary tumor and distant organs [223,

224]. Such setups could simulate the intravasation of tumor cells, their circulation, and subsequent colonization of a metastatic niche in a secondary organ-on-chip [223]. While multi-organ-on-chip systems would significantly enhance the translational relevance of *in vitro* modeling, it is important to note that they require substantially more complex cellular handling, as well as increased time and financial investment to establish [224].

In summary, despite its inherent biological and technical limitations, the biochip model presented in this study demonstrates promising potential for further development. By refining the hardware design and modular adjustments in the cellular components, the platform can be tailored to specific research questions. This study provides a foundational framework for the development of highly translational preclinical models for drug discovery in PDAC.

5.7 Conclusion

The fundamental objective of this work was to establish a PDAC biochip model that, despite its controlled simplicity, reflects key hallmarks of the disease, including immune dysfunction, desmoplastic stroma, and chemoresistance. By integrating tumor-intrinsic factors, stromal components and dynamic immune cell perfusion, the platform overcomes the critical limitations of static *in vitro* cultures and provides a more human-relevant alternative to animal models.

The findings presented here demonstrate that the spatial architecture and cellular composition of the TME are crucial factors for therapeutic resistance and immune evasion. The ability of the presented biochip and PDS models to reproduce these complex interactions highlights their potential as a powerful tool for translational research. Furthermore, by aligning with the 3Rs principles, this model offers a viable path toward reducing the reliance on animal testing in preclinical drug development.

In conclusion, while the platform can be further refined through the integration of additional cellular subtype, it bridges the gap between benchtop research and clinical application, paving the way for more effective, personalized treatments for PDAC patients while upholding the highest ethical standards of modern research.

5 References

1. Ntukidem, O.L., O.J. Ogedegbe, and S. Bai, *Updated trends in incidence and mortality of pancreatic cancer. an analysis of the Surveillance, Epidemiology, and End Results (SEER) database.* Journal of Clinical Oncology, 2025. **43**(4_suppl): p. 786–786.
2. Udrycka, K., et al., *Tumor Characteristics and Clinical Features of the Patient as Prognostic Factors in PDAC.* Cancers (Basel), 2025. **17**(20).
3. Mack, S., et al., *Pancreatic Cancer: Epidemiology, Risk Factors, and Prevention.* Onco, 2025. **5**(3): p. 37.
4. Siegel, R.L., et al., *Cancer statistics, 2025.* CA Cancer J Clin, 2025. **75**(1): p. 10–45.
5. Shi, H., et al., *Nomograms for Predicting the Risk and Prognosis of Liver Metastases in Pancreatic Cancer: A Population-Based Analysis.* J Pers Med, 2023. **13**(3).
6. Mannucci, A. and A. Goel, *Advances in pancreatic cancer early diagnosis, prevention, and treatment: The past, the present, and the future.* CA Cancer J Clin, 2026. **76**(1): p. e70035.
7. Huang, J., et al., *Worldwide Burden of, Risk Factors for, and Trends in Pancreatic Cancer.* Gastroenterology, 2021. **160**(3): p. 744–754.
8. Maisonneuve, P. and A.B. Lowenfels, *Risk factors for pancreatic cancer: a summary review of meta-analytical studies.* International Journal of Epidemiology, 2014. **44**(1): p. 186–198.
9. Naudin, S., et al., *Lifetime and baseline alcohol intakes and risk of pancreatic cancer in the European Prospective Investigation into Cancer and Nutrition study.* International journal of cancer, 2018. **143**(4): p. 801–812.
10. Jiao, L., et al., *Body mass index, effect modifiers, and risk of pancreatic cancer: a pooled study of seven prospective cohorts.* Cancer Causes Control, 2010. **21**(8): p. 1305–14.
11. Michaud, D.S., et al., *Physical Activity, Obesity, Height, and the Risk of Pancreatic Cancer.* JAMA, 2001. **286**(8): p. 921–929.
12. Bosetti, C., et al., *Diabetes, antidiabetic medications, and pancreatic cancer risk: an analysis from the International Pancreatic Cancer Case-Control Consortium.* Annals of Oncology, 2014. **25**(10): p. 2065–2072.
13. Dankner, R., et al., *Time-Dependent Risk of Cancer After a Diabetes Diagnosis in a Cohort of 2.3 Million Adults.* Am J Epidemiol, 2016. **183**(12): p. 1098–106.
14. Brugel, M., et al., *Pesticides and pancreatic adenocarcinoma: A transversal epidemiological, environmental and mechanistic narrative review.* Dig Liver Dis, 2022. **54**(12): p. 1605–1613.
15. Brugel, M., et al., *Association between pancreatic adenocarcinoma risk and concentration of organochlorine pesticides in adipose tissue and urine: A targeted-screening analysis case-control study (PESTIPAC).* United European Gastroenterology Journal, 2024. **12**(7): p. 951–959.
16. Rijkers, A.P., et al., *Risk of Pancreatic Cancer After a Primary Episode of Acute Pancreatitis.* Pancreas, 2017. **46**(8): p. 1018–1022.
17. Klatte, D.C.F., et al., *Pancreatic Cancer Surveillance in Carriers of a Germline CDKN2A Pathogenic Variant: Yield and Outcomes of a 20-Year Prospective Follow-Up.* J Clin Oncol, 2022. **40**(28): p. 3267–3277.

18. Maisonneuve, P., B.C. Marshall, and A.B. Lowenfels, *Risk of pancreatic cancer in patients with cystic fibrosis.* Gut, 2007. **56**(9): p. 1327–8.
19. Klein, A.P., *Pancreatic cancer epidemiology: understanding the role of lifestyle and inherited risk factors.* Nature Reviews Gastroenterology & Hepatology, 2021. **18**(7): p. 493–502.
20. Marstrand-Daucé, L., et al., *Acinar-to-Ductal Metaplasia (ADM): On the Road to Pancreatic Intraepithelial Neoplasia (PanIN) and Pancreatic Cancer.* Int J Mol Sci, 2023. **24**(12).
21. Pian, L.L., et al., *Identification and analysis of pancreatic intraepithelial neoplasia: opportunities and challenges.* Front Endocrinol (Lausanne), 2024. **15**: p. 1401829.
22. Haeberle, L. and I. Esposito, *Pathology of pancreatic cancer.* Transl Gastroenterol Hepatol, 2019. **4**: p. 50.
23. Wood, L.D., et al., *Pancreatic Cancer: Pathogenesis, Screening, Diagnosis, and Treatment.* Gastroenterology, 2022. **163**(2): p. 386–402.e1.
24. Yamaguchi, H., et al., *The discrete nature and distinguishing molecular features of pancreatic intraductal tubulopapillary neoplasms and intraductal papillary mucinous neoplasms of the gastric type, pyloric gland variant.* J Pathol, 2013. **231**(3): p. 335–41.
25. Than, M.T., et al., *KRAS-Driven Tumorigenesis and KRAS-Driven Therapy in Pancreatic Adenocarcinoma.* Mol Cancer Ther, 2024. **23**(10): p. 1378–1388.
26. Rozengurt, E. and G. Eibl, *Pancreatic cancer: molecular pathogenesis and emerging therapeutic strategies.* Signal Transduction and Targeted Therapy, 2026. **11**(1): p. 6.
27. Breen, K.E., et al., *Paired tumor-normal sequencing provides insights into the CDKN2A-associated tumor spectrum.* npj Precision Oncology, 2025. **9**(1): p. 363.
28. Kim, M.P., et al., *Oncogenic KRAS Recruits an Expansive Transcriptional Network through Mutant p53 to Drive Pancreatic Cancer Metastasis.* Cancer Discov, 2021. **11**(8): p. 2094–2111.
29. Grant, T.J., K. Hua, and A. Singh, *Molecular Pathogenesis of Pancreatic Cancer.* Prog Mol Biol Transl Sci, 2016. **144**: p. 241–275.
30. Connor, A.A. and S. Gallinger, *Pancreatic cancer evolution and heterogeneity: integrating omics and clinical data.* Nat Rev Cancer, 2022. **22**(3): p. 131–142.
31. Pedro, B.A. and L.D. Wood, *Early neoplastic lesions of the pancreas: initiation, progression, and opportunities for precancer interception.* J Clin Invest, 2025. **135**(14).
32. Bell, A.T.F., et al., *PanIN and CAF transitions in pancreatic carcinogenesis revealed with spatial data integration.* Cell Syst, 2024. **15**(8): p. 753–769.e5.
33. Strobel, O., et al., *Optimizing the outcomes of pancreatic cancer surgery.* Nat Rev Clin Oncol, 2019. **16**(1): p. 11–26.
34. Springfeld, C., et al., *Neoadjuvant therapy for pancreatic cancer.* Nat Rev Clin Oncol, 2023. **20**(5): p. 318–337.
35. Conroy, T., et al., *Pancreatic cancer: ESMO Clinical Practice Guideline for diagnosis, treatment and follow-up.* Ann Oncol, 2023. **34**(11): p. 987–1002.
36. Mosalem, O.M., et al., *Pancreatic ductal adenocarcinoma (PDAC): clinical progress in the last five years.* Expert Opin Investig Drugs, 2025. **34**(3): p. 149–160.
37. Reddy, A.V., et al., *A safety study of intraoperative radiation therapy following stereotactic body radiation therapy and multi-agent chemotherapy in the*

treatment of localized pancreatic adenocarcinoma: study protocol of a phase I trial. Radiat Oncol, 2022. **17**(1): p. 173.
38. Versteijne, E., et al., *Neoadjuvant Chemoradiotherapy Versus Upfront Surgery for Resectable and Borderline Resectable Pancreatic Cancer: Long-Term Results of the Dutch Randomized PREOPANC Trial.* J Clin Oncol, 2022. **40**(11): p. 1220–1230.
39. Shao, H., et al., *Economic evaluation of NALIRIFOX vs. nab-paclitaxel and gemcitabine regimens for first-line treatment of metastatic pancreatic ductal adenocarcinoma from US perspective.* Cost Effectiveness and Resource Allocation, 2024. **22**(1): p. 70.
40. Strickler, J.H., et al., *Sotorasib in KRAS p.G12C-Mutated Advanced Pancreatic Cancer.* N Engl J Med, 2023. **388**(1): p. 33–43.
41. Bekaii-Saab, T.S., et al., *Adagrasib in Advanced Solid Tumors Harboring a KRAS(G12C) Mutation.* J Clin Oncol, 2023. **41**(25): p. 4097–4106.
42. *A Phase Ib/II Open-label, Multi-center Dose Escalation Study of JDQ443 in Patients With Advanced Solid Tumors Harboring the KRAS G12C Mutation*. 2021.
43. *A Phase 1/2, Open Label Study to Evaluate the Safety, Tolerability, Pharmacokinetics and Efficacy of D-1553 in Subjects With Advanced or Metastatic Solid Tumors With KRasG12C Mutation*, S. Merck and L.L.C. Dohme, Editors. 2020.
44. *A Phase Ia/Ib, Open-label, Multicentre Dose-escalation and Expansion Study to Investigate the Safety, Pharmacokinetics and Preliminary Efficacy of BI 1823911 as a Monotherapy and in Combination With Other Anti-cancer Therapies in Patients With Advanced or Metastatic Solid Tumours Expressing KRAS G12C Mutation*. 2021.
45. *A Phase 1/2 Study of LY3537982 in Patients With KRAS G12C-Mutant Advanced Solid Tumors*, S. Merck and L.L.C. Dohme, Editors. 2021.
46. *A Phase 1/2, Multi-Center, Open-Label Study to Evaluate the Safety, Tolerability, Pharmacokinetics, and Preliminary Evidence of Antitumor Activity of JAB-21822 Monotherapy and Combination Therapy in Adult Patients With Advanced Solid Tumors Harboring KRAS G12C Mutation*. 2021.
47. *A Phase Ia/Ib Dose-Escalation and Dose-Expansion Study Evaluating the Safety, Pharmacokinetics, and Activity of GDC-6036 as a Single Agent and in Combination With Other Anti-cancer Therapies in Patients With Advanced or Metastatic Solid Tumors With a KRAS G12C Mutation*. 2020.
48. Hallin, J., et al., *Anti-tumor efficacy of a potent and selective non-covalent KRAS(G12D) inhibitor.* Nat Med, 2022. **28**(10): p. 2171–2182.
49. *A Phase 1/2 Multiple Expansion Cohort Trial of MRTX1133 in Patients With Advanced Solid Tumors Harboring a KRAS G12D Mutation*. 2023.
50. Jiang, J., et al., *Translational and Therapeutic Evaluation of RAS-GTP Inhibition by RMC-6236 in RAS-Driven Cancers.* Cancer Discov, 2024. **14**(6): p. 994–1017.
51. *RASolute 302: A Phase 3 Multicenter, Open-label, Randomized Study of Daraxonrasib (RMC-6236) Versus Investigator's Choice of Standard of Care Therapy in Patients With Previously Treated Metastatic Pancreatic Ductal Adenocarcinoma (PDAC)*. 2024.
52. Subbiah, V., et al., *Dabrafenib plus trametinib in patients with BRAF(V600E)-mutated biliary tract cancer (ROAR): a phase 2, open-label, single-arm, multicentre basket trial.* Lancet Oncol, 2020. **21**(9): p. 1234–1243.

53. Kim, D.W., et al., *The phase I/II eNRGy trial: Zenocutuzumab in patients with cancers harboring NRG1 gene fusions.* Future Oncol, 2024. **20**(16): p. 1057–1067.
54. Subbiah, V., et al., *Tumour-agnostic efficacy and safety of selpercatinib in patients with RET fusion-positive solid tumours other than lung or thyroid tumours (LIBRETTO-001): a phase 1/2, open-label, basket trial.* Lancet Oncol, 2022. **23**(10): p. 1261–1273.
55. Meric-Bernstam, F., et al., *Efficacy and Safety of Trastuzumab Deruxtecan in Patients With HER2-Expressing Solid Tumors: Primary Results From the DESTINY-PanTumor02 Phase II Trial.* J Clin Oncol, 2024. **42**(1): p. 47–58.
56. Hong, D.S., et al., *Larotrectinib in patients with TRK fusion-positive solid tumours: a pooled analysis of three phase 1/2 clinical trials.* Lancet Oncol, 2020. **21**(4): p. 531–540.
57. Doebele, R.C., et al., *Entrectinib in patients with advanced or metastatic NTRK fusion-positive solid tumours: integrated analysis of three phase 1-2 trials.* Lancet Oncol, 2020. **21**(2): p. 271–282.
58. Drilon, A., et al., *Repotrectinib in ROS1 Fusion-Positive Non-Small-Cell Lung Cancer.* N Engl J Med, 2024. **390**(2): p. 118–131.
59. Golan, T., et al., *Maintenance Olaparib for Germline BRCA-Mutated Metastatic Pancreatic Cancer.* N Engl J Med, 2019. **381**(4): p. 317–327.
60. Ju, Y., et al., *Barriers and opportunities in pancreatic cancer immunotherapy.* NPJ Precis Oncol, 2024. **8**(1): p. 199.
61. Thankachan, S.V., et al., *Tumor Microenvironment: Recent Advances in Immunotherapies of Pancreatic Cancer.* Medicina (Kaunas), 2025. **61**(10).
62. Hodi, F.S., et al., *Improved survival with ipilimumab in patients with metastatic melanoma.* N Engl J Med, 2010. **363**(8): p. 711–23.
63. Wang, J., T. Yang, and J. Xu, *Therapeutic Development of Immune Checkpoint Inhibitors.* Adv Exp Med Biol, 2020. **1248**: p. 619–649.
64. Dang, T.O., et al., *Pembrolizumab for the treatment of PD-L1 positive advanced or metastatic non-small cell lung cancer.* Expert Rev Anticancer Ther, 2016. **16**(1): p. 13–20.
65. Kim, J., et al., *The Cancer Genome Atlas Expression Subtypes Stratify Response to Checkpoint Inhibition in Advanced Urothelial Cancer and Identify a Subset of Patients with High Survival Probability.* Eur Urol, 2019. **75**(6): p. 961–964.
66. Kasamon, Y.L., et al., *FDA Approval Summary: Nivolumab for the Treatment of Relapsed or Progressive Classical Hodgkin Lymphoma.* Oncologist, 2017. **22**(5): p. 585–591.
67. Kudo, M., *Targeted and immune therapies for hepatocellular carcinoma: Predictions for 2019 and beyond.* World J Gastroenterol, 2019. **25**(7): p. 789–807.
68. Arafat Hossain, M., *A comprehensive review of immune checkpoint inhibitors for cancer treatment.* Int Immunopharmacol, 2024. **143**(Pt 2): p. 113365.
69. Tsujikawa, T., et al., *Evaluation of Cyclophosphamide/GVAX Pancreas Followed by Listeria-Mesothelin (CRS-207) with or without Nivolumab in Patients with Pancreatic Cancer.* Clin Cancer Res, 2020. **26**(14): p. 3578–3588.
70. Katz, M.H.G., et al., *Multicenter randomized controlled trial of neoadjuvant chemoradiotherapy alone or in combination with pembrolizumab in patients with resectable or borderline resectable pancreatic adenocarcinoma.* J Immunother Cancer, 2023. **11**(12).

71. Gross, N.E., et al., *Phosphodiesterase-5 inhibition collaborates with vaccine-based immunotherapy to reprogram myeloid cells in pancreatic ductal adenocarcinoma.* JCI Insight, 2024. **9**(18).
72. O'Reilly, E.M., et al., *Durvalumab With or Without Tremelimumab for Patients With Metastatic Pancreatic Ductal Adenocarcinoma: A Phase 2 Randomized Clinical Trial.* JAMA Oncol, 2019. **5**(10): p. 1431–1438.
73. Balsano, R., et al., *Pancreatic Ductal Adenocarcinoma and Immune Checkpoint Inhibitors: The Gray Curtain of Immunotherapy and Spikes of Lights.* Curr Oncol, 2023. **30**(4): p. 3871–3885.
74. Sharma, P., et al., *Efficacy and tolerability of tremelimumab in patients with metastatic pancreatic ductal adenocarcinoma.* Journal of Clinical Oncology. **36**(4_suppl): p. 470–470.
75. Brahmer, J.R., et al., *Safety and activity of anti-PD-L1 antibody in patients with advanced cancer.* N Engl J Med, 2012. **366**(26): p. 2455–65.
76. Royal, R.E., et al., *Phase 2 trial of single agent Ipilimumab (anti-CTLA-4) for locally advanced or metastatic pancreatic adenocarcinoma.* J Immunother, 2010. **33**(8): p. 828–33.
77. Kalyan, A., et al., *Ipilimumab and gemcitabine for advanced pancreas cancer: A phase Ib study*. 2016, American Society of Clinical Oncology.
78. Ma, J., et al., *Immune checkpoint inhibitors combined with chemotherapy for the treatment of advanced pancreatic cancer patients.* Cancer Immunol Immunother, 2020. **69**(3): p. 365–372.
79. Weiss, G.J., et al., *Phase Ib/II study of gemcitabine, nab-paclitaxel, and pembrolizumab in metastatic pancreatic adenocarcinoma.* Invest New Drugs, 2018. **36**(1): p. 96–102.
80. Reiss, K.A., et al., *Niraparib plus nivolumab or niraparib plus ipilimumab in patients with platinum-sensitive advanced pancreatic cancer: a randomised, phase 1b/2 trial.* Lancet Oncol, 2022. **23**(8): p. 1009–1020.
81. Pishvaian, M.J., et al., *A Phase I/II Study of Veliparib (ABT-888) in Combination with 5-Fluorouracil and Oxaliplatin in Patients with Metastatic Pancreatic Cancer.* Clin Cancer Res, 2020. **26**(19): p. 5092–5101.
82. Naing, A., et al., *Abstract CT177: Epacadostat plus durvalumab in patients with advanced solid tumors: preliminary results of the ongoing, open-label, phase I/II ECHO-203 study.* Cancer Research, 2018. **78**(13_Supplement): p. CT177–CT177.
83. Bockorny, B., et al., *BL-8040, a CXCR4 antagonist, in combination with pembrolizumab and chemotherapy for pancreatic cancer: the COMBAT trial.* Nat Med, 2020. **26**(6): p. 878–885.
84. Wang-Gillam, A., et al., *Phase I study of defactinib combined with pembrolizumab and gemcitabine in patients with advanced cancer*. 2018, American Society of Clinical Oncology.
85. Al-Khinji, A., et al., *Immune checkpoint inhibitors in pancreatic adenocarcinoma: a systematic review and meta analysis of clinical outcomes.* Front Oncol, 2025. **15**: p. 1569884.
86. Marabelle, A., et al., *Pembrolizumab in microsatellite-instability-high and mismatch-repair-deficient advanced solid tumors: updated results of the KEYNOTE-158 trial.* Nat Cancer, 2025. **6**(2): p. 253–258.
87. Qi, C., et al., *Claudin18.2-specific CAR T cells in gastrointestinal cancers: phase 1 trial interim results.* Nat Med, 2022. **28**(6): p. 1189–1198.

88. Liu, Y., et al., *Anti-EGFR chimeric antigen receptor-modified T cells in metastatic pancreatic carcinoma: A phase I clinical trial.* Cytotherapy, 2020. **22**(10): p. 573–580.
89. Feng, K., et al., *Phase I study of chimeric antigen receptor modified T cells in treating HER2-positive advanced biliary tract cancers and pancreatic cancers.* Protein Cell, 2018. **9**(10): p. 838–847.
90. Haas, A.R., et al., *Phase I Study of Lentiviral-Transduced Chimeric Antigen Receptor-Modified T Cells Recognizing Mesothelin in Advanced Solid Cancers.* Mol Ther, 2019. **27**(11): p. 1919–1929.
91. Czaplicka, A., et al., *Chimeric Antigen Receptor T Cell Therapy for Pancreatic Cancer: A Review of Current Evidence.* Cells, 2024. **13**(1).
92. Wang, W., et al., *Breakthrough of solid tumor treatment: CAR-NK immunotherapy.* Cell Death Discov, 2024. **10**(1): p. 40.
93. Reiss, K.A., et al., *CAR-macrophage therapy for HER2-overexpressing advanced solid tumors: a phase 1 trial.* Nat Med, 2025. **31**(4): p. 1171–1182.
94. Wei, D., et al., *CAR-Macrophage Cell Therapy: A New Era of Hope for Pancreatic Cancer.* Clin Cancer Res, 2025. **31**(19): p. 4018–4031.
95. Klieser, E., et al., *Role of histone deacetylases in pancreas: Implications for pathogenesis and therapy.* World J Gastrointest Oncol, 2015. **7**(12): p. 473–83.
96. Krauß, L., et al., *Epigenetic control of pancreatic cancer metastasis.* Cancer Metastasis Rev, 2023. **42**(4): p. 1113–1131.
97. Marks, P.A., *Discovery and development of SAHA as an anticancer agent.* Oncogene, 2007. **26**(9): p. 1351–6.
98. Xiang, X.S., et al., *Histone deacetylases: A novel class of therapeutic targets for pancreatic cancer.* Biochim Biophys Acta Rev Cancer, 2022. **1877**(1): p. 188676.
99. Cai, M.H., et al., *Depletion of HDAC1, 7 and 8 by Histone Deacetylase Inhibition Confers Elimination of Pancreatic Cancer Stem Cells in Combination with Gemcitabine.* Sci Rep, 2018. **8**(1): p. 1621.
100. Elrakaybi, A., et al., *Epigenetics in Pancreatic Ductal Adenocarcinoma: Impact on Biology and Utilization in Diagnostics and Treatment.* Cancers (Basel), 2022. **14**(23).
101. Xue-Song, X., et al., *Histone deacetylases: A novel class of therapeutic targets for pancreatic cancer.* Biochimica et Biophysica Acta (BBA) - Reviews on Cancer, 2022. **1877**(1): p. 188676.
102. *A Phase 2 Clinical Trial of Entinostat in Combination With Nivolumab for Patients With Previously Treated Unresectable or Metastatic Cholangiocarcinoma and Pancreatic Adenocarcinoma*, P. Syndax, S. Bristol-Myers, and I. National Cancer, Editors. 2017.
103. Poklepovic, A.S., et al., *A phase 1 study of neoadjuvant chemotherapy followed by concurrent chemoradiation with gemcitabine, sorafenib, and vorinostat in pancreatic cancer.* Journal of Clinical Oncology, 2021. **39**(15_suppl): p. e16268–e16268.
104. Ischenko, I., O. Petrenko, and M.J. Hayman, *A MEK/PI3K/HDAC inhibitor combination therapy for KRAS mutant pancreatic cancer cells.* Oncotarget, 2015. **6**(18): p. 15814–27.
105. Pratticò, F. and I. Garajová, *Focus on Pancreatic Cancer Microenvironment.* Curr Oncol, 2024. **31**(8): p. 4241–4260.
106. Bräutigam, K., et al., *Tumor immune microenvironment in pancreatic ductal adenocarcinoma revisited - Exploring the "Space".* Cancer Lett, 2025. **622**: p. 217699.

107. Mercanti, L., et al., *PDAC, the Influencer Cancer: Cross-Talk with Tumor Microenvironment and Connected Potential Therapy Strategies.* Cancers (Basel), 2023. **15**(11).
108. Lovecek, M., et al., *Perineural Invasion in Pancreatic Ductal Adenocarcinoma: Recapitulating Its Importance and Defining Future Directions.* United European Gastroenterol J, 2025. **13**(9): p. 1678–1689.
109. Barrera, L.N., et al., *Fibroblasts from Distinct Pancreatic Pathologies Exhibit Disease-Specific Properties.* Cancer Res, 2020. **80**(13): p. 2861–2873.
110. Norton, J., et al., *Pancreatic Cancer Associated Fibroblasts (CAF): Under-Explored Target for Pancreatic Cancer Treatment.* Cancers (Basel), 2020. **12**(5).
111. Morgan, A., et al., *Medical Biology of Cancer-Associated Fibroblasts in Pancreatic Cancer.* Biology (Basel), 2023. **12**(8).
112. Wu, Y., et al., *The Role of Stellate Cells in Pancreatic Ductal Adenocarcinoma: Targeting Perspectives.* Front Oncol, 2020. **10**: p. 621937.
113. Provenzano, P.P., et al., *Enzymatic targeting of the stroma ablates physical barriers to treatment of pancreatic ductal adenocarcinoma.* Cancer Cell, 2012. **21**(3): p. 418–29.
114. Ajina, R. and L.M. Weiner, *T-Cell Immunity in Pancreatic Cancer.* Pancreas, 2020. **49**(8): p. 1014–1023.
115. Thomas, D. and P. Radhakrishnan, *Pancreatic Stellate Cells: The Key Orchestrator of The Pancreatic Tumor Microenvironment.* Adv Exp Med Biol, 2020. **1234**: p. 57–70.
116. Zhang, A., et al., *Cancer-associated fibroblasts promote M2 polarization of macrophages in pancreatic ductal adenocarcinoma.* Cancer Med, 2017. **6**(2): p. 463–470.
117. Garg, B., et al., *NFκB in Pancreatic Stellate Cells Reduces Infiltration of Tumors by Cytotoxic T Cells and Killing of Cancer Cells, via Up-regulation of CXCL12.* Gastroenterology, 2018. **155**(3): p. 880–891.e8.
118. Whittle, M.C. and S.R. Hingorani, *Fibroblasts in Pancreatic Ductal Adenocarcinoma: Biological Mechanisms and Therapeutic Targets.* Gastroenterology, 2019. **156**(7): p. 2085–2096.
119. Tanaka, H.Y., et al., *Therapeutic Strategies to Overcome Fibrotic Barriers to Nanomedicine in the Pancreatic Tumor Microenvironment.* Cancers (Basel), 2023. **15**(3).
120. Hartupee, C., et al., *Pancreatic cancer tumor microenvironment is a major therapeutic barrier and target.* Front Immunol, 2024. **15**: p. 1287459.
121. Locati, M., G. Curtale, and A. Mantovani, *Diversity, Mechanisms, and Significance of Macrophage Plasticity.* Annu Rev Pathol, 2020. **15**: p. 123–147.
122. Yang, S., Q. Liu, and Q. Liao, *Tumor-Associated Macrophages in Pancreatic Ductal Adenocarcinoma: Origin, Polarization, Function, and Reprogramming.* Front Cell Dev Biol, 2020. **8**: p. 607209.
123. Hu, H., et al., *The M2 phenotype of tumor-associated macrophages in the stroma confers a poor prognosis in pancreatic cancer.* Tumor Biology, 2016. **37**: p. 8657–8664.
124. Atanasov, G., et al., *TIE2-expressing monocytes and M2-polarized macrophages impact survival and correlate with angiogenesis in adenocarcinoma of the pancreas.* Oncotarget, 2018. **9**(51): p. 29715–29726.
125. Zhang, R., et al., *CXCL5 overexpression predicts a poor prognosis in pancreatic ductal adenocarcinoma and is correlated with immune cell infiltration.* J Cancer, 2020. **11**(9): p. 2371–2381.

126. Yang, Y., et al., *M2 Macrophage-Derived Exosomes Promote Angiogenesis and Growth of Pancreatic Ductal Adenocarcinoma by Targeting E2F2.* Mol Ther, 2021. **29**(3): p. 1226–1238.
127. Poh, A.R. and M. Ernst, *Tumor-Associated Macrophages in Pancreatic Ductal Adenocarcinoma: Therapeutic Opportunities and Clinical Challenges.* Cancers (Basel), 2021. **13**(12).
128. Lin, H.J., et al., *Polarization of Cancer-Associated Macrophages Maneuver Neoplastic Attributes of Pancreatic Ductal Adenocarcinoma.* Cancers (Basel), 2023. **15**(13).
129. Liou, G.Y., et al., *Macrophage-secreted cytokines drive pancreatic acinar-to-ductal metaplasia through NF-κB and MMPs.* J Cell Biol, 2013. **202**(3): p. 563–77.
130. Wang, S., et al., *Targeting M2-like tumor-associated macrophages is a potential therapeutic approach to overcome antitumor drug resistance.* NPJ Precis Oncol, 2024. **8**(1): p. 31.
131. Deswal, B., U. Bagchi, and S. Kapoor, *Curcumin Suppresses M2 Macrophage-derived Paclitaxel Chemoresistance through Inhibition of PI3K-AKT/STAT3 Signaling.* Anticancer Agents Med Chem, 2024. **24**(2): p. 146–156.
132. Zhang, J., et al., *Multi-omics analysis reveals the chemoresistance mechanism of proliferating tissue-resident macrophages in PDAC via metabolic adaptation.* Cell Rep, 2023. **42**(6): p. 112620.
133. Kuwada, K., et al., *The epithelial-to-mesenchymal transition induced by tumor-associated macrophages confers chemoresistance in peritoneally disseminated pancreatic cancer.* J Exp Clin Cancer Res, 2018. **37**(1): p. 307.
134. Nywening, T.M., et al., *Targeting both tumour-associated CXCR2(+) neutrophils and CCR2(+) macrophages disrupts myeloid recruitment and improves chemotherapeutic responses in pancreatic ductal adenocarcinoma.* Gut, 2018. **67**(6): p. 1112–1123.
135. Buchholz, S.M., et al., *Depletion of Macrophages Improves Therapeutic Response to Gemcitabine in Murine Pancreas Cancer.* Cancers (Basel), 2020. **12**(7).
136. Zheng, C., et al., *IFNα-induced BST2(+) tumor-associated macrophages facilitate immunosuppression and tumor growth in pancreatic cancer by ERK-CXCL7 signaling.* Cell Rep, 2024. **43**(4): p. 114088.
137. Daley, D., et al., *NLRP3 signaling drives macrophage-induced adaptive immune suppression in pancreatic carcinoma.* J Exp Med, 2017. **214**(6): p. 1711–1724.
138. Palsson-McDermott, E.M., et al., *Pyruvate Kinase M2 Is Required for the Expression of the Immune Checkpoint PD-L1 in Immune Cells and Tumors.* Front Immunol, 2017. **8**: p. 1300.
139. Daley, D., et al., *Dectin 1 activation on macrophages by galectin 9 promotes pancreatic carcinoma and peritumoral immune tolerance.* Nat Med, 2017. **23**(5): p. 556–567.
140. Tsukamoto, M., et al., *PD-L1 expression enhancement by infiltrating macrophage-derived tumor necrosis factor-α leads to poor pancreatic cancer prognosis.* Cancer Sci, 2019. **110**(1): p. 310–320.
141. Goulart, M.R., et al., *T cells in pancreatic cancer stroma.* World J Gastroenterol, 2021. **27**(46): p. 7956–7968.
142. Protti, M.P. and L. De Monte, *Immune infiltrates as predictive markers of survival in pancreatic cancer patients.* Front Physiol, 2013. **4**: p. 210.
143. Huber, M., et al., *The Immune Microenvironment in Pancreatic Cancer.* Int J Mol Sci, 2020. **21**(19).

144. Kerk, S.A., et al., *Metabolic networks in mutant KRAS-driven tumours: tissue specificities and the microenvironment.* Nat Rev Cancer, 2021. **21**(8): p. 510–525.
145. Dey, P., et al., *Oncogenic KRAS-Driven Metabolic Reprogramming in Pancreatic Cancer Cells Utilizes Cytokines from the Tumor Microenvironment.* Cancer Discov, 2020. **10**(4): p. 608–625.
146. Wang, S., Z. Li, and G. Hu, *Prognostic role of intratumoral IL-17A expression by immunohistochemistry in solid tumors: a meta-analysis.* Oncotarget, 2017. **8**(39): p. 66382–66391.
147. Hegde, S., et al., *Dendritic Cell Paucity Leads to Dysfunctional Immune Surveillance in Pancreatic Cancer.* Cancer Cell, 2020. **37**(3): p. 289–307.e9.
148. Liu, W., X. Wang, and W. Wu, *Role and functional mechanisms of IL-17/IL-17R signaling in pancreatic cancer (Review).* Oncol Rep, 2024. **52**(5).
149. McAllister, F., et al., *Oncogenic Kras activates a hematopoietic-to-epithelial IL-17 signaling axis in preinvasive pancreatic neoplasia.* Cancer Cell, 2014. **25**(5): p. 621–37.
150. Ene-Obong, A., et al., *Activated pancreatic stellate cells sequester CD8+ T cells to reduce their infiltration of the juxtatumoral compartment of pancreatic ductal adenocarcinoma.* Gastroenterology, 2013. **145**(5): p. 1121–32.
151. Rodriguez, E., et al., *In-depth immune profiling of peripheral blood mononuclear cells in patients with pancreatic ductal adenocarcinoma reveals discriminative immune subpopulations.* Cancer Sci, 2024. **115**(7): p. 2170–2183.
152. Papalampros, A., et al., *Unique Spatial Immune Profiling in Pancreatic Ductal Adenocarcinoma with Enrichment of Exhausted and Senescent T Cells and Diffused CD47-SIRPα Expression.* Cancers (Basel), 2020. **12**(7).
153. Wan, S., et al., *Tumor infiltrating T cell states and checkpoint inhibitor expression in hepatic and pancreatic malignancies.* Front Immunol, 2023. **14**: p. 1067352.
154. Yousuf, S., et al., *Spatially Resolved Multi-Omics Single-Cell Analyses Inform Mechanisms of Immune Dysfunction in Pancreatic Cancer.* Gastroenterology, 2023. **165**(4): p. 891–908.e14.
155. Saka, D., et al., *Mechanisms of T-Cell Exhaustion in Pancreatic Cancer.* Cancers (Basel), 2020. **12**(8).
156. Chen, L., *Co-inhibitory molecules of the B7-CD28 family in the control of T-cell immunity.* Nat Rev Immunol, 2004. **4**(5): p. 336–47.
157. Li, H.B., Z.H. Yang, and Q.Q. Guo, *Immune checkpoint inhibition for pancreatic ductal adenocarcinoma: limitations and prospects: a systematic review.* Cell Commun Signal, 2021. **19**(1): p. 117.
158. Long, L., et al., *The promising immune checkpoint LAG-3: from tumor microenvironment to cancer immunotherapy.* Genes Cancer, 2018. **9**(5-6): p. 176–189.
159. Kane, L.E., et al., *The Hallmarks of Pancreatic Cancer.* Cancer Lett, 2026: p. 218437.
160. Gioeli, D., et al., *Development of a multicellular pancreatic tumor microenvironment system using patient-derived tumor cells.* Lab on a Chip, 2019. **19**(7): p. 1193–1204.
161. Xie, B.H., J.; Mundorf, V.; Betz, J.; Reimche, I.; Erkan, M.; Büdeyri, I.; Gesell, A.; Kerr, R.G.; Ariantari, N.P.; et al, *Pseudopterosin and O-Methyltylophorinidine Suppress Cell Growth in a 3D Spheroid Co-Culture Model of Pancreatic Ductal Adenocarcinoma.* Bioengineering, 2020.

162. He, M., et al., *Preclinical mouse models for immunotherapeutic and non-immunotherapeutic drug development for pancreatic ductal adenocarcinoma.* Ann Pancreat Cancer, 2020. **3**.
163. Boilève, A., et al., *Organoids for Functional Precision Medicine in Advanced Pancreatic Cancer.* Gastroenterology, 2024. **167**(5): p. 961–976.e13.
164. Gündel, B., et al., *Pancreatic Ductal Adenocarcinoma: Preclinical in vitro and ex vivo Models.* Front Cell Dev Biol, 2021. **9**: p. 741162.
165. Atat, O.E., et al., *3D modeling in cancer studies.* Human Cell, 2022. **35**(1): p. 23–36.
166. Kunz-Schughart, L.A., et al., *A heterologous 3-D coculture model of breast tumor cells and fibroblasts to study tumor-associated fibroblast differentiation.* Exp Cell Res, 2001. **266**(1): p. 74–86.
167. Tanaka, H.Y., et al., *Heterotypic 3D pancreatic cancer model with tunable proportion of fibrotic elements.* Biomaterials, 2020. **251**: p. 120077.
168. Ware, M.J., et al., *Generation of an in vitro 3D PDAC stroma rich spheroid model.* Biomaterials, 2016. **108**: p. 129–42.
169. Lazzari, G., et al., *Multicellular spheroid based on a triple co-culture: A novel 3D model to mimic pancreatic tumor complexity.* Acta Biomater, 2018. **78**: p. 296–307.
170. Liu, X., et al., *3D heterospecies spheroids of pancreatic stroma and cancer cells demonstrate key phenotypes of pancreatic ductal adenocarcinoma.* Transl Oncol, 2021. **14**(7): p. 101107.
171. Giustarini, G., et al., *Characterization of 3D heterocellular spheroids of pancreatic ductal adenocarcinoma for the study of cell interactions in the tumor immune microenvironment.* Front Oncol, 2023. **13**: p. 1156769.
172. Bidan, N., et al., *Multicellular tumor spheroid model to study the multifaceted role of tumor-associated macrophages in PDAC.* Drug Delivery and Translational Research, 2024. **14**(8): p. 2085–2099.
173. Madsen, N.H., et al., *Monocyte Infiltration and Differentiation in 3D Multicellular Spheroid Cancer Models.* Pathogens, 2021. **10**(8).
174. Kuen, J., et al., *Pancreatic cancer cell/fibroblast co-culture induces M2 like macrophages that influence therapeutic response in a 3D model.* PLoS One, 2017. **12**(7): p. e0182039.
175. Morceau, F., et al., *Pancreatic Cancer Organoids: Modeling Disease and Guiding Therapy.* Cancers (Basel), 2025. **17**(23).
176. Lahusen, A., et al., *A pancreatic cancer organoid-in-matrix platform shows distinct sensitivities to T cell killing.* Sci Rep, 2024. **14**(1): p. 9377.
177. Eguren-Santamaria, I., et al., *Preclinical ex vivo and in vivo models to study immunotherapy agents and their combinations as predictive tools toward the clinic.* J Immunother Cancer, 2025. **13**(10).
178. Sontheimer-Phelps, A., B.A. Hassell, and D.E. Ingber, *Modelling cancer in microfluidic human organs-on-chips.* Nat Rev Cancer, 2019. **19**(2): p. 65–81.
179. Geyer, M. and K. Queiroz, *Microfluidic Platforms for High-Throughput Pancreatic Ductal Adenocarcinoma Organoid Culture and Drug Screening.* Front Cell Dev Biol, 2021. **9**: p. 761807.
180. Xu, H., et al., *Tumor-microenvironment-on-a-chip: the construction and application.* Cell Commun Signal, 2024. **22**(1): p. 515.
181. Schuster, B., et al., *Automated microfluidic platform for dynamic and combinatorial drug screening of tumor organoids.* Nat Commun, 2020. **11**(1): p. 5271.

182. Zhu, Y., et al., *Dynamic microphysiological system chip platform for high-throughput, customizable, and multi-dimensional drug screening.* Bioact Mater, 2024. **39**: p. 59–73.
183. Sgarminato, V., et al., *PDAC-on-chip for in vitro modeling of stromal and pancreatic cancer cell crosstalk.* Biomaterials Science, 2023. **11**(1): p. 208–224.
184. Geyer, M., et al., *The tumor stroma influences immune cell distribution and recruitment in a PDAC-on-a-chip model.* Front Immunol, 2023. **14**: p. 1155085.
185. Geyer, M., et al., *A microfluidic-based PDAC organoid system reveals the impact of hypoxia in response to treatment.* Cell Death Discov, 2023. **9**(1): p. 20.
186. Haque, M.R., et al., *Patient-derived pancreatic cancer-on-a-chip recapitulates the tumor microenvironment.* Microsyst Nanoeng, 2022. **8**: p. 36.
187. Drifka, C.R., et al., *A bioengineered heterotypic stroma-cancer microenvironment model to study pancreatic ductal adenocarcinoma.* Lab Chip, 2013. **13**(19): p. 3965–75.
188. Lai Benjamin, F.L., et al., *Recapitulating pancreatic tumor microenvironment through synergistic use of patient organoids and organ-on-a-chip vasculature.* Adv Funct Mater, 2020. **30**(48).
189. Deipenbrock, A., et al., *Modelling of the multicellular tumor microenvironment of pancreatic ductal adenocarcinoma (PDAC) on a fit-for-purpose biochip for preclinical drug discovery.* Lab Chip, 2025.
190. Heinrich, M.A., et al., *Translating complexity and heterogeneity of pancreatic tumor: 3D in vitro to in vivo models.* Adv Drug Deliv Rev, 2021. **174**: p. 265–293.
191. Vudatha, V., et al., *In vivo models of pancreatic ductal adenocarcinoma.* Adv Cancer Res, 2023. **159**: p. 75–112.
192. Bisht, S. and G. Feldmann, *Animal models for modeling pancreatic cancer and novel drug discovery.* Expert opinion on drug discovery, 2019. **14**(2): p. 127–142.
193. Kim, M.P., et al., *Generation of orthotopic and heterotopic human pancreatic cancer xenografts in immunodeficient mice.* Nature protocols, 2009. **4**(11): p. 1670–1680.
194. Pompili, L., et al., *Patient-derived xenografts: a relevant preclinical model for drug development.* Journal of Experimental & Clinical Cancer Research, 2016. **35**(1): p. 189.
195. Shultz, L.D., et al., *Humanized mice for immune system investigation: progress, promise and challenges.* Nat Rev Immunol, 2012. **12**(11): p. 786–98.
196. Shakiba, M. and D.A. Tuveson, *Macrophages and fibroblasts as regulators of the immune response in pancreatic cancer.* Nat Immunol, 2025. **26**(5): p. 678–691.
197. Weizman, N., et al., *Macrophages mediate gemcitabine resistance of pancreatic adenocarcinoma by upregulating cytidine deaminase.* Oncogene, 2014. **33**(29): p. 3812–9.
198. D'Errico, G., et al., *Tumor-associated macrophage-secreted 14-3-3ζ signals via AXL to promote pancreatic cancer chemoresistance.* Oncogene, 2019. **38**(27): p. 5469–5485.
199. Sherman, M.H. and G.L. Beatty, *Tumor Microenvironment in Pancreatic Cancer Pathogenesis and Therapeutic Resistance.* Annu Rev Pathol, 2023. **18**: p. 123–148.

200. Poyia, F., et al., *The Role of Tumor Microenvironment in Pancreatic Cancer Immunotherapy: Current Status and Future Perspectives.* Int J Mol Sci, 2024. **25**(17).
201. Shi, J., et al., *Crosstalk between the tumor immune microenvironment and metabolic reprogramming in pancreatic cancer: new frontiers in immunotherapy.* Front Immunol, 2025. **16**: p. 1564603.
202. Jin, G., et al., *Histone deacetylase inhibitors enhance endothelial cell sprouting angiogenesis in vitro.* Surgery, 2011. **150**(3): p. 429–35.
203. Wong, S.H.M., et al., *E-cadherin: Its dysregulation in carcinogenesis and clinical implications.* Crit Rev Oncol Hematol, 2018. **121**: p. 11–22.
204. Kim, D.J., et al., *Suppression of TGFβ-mediated conversion of endothelial cells and fibroblasts into cancer associated (myo)fibroblasts via HDAC inhibition.* Br J Cancer, 2018. **118**(10): p. 1359–1368.
205. Väyrynen, S.A., et al., *Composition, Spatial Characteristics, and Prognostic Significance of Myeloid Cell Infiltration in Pancreatic Cancer.* Clin Cancer Res, 2021. **27**(4): p. 1069–1081.
206. Blise, K.E., et al., *Machine Learning Links T-cell Function and Spatial Localization to Neoadjuvant Immunotherapy and Clinical Outcome in Pancreatic Cancer.* Cancer Immunol Res, 2024. **12**(5): p. 544–558.
207. Carter, J.A., et al., *Overcoming CXCR4-Mediated T-Cell Exclusion Potentiates Antitumor Cytotoxicity in Fibrolamellar Carcinoma.* Gastroenterology.
208. Feig, C., et al., *Targeting CXCL12 from FAP-expressing carcinoma-associated fibroblasts synergizes with anti-PD-L1 immunotherapy in pancreatic cancer.* Proc Natl Acad Sci U S A, 2013. **110**(50): p. 20212–7.
209. James, T.N., et al., *Organoid Modeling of the Tumor Immune Microenvironment.* Cell, 2018. **175**(7): p. 1972–1988.e16.
210. Daunke, T., et al., *Expression and role of the immune checkpoint regulator PD-L1 in the tumor-stroma interplay of pancreatic ductal adenocarcinoma.* Front Immunol, 2023. **14**: p. 1157397.
211. Yu, C., R. Kang, and D. Tang, *Organoids Models of Pancreatic Duct Adenocarcinoma*, in *Ferroptosis: Methods and Protocols*, G. Kroemer and D. Tang, Editors. 2023, Springer US: New York, NY. p. 45–60.
212. Gout, J., et al., *Pancreatic organoids as cancer avatars for true personalized medicine.* Adv Drug Deliv Rev, 2025. **224**: p. 115642.
213. Beutel, A.K., et al., *A Prospective Feasibility Trial to Challenge Patient–Derived Pancreatic Cancer Organoids in Predicting Treatment Response.* Cancers, 2021. **13**(11): p. 2539.
214. Bi, Y., et al., *Tumor-on-a-chip platform to interrogate the role of macrophages in tumor progression.* Integr Biol (Camb), 2020. **12**(9): p. 221–232.
215. Adnan, D., et al., *A Patient-Derived Organ-on-Chip Platform for Modeling the Tumor Microenvironment and Drug Responses in Pancreatic Cancer.* Adv Sci (Weinh), 2026: p. e08934.
216. Zushin, P.-J.H., S. Mukherjee, and J.C. Wu, *FDA Modernization Act 2.0: transitioning beyond animal models with human cells, organoids, and AI/ML-based approaches.* The Journal of Clinical Investigation, 2023. **133**(21).
217. Russell, W. and R. Burch, *The Principles of Humane Experimental.* Technique London: Methuen, 1959.
218. Ma, C., et al., *Organ-on-a-Chip: A New Paradigm for Drug Development.* Trends Pharmacol Sci, 2021. **42**(2): p. 119–133.

219. Perez, V.M., J.F. Kearney, and J.J. Yeh, *The PDAC Extracellular Matrix: A Review of the ECM Protein Composition, Tumor Cell Interaction, and Therapeutic Strategies.* Front Oncol, 2021. **11**: p. 751311.
220. Cao, U.M.N., et al., *Microfluidic Organ-on-A-chip: A Guide to Biomaterial Choice and Fabrication.* Int J Mol Sci, 2023. **24**(4).
221. Szekerczés, T., et al., *Exploration of Patient-Derived Pancreatic Ductal Adenocarcinoma Ex Vivo Tissue for Treatment Response.* Antioxidants (Basel), 2023. **12**(1).
222. Moro, C.F., et al., *Drug-induced tumor-specific cytotoxicity in a whole tissue ex vivo model of human pancreatic ductal adenocarcinoma.* Front Oncol, 2022. **12**: p. 965182.
223. Konopka, J., et al., *Multi-Organ-on-Chip approach to exploring breast cancer liver metastases concerning the endothelial barrier and the influence of immune cells.* Nanomedicine, 2026. **71**: p. 102890.
224. Vasconez Martinez, M.G., M. Frauenlob, and M. Rothbauer, *An update on microfluidic multi-organ-on-a-chip systems for reproducing drug pharmacokinetics: the current state-of-the-art.* Expert Opin Drug Metab Toxicol, 2024. **20**(6): p. 459–471.

6 Appendix

List of supplementary Figures

Supplementary Figure 2.1 1	Upregulation of E-cadherin expression in PANC-1 cells. PANC-1 cells were treated with MPK544, SAHA and tubastatin A for 72 h. mRNA levels of E-cadherin in PANC-1 cells were analyzed by qRT-PCR (A) and at the protein level by western blot (B, C). Representative western blots are shown (B). Error bars indicate the standard errors of the mean (of at least three independent experiments, with * = $p \leq 0.05$; ** = $p \leq 0.01$; *** = $p \leq 0.001$; and **** = $p \leq 0.0001$).
Supplementary Figure 2.1 2	E-cadherin expression in PANC-1 spheroids after 72h of treatment with MPK544 or SAHA. DAPI-staining of nuclei (405 nm); staining of the proliferation marker Ki67 (488 nm); staining of E-cadherin (647 nm); merging of all three channels. Imaging of spheroids with the CQ1 High-Content Spinning Disk System (Yokogawa Electric Corporation). IC50 values for PANC-1 spheroids are 2.17µM for SAHA and 2.20 µM for MPK544.
Supplementary Figure 2.2 1.	Permeability assay of HUVEC layer. FITC dextran assay was performed to measure the barrier integrity of the HUVEC layer after 72 h under static or flow conditions and in the presence or absence of co-culture spheroids, with or without the addition of Matrigel. FITC dextran solution was added into the top channel. After 1 h the leakage into the middle channel was determined via fluorescence measurement. Error bars indicate the standard errors of the mean of three independent experiments, with **= $p \leq 0.01$.
Supplementary Figure 2.2 2.	Integrity of the vasculature consisting of HUVEC in the presence of co-culture spheroids in the biochip after 72 h. The vasculature remains stable in the presence of the co-culture spheroids under static conditions (top row). In the presence of the spheroids and under flow conditions, the endothelial cells do not show a stable vasculature (bottom row). The endothelial markers VE-cadherin (green), von Willebrand factor (vWF; red) and the nuclear dye DAPI (blue) were stained. Representative image of several random field images. Scale bar is 200 µm.
Supplementary Figure 2.2 3	Cytokine expression in PANC-1 cells, PSC cells, co-culture spheroids and PANC-1 spheroids. PANC-1 cells, PSC cells, co-culture spheroids and PANC-1 spheroids were cultivated for 72h in 3D medium.

	mRNA levels of TNF-α (A), IL-8 (B), and IL-6 (C) were analyzed by qRT-PCR. Error bars indicate standard errors of mean (of at least three independent experiments, with; ** = p ≤ 0.01; *** = p ≤ 0.001; and **** = p ≤ 0.0001)
Supplementary Figure 2.2 4	Cultivation of HUVEC in the biochip. HUVEC were cultivated in the presence of conditioned media from co-culture spheroids for 72 h under static (top row) or flow (bottom row) conditions. The endothelial markers vascular endothelial (VE-) cadherin (green), von Willebrand factor (vWF; red) and the nuclear dye DAPI (blue) were stained. Representative image of several random field images. Scale bar is 200 µm.
Supplementary Figure 2.2 5	Live / Dead staining of HUVEC layer after treatment with SAHA. HUVECs were stained with Calcein (green) and Ethidium homodimer-1(red) after 72 h treatment with 1.5, 2.5 or 3.5 µM SAHA, untreated cells served as control. Green staining shows viable cells, red staining indicates dead cells. Representative image of several random field images. Scale bar is 200 µm.
Supplementary Figure 2.2 6	IF staining of PANC-1 spheroids after addition of primary monocytes. PANC-1 spheroids were seeded into 96-well plates and primary monocytes were added at day 4 of the cultivation. After 72 h of co-cultivation the PANC-1 spheroids were stained for the tumor cell marker Ki67 (green), the immune cell marker CD45 (purple), and the M2 marker CD163 (red); merging of all channels. Shown as maximum intensity projection MIP of a z-Stack. Scale is 500 µm.
Supplementary Figure 2.2 7	Time course of macrophage polarization after infiltration of the co-culture spheroids. $CD14^+$ monocytes were added to 4-day-old spheroids and were analyzed by flow cytometry 72 h, 96 h, and 168 h after infiltration. Macrophages identified as $CD11b^+$ and $CD45^+$ were analyzed for surface expression of (A) CD163, (B) CD206, (C) CD86, and (D) HLA-DR. Infiltrated cells were compared to unstimulated monocytes as controls. Error bars indicate the standard errors of the mean of three independent experiments, with * = p ≤ 0.05; ** = p ≤ 0.01; ***= p ≤ 0.005; **** = p ≤ 0.0001.
Supplementary Figure 2.3 1	Workflow for quantification of $CD4^+$ and $CD8^+$ T cells in PDAC tissue slices. Formalin-fixed paraffin-embedded (FFPE) tissue slices were subjected to immunofluorescence staining for CD4 and CD8, followed by nuclear counterstaining with DAPI. Individual nuclei were segmented based on DAPI staining, and CD4/CD8 fluorescence intensity was

	quantified in the vicinity of each nucleus. Cells were classified as $CD4^+$ or $CD8^+$ according to predefined marker-specific fluorescence intensity thresholds applied uniformly across all samples. The total number of $CD4^+$ and $CD8^+$ T cells was quantified per image and summarized for each patient. The schematic illustrates representative identification of $CD4^+$/$CD8^+$ T cells, nucleus-based cell assignment, and subsequent quantification of T-cell subset frequencies. Created with BioRender.
Supplementary Figure 2.3 2	Overview of the semi-automatic spheroid analysis pipeline. Three-channel raw images (A) were separated by channel and quantile normalized (B). The TWANG segmentation algorithm was used for instance segmentation of the T-cells (C). The shell's interior region was manually defined using a graphical user interface (D) and T-cell segmentations were associated with the interior/exterior region, respectively, based on their overlap with the manually defined interior region. Quantifications include distance distributions of T-cells from the interior centroid as well as absolute counts and occurrence frequencies of T-cells in the interior/exterior regions (E).
Supplementary Figure 2.3 3	CXCL12 and CXCR4 expression. mRNA Expression levels of CXCL12 and CXCR4 were analyzed by RT-PCR. (A) Comparison of different mRNA levels in PANC-1, PSC, Co-culture spheroids, PANC-1 monospheroids, and naïve CD3 T-cells isolated from healthy donors PBMC. (B) Expression of CXCL12 and CXCR4 mRNA levels in patient-derived tumor cells, CAF, patient-derived spheroids and CD3 T-cells isolated form the patients PBMC. Error bars indicate the standard errors of the mean of three independent experiments, with * = $p \leq 0.05$; ** = $p \leq 0.01$; **** = $p \leq 0.0001$.
Supplementary Figure 2.3 4	Characterization of primary patient-derived cells. Representative immunofluorescence images are shown. (A) Primary tumor cells were isolated form primary PDAC tumor tissue. Expression of tumor cell markers was analyzed conducting immunofluorescence staining. The following markers were co-stained with the nuclei (blue): vimentin, pan cytokeratin, cytokeratin 7, E-cadherin, CD44, Epcam, Ki67, and N-cadherin. (B) Immunofluorescence staining of primary CAF for the fibroblast marker α-SMA (green) and the nuclei (blue). Magnification 40x, scale bar 100 µm.

Supplementary Figure 2.3 5	Composition of patient-derived spheroids (PDS). Representative immunofluorescence images of a PDS are shown. Spheroids composed of patient derived tumor cells and patient derived CAF were generated and stained for the fibroblast marker α-SMA (red), the and the tumor cell marker cytokeratin 7 (green), and the nuclei (blue) Shown are representative maximum intensity projections (MIP) from a whole z-stack for the single channels alongside a merge of all fluorescence channels. Scale bar, 500 µm; magnification, 10×.
Supplementary Figure 2.3 6	IFN-γ, Granzyme B and perforin protein expression following treatment with pembrolizumab. Patient-derived spheroids were infiltrated with $CD3^+$ T-cells isolated from autologous patient-derived PBMC. Pembrolizumab (10 µg/mL) was added at the time of T-cell infiltration and maintained for 72 h. IFN-γ (A), Granzyme B (B) and perforin (C) expression in $CD8^+$ T-cells were quantified by flow cytometry. Data represent the mean ± SEM of three independent experiments. Statistical significance is indicated as *$p \leq 0.05$.
Supplementary Figure 2.3 7	Effect of pembrolizumab treatment on PD-1 surface expression. PANC-1 spheroids were generated prior to infiltration with $CD3^+$ T-cells isolated from peripheral blood mononuclear cells (PBMC) of healthy donors. Pembrolizumab (1 µg/mL or 10 µg/mL) was added at the time of T-cell infiltration and maintained for 72 h. Representative flow cytometry histograms depicting PD-1 surface expression in $CD4^+$ (A) and $CD8^+$ (B) T-cells following 72 h of pembrolizumab treatment. Quantitative analysis of PD-1 expression in $CD4^+$ (C) and $CD8^+$ (D) T-cells after 72 h of treatment. Untreated spheroids served as controls.

List of supplementary Tables

Supplementary Table 2.2.1	Gradient for UHPLC / HRMS measurement.
Supplementary Table 2.2.2	The cytotoxic efficacy of the HDAC inhibitor vorinostat represented by the respective IC50 values in 2D HUVEC cultures as well as in 3D PANC-1 spheroids and co-culture spheroids after 72 h incubation. The arithmetic means and their respective standard deviations of three independent experiments are depicted.
Supplementary Table 2.3.1	Clinicopathological characteristics of the PDAC patient cohort included in this study.

List of Schemes

Scheme 2.1.1.	Derivatisation of **KSK64**
Scheme 2.1.2	Retrosynthetic analysis of **MPK544**
Scheme 2.1.3	Synthesis of 7-amino-N-(benzyloxy)heptanamide 5. i) 1.50 eq hydroxylamine-O-sulfonic acid, HCO2H; ii) 1.00 eq nBuLi, 1.00 eq Boc2O, THF; iii) 10.0 eq LiOH, THF/H2O iv)
Scheme 2.1.4.	Synthesis of the **MPK544** (8). i) 0.330 eq triphosgene, 1.00 eq DIPEA, DCM; ii) H2, Pd/C, MeOH

Publications and participation at scientific conferences

Publications

Deipenbrock, A. et al. (2026), Targeting stroma-mediated T-cell exclusion and functional exhaustion in pancreatic ductal adenocarcinoma (PDAC) through CXCR4 and PD-1 blockade, submitted to Front. Immunol. - Cancer Immunity and Immunotherapy (First author)

Deipenbrock, A., Wilmes, B.E., Sommermann, T., et al. (2025). Modelling of the multicellular tumor microenvironment of pancreatic ductal adenocarcinoma (PDAC) on a fit-for-purpose biochip for preclinical drug discovery. Lab on a Chip, 25(9), 2168–2181. https://doi.org/10.1039/d4lc01016g (First author; cover article), **awarded for the Paper of the 2nd Quarter 2025 by the 3R network NRW**

Schiedlauske, K., **Deipenbrock, A.**, Pflieger, M., et al. (2024). Novel Histone Deacetylase (HDAC) Inhibitor Induces Apoptosis and Suppresses Invasion via E-Cadherin Upregulation in Pancreatic Ductal Adenocarcinoma (PDAC). Pharmaceuticals, 17(6), 752. https://doi.org/10.3390/ph17060752 (Co-first author)

El-Kashef, D.H., Obidake, D.D., **Deipenbrock, A.**, Schiedlauske, K., et al. (2023). Indole Diketopiperazine Alkaloids from the Marine Sediment-Derived Fungus Aspergillus chevalieri against Pancreatic Ductal Adenocarcinoma. Marine Drugs, 22(1), 5. https://doi.org/10.3390/md22010005 (Co-author)

Conference Participations

3rd Annual Meeting of the 3R Competence Network NRW, Vaals, Netherlands - November 2025

- Oral presentation:" Modelling of the multicellular tumor microenvironment of pancreatic ductal adenocarcinoma (PDAC) on a fit-for-purpose biochip for preclinical drug discovery"

Cold spring harbor laboratory Meeting "Bioengineered tissue systems & models", New York, USA -September 2025

- Oral presentation: „A 3D immunocompetent PDAC model reflects the T-cell checkpoint profiles observed in patients"

European pancreas congress, Düsseldorf, Germany -July 2023

- Poster presentation:" Comparative spatial analysis of M2 macrophage polarization in a human pancreatic ductal adenocarcinoma (PDAC) tumor microenvironment-on-chip model and in patient-derived tumor slices"

GRK 2158 Retreat, Naples, Italy - March 2025

- Oral presentation: "Immunocompetent 3D pancreatic adenocarcinoma (PDAC) biochip model for preclinical drug testing"
- Session chair

Leipzig Immune ONcology Conference (LION), Leipzig, Germany - November 2024

- Poster presentation:" Immune competent 3D pancreatic adenocarcinoma (PDAC) organoid-on-chip model for preclinical drug testing"

German Pancreas congress, Bonn, Germany – March 2024

- conference participation

Danksagung

An dieser Stelle möchte ich mich bei all den Leuten bedanken, die mich während meiner Promotion begleitet und unterstützt haben. Ohne diese Hilfe wäre diese Dissertation nicht in dieser Form möglich gewesen.

Einen besonderen Dank möchte ich Prof. Dr. Nicole Teusch aussprechen. Danke für die Unterstützung meines Forschungsprojektes mit fortwährendem Interesse und großem Engagement. Ich danke, für die kritischen und konstruktiven wissenschaftlichen Diskussionen, die vertrauensvolle Betreuung, sowie die kontinuierliche Förderung meiner fachlichen Weiterbildung. Gleichermaßen danke ich ebenso PD. Dr. Rüdiger Sorg, der meine Doktorarbeit als zweiter Gutachter und Mentor betreut hat.

Für die vielfältige Unterstützung im Rahmen gemeinsamer Kooperationen bedanke ich mich bei allen Leuten aus dem IMPACT Team, namentlich: Knut Rennert, Martin Raasch, Thomas Sommer und Amélie Paillereau. Danke für Eure Unterstützung und den wertvollen wissenschaftlichen Austausch und die praktische Einarbeitung. Darüber hinaus danke ich dem Team des Pius' Hospital Oldenburg, insbesondere Timur Cetin, Prof. Dr. Dirk Wehye, Martin Hoffmann, und Verena Uslar, für den wertvollen Einblick in die klinische Realität von PDAC-Patienten und die Möglichkeit mit primärem Material zu arbeiten.

Mein besonderer Dank gilt zudem Martina Holz sowie dem Graduiertenkolleg 2158, die meine wissenschaftliche Entwicklung während meiner Promotion durch zahlreiche Veranstaltungen, Fortbildungen und internationale Konferenzen maßgeblich gefördert und geprägt haben.

Ganz besonders danke ich den gesamten aktuellen und ehemaligen Mitgliedern der AG Teusch Dina El-Kashef, Ying Gao, Katja Schiedlauske, Vanessa Wiegand, Lina Hofer, Yuan Wie, Katja Friedrich, Simone Miljanovic, Claudia Eckelskemper, Dounia Asskali, Anna-Lena Wurz, Kyra Moustakas, Ben Eric Wilmes, Katharina Reich, Cheyenne Prat-Marques, und Johanna Hölken, die mich während meiner Promotion begleitet haben. Ihr habt mich stets ermutigt und jederzeit unterstützt es war mir eine große Freude mit euch gemeinsam zu arbeiten.

Insbesondere danke ich hier Kyra und Eric, die mit ihren Abschlussarbeiten maßgeblich zu dem Erfolg dieses Projektes beigetragen haben. Vielen Dank, dass ihr

mir immer zur Seite standet und mir euer Vertrauen für die Mitbetreuung euerer Abschlussarbeiten geschenkt habt.

Liebe Katja F., liebe Katja S., liebe Vanessa und liebe Lina euch danke ich ganz besonders für eure stetige Unterstützung, dafür dass ihr immer ein offenes Ohr für mich hattet und mich durch alle Höhen Tiefen stets motivierend begleitet habt. Ich werde die gemeinsame Zeit mit euch sehr vermissen!

Ein großer Dank geht an meine Freunde, die mich stets unterstützt haben. Ihr wart immer verständnisvoll und habt mir gezeigt, dass es etwas ganz Besonderes ist, was ich erreicht habe. Ich danke euch für eueren Rückhalt und euer Interesse und euren Zuspruch.

Ich danke ganz besonders meinem Freund Manuel. Du bist meine größte Stützte auf die ich mich immer verlassen kann. Ich danke dir für dein Verständnis, deine Geduld und deine stetige Motivation meinen eigenen Weg zu gehen, besonders in Momenten wo mir dies schwerfällt.

Bei meiner Familie möchte ich mich ganz besonders bedanken. Lieber Papa, lieber Nick, liebe Silvia vielen DANK für eure bedingungslose Unterstützung, eure Bereitschaft immer zu verstehen, wie mein Projekt vorangeht und dabei mich als Person nie aus den Augen zu verlieren. Zuletzt möchte ich meiner Mama danken, dafür dass du mich zu einem neugieren und stets wissbegierigen Menschen erzogen hast und mich dabei immer motiviert hast meinen eigenen Weg zu gehen. Auch wenn du diese Arbeit nicht mehr lesen kannst, widme ich diese dir.

Eidesstattliche Erklärung

Hiermit erkläre ich, Alina Deipenbrock, an Eides statt, dass die vorliegende Dissertation von mir selbstständig und ohne unzulässige fremde Hilfe unter Beachtung der „Grundsätze zur Sicherung guter wissenschaftlicher Praxis an der der Heinrich-Heine Universität Düsseldorf“ erstellt worden ist. Die Dissertation wurde in der vorgelegten oder in ähnlicher Form noch bei keiner anderen Fakultät eigereicht. Ich habe bisher keine erfolglosen und erfolgreichen Promotionsversuche unternommen.

Krefeld, 10.06.2026

Alina Deipenbrock